Recovery from Waste Streams: Working Towards a Sustainable Future

Helen L. Parker

PhD

University of York
Department of Chemistry

April 2013

Abstract

The overall aim of this project was to utilise green chemistry methodology to capture potentially harmful, toxic or valuable compounds from wastewater.

Novel mesoporous materials, Starbon®, prepared from naturally abundant polysaccharides, have demonstrated significant potential as adsorbents for the uptake of a range of dyes and phenols. Through the use of different polysaccharide starting materials (starch and alginic acid) and different preparation temperatures, six materials were produced. The resulting materials were characterised by techniques including: solid-state NMR, nitrogen porosimetry, FT-IR, x-ray photoelectron spectroscopy and electron microscopy. The experimental results revealed that the materials exhibited high efficiency to remove dyes and phenols from aqueous media due to their high mesoporous nature. The adsorption process was described well by the Langmuir, Freundlich and Dubinin-Radushkevich isotherms. Thermodynamic analysis of the results indicated that adsorption was a physical process.

Investigations into the capture of palladium from liquid waste and also greener methods of supported nanoparticle formation were also carried out. Biosorption of palladium by alginic acid and seaweed was highly successful, resulting in nanometer sized palladium deposits within the adsorbent. The catalytic activity of these materials was successfully demonstrated through the use of Heck and Suzuki reactions.

Preliminary work exploring the first use of living plants to recover palladium from water and in situ production of catalytically active palladium nanoparticles also is presented. This novel process eliminates the necessity for nanoparticle extraction from the plant and reduces the number of production steps compared to traditional catalyst palladium on carbon. These plant catalysts have demonstrated high catalytic activity in a range of C-C coupling reactions, outperforming traditionally used palladium catalysts.

Table of Contents

List of Figures and Tables

Chapter 1. Introduction

Chapter 2. Starbon® characterisation and application in dye adsorption

Chapter 3. Use of Starbon® for adsorption of phenolics

Chapter 4. Elemental sustainability and prospects for elemental recovery

Chapter 5. Direct synthesis of palladium nanoparticles on alginic acid and seaweed supports

Chapter 6. Nano-palladium catalysts directly from plants

Chapter 7. Experimental

Chapter 9. Appendix

Acknowledgements

Firstly, a massive thanks to everyone who was involved in the making of this thesis. Special thanks go to James and Andy, two fantastic supervisors. You are such an inspiration to me and I cannot thank you enough for the time, opportunities and support you have given me throughout my PhD. Next to Vitaly, I am so grateful to have been given the chance to work with you. Your guidance has been invaluable to me, thank you for teaching me so much. I will never cease to be astounded by the breadth and depth of your knowledge.

For general scientific, laboratory and emotional support throughout my time in York I would like to thank Duncan, Simon, Paul and Alison. I really couldn't have done this without all of your help. Thank you to Jennie for mentoring me on my arrival at the GCC and for your continued collaboration. My thanks also go to the past and present members of the GCC for your ideas, support, assistance, general banter and lots of drinking that has helped me stay sane through the highs and lows of PhD'dom! In particular, Jo and Lucie for the many cocktails, glasses of wine and hours spent gossiping! I have been so lucky to make such truly wonderful friends during my time here.

I would also like to send special thanks out to all of my amazing friends both in York and all over the world that I have collected along the way (you know who you are). Your friendships are all so special to me and spending time with you has provided welcome distraction from the PhD stress. To my family both Parker's and Andrew's, especially my brothers Iain and David, thank you for all of your love and encouragement.

And finally, my very special thanks to Steve. You are my best friend, my partner and my rock. You have helped me through every stage of this, celebrating the successes and cheering my up when it has all seemed bleak. I love you and it wouldn't have been the same without you.

Declaration

Some of the results presented in this thesis were obtained through collaboration with others, details as follows:

- Chapter 2 – SEM images (A-C) obtained by Dr Andrew Hunt.
- Chapter 4 – Research for sections of this chapter was carried out with the assistance of Dr J. Dodson.
- Chapter 5 – Impregnation of seaweed was carried out by Dr J. Dodson.
- Chapter 6 – Arabidopsis plants were grown by Dr L. Rylott.

All other results are the work of the author. Aspects of work presented in this thesis have been included in publications, references as follows:

- H. L. Parker, A. J. Hunt, V. L. Budarin, P. S. Shuttleworth, K. L. Miller & J. H. Clark, The importance of being porous: polysaccharide-derived mesoporous materials for use in dye adsorption. *RSC Advances*, 2012, 2, 8992-8997
- J. R. Dodson, A. J. Hunt, H. L. Parker, Y. Yang & J. H. Clark, Elemental sustainability: towards the total recovery of scarce metals, *Chemical Engineering and Processing: Process Intensification*, 2012, 51, 69-78
- Book chapter titled “Mining municipal waste: prospective for elemental recovery” authored by J. Dodson and H. L. Parker for book called “Elemental Recovery and Sustainability”, edited by A. J. Hunt, RSC Publishing, London, 2013

The work presented in this thesis has not previously been submitted for a degree at this or any other university.

Helen L. Parker

2013

Chapter 1

Introduction

Chapter 1.

Introduction

During the nineteenth century it was the common belief that nature could provide a seemingly endless supply of raw materials for industry. The volume of natural resources available seemed insurmountably vast and perpetually regenerating regardless of how much was taken or what pollution was released into it.*(1)* We now know this could not be further from the truth. Today it is well understood that the demands placed upon the natural world have gone far beyond what it is able to sustain.

Green chemistry, defined by Paul Anastas and John Warner as "the design of chemical products and processes that reduce or eliminate use and generation of hazardous substances", strives to bridge the gap between developing efficient manufacturing and sustaining the environment.*(2)*

The chemical industry defines environmental impact or risk of processes by:

$$\text{Risk} = \text{Hazard} \times \text{Exposure}$$

Traditionally, this risk has been reduced by controlling exposure, however green chemistry takes the alternative approach aiming to limit risk by reducing hazard.*(3)* The term hazard in this context refers to anything that may threaten human or environmental health, such as; toxicity, physical risks, global climate change and resource depletion.*(4)*

This thesis will go on to present work focused on utilising green chemistry methodology in order to limit the known hazards of certain chemical processes, specifically focusing on reducing hazard by eliminating resource depletion.

1.1 Waste & what it's costing us

Waste is an easily identifiable problem facing society today. Whether it is the CO_2 emissions from power stations, household refuse or contaminated water from a chemical plant, it is a problem that requires tackling.

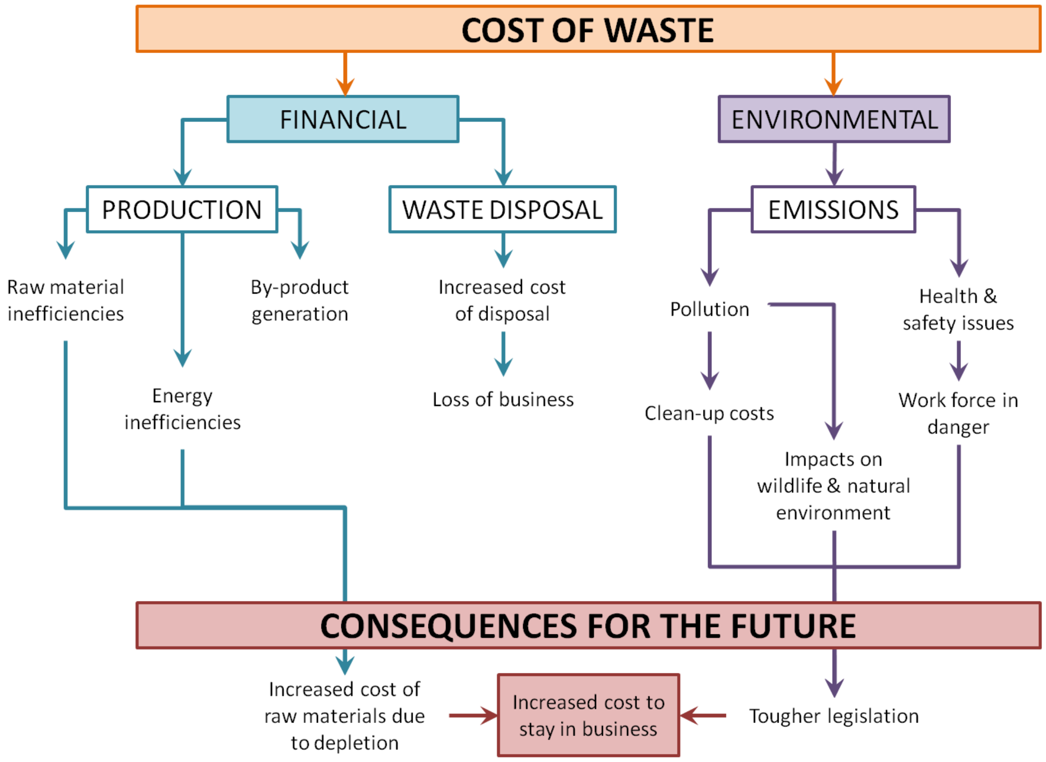

Figure 1.1 Diagram showing the cost of waste and its potential impact on business in the future.*(5)*

The cost of waste can be enormous both financially and environmentally (Figure 1.1). In the USA waste disposal costs run to the hundreds of billions of dollars per year.*(5)* Although the environmental cost cannot be so easily quantified, released waste can devastate wildlife populations and lead to brain damage in humans.*(6)*

Whilst legislation has been effective in improving environmental conditions by limiting the release of hazardous chemicals, they are still being discharged in considerable amounts. In 2000 the USA released 7 billion lbs (3.2×10^8 kg) of toxic waste into the environment.*(3)* There is also the problem that developing countries do not enforce the same emissions standards and thus huge quantities of waste are released directly into the environment.*(7)*

1.2 Treatment of chemically contaminated wastewater

Of all the water on the planet 97.5% is present as sea water, the other 2.5% is fresh water of which, 1.75% is trapped in polar caps and glaciers and only the remaining 0.75% is potentially available for use (Figure 1.2 (a)). In reality, it is only 0.007% of the world's water that is readily accessible for direct human use.(*8*)

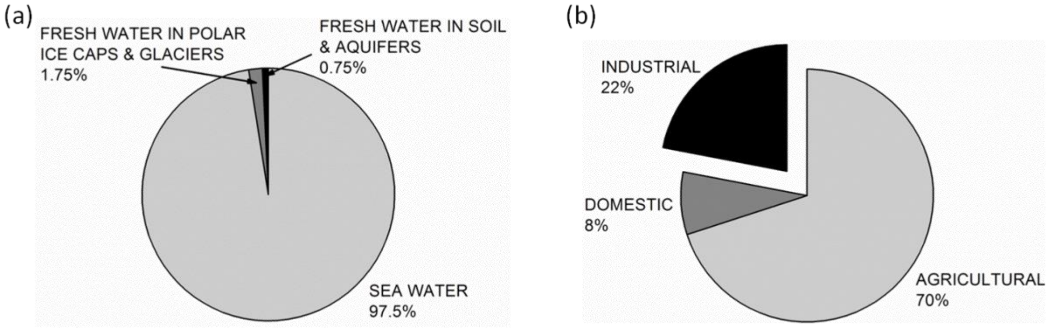

Figure 1.2 Pie charts of (a) water distribution on Earth and (b) proportion of fresh water used by different sectors.(*8*)

The use of this small percentage of clean, fresh water is dominated by agriculture (70%), followed by industry (22%) and domestic (8%) (Figure 1.2 (b)).(*8, 9*) Water consumption is dramatically increasing due to demographic growth and the expansion of industrial activity, whilst its supply remains constant.*(7)* As a result of limited water availability the control of water pollution is of significant importance. Unfortunately every sector that uses water also produces wastewater that requires treatment prior to it being safe for reuse.

1.2.1 Potential wastewater contaminants

Industries such as, agro-processing, textile dyeing, abattoirs and tanneries can cause the presence of toxic chemicals in water.(*10*) The potential contamination of fresh water supplies with this waste is one of the key environmental issues we are facing today.(*11*)

A wide variety of pollutants are released in wastewater but they can easily be separated into three categories:

- *Biological*: The biological agents are typically bacterial, e.g. *Salmonella typhosa*, which occur in domestic and sewage effluent.(*12*) The presence of bacteria in water is dangerous as it can lead to water borne diseases like typhoid.
- *Heat*: Due to the high heat capacity of water it is commonly used as a cooling medium and as a result many industrial plants release water carrying excess heat into the environment. This increasing water temperature can have adverse effects on aquatic life and water quality.(*12*)
- *Chemical*: Heavy metals, dyes, phenols, detergents, pesticides and polychlorinated biphenyls are the most commonly occurring chemicals found in wastewater.(*12*) Although the compounds are usually present only at low concentrations many threaten considerable toxicological and ecotoxicological concerns.(*11*)

1.2.2 Wastewater treatment methodologies

Of interest to this thesis is the treatment and removal of *chemically* contaminated wastewater. Figure 1.3 shows the path of polluted water from production to treatment.(*12*) Methods of water treatment are a heavily researched area and thus a wide variety of different techniques exist. The most widely investigated are physical techniques due to their relative ease and adaptability.

The feasibility of any wastewater recycling technique relies on the cost of construction, operation and maintenance it requires. Adsorption is considered the best and most universal of all of the physical techniques available, as it can be used for a wide variety of different treatments. It is also rapid, effective and low cost for set up and operation (Table 1.1).(*9*)

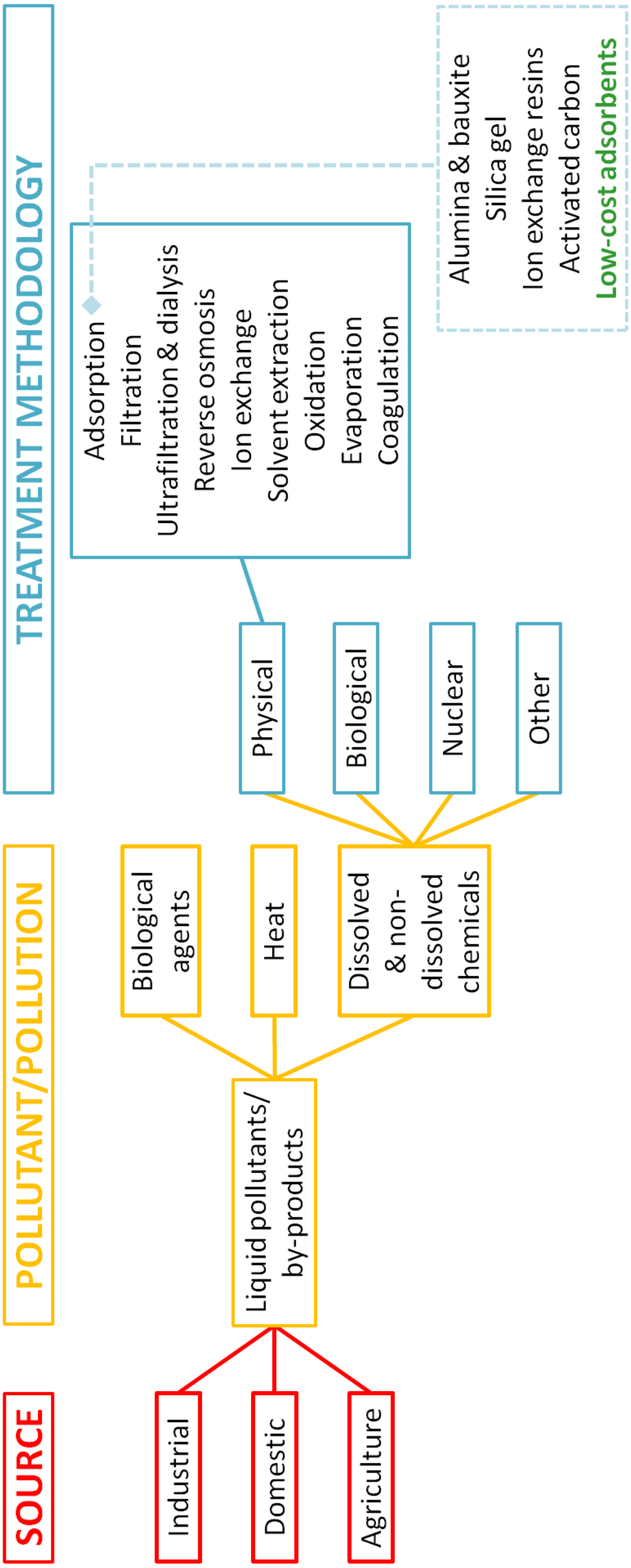

Figure 1.3 Schematic showing path of pollution in wastewater from generation to treatment.

Table 1.1 Cost of wastewater treatment methodology.(*9*)

Treatment methodology	Cost [US $/1,000,000 L water treated]
Adsorption	50-150
Filtration	25-450
Ultrafiltration & dialysis	15-400
Reverse osmosis	20-450
Ion exchange	50-200
Solvent extraction	250-2500
Oxidation	100-2000
Evaporation	15-200
Coagulation	25-500

A range of different adsorbents are available for adsorption applications, including alumina and bauxite, silica gel and activated carbons (Figure 1.3).

1.2.2.1 Alumina and bauxite

These adsorbents are effective for the removal of heavy metals from aqueous waste streams.*(13)* Bauxite is an alumina containing mineral and can be used as is, alternatively the alumina can be extracted and is also an effective adsorbent. This material was very popular in the 1990's and early 2000's although it is not commonly used today. The likely reason for this drop in popularity is the rising price of alumina which has increased from approximately $130 per ton in 1995 to $430 per ton in 2011.*(14, 15)*

1.2.2.2 Silica gel

Silica gels are useful adsorbents due to their porous texture, high surface area and mechanical stability.*(16)* However, these materials have some limitations that restrict their appeal as adsorbents; siliceous materials have a low resistance to alkali media and are therefore only able to be used in acidic solutions.*(17)* The porosity of the materials also tends to be in the microporous size range, limiting their use with large molecules, for example, dyes.

1.2.2.3 Activated carbon

These are the most popular materials used for adsorption. The US Environmental Protection Agency has named them as one of the best environmental control technologies available.*(17)* Coal is the most common starting material for activated carbons, although theoretically any carbonaceous starting material could be used.(*18*) Activated carbons offer very high surface areas and porosities which are essential to good adsorptive performance. Their adsorption is non-specific and so can be applied to a variety of different types of contamination, although their microporosity makes them less effective for larger molecules. As with the other materials studied it is cost that can limit large scale use of this material.(*17, 19*)

Due to the problems associated with these conventional adsorbents, namely high cost, research interests have turned towards finding alternative, low-cost adsorbents.(*19*)

1.2.3 Non-conventional, low-cost adsorbents

An adsorbent can potentially be considered low-cost if it requires little processing, is abundant in nature or it is a by-product or waste material from another industry.(*20*) A search of literature reveals the variety of different natural materials and waste being tested as adsorbents (Table 1.2).

Of these different materials the most abundant are natural zeolites, clays and chitin (or chitosan). Despite these materials being low cost and widely available there are a number of drawbacks that makes them less appealing from a green chemistry perspective. Firstly, natural zeolites and clays require energy input to extract them from their deposits in the ground, also processing is required to isolate the correct forms of the materials for use.(*21*) With regard to chitin there are also environmental problems associated with extraction and processing to retrieve chitin from crustacean waste. There is also a further deacetylation step to form the usable material chitosan.*(17)*

Table 1.2 Alternative adsorbent materials and surface area of adsorbents.

Material	Surface area of adsorbent [m^2 g^{-1}]	Ref.
Treated cotton	-	(*22*)
Chitosan	0.5	(*23*)
Hazelnut shell	441 ^{a}	(*24*)
Saw dust - walnut	-	(*25*)
Corncob	943 ^{a}	(*26*)
Activated sewage sludge	390 ^{a}	(*27*)
Soy meal hull	0.8	(*28*)
Banana peel	22	(*29*)
Orange peel	22	(*29*)
Fly ash	5.5	(*30*)
Hen feathers	-	(*31*)
Clay - kaolinite	3.8	(*32*)
Eucalyptus bark	0.6	(*33*)
Hair	-	(*34*)
Apricot shell	783 ^{a}	(*35*)
Dead fungus	-	(*36*)
Yellow passion fruit	30	(*37*)
Guava leaf powder	-	(*38*)
Beer brewery waste	4.5	(*39*)
Jack fruit peel	-	(*40*)
Spent tea leaves	0.8	(*41*)
Sunflower stalks	1.2	(*42*)
Plum kernel	353 ^{a}	(*26*)
Sugar-industry-mud	-	(*43*)
Natural zeolite	16	(*44*)
Red mud	-	(*45*)
Garlic peel	0.6	(*46*)

^{a}Surface area increased due to processing of adsorbent feedstock.

Next only to cellulose, starch is the most abundant carbohydrate in the world.*(17)* Starch offers the advantages of natural zeolites, clays and chitin in that it is low cost due to its plentiful supply. It also has the added advantage of not requiring extraction from the ground or significant chemically and energetically demanding isolation from a waste stream. Unfortunately the properties of starch limit its usefulness as an adsorbent material: it offers virtually no surface area, <1 m^2 g^{-1}, and no porosity.(*47, 48*) Also the hydrophilic nature of starch further constrains its use.*(17)* Overcoming these limitations, however, would enable access to an incredibly unique raw material for use in adsorption.

1.3 Starbon®: the solution to pollution

1.3.1 Starch availability and characteristics

Starches are the principal food reserve polysaccharide in the animal kingdom.(*49*) It is a vital component of the human diet as it is the major source of carbohydrates. Starch is produced on a very large, industrial scale, in 2000 over 48 million tons of starch was produced worldwide (Table 1.3).(*50*) Starch is commonly derived from maize, wheat and potato but it can also be extracted from other sources such as cassava.

Table 1.3 Worldwide starch production in 2000.(*50*)

			Starch (million tons)		
	Maize	Potatoes	Wheat	Other	Total
EU	3.9	1.8	2.8	0.0	8.4
USA	24.6	0.0	0.3	0.0	24.9
Other	10.9	0.8	1.1	2.5	15.2
World	39.4	2.6	4.1	2.5	48.5

There are a wide variety of different modified, unmodified and starch derived products that are used across a range of industries, but predominantly the production of food and feed utilise the majority of starch produced (Figure 1.4). In addition to commercially available sources, starches can also be isolated from waste streams, such as potatoes where starch can be found in the waste from crisp manufacture.(*51*) This is advantageous as there is the possibility to utilise this waste starch for chemical purposes, rather than starch that is required for food.

Starch naturally occurs in a water insoluble, partially crystalline (approximately 30%) granular form.(*49*) Starch consists of two main polysaccharides: amylose and amylopectin.(*52*) The structures of these molecules are shown in Figure 1.5.

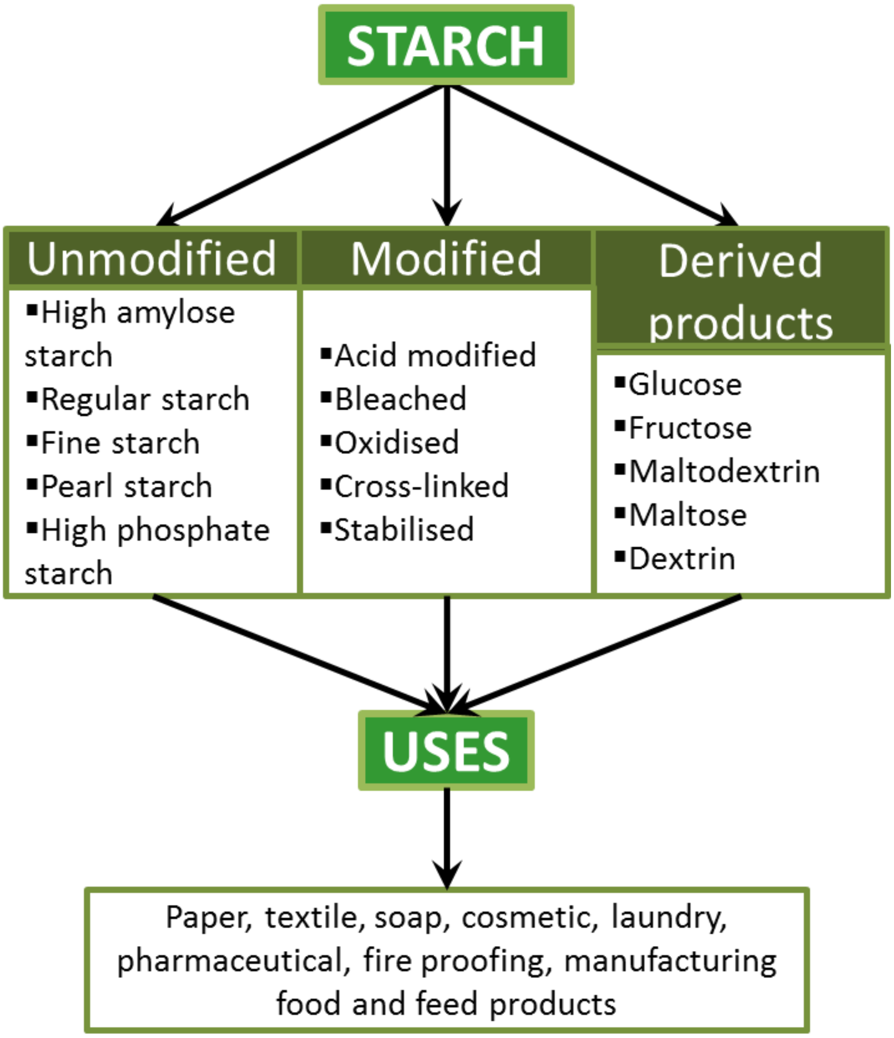

Figure 1.4 Different forms of starch and some examples of the industries that utilise them.(*49*)

Amylose is a linear polymer that consists of D-gluopyranose units linked through α(1→ 4) glycosidic linkages. Amylopectin is a branched polymer, mainly consisting of glucopyranose units liked by α(1→ 4) glycosidic bonds, however α(1→ 6) glycosidic linkages also occur creating branched units.(*53*)

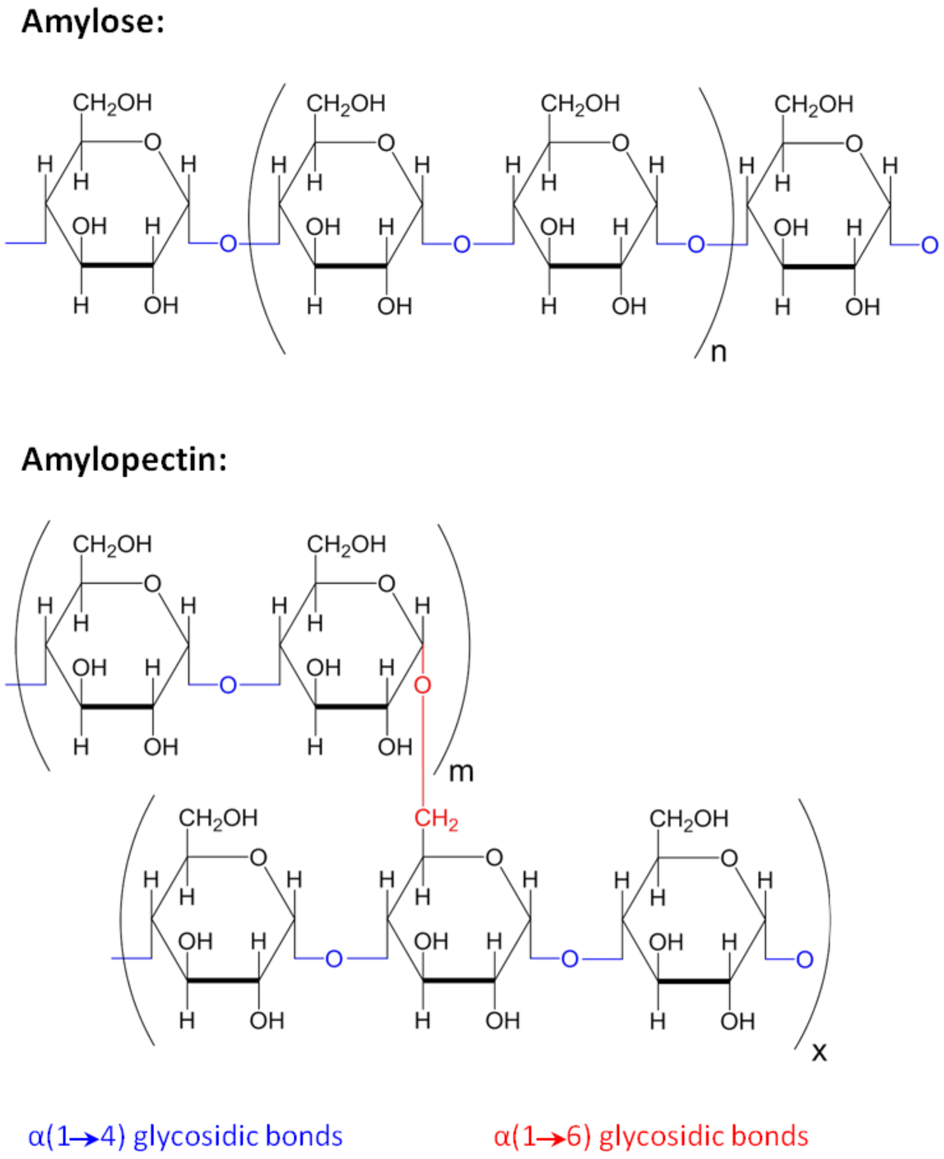

Figure 1.5 Structure of amylose and amylopectin.

The branching of amylopectin is not random. Results of debranching experiments carried out on amylopectin have shown that it commonly consists of two chain lengths, denoted in units of degree of polymerisation (DP): short chains of between 12 – 14 DP and long chains of approximately 45 DP.(*52, 54, 55*) The ratio of chain lengths varies depending on the origin of the starch but generally small chains are the most abundant by weight and number. The main consequence of amylopectin branching is that it causes the resulting structure of starch to have a very tangled appearance and hinders potential chain separation.

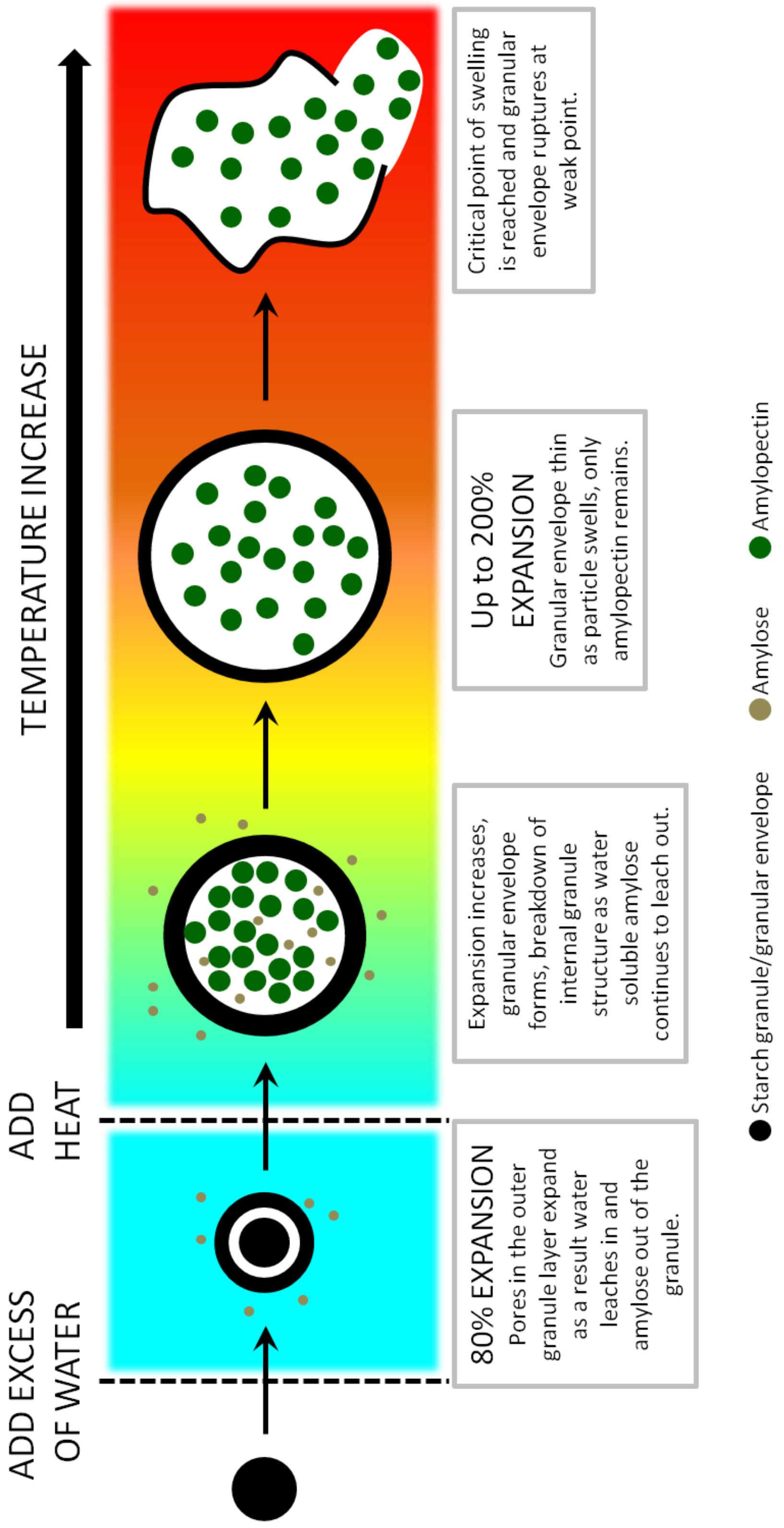

Figure 1.6 Schematic showing the molecular events occurring during starch gelatinisation.(*56, 57*)

1.3.2 Expansion of starch to form porous materials

Manipulation of the starch is frequently required for use in industry processing.(*52*) The most simple and common method of processing is heating of the starch in an excess of water, this results in many physical changes within the starch granule giving rise to gelatinisation. Gelatinisation is the term given to the process of loss of crystallinity and simultaneous swelling of a starch granule.(*57*) A starch granule can swell to many times its original size and if heated enough maximum swelling of the granule is reached causing the granule to rupture. A simplified diagram of what occurs during gelatinisation is shown in Figure 1.6.

The granular surface (the outermost layer of the granule) modulates the expansion of the granule, more specifically swelling is a property of the amylopectin found in the surface.(*57*) The extent of crystallinity of the amylopectin determines the onset of the gelatinisation process.(*58*) Different starches contain varying amounts of amylopectin and therefore the temperature of maximum swelling, defined as the temperature at which the swelling of a granule is complete and granular disruption has occurred, changes depending on the starch origin (Figure 1.7). The main outcome of the swelling of starch is a significant expansion of its surface area, from less than 1 m^2 g^{-1} to between 100 – 180 m^2 g^{-1}. The porosity of the material is also enlarged as a result.(*59*)

Once the starch has been gelatinised the product is a near homogeneous, viscous, aqueous solution of dissolved starch. If this mixture is allowed to cool there is a strong driving force towards crystallisation. During cooling there is an obvious phase separation where the amylose in solution rapidly turns opaque and forms an elastic gel due to the formation of polymer aggregates. These processes which occur when the starch is cooled are known as retrogradation.(*52*) If the retrogradation process is allowed to go on too long the expanded structure of the starch will begin to collapse, due to the interaction of starch with water. Therefore, to maintain the increased surface area and porosity the water must be removed from the solution and replaced with solvents with a lower surface tension, for example, ethanol.(*59*) After solvent exchange and drying the result of this process is an expanded starch powder that overcomes some of the drawbacks that has limited the use of starch as an adsorbent material so far.

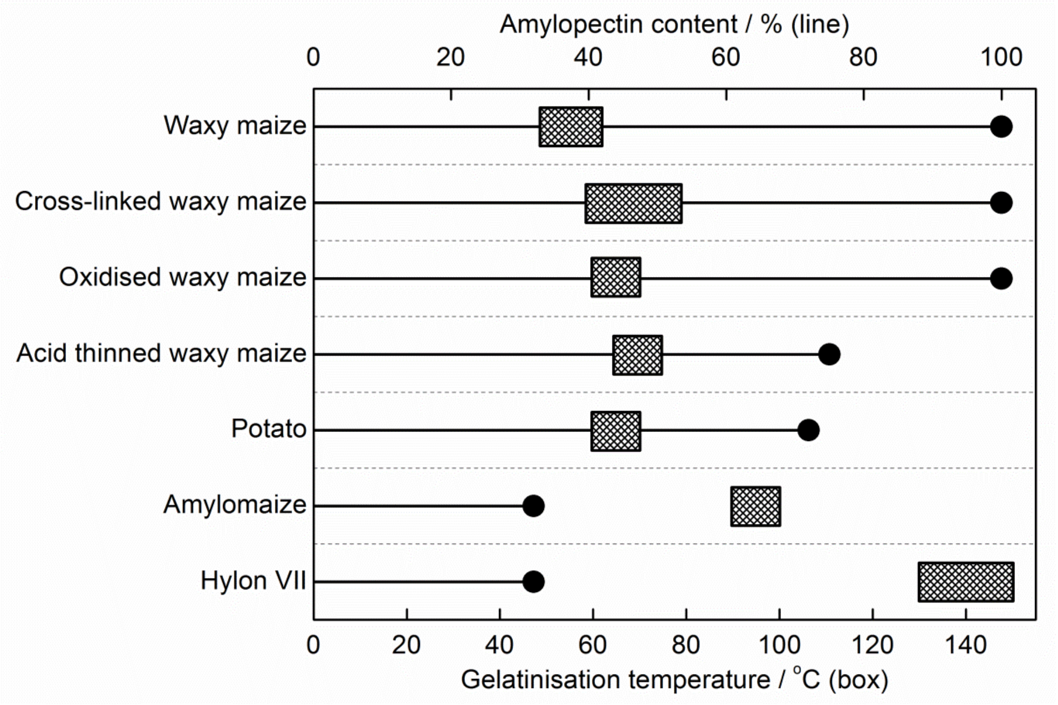

Figure 1.7 The gelatinisation temperature (box) and amylopectin content (line) of a variety of different starches.(*57*)

The work presented in this thesis utilises a number of starch derived adsorbent materials for waste water treatment all of which have been prepared using the steps of gelatinisation, retrogradation and solvent exchange in order to increase their surface area and porosity. The materials were derived from high amylose corn starch, such as Hylon VII. Hylon VII starch is unique in that it has a particularly high amylose content and low amylopectin content compared to other starches (Figure 1.7). Hylon VII granules contain a thick surface coating or sheath, not commonly seen for other starches, that is not easily disrupted, thus limiting the swelling to occur only at high temperatures.(*57*) Evidence from previous studies of Hylon VII indicates that this coating is likely a lysophospholipid and amylose complex that is particularly resilient to swelling.(*60*) These distinctive properties were taken into account when preparing starch derived adsorbent materials used for this work. The development of the materials used throughout this thesis is discussed further in Section 1.3.5.

1.3.3 Exploring other polysaccharides: alginic acid

Along with starch there are numerous other polysaccharides that fulfil most of the properties required for adsorbents, e.g. presence of numerous and diverse surface functionalities, insolubility in most organic solvents, inherent chirality, thermal stability and existing industrial production.(*61*) Of the family of polysaccharides available alginic acid that is extracted from brown algae (a group of species of seaweed) is one of the most desirable.

Seaweeds are probably one of the least energy intensive source of biomass obtainable and offers the added advantage that production can be increased without competing with existing food resources.(*62*) Alginic acid, as the name suggests, is a naturally occurring acidic linear copolymer of mannuronic and guluronic acid building blocks.(*63*) It has a reported pKa value of between 3.0 – 3.8 indicating relatively strong acid potential.(*53, 64*) It is of significant commercial importance and is available on an industrial scale.(*62*)

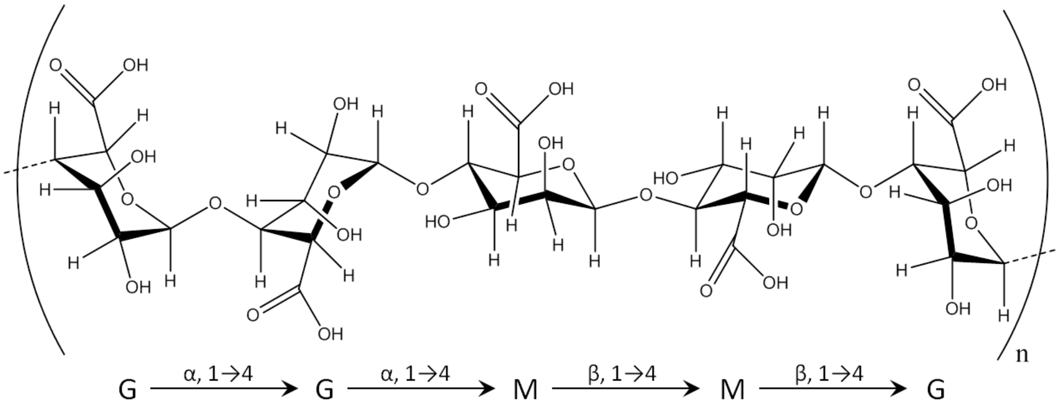

Figure 1.8 The structure of alginic acid showing bonding of units of mannuronic and guluronic acid.

The structure of alginic acid is shown in Figure 1.8, it is made up of (1→4) linked β-D-mannuronic acid (M) and α-L-guluronic acid (G) residues. The polysaccharide can be synthesised as homopolymeric units of either M or G residues or heteropolymer segments of M and G sequences, the ratio of M to G present in the alginic acid varies depending on the origin of the seaweed and the season it is harvested.(*65*)

Alginic acid has the potential to be expanded using water in the same way as starch. The swelling ability and stability of the resulting gel is dictated by the guluronic acid residues within the alginic acid structure. The higher the guluronic acid concentration and the longer the chains that it forms the better the gelatinisation properties of the alginic acid (Figure 1.9).(*66*)

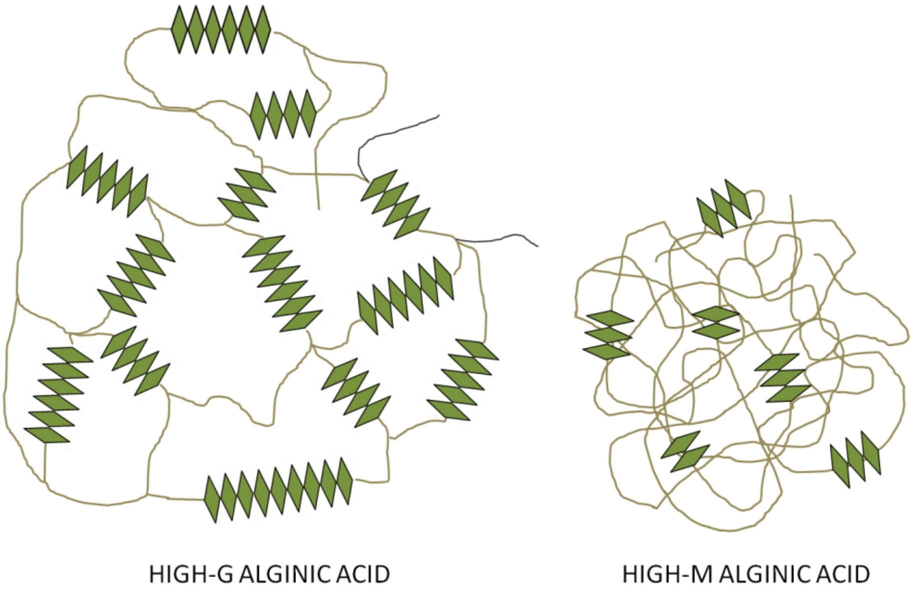

Figure 1.9 A suggested model for the network structure formed in alginic acid gels with different size guluronic units.(*66*)

As with starch, alginic acid gels present a highly open structure with increased surface area and porosity. However, this expanded structure is difficult to maintain once the material has been dried. Evaporative drying results in the collapse of the gel structure, even after the water has been exchanged for ethanol and does not retain accessibility to the alginic acid functionalities.(*62*) The technique of drying using supercritical carbon dioxide avoids shrinkage of the gels and can result in an increase in surface area of > 60% and pore volumes of > 40% than vacuum dried, expanded alginic acid materials. The average pore diameter also increases from 16 nm to 25 nm using supercritical drying.(*53*)

The differences in the structure of alginic acid compared with starch is likely to give rise to differing behaviour of the two materials during the gelatinisation and the retrogradation step of the expansion process. The most pronounced effect this will have on the resulting materials will be a difference in mesoporous character.(*65*)

The importance of mesoporosity of materials for adsorption and catalysis will be discussed in detail is Section1.3.4. At this point it is enough to say that the ability to create materials with differing porous networks is highly advantageous for the range of applications and molecules tested in this thesis.

1.3.4 The emergence and importance of mesoporous materials for adsorption and catalysis

Porous materials are of particular interest to the scientific community due to their ability to interact with atoms, ions and molecules not only at their surfaces but also throughout the bulk of the material.(*67*) As a result of this porous nature these materials also have a high surface area making them technically useful for a variety of applications including; adsorption, catalysis and as catalyst supports.(*68*)

The pores of solid materials are classified according to their size into three groups: macropores are the largest with pore size > 50 nm, mesopores are pores in the range of ≥ 2 ≤ 50 nm and micropores are the smallest pores with diameters < 2 nm (Figure 1.10and Table 1.4).(*69*)

Traditionally microporous materials e.g. zeolites and activated carbons, were employed for chemical applications. However, their applicability is limited by the relatively small pore openings that restrict diffusion of adsorbates or reagents in and out of the pore network.(*70*) In response to this problem the focus of materials chemistry became the enlargement of pores and development of the ability to control pore size during the fabrication of new porous solids.(*67, 68*)

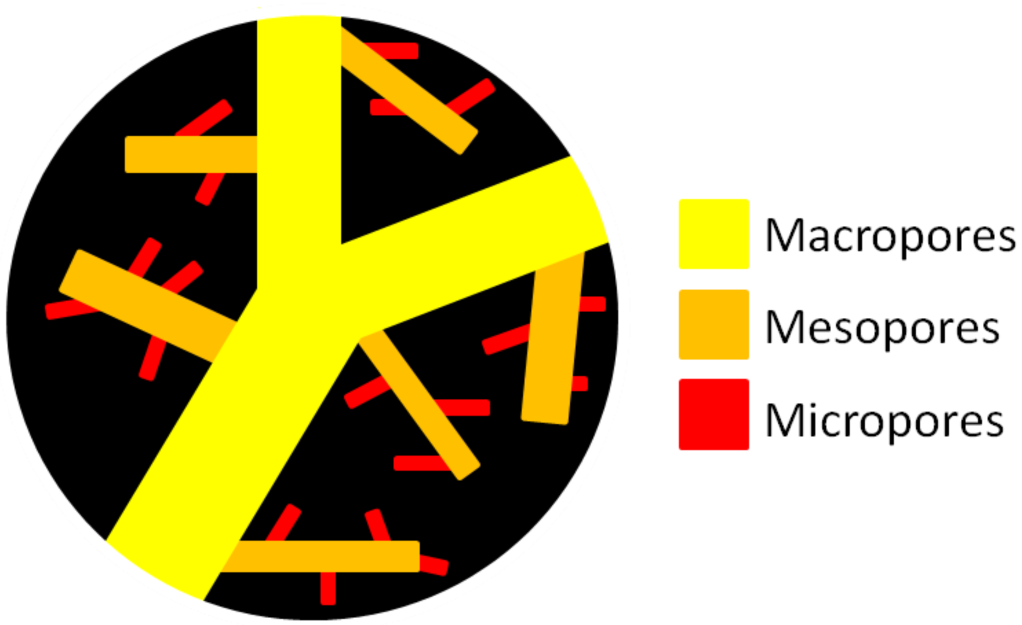

Figure 1.10 Diagram showing the pore hierarchy in porous solids.

Table 1.4 Pore classifications and sizes.

Pore type	Pore size
Micropore	< 2 nm
Mesopore	≥ 2 ≤ 50 nm
Macropore	> 50 nm

In 1992 Kresge *et al.* from Mobil Research and Development Corporation published a seminal paper describing the synthesis of novel, ordered, mesoporous silica materials named MCM-41.(*71*) The groups used an organic template that was coated in silica, the template was then removed leaving behind a highly structured silica solid (Figure 1.11). By altering the template these mesoporous materials could be made with varying structures and pore diameters that can be controlled over a wide range of 2 – 30 nm.(*72*) What these materials offered was the opportunity for size and/or shape selective adsorption and catalysis of large species that was previously difficult to achieve with microporous materials.

Ryoo *et al.* took this work further and by using the MCM-type silica materials as templates themselves the group produced highly ordered mesoporous carbon materials (Figure 1.12).(*72-75*) The advantage of these solids is that they offer different physiochemical properties compared with silica materials whilst offering a similarly ordered, mesoporous structure.

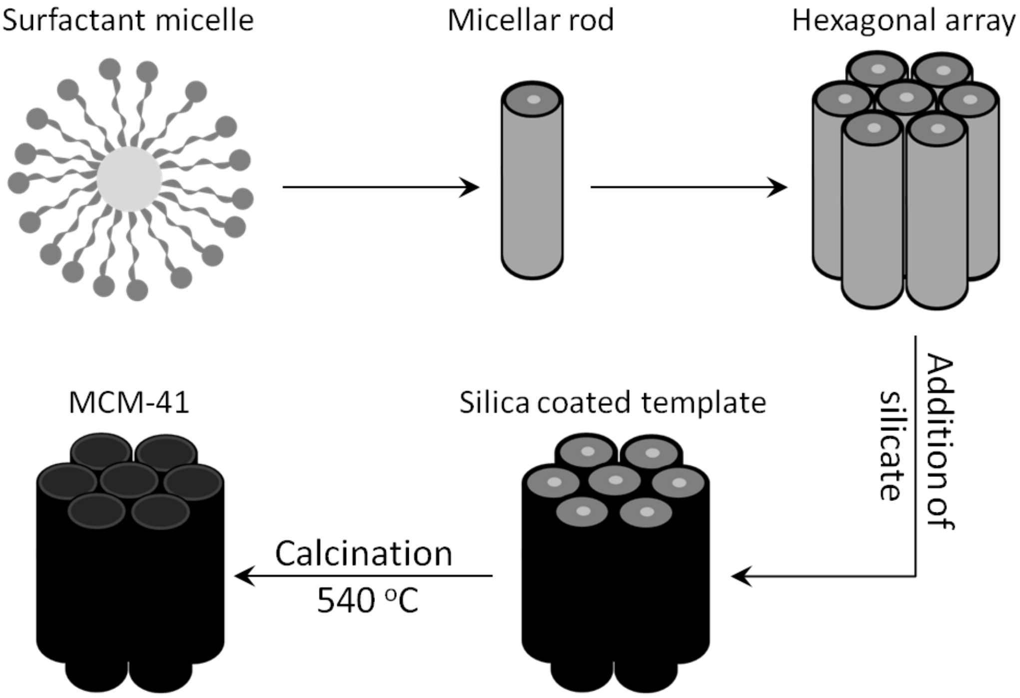

Figure 1.11 Schematic drawing for the synthesis of MCM-41. Hexagonal arrays of micellar rods form with the polar group of the surfactant on the outside. Silica species then occupy the spaces between the rods. The calcination step burns off the micelle (organic) material leaving behind hollow silica cylinders.(*71*)

Unfortunately, from a green chemistry perspective the use of these templating methods (Figure 1.11 and Figure 1.12) for production is highly undesirable. The syntheses involve considerable numbers of complex steps – especially for the carbon materials – there is also a large degree of waste generated which is mainly caused by the removal of the template. This all adds up to a rather costly and resource inefficient process.(*59*)

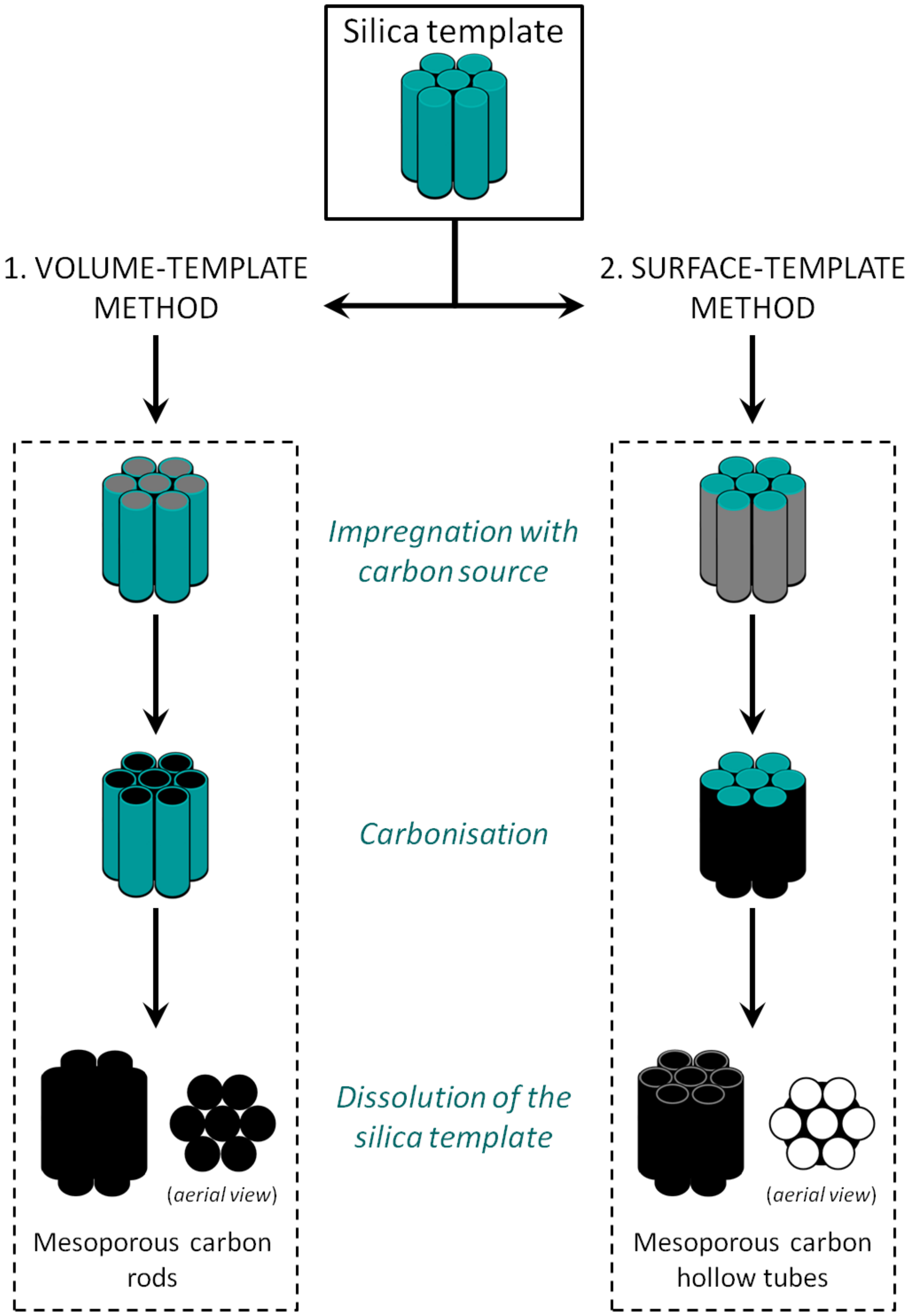

Figure 1.12 Synthesis of mesoporous carbon materials using a silica template, via 1. volume-template method and 2. surface-template method.(*73-75*)

1.3.5 Starbon® development & early applications

Researchers at the Green Chemistry Centre of Excellence, based at the University of York have demonstrated a novel approach to the generation of mesoporous, carbonaceous materials without the use of a templating agent.

This novel family of porous carbon based materials, which have been derived from polysaccharide precursors (starch and alginic acid) have been defined under the patented and trademarked name "Starbon®".(*76*)

The method developed exploits the natural ability of starch and alginic acid to form a nanochannelled biopolymer structure when expanded in water that can act as a natural template.(*77*) The process comprises three major steps, illustrated in Figure 1.13 and described in more detail below:

1. *Native polymer expansion via polysaccharide aqueous gel preparation:* this is the key process step as it expands the polysaccharide structure. The swelling results in the formation a predominantly mesoporous pore network.
2. *Production of a mesoporous solid via solvent exchange and drying:* as discussed in Section 1.3.2 the water used in the gelling step must be removed to prevent collapse of the porous polysaccharide structure. In this process the water is replaced with ethanol. The drying of the materials differs depending on the polysaccharide starting material. For starch it can simply be vacuum dried, whereas alginic acid drying is more complex requiring supercritical CO_2 to ensure the mesoporous nature of the material is maintained.
3. *Thermal carbonisation:* the mesoporous structure of the expanded and dried materials is finally fixed by thermolysis. This stabilises the materials so that they maintain their structure when exposed to a range of different conditions.(*78*) For the starch derived materials the carbonisation process is catalysed using the organic acid *para*-toluenesulfonic acid.(*59*) Alginic acid has the advantage that it can self catalyse its own carbonisation due to its natural acidic character.(*65*)

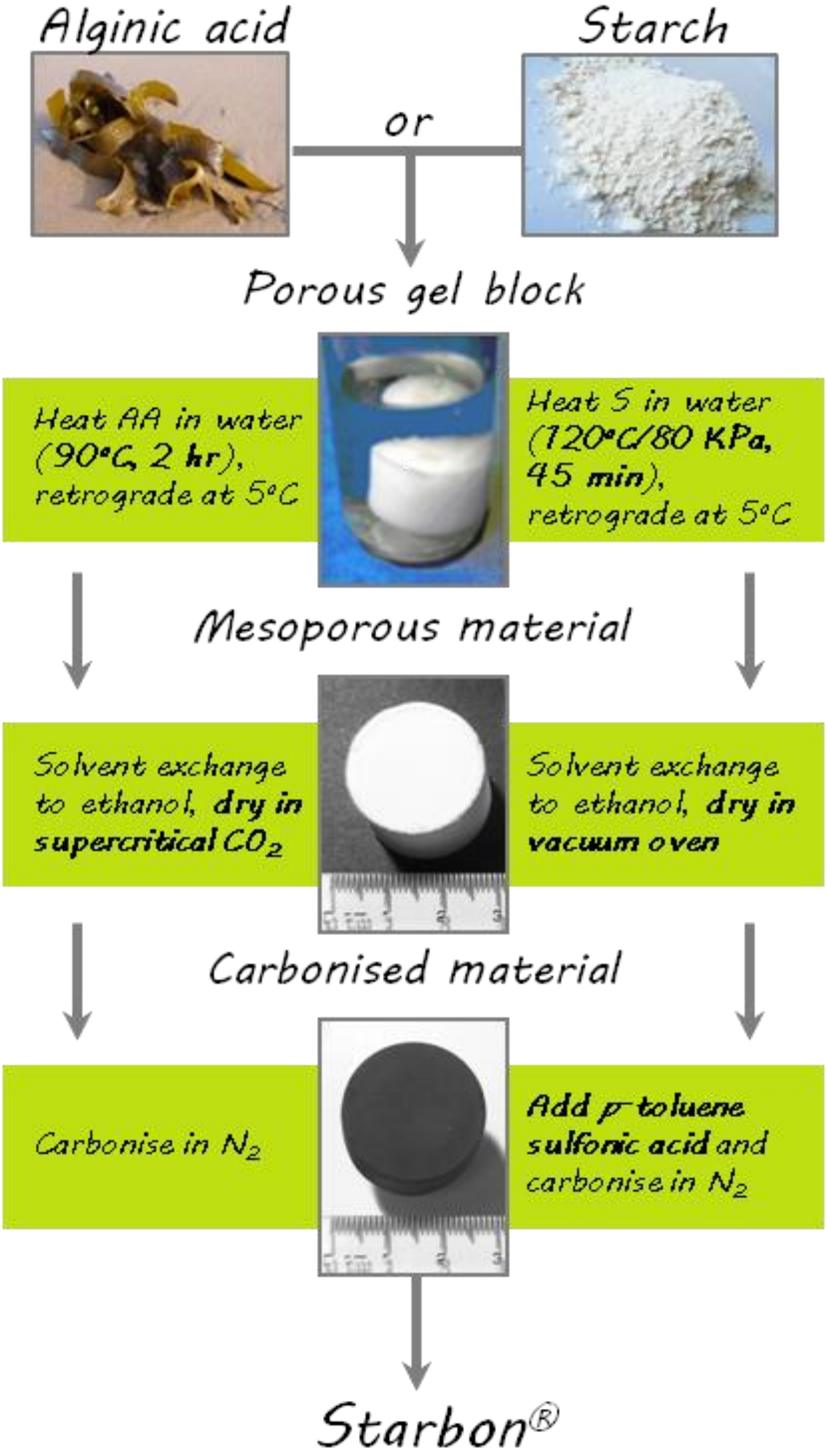

Figure 1.13 Schematic showing preparation procedures for starch and alginic acid derived Starbon®.

> The surface properties of the materials can be cleverly controlled by varying the temperature of carbonisation (between 200 – 1000 °C) that allows for the production of a range of materials with different functional properties. At lower temperatures (200 – 300 °C) the materials retain their polysaccharide-like character, as the temperature is increased this is lost as much of the surface oxygen content of the materials is removed. At high temperatures (800 – 1000 °C) the materials become graphitic-like with a high degree of surface aromatic content.(*78*)

This easily tuneable surface character enables the use of Starbon® for a wide range of applications as shown in Figure 1.14.

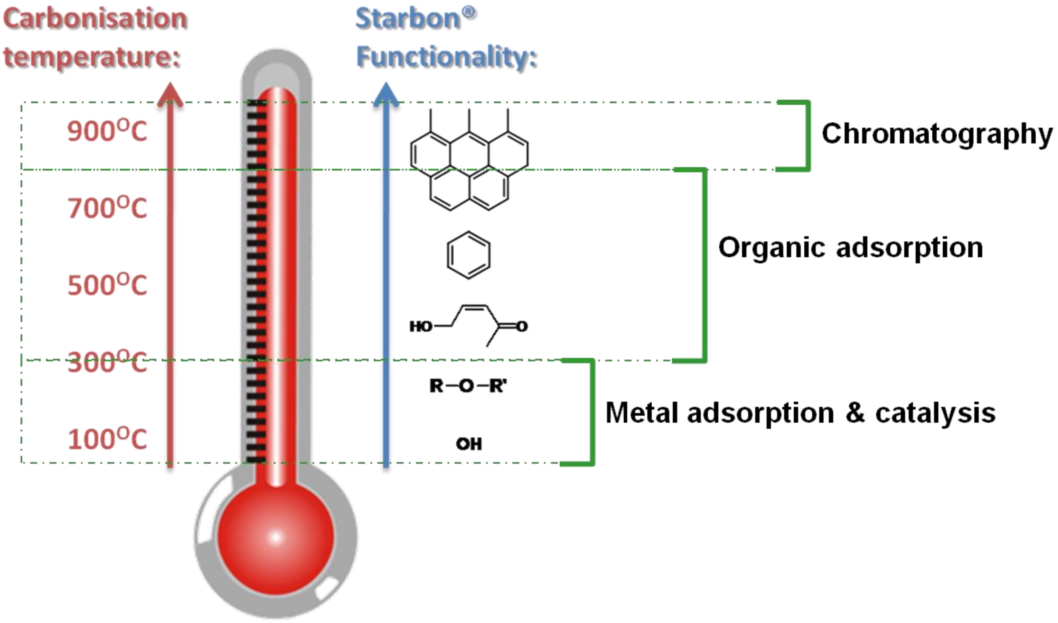

Figure 1.14 Diagram showing the changing surface functionality of Starbon® with increase in carbonisation temperature and also which applications the Starbon® can be used for dependent on their surface characteristics.

Starbon® materials have pore volumes and sizes equal to materials prepared by conventional template routes with a number of added advantages: firstly the Starbon® methodology is a simpler and less wasteful process than templating.(*79*) Secondly utilising the natural porous structure of starch and alginic acid as a template reduces the likelihood of collapse that is associated with the use of micellar templates. These templates are liable to collapse when exposed to thermal treatment for carbonisation resulting in a loss of porosity.(*80*)

This highly successful research into the development of Starbon® has led on to a number of further projects investigating their use in various applications and how the materials perform in comparison with other, more conventional porous materials. These include: the use of sulfonated (starch derived) Starbon® prepared by impregnating Starbon® with sulphuric acid for a range of esterification reactions of organic acids. The materials were very efficient catalysts giving excellent yields with > 99% selectivity and outperforming commercially available carbons e.g. DARCO® and NORIT® that were sulfonated in the same way.(*78, 81*)

Another previously researched application of starch-derived Starbon® was the formation of supported palladium nanoparticles (Figure 1.15). These materials were effectively used for the catalysis of C-C coupling reactions, such as, Heck, Suzuki and Sonogashira reactions, again giving high product yields and selectivities.(*82*) Finally, preliminary work has also been published utilising alginic acid-derived Starbon® as chromatographic stationary phases for polar analyte separations.(*65*) The materials were able to successfully separate a mixture of different sugars giving separations almost identical to the separation columns used commercially.

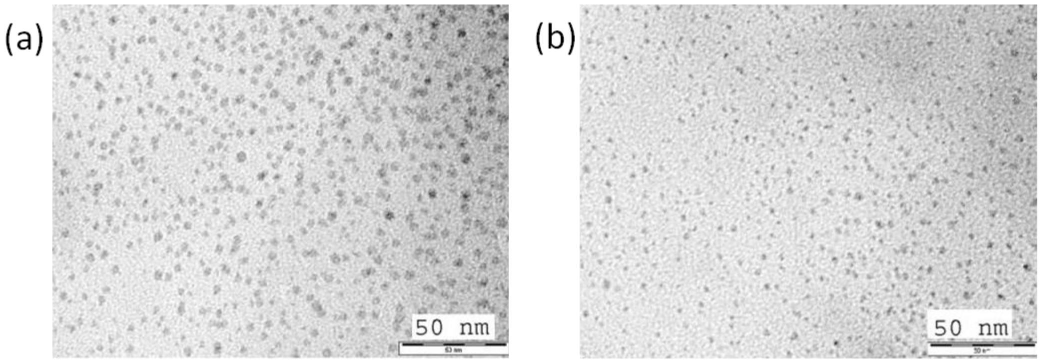

Figure 1.15 Transmission electron micrographs (TEM) of Pd-starch-Starbon® materials prepared in (a) acetone and (b) ethanol. *(TEM micrographs reproduced with the permission of Dr Vitaly Budarin.*)

Prior to this project, exploration into the use of Starbon® as adsorbent materials had only been preliminary with in-depth analysis of their performance remaining lacking. Therefore, one of the focuses of the work presented in this thesis was to determine the efficacy of Starbon® for the removal of organic pollutants from wastewater and evaluate their efficiency with other commercially available activated carbon adsorbents. Should Starbon® prove to perform well they could offer a greener, more sustainable alternative to the other adsorbents currently being used and also overcome some of the short comings of other low-cost adsorbents that so far have not been successfully employed on a large scale.

1.4 Supported metallic nanoparticles

As briefly mentioned in Section 1.3.5, starch-derived Starbon® have previously been investigated as supports for palladium nanoparticles. The area of nanoparticles is one that is rapidly growing in interest and importance and therefore another focus of this thesis is to further the previous work using alginic acid-derived Starbon® for nanoparticle formation and also investigate other sustainable production methods.

1.4.1 What are nanoparticles?

The name nanoparticle describes nanosized structures in which at least one of its phases has a dimension in the nanometre size range of 1 to 100 nm.(*83*) This term can therefore be applied to a wide range of things or materials, for instance: biological structures like viruses, cells and enzymes, or materials such as polycrystals, porous solids with particle sizes in the nano range or nanometre sized metal clusters (metallic nanoparticles) dispersed onto a porous support.

Metallic nanoparticles (MNPs) are receiving more and more interest from the scientific community due to the remarkable properties they present compared to the bulk of the same metal. At the nanometre scale metallic clusters only consist of a collection of a few atoms and as a result the atoms are located on the surface (or one layer removed) as opposed to the interior –

as would be seen for bulk metal. This characteristic results in superior catalytic activity and specificity of interaction of the MNPs.(*84, 85*)

1.4.2 Colloidal vs supported nanoparticles

Unfortunately, the remarkable characteristic of MNPs of being so highly active is also the cause of the main problem associated with them: existing at such a small size makes the particles thermodynamically unstable and when MNPs are synthesised or present in a reaction as a colloidal suspension the result is often aggregation and deactivation of the particles due to a decrease in the surface area to volume ratio and the interfacial free energy of the particles (Figure 1.16).(*86*) It is important to increase the stability of MNPs to give them a longer lifetime during storage and use.

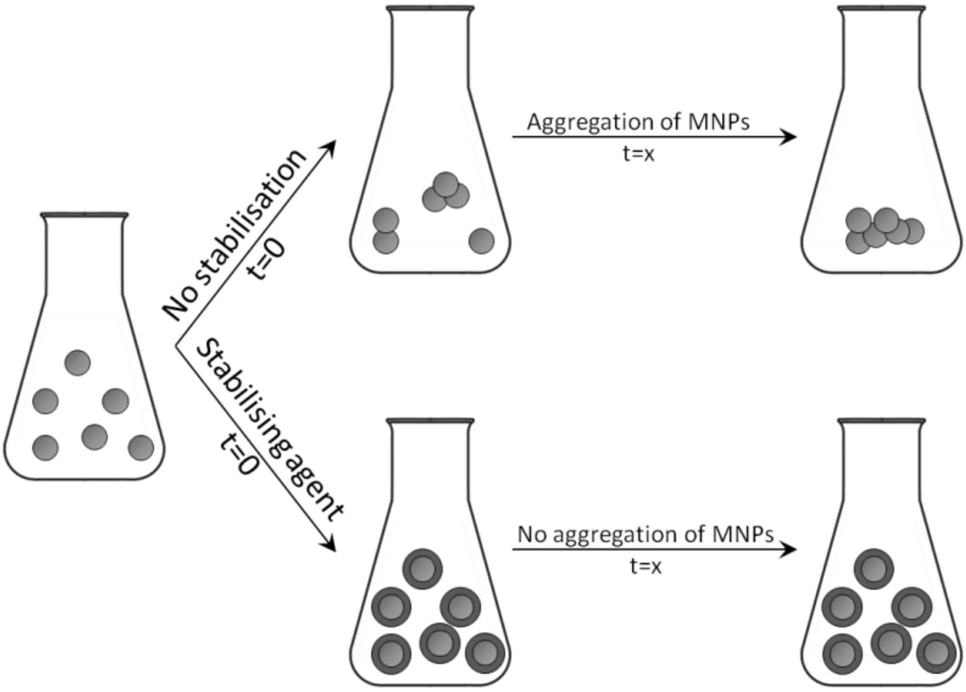

Figure 1.16 Schematic showing the aggregation of MNPs with and without stabilising agent.(*86*)

The union of the two previously unrelated fields of porous materials and nanoparticle technology offers a practical and efficient solution to this problem. Research has shown that the use of porous solids, with well defined meso and microporous networks, as MNP supports can effectively reduce particle agglomeration and have the added advantage of inhibiting MNP growth during their synthesis.(*83*) By careful choice of support or tailoring of its characteristics the size and shape of MNPs can also be easily controlled.

Supported MNPs also offer the added advantage that they are more easily recoverable than colloidal particles after use. Thus, reducing the proportion of MNPs lost into the environment as waste. The concern over the release of MNPs into the environment and the effect their bioaccumulation may have on natural systems is growing rapidly.(*87*) There is little understanding of the unique toxicological properties of MNPs and their long term impact on ecosystems and humans.(*88*) Therefore, utilising techniques to limit their release, such as supporting the MNPs, is vital.

1.4.3 The importance of palladium and nanoparticles in catalysis

Palladium is arguably the most ubiquitous metal currently used in organic synthesis.(*89*) Its great degree of versatility and ability to tolerate many different functional groups means it can be used to conduct thousands of different transformations with organic molecules.(*90*) Palladium is probably most famous for its involvement in facilitating C-C bond forming reactions, such as the Heck and Suzuki couplings, which are fundamental to the fine chemical and pharmaceutical industries.(*91*)

Homogeneous palladium catalysts have been most commonly used for this type of synthesis in industry as they offer better efficiency and selectivity than heterogeneous catalysts.(*92*) However, use of homogeneous catalysts has the major disadvantage of an inability to recover the catalyst after use. As a result of this the palladium requires costly recovery from the reaction waste stream. The key advantage of using heterogeneous catalysts is that due to their insolubility they are simply recovered from the reaction mixture using filtration and can be reused in subsequent reactions.

Fortunately, nanoparticle catalysts can bridge the gap between homo and heterogeneous. Due to their small size MNPs can mimic metal surface activation in catalysis as seen with homogeneous catalysts therefore offering the same selectivity and efficiency, whilst also being separable from the reaction mixture (this is most easily achieved when using supported MNPs) so are recoverable and reusable like heterogeneous catalysts.(*92*)

Due to these favourable characteristics MNPs have gained much attention from the research communities of both homogeneous and heterogeneous chemists, however, industry has not yet adopted them into processes as readily. What are limiting the widespread use of MNPs is likely their methods of synthesis which are not yet viable on a large scale and further work is required in this area.

1.4.4 Green synthesis of supported metallic nanoparticles

There are a wide range of different preparation techniques that have been employed for the synthesis of MNPs. They can generally be divided into two categories: bottom-up approaches where atoms are assembled into nanostructures or top-down approaches where material is removed from a bulk leaving behind nanostructures.(*84*) Some important techniques for each methodology are listed in Figure 1.17.

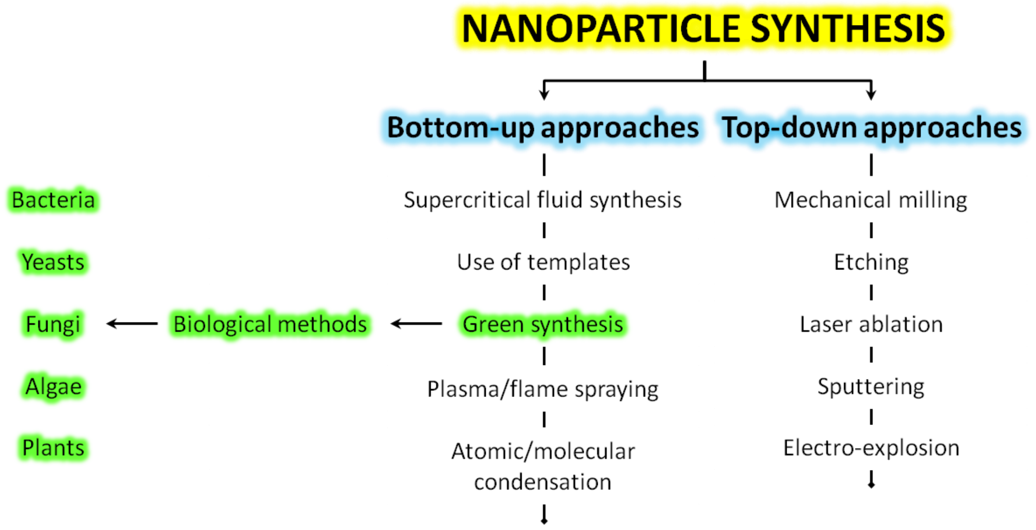

Figure 1.17 Some important methods of nanoparticle synthesis, highlighting where green synthesis techniques fit in.(*93*)

From a sustainable chemistry perspective top-down approaches to MNP production are highly undesirable due to the disproportionately large amounts of waste that result from these techniques. For a bottom-up approach, the synthesis requires three key constituents: a molecular precursor (i.e. a metal salt), a molecular stabiliser and a reducing agent.(*94*) Unfortunately, these techniques can involve many synthetic steps and often use highly toxic chemicals, e.g. for the popular method of palladium nanoparticles synthesis the metal precursor Na_2PdCl_4 is first reduced by $NaBH_4$ in a biphasic organic-solvent-water system, followed by subsequent addition of the stabiliser (4-dimethylamino)pyridine.(*95*)

In light of this, greener more sustainable synthesis methods are being widely researched. It has emerged recently that the use of biological techniques using plants or microorganisms as an environmentally friendly route to MNPs could offer a suitable alternative to conventional synthesis methods.(*93*) Research in this area is still in early stages, however it has been shown that the MNPs produced using plants or plant extracts are more stable and easier to produce on a large scale than those from other biological systems.

These results have inspired some of the work carried out for this project where natural materials, i.e. alginic acid and living plants have been investigated for their effectiveness in synthesis and support of palladium nanoparticles.

1.5 Project aims

The aim of this thesis is to provide an in-depth investigation into the capture of potentially harmful components from aqueous waste streams using starch and alginic acid derived Starbon® as sustainable adsorbent materials (Chapters 2 & 3).

In addition, another focus of this thesis is the development of greener methods for the production of supported palladium nanoparticles (Chapters 5 & 6). Coupled to this the emerging problem of decreasing availability of precious metals (e.g. palladium) that are vital for a vast range of chemical and industrial applications is also discussed in detail in Chapter 4.

Overall, the key themes that run throughout this entire work are that of sustainability both of materials and the environment and in addition being mindful of resource efficiency and remembering that nothing is available in a boundless supply.

Chapter 2

Starbon® characterisation and application in dye adsorption

Aspects of the work presented in this chapter have appeared in:

H. L. Parker, A. J. Hunt, V. L. Budarin, P. S. Shuttleworth, K. L. Miller & J. H. Clark, The importance of being porous: polysaccharide-derived mesoporous materials for use in dye adsorption. *RSC Advances*, 2012, 2, 8992-8997

Poster given at RSC Atmospheric and Environmental Chemistry Forum, London, UK, June 2010

Oral presentation given at Alg'n'Chem: Algae, new resources for industry? Montpellier, France, November 2011

Oral presentation given at Starbon® Day meeting, York, UK, September 2012

SEM images of starch, expanded starch and S300 were obtained by Dr.A. Hunt, Green Chemistry Centre of Excellence, University of York, York, YO10 5DD.

Chapter 2.

Starbon® characterisation and application in dye adsorption

2.1 Introduction

Chemicals such as dyes and pigments are used in various sectors of industry including textile manufacture, leather tanning, paper production, food technology and cosmetics manufacture, to name but a few.(*96*) These synthetic organic compounds consume vast quantities of water in their use and have a visible effect on water quality. The annual production of dyes and pigments is in excess of 7×10^5 tonnes, of which an estimated 2–15% is lost in the effluent during the dyeing process.(*97-100*) In some cases water colouration can be observed in dye concentrations of less than 1 ppm.(*101, 102*) Many of these dyes are toxic, even carcinogenic, persistent in the environment and non-biodegradable.(*103*) The impact of releasing such waste streams into water courses can be dramatic and poses a significant hazard to both aquatic life and animals further up the food chain including humans.(*104-107*)

Many dyes are resistant to aerobic digestion, stable to light, heat, water and oxidation making treatment a significant challenge.(*108, 109*) Biological, chemical, and physical methods are available for the removal of such dyes. Physical adsorption using activated carbons as an adsorption matrix is efficient and considerable attention has focused on their use.(*110-112*)

There are a wide variety of biomass derived activated carbons that have shown effective dye adsorption, however, these materials can be limited due to cost, availability – both in abundance and worldwide location - and are frequently limited in practical use because of micropore size resulting in large volumes required to improve rates of extraction.(*113*)

Polysaccharides including starch and alginic acid are relatively inexpensive, non-toxic, biodegradable, possess polyfunctionality, have great potential for chemical modification and are found in nearly every geographical location on the planet.(*114, 115*) The extensive use of non-ionic polysaccharides (such as starch) as adsorbents, has been restricted by low surface area (< 1 m^2g^{-1}), low degree of mesoporosity and limited potential to hydrogen bond with dyes due to extensive intramolecular chain interactions. Anionic polysaccharides (such as alginic acid) have also previously shown limited success for use in adsorption, the main reason being electrostatic repulsion between the polymer surface and the dye.(*47*) The development of polysaccharide derived, mesoporous materials, Starbon®, with large pore volume and surface areas opens new doors to dye adsorption. Their mesoporous nature makes them ideal materials for the uptake of large, bulky molecules like dyes.

Within this chapter, the preparation and characterisation of Starbon® and their application as adsorbents for bulky dye molecules is described. By varying the adsorbent type and preparation temperature a range of mesoporous materials are produced and these are utilised to clarify the importance of pore texture, surface functionality and dye molecular size on adsorption capacity. Commercially available activated carbon, Norit, is also used in this work as a basis for comparison.

2.1.1 Aims

The overall objective of this chapter is to provide an introduction to the Starbon® materials used throughout Chapters 2, 3 and 5. A description of the preparation procedure will be given in this chapter, however, as this was not the focus of this thesis it is only brief and for a more in-depth description of the development of these materials please see references (*53*), (*65*) and (*59*).

The aims of the work presented herein:

- To investigate the influence that the nature of the native polysaccharide has on the physiochemical properties of the Starbon®.
- To optimise pore structure and surface functionality of the Starbon® for application in the adsorption of dye molecules.
- To propose the possible adsorption mechanism on the surface of the Starbon® using adsorption thermodynamics.

2.2 Results and Discussion

2.2.1 Preparation of Starbon®

The preparation of the starch derived Starbon® was carried out using the method previously published by Budarin *et al.*, and the preparation of the alginic acid derived Starbon® was carried out using the previously published method of White *et al.*.(*59, 65*)

A typical method of preparation comprises three main stages:

1. Gelatinisation and expansion
2. Retrogradation and solvent exchange
3. Drying and carbonisation

Gelatinisation is defined as a simultaneous loss of crystal structure of the polysaccharide and expansion of the polysaccharide granule to produce porosity.(*116*) To achieve this the polysaccharide (starch or alginic acid) is mixed with water in a 1 g:20 ml ratio and heated for the desired time. The expansion of alginic acid is carried out at 363 K and ambient pressure whereas starch requires slightly harsher conditions of 393 K/80 kPa due to the more tangled nature of the polymer caused by the mixture of amylose and amylopectin.

Once step one is complete a sol-like suspension is achieved and this is allowed to cool to room temperature. The mixture is then left to retrograde for 24 hours at 278 K. This retrogradation allows the expanded polysaccharide to slightly recrystalize thus adding stability to the pore structure created in the expansion. The next stage of exchanging water with a lower surface tension solvent – in this case ethanol – further protects the porous network by preventing collapse when drying.

The method of drying of the expanded materials differs depending on the starting material, whilst the starch derived materials can be dried easily in a vacuum oven this is not suitable for the alginic acid derived materials where vacuum drying results in a loss of surface area of the materials.(*53*) Supercritical carbon dioxide (scCO_2) was used to successfully dry the alginic acid materials while also maintaining a high surface area. This is followed by carbonisation of the materials under nitrogen to increase the stability of the materials and preserve the pore structure. Due to the acidic nature and occurrence of sodium and calcium in alginic acid carbonisation can be carried out directly.(*117, 118*) Starch does not possess the necessary characteristics to self catalyse the carbonisation process and so is doped with 5% w/w *p*-toluenesulfonic acid which enables the carbonisation to occur. Heating of the materials creates changes in the physical and chemical characteristics and, for the purposes of this work, materials were prepared at 573, 723 and 1073 K to determine the affect different preparation temperatures has on the adsorbent properties of the materials. Six types of Starbon® were synthesised for this work described in Table 2.1 along with the abbreviated name that will be used throughout this thesis. Norit, commercially available, activated carbon was used as a basis for comparison with Starbon®.

Table 2.1 Starbon® description and abbreviation.

Starting material	Preparation temperature [K and ^{o}C]	Abbreviation
Starch	573 / 300	S300
	723 / 450	S450
	1073 / 800	S800
Alginic acid	573 / 300	A300
	723 / 450	A450
	1073 / 800	A800

2.2.2 Physical and chemical properties of Starbon®

Scanning electron micrograph (SEM) images of Starbon® show the formation of an increasingly porous structure from parent material to finally carbonised product (Figure 2.1). The textural properties of starch derived Starbon® differ significantly to those derived from alginic acid. The structure of S300 is granular in nature, but A300 can be described as a fluffy, porous, web-like structure. Transmission electron micrograph (TEM) images also further exemplify this wispy feature of alginic acid and A300 (Figure 2.2).

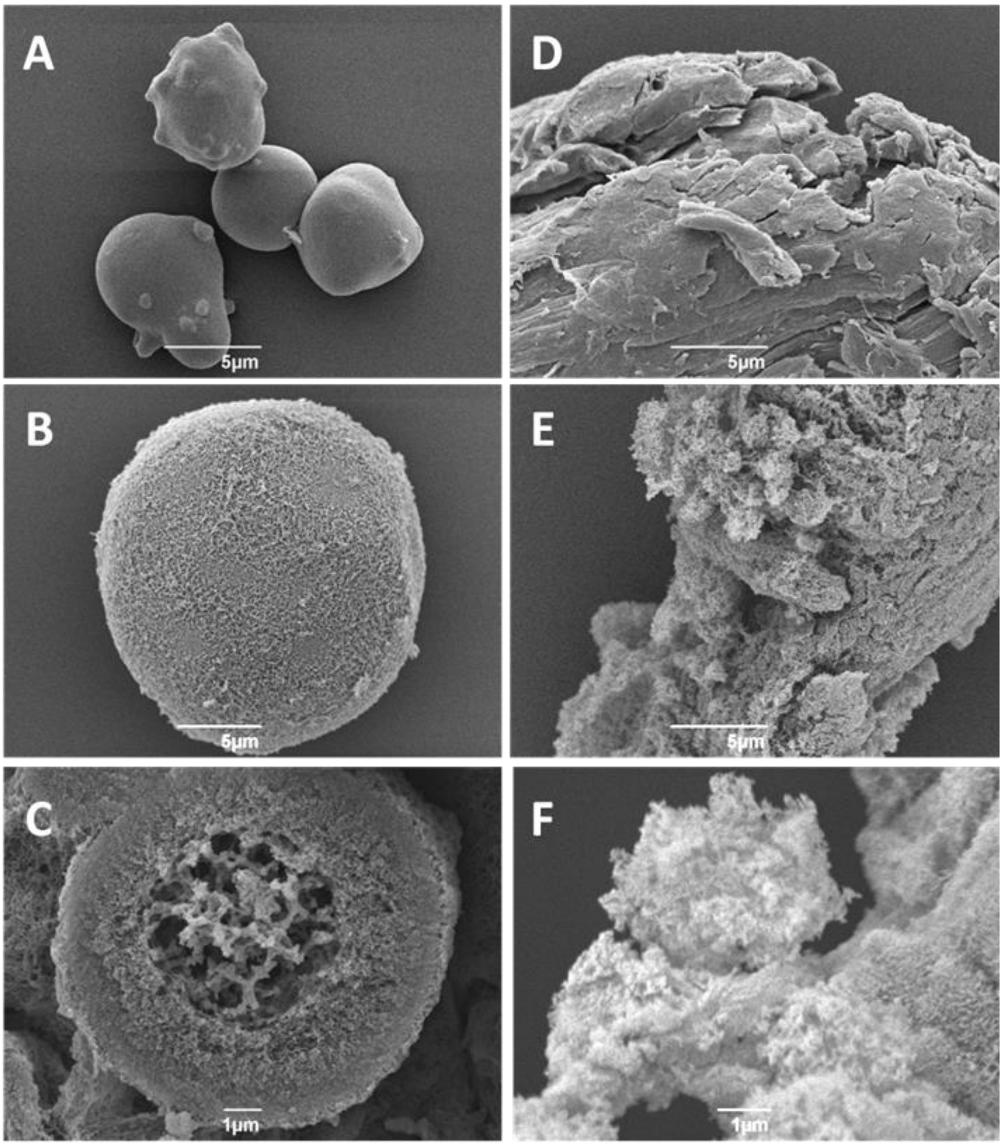

Figure 2.1 SEM images (A) starch, (B) expanded starch, (C) S300, (D) alginic acid, (E) expanded alginic acid and (F) A300.

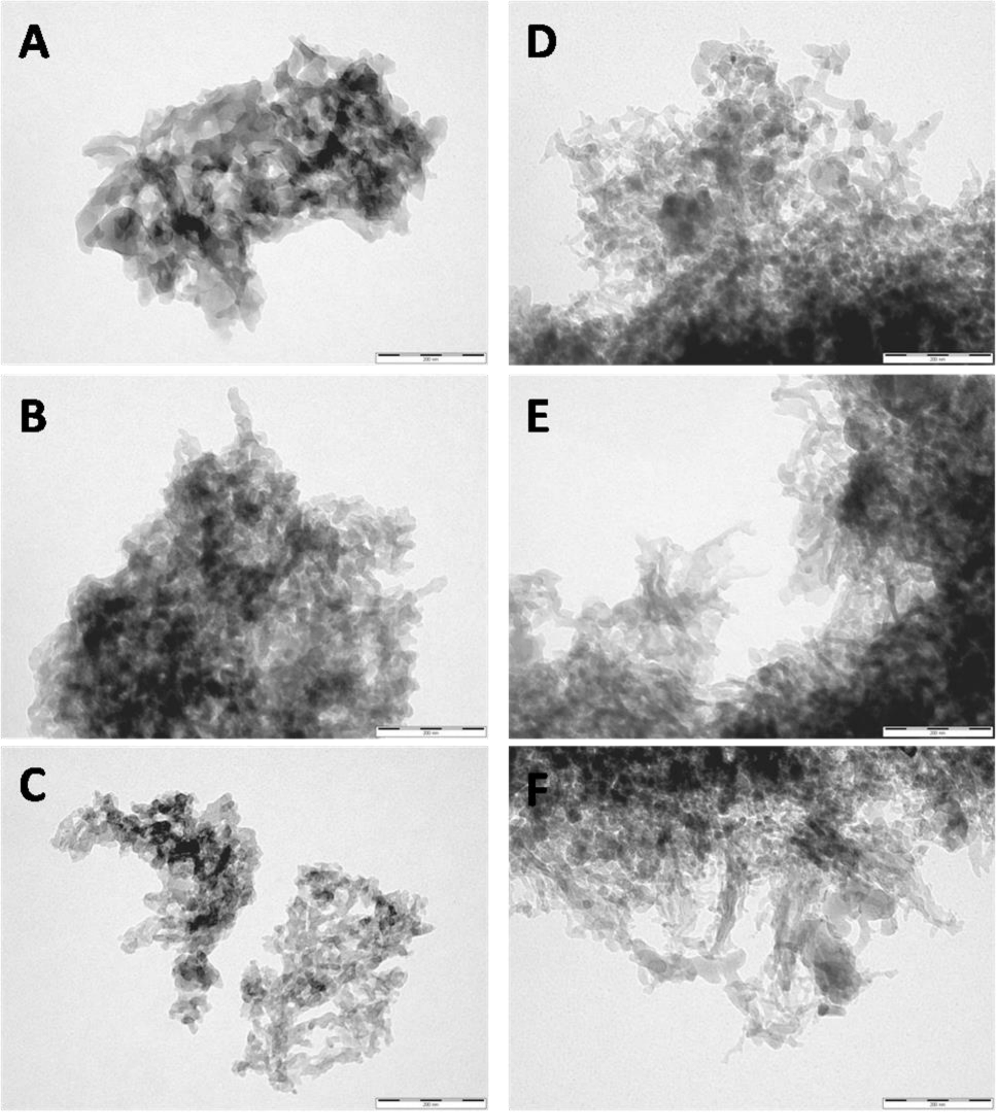

Figure 2.2 TEM images (A) starch, (B) expanded starch, (C) S300, (D) alginic acid, (E) expanded alginic acid and (F) A300.

The solid state ^{13}C-MAS NMR spectra of a range of Starbon® materials demonstrate near identical changes in surface functionality on heating of the materials (Figure 2.3), original data available in Appendix 1). This can be attributed to the inherent hydroxyl-rich nature of all polysaccharide materials. At 573 K resonances between 50-100 ppm disappear signifying a loss of the acetal and alcohol functionalities of the polysaccharides. The appearance of aliphatic carbons resulting from increased thermal degradation of starch and alginic acid are represented by a broad resonance between 10-50 ppm. As the preparation temperature increases aromatic rings, such as substituted phenols, benzenes and furans form cross linked structures. At 723 K the relative intensity of aromatic carbon resonances is significantly increased and the high field aliphatic resonance is decreased. This is in good agreement with infrared (IR) data for both starch and alginic acid Starbon® samples (Figure 2.4) and concisely shows the transformation from hydroxyl-rich polysaccharides to aliphatic/alkene groups and further into highly aromatic materials.

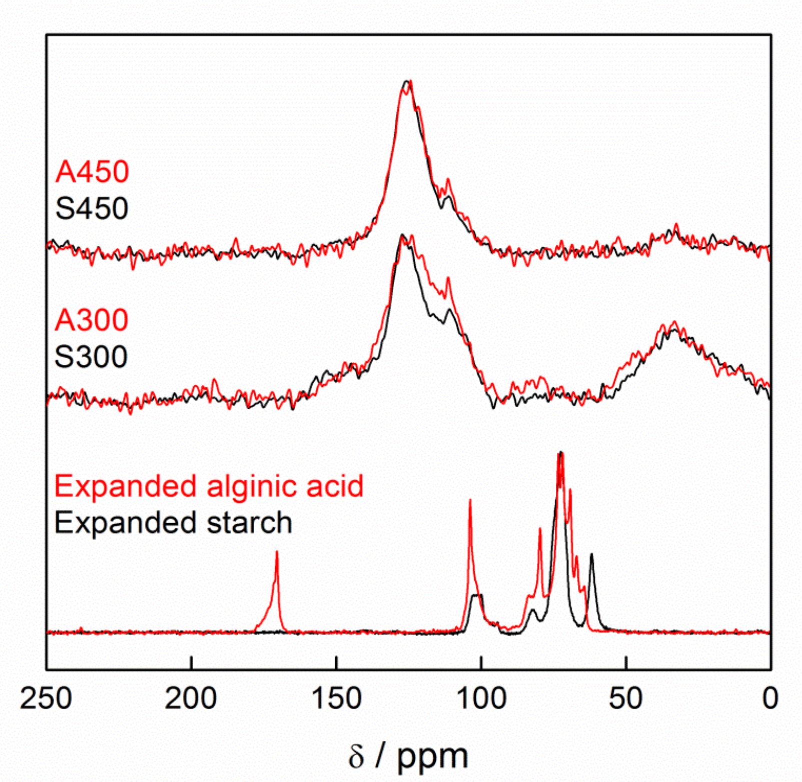

Figure 2.3 Overlaid ^{13}C MAS NMR spectra of expanded starch, S300, S450 (black) and expanded alginic acid, A300 and A450 (red).

This NMR data would indicate a move towards aromatic structures at higher temperatures, however, the NMR probe was unable to be tuned for S800 and A800. In addition it was not possible to analyse Norit using this technique. It is speculated that this is an indication of a degree of electrical conductivity, indicative of some graphitic character. X-ray photoelectron spectroscopy (XPS) analysis was used to enable surface characterisation of high temperature materials and Norit. Table 2.2 shows different elements and concentrations that were observed for the materials.

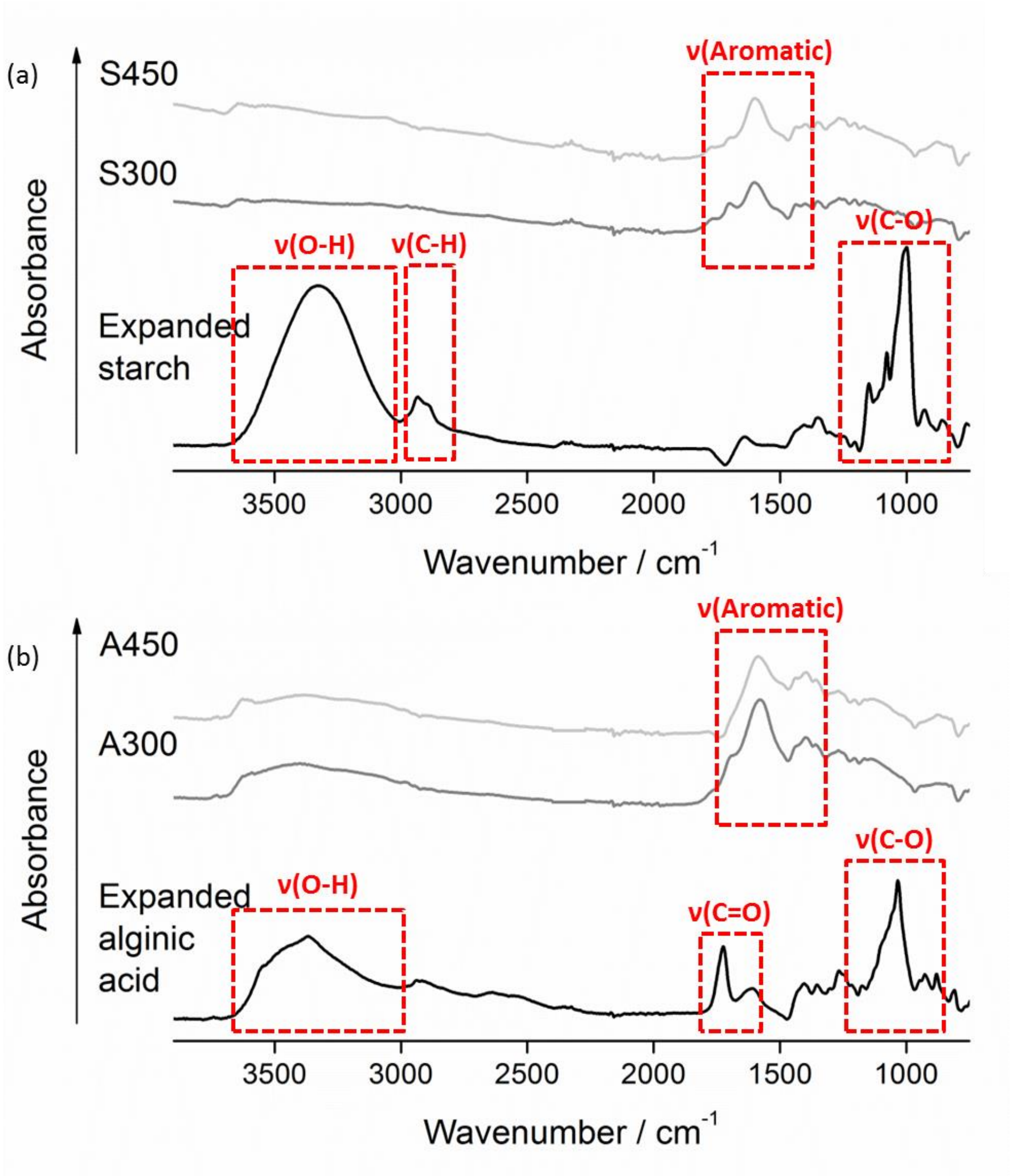

Figure 2.4 IR spectra of (a) expanded starch, S300, S450 and (b) expanded alginic acid, A300 and A450.

Table 2.2 Content of elements in Starbon® from XPS analysis.

	% Atomic Content					
	C	O	S	Na	Ca	Si
S300	85.7	14.3	0.1	-	-	-
S800	98.3	1.8	-	-	-	-
A300	81.9	16.1	0.4	1.0	0.7	-
A800	88.7	8.2	0.4	2.2	0.5	-
Norit	93.0	6.4	-	0.1	-	0.5

As expected from NMR and IR analysis oxygen content is lower for the high temperature materials, S800 and A800. S300 shows the presence of SO_2, binding energy (BE) 168.0 eV, which is likely due to some residual *p*-toluenesulphonic acid catalyst used in the carbonisation process. The presence of elemental Na, BE 1072 ± 1.0 eV, $CaSO_4$, BE 347.5 ± 0.2 eV and CaO, BE 351.0 ± 0.5 eV in A300 and A800 is most likely a result of the alginic acid extraction process.(*118*)

Deconvolution of the C 1s and O 1s spectra of the adsorbents gives the individual component peaks (Figure 2.5 and Figure 2.6). Depending on BE each peak corresponds to different carbon and oxygen species (Table 2.3).(*119*) S800 and A800 spectra clearly show the presence of aromaticity in good agreement with NMR observation. S300 and S800 exhibit a relatively large amount of surface C-O groups compared to A300 and A800 which may affect the adsorbent properties.(*120*)

Analysis of Norit (Figure 2.7) shows that it compares well to Starbon® with similar surface characteristics to S800. It exhibits a similar degree of aromaticity (28 % for S800 compared to 27 % for Norit), also the surface oxygen groups are predominantly C-O as with S800. Overall the XPS analysis shows that Norit is an appropriate commercially available material for use as a comparison with Starbon®.

Table 2.3 Composition of Starbon® components from XPS spectra.

	Peak	BE [eV]	Chemical State	%				
				S300	S800	A300	A800	Norit
Carbon	I	284.7 ± 0.2	C-C	53	32	66	37	27
	II	285.2 ± 0.3	C-C (Ar)	-	28	-	45	27
	III	285.8 ± 0.3	C-O	30	18	11	-	31
	IV	289.0 ± 1.0	COO	17	22	23	18	6
	V	290.3 ± 0.2	π-π* C (Ar)	-	-	-	-	9
Oxygen	I	531.3 ± 0.2	C-O	-	-	60	-	-
	II	532.0 ± 0.2	C=O	34	-	-	100	19
	III	533.4 ± 0.2	C-O	66	100	40	-	81

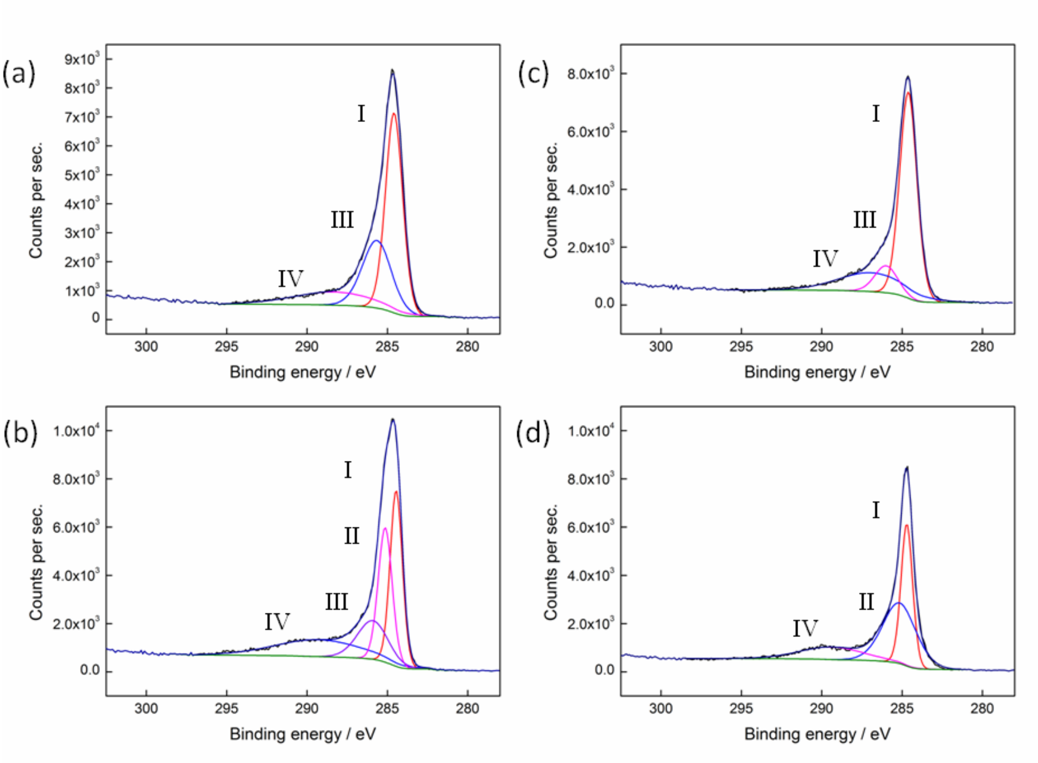

Figure 2.5 Carbon XPS spectra of C1s (a) S300, (b) S800, (c) A300, (d) A800.

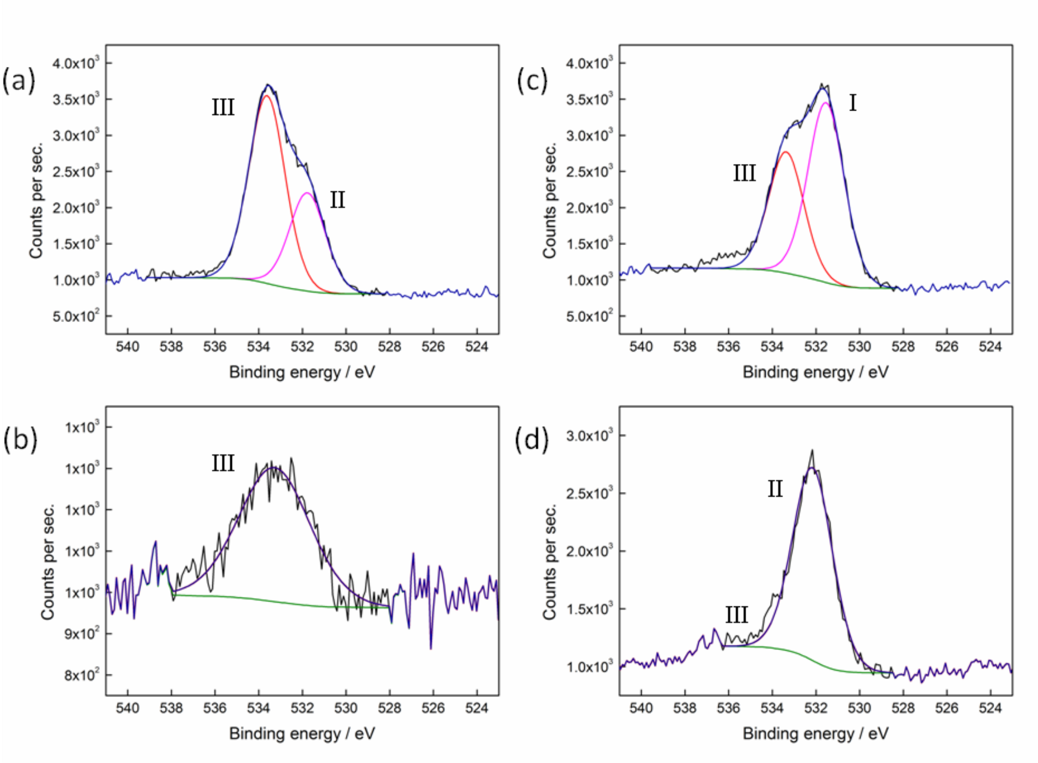

Figure 2.6 Oxygen XPS spectra O1s (a) S300, (b) S800, (c) A300, (d) A800.

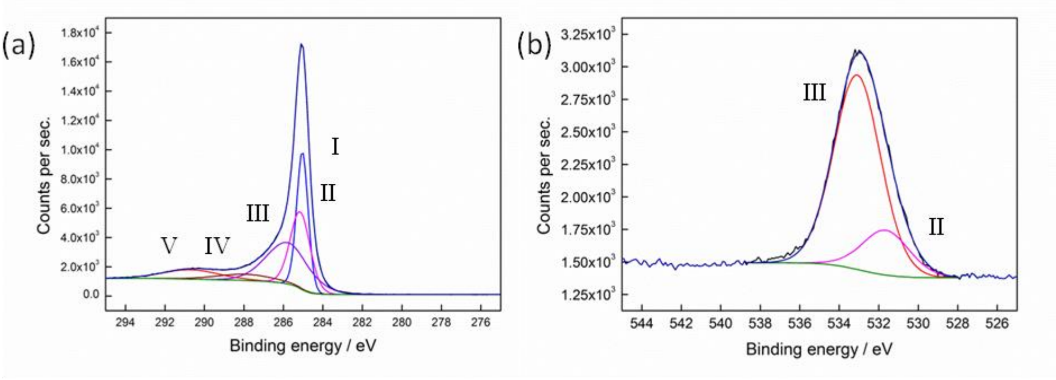

Figure 2.7 Norit XPS spectra of (a) carbon and (b) oxygen.

Nitrogen adsorption porosimetry was used to give a quantitative analysis of the textural properties of the materials. Characterisation of the isotherms produced from the analysis showed type IV isotherm profiles with H3 hysteresis loop classification (Figure 2.8) for all of the Starbon® materials.(*121*) The type IV isotherm can be divided into two distinct parts:

- The initial part of the isotherm (up to P/Po 0.8) can be attributed to monolayer-multilayer adsorption. It is commonly interpreted as the stage at which the monolayer is full and multilayer adsorption begins.(*121*)
- The hysteresis loop clearly seen at P/Po above 0.8 is generally associated with capillary condensation and is significant of mesoporous adsorbents. The H3 type loop is usually given by adsorbents that contain slit-shaped pores.(*122*)

For S300 the low pressure, desorption volume (red) remains above the adsorption volume (black), this is indicative of an adsorbent containing some micropore character (Figure 2.8 (a)). It is not possible to remove all of the residual adsorbed nitrogen from inside the pores due to their small entrance diameter.(*121*) Closer examination of the S450 and S800 isotherms show that this is also occurring to a small extent. This feature is not apparent on any of the alginic acid derived material isotherms suggesting that there are little to no micropores present in these adsorbents.

The shape of the Norit isotherm most closely resembles the type I isotherm indicative of microporous solids (Figure 2.8 (g)). These materials have relatively small external surfaces and the limiting uptake is being determined by the accessible micropore volume rather than internal surface area.(*121*)

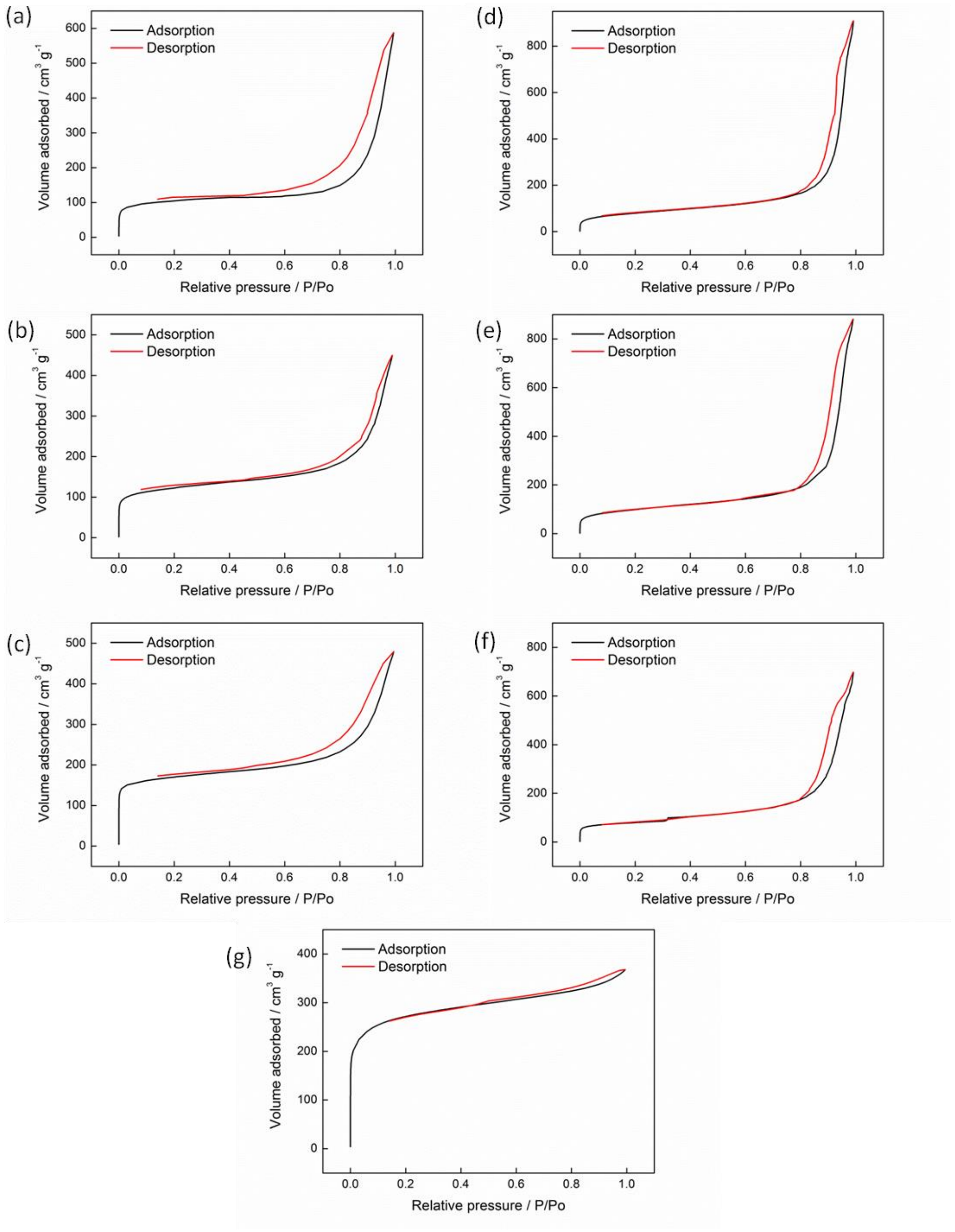

Figure 2.8 Nitrogen adsorption isotherms for (a) S300, (b) S450, (c) S800, (d) A300, (e) A450, (f) A800 and (g) Norit.

A summary of material properties is given in Table 2.4. The Brunauer Emmett and Teller (BET) isotherm shows that the surface areas of starch derived Starbon® increases from 332 to 535 m^2 g^{-1} with increase in preparation temperature, this correlates with an increase in micropore formation in the materials. A decrease in total pore volume and average pore diameter is observed at higher temperatures due to shrinking of the larger, less stable macro and mesopores.(*123*)

The trend in surface area is similar for A300 to A450 with an increase in surface area and microporosity. However, surface area sharply decreases from A450 to A800, this may be attributed to the coalescence of micropores into mesopores at higher temperatures. As with S300 to S800 a reduction in average pore diameter was also observed between A300 and A800 due to the contraction of pores.

Table 2.4 Porosimetry characteristics of Starbon® and Norit.

	S300	S450	S800	A300	A450	A800	Norit
S_{BET} [m^2 g^{-1}]	332	402	535	280	402	265	798
S>2nm [m^2 g^{-1}]	153	131	133	214	232	247	102
Total pore volume [cm^3 g^{-1}]	0.82	0.69	0.75	1.41	1.36	1.08	0.57
Average pore diameter [nm] desorption	17	12	12	19	17	15	4
Microporous volume [cm^3 g^{-1}]	0.17	0.15	0.22	0.11	0.14	0.04	0.42
% Microporosity	20	22	29	8	10	4	79

Norit exhibited the highest BET surface area of all of the materials at 798 m^2 g^{-1}, this is characteristic of an almost completely microporous solid. Due to Norit exhibiting similar surface functionality compared to Starbon® (as seen from XPS analysis) and the lack of any mesopore character in Norit it is an ideal material for comparison with Starbon® as it can help to determine the affect of mesoporosity on adsorption.

2.2.3 Dye adsorption capacities related to material properties

To understand the adsorption on the material surface and to establish the relationship between pore textural properties and the adsorption ability, the adsorption of methylene blue (MB), acid blue 92 (AB), Nile blue A (NB) and mordant yellow 10 (MY) were studied by the Starbon® materials (Figure 2.9), for comparison Norit was also used as an adsorbent.

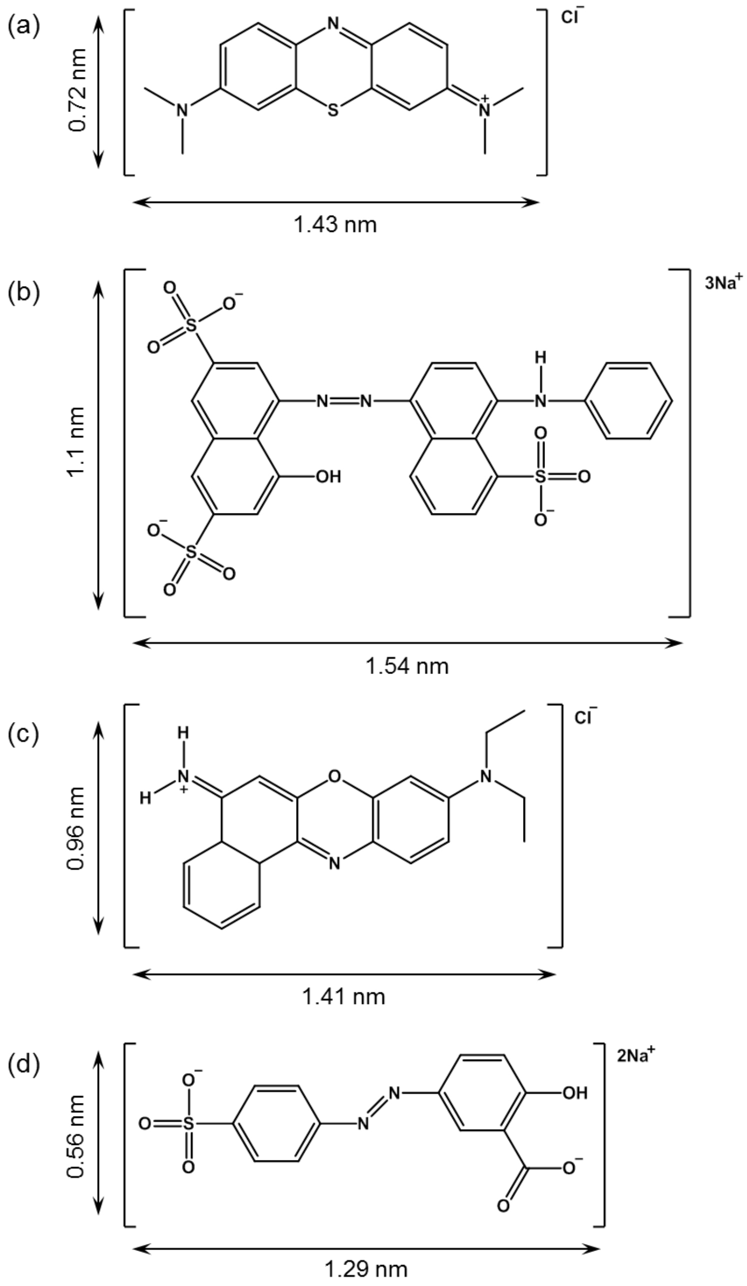

Figure 2.9 Structures and dimensions of (a) methylene blue, (b) acid blue 92, (c) Nile blue A and (d) mordant yellow 10.

Table 2.5 Adsorption capacity and surface area of dye coverage.

	Methylene blue			Acid blue 92			Nile blue A			Mordant yellow 10		
	Adsorption capacity [mg g^{-1}]	Surface area of coverage [m^2 g^{-1}]	% of surface covered[a]	Adsorption capacity [mg g^{-1}]	Surface area of coverage [m^2 g^{-1}]	% of surface covered[a]	Adsorption capacity [mg g^{-1}]	Surface area of coverage [m^2 g^{-1}]	% of surface covered[a]	Adsorption capacity [mg g^{-1}]	Surface area of coverage [m^2 g^{-1}]	% of surface covered[a]
Norit	42	81	10	49	72	9	66	152	19	50	59	7
S300	36	70	21	27	40	12	40	92	28	24	28	8
S450	49	95	24	41	60	15	46	106	26	22	26	6
S800	52	101	19	39	57	11	61	140	26	76	90	17
A300	186	361	129	82	120	43	83	191	68	12	14	5
A450	108	209	52	72	106	26	54	124	31	6	7	2
A800	97	188	71	108	158	60	53	121	46	67	80	30

[a] Percentage based on surface area calculated from N_2 adsorption.

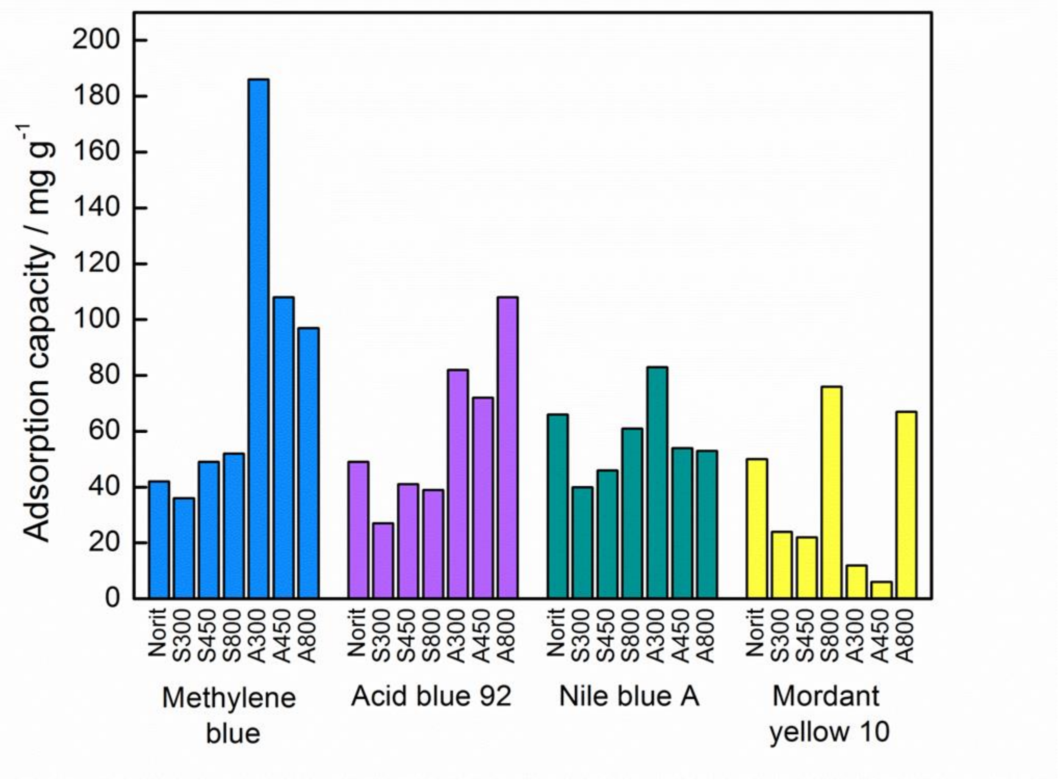

Figure 2.10 Adsorption capacities of Norit and Starbon® adsorbents.

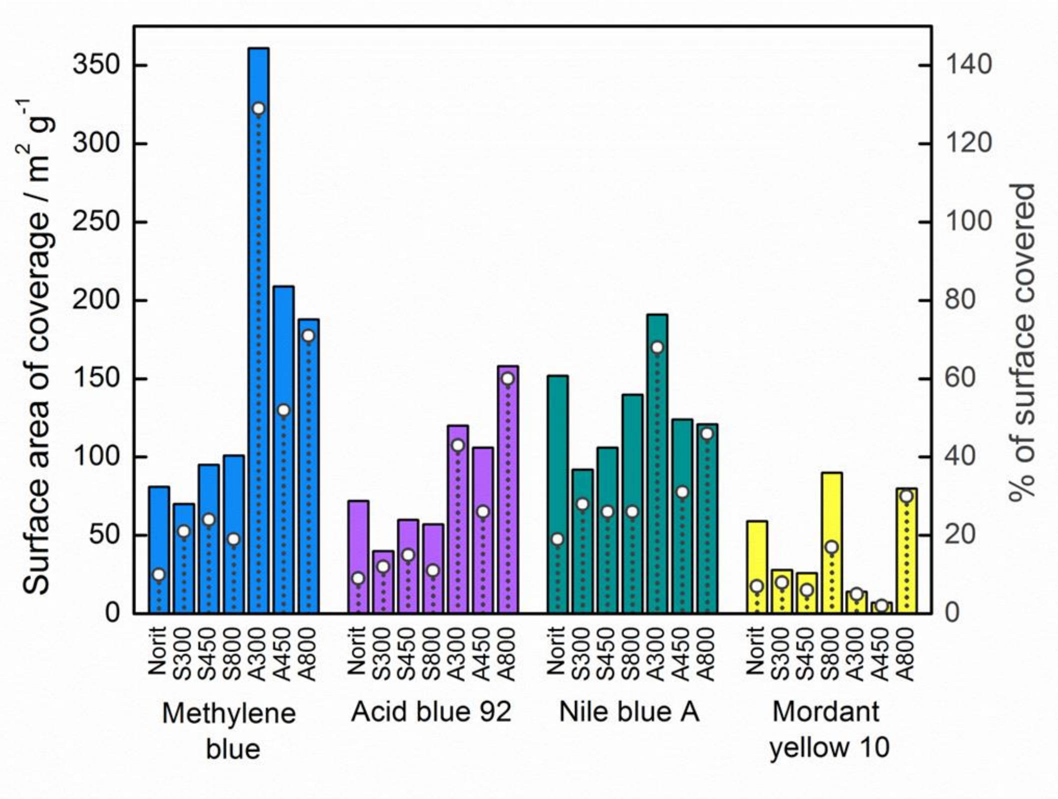

Figure 2.11 Surface area of coverage (bar) and % of surface coverage (line and dot) of Norit and Starbon® adsorbents,

Table 2.5 compiles the adsorption capacities of MB, AB, NB and MY on the various materials, this data enabled an estimation of the dye surface area coverage, using the size of each dye molecule (Figure 2.9).

An order of adsorption capacity for MB, a cationic dye, was: A300 >> A450 > A800 >> S800 > S450 > Norit > S300. A300 was a highly effective adsorber of MB, adsorption capacity was 186 mg g^{-1} which is more than four times higher than Norit at 42 mg g^{-1}. The calculated surface area of dye coverage was higher than BET surface area for N_2 adsorption, this could be due to high carbonyl oxygen functionality of the adsorbent surface (Table 2.3) resulting in a high affinity between the dye molecule and the adsorbent, as represented below:(*120*)

$$C{=}O^{\delta-} + MB^{\delta+} \rightarrow C{=}O{-}{-}{-}MB$$

It can also be attributed to large mesopores, average diameter of 19 nm, allowing for effective diffusion of dye into the pore structure (Table 2.4). The adsorbed MB is able to occupy all the porous volume, giving the appearance of a larger surface area of dye coverage.(*124*)

The adsorption capacities of the materials for AB are in the order of A800 > A300 > A450 >> Norit > S450 > S800 > S300. A800 is the most efficient adsorbent for this dye, exhibiting twice the adsorption capacity of Norit (108 mg g^{-1} compared to 49 mg g^{-1}), this is due to the combination of high mesoporosity and high aromaticity unique to A800 which facilitates strong π-π interactions with the free electrons of the dye molecule present in the aromatic ring and multipule bonds.(*125*) A300 adsorption of AB is significantly lower than MB adsorption, likely caused by electrostatic repulsion between the anionic dye and anionic polymer surface.(*47, 120*)

For MB and AB adsorption the materials S300, S450 and S800 exhibit significantly lower adsorption capacities than A300, A450 and A800 and similar capacities compared to Norit for both dyes. As S300, S450 and S800 exhibit pore volumes and diameters closer to the alginic acid derived materials than Norit it can be assumed that this is not the factor limiting dye uptake. Rather it could likely be due to the high concentration of C-O groups (such as hydroxyl groups) on the surface of the starch derived adsorbents and Norit that results in their similar adsorbent capacities.

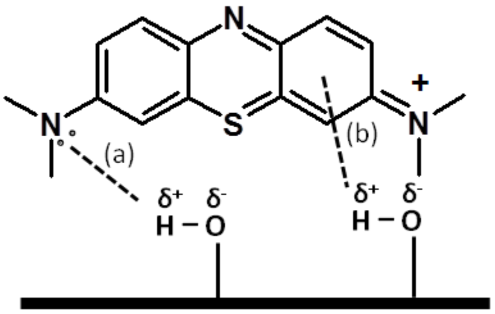

Figure 2.12 Methylene blue-polysaccharide interactions: (a) dipole-dipole hydrogen bonding interactions, (b) Yoshida H-bonding.

In this case molecules are likely to be attracted to the surface due to:

a. Dipole-dipole interactions between the hydrogen on the adsorbent surface and the electropositive groups on the dye (Figure 2.12).
b. Yoshida hydrogen bonding between the OH groups and the aromatic rings (Figure 2.12).

This correlates well with observations for similar systems.(*47, 126, 127*) However, this highly functionalised surface can also give rise to hydrogen bonding with the water present in the system, thus, competing for adsorption sites and vastly reducing uptake of the dye.(*128, 129*) The higher degree of graphitisation of the alginic acid derived materials prevents this competition occurring.

For the adsorption of NB and MY the alginic acid derived Starbon® perform less effectively exhibiting lower adsorption capacities closer to those of the starch-derived materials and Norit. The order of adsorption capacity for NB is: A300 > Norit > S800 > A450 > A800 > S450 > S300 and MY is: S800 > A800 > Norit > S300 > S450 > A300 > A450. Comparison of uptake of the two cationic dyes NB and MB shows that the adsorption capacities of S300, S450 and S800 stay relatively constant despite the slight differences in chemical structure of the dyes. The substantial decrease of approximately half in the adsorption capacity of A300, A450 and A800 is difficult to explain. There are some subtle differences between NB and MB such as: the addition of an aromatic ring, the exchange of sulphur for an oxygen and the increase in the steric bulk of the molecule due to the addition of ethyl groups. However, none of these changes on their own are likely to have a significant effect on dye adsorption, therefore, it must be a combination of these factors. Unfortunately the adsorption capacity of MY by A300 and A450 is very low, as with AB this is likely caused by electrostatic repulsion between the surface of the adsorbent and the dye. This effect is increased in this instance due to the lack of electropositive groups (e.g. sulphur and aromatic rings) present in MY to counter the effect of the electron-withdrawing oxygen groups.(*125*) For S800 adsorption capacity of MY is almost double that seen for AB, this result would suggest that adsorption in this case is not so dependent on the chemical nature of the dye but rather that size of dye influences adsorption capacity.

The microporous material Norit, demonstrated low adsorption with only a small amount, between 7 – 19%, coverage of the total surface area achieved. It has been previously reported that for adsorbents with small pore diameters pore blockage may occur due to the aggregation of bulky molecules, such as dyes, in the pore orifice.(*120*) Therefore the full surface area of the adsorbent cannot be utilised, reducing effectiveness of adsorption. This combined with the low pore volume of Norit are the likely causes of the poor adsorption capacity.

2.2.4 Adsorption isotherm analysis of dye adsorption by Starbon®

In order to investigate the mechanism of dye adsorption on to the Starbon® the experimental data were applied to the Langmuir, Freundlich and Dubinin-Radushkevich (D-R) isotherm equations. The constant parameters of the isotherm equations for this adsorption process were calculated by regression using the linear form of the isotherm equations. The constant parameters and correlation coefficient (R^2) are summarized in Table 2.6 – Table 2.12 (graphs showing original data and isotherm fitting can be seen in Appendix 1).

2.2.4.1 Langmuir isotherm

Langmuir proposed an equation to determine the monolayer adsorption capacity of a solid.(*130*) The Langmuir adsorption isotherm has been successfully applied to many adsorption processes. The linear form of the isotherm is represented by the following equation:

$$\frac{Ce}{qe} = \frac{1}{K_L} + \frac{a_L}{K_L} Ce$$

$$Q_0 = \frac{K_L}{a_L}$$

Where Ce is the dye concentration at equilibrium (mg L^{-1}), qe the adsorption capacity at equilibrium and a_L (L mg^{-1}) and K_L (L g^{-1})are Langmuir adsorption constants. Q_0 is the monolayer adsorption capacity of the solid (mg g^{-1}).

This model assumes monolayer coverage of adsorbate on the homogeneous surface of the adsorbent. This isotherm makes the simple assumption that adsorption is occurring at specific homogeneous sites within the adsorbent and once an adsorbate molecule is occupying this site no further adsorption can take place on it.(*131*)

2.2.4.2 Freundlich isotherm

The Freundlich equation is employed to describe multilayer adsorption on heterogeneous surfaces, which is characterised by the heterogeneity factor *n*. The empirical equation is written as:

$$qe = kf\ Ce^{1/n}$$

The linear form of the equation is used for this work and can be obtained by taking the logarithm:

$$\ln qe = \ln kf + \frac{1}{n} \ln Ce$$

Where *kf* is the Freundlich constant and is linked to adsorption capacity of the solid. The heterogeneity factor, *n*, signifies the intensity of adsorption. An *n* of close to or greater than unity indicates favourable adsorption of the adsorbate molecule.(*132*) The Freundlich equation is related to the Langmuir equation however it models for adsorption on an amorphous or heterogeneous surface where the amount of adsorbed material is the summation of adsorption on all sites. This isotherm describes multilayer adsorption.(*133, 134*)

2.2.4.3 Dubinin-Radushkevich isotherm (D-R)

The equation proposed by Dubinin and Radushkevich can be used to describe adsorption onto porous solids, it assumes no homogeneous surface of the adsorbent.(*135*) Assuming the adsorption is limited to a monolayer the D-R equation can be used to estimate the energy of adsorption.(*136*) The equation is written as:

$$\boldsymbol{qe = q_m \, e^{(-K'\varepsilon^2)}}$$

The linear form of the equation was used to model the adsorption, where ε, the Polanyi potential, is equal to:

$$\boldsymbol{\ln qe = \ln q_m - K'\varepsilon^2}$$

$$\boldsymbol{\varepsilon = RT \ln\left(1 + \frac{1}{Ce}\right)}$$

Where q_m signifies the monolayer saturation capacity (L g^{-1}) and K' the constant of adsorption energy which gives the mean free energy (E) of adsorption per molecule of adsorbate when it is transferred to the surface of the solid from the solution and can be calculated from the following relationship:(*137*)

$$\boldsymbol{E = \frac{1}{\sqrt{2K'}}}$$

The mean adsorption energy (E) gives information about chemical and physical adsorption, where E in the range of 8-16 kJ mol^{-1} indicates physical adsorption of the adsorbate.(*138*) This isotherm is not suitable for solids with fine micropore systems.(*139*)

Table 2.6 Norit isotherm parameters.[a]

Isotherm parameters	MB			AB			NB			MY		
Langmuir												
a_L (L mg^{-1})	0.42	±	0.09	0.16	±	0.004	3.9	±	0.59	3.0	±	0.15
Q_0 (mg g^{-1})	12.0	±	13.4	18.3	±	1.6	59.5	±	58.7	23.6	±	135.7
R^2	0.9069			0.9985			0.9326			0.9399		
Freundlich												
kf	0.57	±	0.94	-	-	-	64.6	±	13.6	28.9	±	2.6
n	0.32	±	0.05	-	-	-	-1.4	±	0.49	-5.6	±	1.3
R^2	0.9407			-	-	-	0.8235			0.9303		
D-R												
q_m x10^{-3} [mol g^{-1}]	-	-	-	-	-	-	-	-	-	-	-	-
K' x10^{-8} [mol^2 J^{-2}]	-	-	-	-	-	-	-	-	-	-	-	-
E (kJ mol^{-1})	-	-	-	-	-	-	-	-	-	-	-	-
R^2	-	-	-	-	-	-	-	-	-	-	-	-

[a] Data with an R^2 less than 0.75 has not been included.

Table 2.7 S300 isotherm parameters.[a]

Isotherm parameters	MB			AB			NB			MY		
Langmuir												
a_L [L mg^{-1}]	6.0	±	0.19	0.11	±	0.02	-	-	-	0.01	±	0.002
Q_0 [mg g^{-1}]	0.96	±	13.2	11.1	±	1.6	-	-	-	110.5	±	30.6
R^2	0.8588			0.9001			-	-	-	0.9225		
Freundlich												
Kf	-	-	-	3.1 x10^{-7}	±	1.4 x10^{-6}	2.5	±	2.4	0.72	±	0.26
n	-	-	-	0.20	±	0.02	0.81	±	0.18	0.81	±	0.08
R^2	-	-	-	0.9826			0.8499			0.9768		
D-R												
q_m x10^{-3} [mol g^{-1}]	-	-	-	122.3	±	84.8	62.3	±	52.9	-	-	-
K' x10^{-8} [mol^2 J^{-2}]	-	-	-	1.4	±	0.19	0.93	±	0.26	-	-	-
E [kJ mol^{-1}]	-	-	-	6.0	±	0.42	7.35	±	1.0	-	-	-
R^2	-	-	-	0.9615			0.8550			-	-	-

[a] Data with an R^2 less than 0.75 has not been included.

Table 2.8 S450 isotherm parameters.[a]

Isotherm parameters	MB			AB			NB			MY		
Langmuir												
a_L [L mg^{-1}]	0.24	±	0.02	0.25	±	0.03	2.0	±	0.28	-	-	-
Q_0 [mg g^{-1}]	44.9	±	8.6	13.7	±	9.5	23.1	±	78.0	-	-	-
R^2	0.9839			0.9734			0.9170			-	-	-
Freundlich												
Kf	12.9	±	1.2	3.1	±	1.3	69.3	±	14.9	0.04	±	0.04
n	2.5	±	0.26	2.0	±	0.35	-2.5	±	0.96	0.47	±	0.05
R^2	0.9601			0.8852			0.8021			0.9400		
D-R												
q_m x10^{-3} [mol g^{-1}]	0.70	±	0.17	0.26	±	0.10	-	-	-	315.6	±	100.9
K' x10^{-8} [mol^2 J^{-2}]	0.29	±	0.04	0.28	±	0.08	-	-	-	1.5	±	0.06
E [kJ mol^{-1}]	13.1	±	0.89	11.4	±	1.15	-	-	-	5.8	±	0.12
R^2	0.9673			0.8878			-	-	-	0.9969		

[a] Data with an R^2 less than 0.75 has not been included.

Table 2.9 S800 isotherm parameters.[a]

Isotherm parameters	MB			AB			NB			MY		
Langmuir												
a_L [L mg^{-1}]	77.8	±	0.58	0.85	±	0.009	0.28	±	0.08	-	-	-
Q_0 [mg g^{-1}]	70.3	±	40.7	45.3	±	21.5	84.8	±	66.1	-	-	-
R^2	0.9999			0.9998			0.8602			-	-	-
Freundlich												
Kf	177.4	±	5.1	0.01	±	0.03	20.7	±	5.0	3.9	±	2.3
n	1.9	±	0.05	0.44	±	0.06	2.2	±	0.52	0.82	±	0.11
R^2	0.9986			0.9590			0.8205			0.9528		
D-R												
q_m x10^{-3} [mol g^{-1}]	16.4	±	2.8	-	-	-	12.4	±	1.5	-	-	-
K' x10^{-8} [mol^2 J^{-2}]	0.33	±	0.02	-	-	-	0.61	±	0.02	-	-	-
E [kJ mol^{-1}]	12.2	±	0.30	-	-	-	9.03	±	0.12	-	-	-
R^2	0.9952			-	-	-	0.9985			-	-	-

[a] Data with an R^2 less than 0.75 has not been included.

Table 2.10 A300 isotherm parameters.[a]

Isotherm parameters	MB			AB			NB			MY		
Langmuir												
a_L [L mg^{-1}]	-	-	-	0.08	±	0.03	9.1	±	0.21	-	-	-
Q_0 [mg g^{-1}]	-	-	-	5.2	±	5.9	232.5	±	89.3	-	-	-
R^2	-	-	-	0.8152			0.9974			-	-	-
Freundlich												
Kf	4.3x10^3	±	1.5 x10^3	-	-	-	4.8	±	0.76	-	-	-
n	0.87	±	0.07	-	-	-	-1.2	±	0.06	-	-	-
R^2	0.9707			-	-	-	0.9914			-	-	-
D-R												
q_m x10^{-3} [mol g^{-1}]	7.6x10^3	±	4.5x10^3	-	-	-	-	-	-	-	-	-
K' x10^{-8} [mol^2 J^{-2}]	0.64	±	0.06	-	-	-	-	-	-	-	-	-
E [kJ mol^{-1}]	8.86	±	0.39	-	-	-	-	-	-	-	-	-
R^2	0.9767			-	-	-	-	-	-	-	-	-

[a] Data with an R^2 less than 0.75 has not been included.

Table 2.11 A450 isotherm parameters.[a]

Isotherm parameters	MB			AB			NB			MY		
Langmuir												
a_L [L mg^{-1}]	183.7	±	0.15	0.07	±	2.8x10^{-4}	2.1	±	0.17	-	-	-
Q_0 [mg g^{-1}]	157.4	±	28.2	51.4	±	0.64	608.0	±	261.4	-	-	-
R^2	1.000			0.9999			0.9867			-	-	-
Freundlich												
Kf	145.3	±	21.1	3.5	±	0.75	261.3	±	44.5	-	-	-
n	9.9	±	2.4	1.2	±	0.09	2.4	±	0.38	-	-	-
R^2	0.8199			0.9887			0.9031			-	-	-
D-R												
q_m x10^{-3} [mol g^{-1}]	0.81	±	0.18	0.58	±	0.13	13.5	±	2.4	-	-	-
K' x10^{-8} [mol^2 J^{-2}]	0.06	±	0.01	0.39	±	0.04	0.27	±	0.02	-	-	-
E [kJ mol^{-1}]	29.8	±	3.9	11.3	±	0.57	13.6	±	0.40	-	-	-
R^2	0.8700			0.9701			0.9930			-	-	-

[a] Data with an R^2 less than 0.75 has not been included.

Table 2.12 A800 isotherm parameters.[a]

Isotherm parameters	MB			AB			NB			MY		
Langmuir												
a_L [L mg^{-1}]	5.6	±	0.59	0.16	±	0.03	16.0	±	0.38	-	-	-
Q_0 [mg g^{-1}]	178.2	±	112.4	184.6	±	150.3	597.6	±	272.1	-	-	-
R^2	0.9780			0.9215			0.9977			-	-	-
Freundlich												
Kf	-	-	-	29.8	±	8.1	345.9	±	75.3	1.5	±	0.68
n	-	-	-	2.1	±	0.26	3.9	±	0.59	0.67	±	0.06
R^2	-	-	-	0.9587			0.9101			0.9783		
D-R												
q_m x10^{-3} [mol g^{-1}]	-	-	-	209.4	±	163.5	6.3	±	3.5	-	-	-
K' x10^{-8} [mol^2 J^{-2}]	-	-	-	1.1	±	0.25	0.15	±	0.05	-	-	-
E [kJ mol^{-1}]	-	-	-	6.6	±	0.73	18.4	±	2.8	-	-	-
R^2	-	-	-	0.9070			0.7672			-	-	-

[a] Data with an R^2 less than 0.75 has not been included.

For S300 (Table 2.7) AB, NB and MY best fitted to the Freundlich equation, this is expected as the large pore diameter, 17 nm, allows for good accessibility to the pores and multilayer filling. It was only possible to adequately fit the MB data to the Langmuir isotherm which suggests only monolayer coverage is being achieved which could be caused by unfavourable interaction of the dye with the adsorbent surface. Overall for S450 and S800 the Langmuir isotherm also gave the best fitting to the data, with the exception of MY which was best described by the Freundlich equation. Due to MY being the smallest dye it is likely to fit easily into the adsorbent pores resulting in multilayer adsorption.(*140*)

MB adsorption on A300 (Table 2.10) correlated well to the Freundlich isotherm, this is in agreement with the experimental observations where very high adsorption of MB above the S_{BET} of the adsorbent was observed, clearly signifying multilayer and pore filling is occurring. The heterogeneity factor ‘n’ of 0.87 is very close to unity indicating that MB is being favourably adsorbed. AB adsorption onto A800 (Table 2.12) also showed the best affinity to the Freundlich isotherm. This is expected due to the very high degree of aromaticity of A800 and AB, there is strong π- π attraction between adsorbate and adsorbent and adsorbate and adsorbate. A combination of this along with the large pore diameter and relatively flat conformation of AB stacking and multilayer adsorption is easily achieved. This can also be seen for MY. For the remainder of the dyes adsorbed onto A300, A450 and A800 the Langmuir isotherm gives the best fitting to the data. Unfortunately due to the poor uptake of MY by A300 and A450 it was not possible to achieve good isotherm analysis of the data. For the adsorbents where it could be modelled the mean free energies of adsorption (E) calculated from the D-R isotherm were all in the range of physisorption.(*141*)

Overall adsorption by Norit showed best affinity to the Langmuir isotherm. This is in accordance with the microporous nature of the material meaning that only monolayer coverage can be achieved. Not unsurprisingly the D-R isotherm could not be used to model the data due to the nature of the adsorbent.(*139*)

2.2.5 Thermodynamic study of adsorption of MB and AB

To further understand the adsorption process taking place between Starbon® and dye thermodynamic parameters were evaluated (Table 2.13 and Table 2.14) (graphs showing original data can be seen in Appendix 1). This study was only carried out for adsorption of MB and AB on S300, S800, A300, A800 and Norit as these systems gave the best adsorption data to enable analysis. The analysis was carried out at 5 K intervals across a range of temperatures from 298 K to 318 K.

The van't Hoff equation was used to calculate the values of enthalpy (ΔH) and entropy (ΔS):

$$\boldsymbol{lnK = \frac{\Delta S}{R} - \frac{\Delta H}{RT}}$$

Where K is the equilibrium constant at temperature T (K) and R gas constant (8.314 J mol^{-1} K^{-1}). The Gibbs free energy was calculated to determine the feasibility of adsorption, using the equation:

$$\boldsymbol{\Delta G = -RTlnK}$$

All of the adsorbents show a positive value of ΔH suggestive of an endothermic adsorption process taking place, in this case adsorption increases with increasing temperature of the system, this is common for this type of system.(*142*) Adsorption in a solid/liquid system such as the one presented here takes place in two steps: (a) desorption of the molecules of solvent (water) previously adsorbed by the adsorbent (b) adsorption of the adsorbate. Endothermic adsorption suggests that the adsorbate and adsorbent are not strongly interacting on the surface and that the energy required to first displace the water molecules already adsorbed on the adsorbent is larger than the energy being produced by adsorbent/adsorbate interaction.(*143*)

The value of entropy is also positive due to increased randomness at the solid/solution interface upon uptake of dye, due to the release of solvent (water) from the surface of the adsorbent.(*144*) The values of ΔS for A300 and A800 are significantly larger that the values for S300 and S800, this may indicate that different modes of adsorption of MB are occurring for the two materials.

Figure 2.13 represents potential relationships between the dye and different adsorbent surfaces. Differing interactions of the dye, for example, a flat orientation of the dye with the adsorbent surface compared with end on adsorption of the dye, will release different amounts of solvent (water) from the surface and therefore affect the entropic value. The very large entropy values of A300 and A800 could suggest that the dye is adsorbing flat onto the surface which is possible due to the large pore diameters of the materials.

Table 2.13 Thermodynamic parameters of methylene blue adsorption.

	Temp. [K]	ln K	ΔG [kJ mol^{-1}]	ΔH [kJ mol^{-1}]	ΔS [J $mol^{-1}K^{-1}$]	R^2
Norit	298	1.2	-2.9	37.2 ± 4.4	129.6 ± 14.8	0.9592
	308	1.0	-2.7			
	318	0.7	-1.9			
S300	298	-0.8	1.9	20.8 ± 0.8	62.2 ± 2.5	0.9961
	308	-0.6	1.6			
	318	-0.4	1.1			
S800	298	-0.9	2.2	28.0 ± 2.6	85.5 ± 8.8	0.9653
	308	-0.8	2.0			
	318	-0.8	2.1			
A300	298	0.6	-1.4	104.4 ± 9.9	346.4 ± 33.2	0.9649
	308	0.5	-1.3			
	318	0.6	-1.6			
A800	298	0.7	-1.7	110.6 ± 5.9	377.9 ± 19.8	0.9887
	308	1.2	-3.1			
	318	3.7	-9.7			

This theory is supported by the high value of enthalpy for these adsorbents indicating relatively high energy input into the system is required to release water from the surface to enable adsorption. ΔG for these materials is negative demonstrating that adsorption is spontaneous in these cases.(*144*)

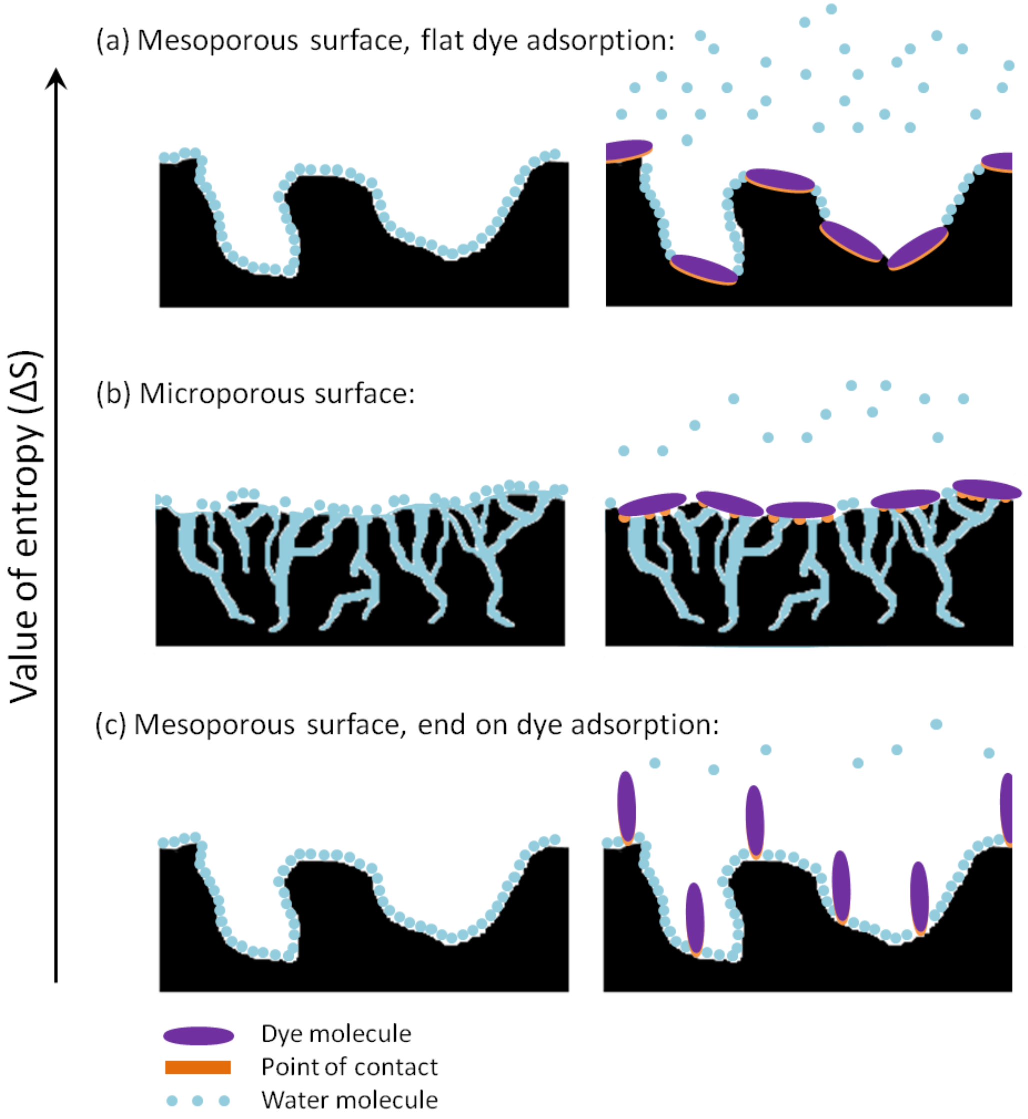

Figure 2.13 Schematic representation of water release caused by dye adsorption on to (a) mesoporous surface, flat orientation, (b) microporous surface and (c) mesoporous surface, end on orientation. (The points of contact between the dye and surface are highlighted in orange.) (Components of image not drawn to scale.)

As discussed in Section 2.2.3 due to the nature of S300 and S800 interaction with cationic dyes such as MB is likely to occur through interaction with the electron rich atoms which could feasibly lead to end on orientation of the dye leading to less release of water and a lower value of ΔS. Interestingly, the positive values of ΔG show adsorption of the dye is not spontaneous for these materials which may suggest this isn't a favorable process.

Table 2.14 Thermodynamic parameters of acid blue adsorption.

	Temp. [K]	Ln K	ΔG [kJ mol^{-1}]	ΔH [kJ mol^{-1}]	ΔS [J mol^{-1}K^{-1}]	R^2
Norit	298	-1.1	2.7	47.4 ± 4.7	149.3 ± 15.3	0.9715
	308	-0.5	1.3			
	318	-1.2	3.2			
S300	298	-2.4	5.9	15.2 ± 1.5	36.6 ± 5.2	0.9503
	308	-2.5	6.4			
	318	-2.6	6.9			
S800	298	-1.7	4.2	58.2 ± 15.1	165.5 ± 50.6	0.8224
	308	-1.6	4.1			
	318	-1.7	4.5			
A300	298	-2.7	6.7	27.7 ± 1.7	62.6 ± 5.7	0.9922
	308	-2.8	7.2			
	318	-2.9	7.7			
A800	298	-0.05	0.1	40.6 ± 8	126.5 ± 26.2	0.8915
	308	-0.8	2.0			
	318	0.08	-0.2			

The values of ΔH and ΔS for AB adsorption are positive for all adsorbents. The reduction in the enthalpy and entropy of S300, A300 and A800 compared to MB adsorption suggest that there is less of an enthalpic barrier. The values of ΔS for S800 and A800 are much closer in range than observed for MB adsorption, this implies that adsorption of AB on to these adsorbents may be occurring via a similar mechanism. The increase in entropy of S800 (from 85.5 KJ mol^{-1} for MB to 165.5 kJ mol^{-1} for AB) point toward a flatter orientation of the dye on the adsorbent surface. However the entropy values of S800 and A800 are not high enough to indicate that this is happening to the same extent as seen for MB. Therefore, it is possible that adsorption of the dye is due to stacking of the dye molecules onto one another and thus less solvent (water) is released from the adsorbent surface and the entropy is lowered. The values of ΔG are all positive for acid blue adsorption indicative of the non-spontaneous nature of the adsorption process.

The thermodynamic parameters ΔH and ΔS for adsorption using Norit stay relatively similar for MB and AB, this would suggest that the adsorption process is unaffected by the nature of the dye but rather is limited by the nature of the adsorbent. The only significant difference can be observed for the values of ΔG which are negative for MB and positive for AB adsorption. This difference is likely to be causes by the cationic vs anionic nature of the dyes affecting how favorably they interact with the surface of the adsorbent.

2.2.6 Comparison of rate of adsorption of MB and AB

Information relating to the kinetic adsorption activity of Starbon® was vital for its use in applications, such as water treatment.

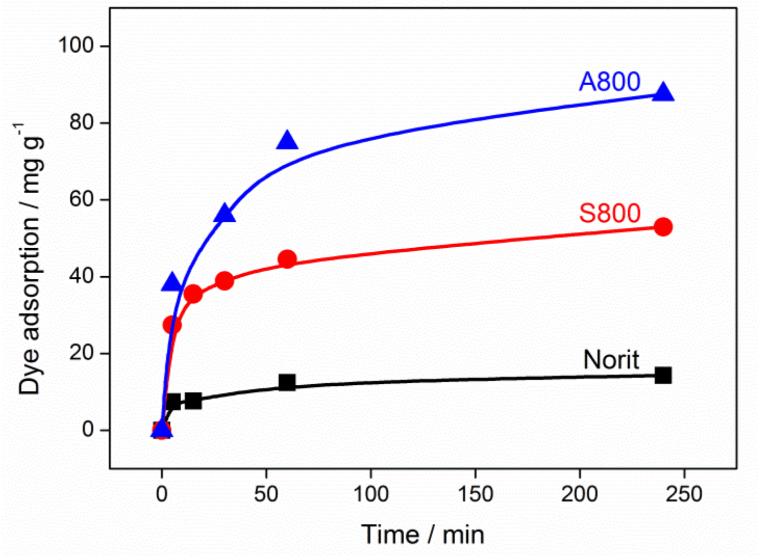

Figure 2.14 Rate of uptake of methylene blue by Norit, S800 and A800.

Figure 2.14 plots the adsorption of MB onto three adsorbents versus time. A800 showed the fastest rate of adsorption, with the majority of the dye being adsorbed within the first 60 minute and Norit is the slowest and least efficient of the materials. A similar correlation was observed for AB adsorption (Figure 2.15). These results gives evidence for the importance of larger pore in adsorbents as they allow for free transportation of the dye within the pore structure leading to fast uptake of the dye.(*145*)

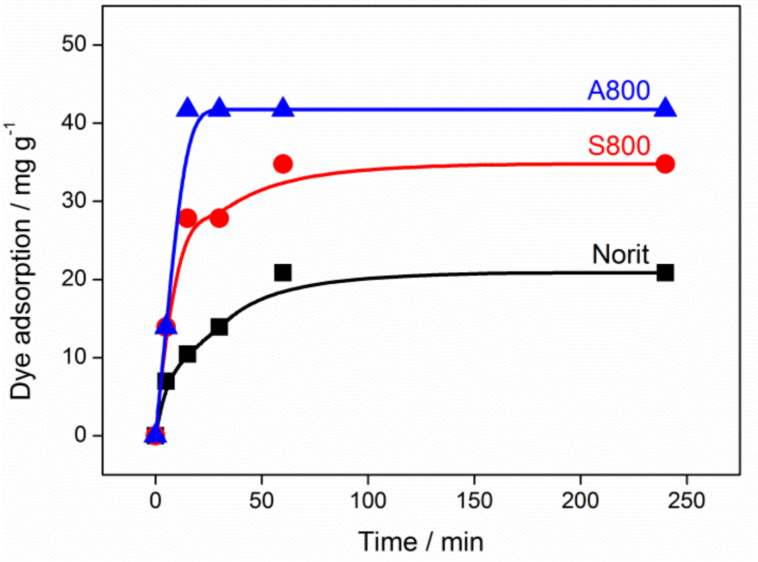

Figure 2.15 Rate of uptake of acid blue by Norit, S800 and A800.

2.3 Conclusion

Mesoporous materials were successfully prepared from starch and alginic acid starting materials without the use of a template. Characterisation of the materials using porosimetry showed that the alginic acid derived Starbon® exhibit a higher degree of mesoporosity than the starch derived Starbon®. This is a likely result of the tangled nature of starch due to the branched amylopectin chains that restricts pore sizes. Solid-state NMR, IR and XPS analysis showed the changing surface functionality of the materials with increasing preparation temperature, from an oxygen rich surface (S300 and A300) to an aromatic surface (S800 and A800).

Highly efficient adsorption of dyes can be achieved using all of the Starbon®. The results show that Starbon® have better uptake capacities than commercial activated carbon, Norit, for the majority of dyes tested despite having significantly smaller surface areas thus showing that large pore volumes and pore diameters are principally important for fast and effective dye uptake. In particular, A300 and A800 adsorbents with mesoporosity of above 80%, pore diameters between 14 – 19 nm and pore volumes above 1 cm^{3}g^{-1}, but with less than 300 m^2 g^{-1} surface area, show high adsorption capacities, e.g. A300 shows adsorption capacity of 186 mg g^{-1} for MB, more than four times higher than Norit. Kinetic analysis also showed the advantages of large pore diameters and volumes in allowing for fast and effective uptake of dyes, with A800 being the fastest to uptake dye and Norit the slowest.

Isotherm analysis showed that the adsorption data for Starbon® correlated well to either the Langmuir or Freundlich models depending on the adsorbent/adsorbate system. The D-R model could also be applied to the majority of the materials and showed that the adsorption process occurring was physisorption. Norit adsorption data was best modelled by the Langmuir isotherm which is to be expected for a material that it almost entirely microporous as no multilayer adsorption can occur. Thermodynamic parameters for all of the systems were useful to gain further knowledge of the adsorption mechanism that was taking place. It showed that the pore size and surface functionality of the adsorbent strongly influenced the interaction with the dye. All of the values of enthalpy and entropy were positive indicating endothermic adsorption was occurring and also that randomness was increasing in the system due to the release of water from the adsorbent interface. The magnitude of enthalpy and entropy varied and were generally much higher for the alginic acid materials than the starch materials. It was concluded that two different modes of adsorption were occurring: for A300 and A800 it was likely that the dye was being adsorbed in a flat orientation leading to more water release and higher thermodynamic parameter values, whereas for S300 and S800 the dye was being adsorbed in an end-on orientation, thus reducing water release from the surface.

Overall, it can be concluded that for the adsorption of dye molecules as investigated here it is advantageous to use adsorbents with a large mesoporous character, such as Starbon®, rather than microporous adsorbents regardless of surface area of the materials.

Chapter 3

Use of Starbon® for adsorption of phenolics

Aspects of the work presented in this chapter have appeared in:

Poster given at RSC Atmospheric and Environmental Chemistry Forum,
London, UK, June 2010

Oral presentation given at Alg'n'Chem: Algae, new resources for industry?
Montpellier, France, November 2011

Oral presentation given at Starbon® Day meeting, York, UK, September 2012

Chapter 3.

Use of Starbon® for Adsorption of Phenolics

3.1 Introduction

Phenolic compounds are released into the environment as part of many industrial effluents, including; petroleum refineries, steel foundries and herbicide industries.(*146*) They are potentially toxic and carcinogenic, posing significant threat to the biosphere. Therefore, it is imperative that they are removed from wastes for safe disposal.

Work in Chapter 2 has already shown that Starbon® are efficient adsorbers of large organic molecules such as dyes, however, their affinity to adsorb small organic molecules has not before been investigated. Herein, work is presented showing the feasibility of four Starbon® adsorbents S300, S800, A300 and A800 and commercially available activated carbon, Norit, for removal of a range of phenolics from aqueous solutions. As in Chapter 2 the affect of differing polysaccharide type on adsorption capacity is investigated, along with the effects of contact time and adsorption temperature.

Six phenols were used for this work, these particular molecules were chosen as they gave an array of functional groups, were water soluble and many are involved in pharmaceutical processes (Figure 3.1).

3.1.1 Aims

The aims of the work presented herein:

- Determine the influence of mesoporosity and surface functionality of Starbon® on the uptake of phenolic compounds.
- To ascertain the effect, if any, of differing phenolic functional groups on their adsorption by Starbon®.

- Propose a potential mechanism for phenolic adsorption onto the surface of Starbon® using thermodynamic and phenol desorption studies.

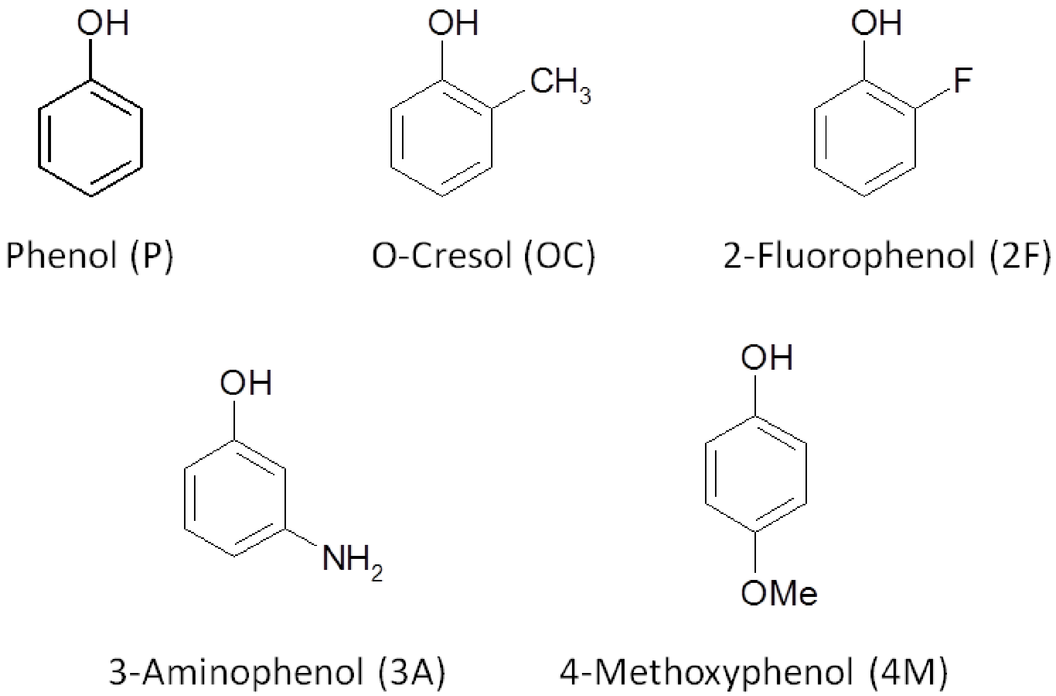

Phenol (P) O-Cresol (OC) 2-Fluorophenol (2F)

3-Aminophenol (3A) 4-Methoxyphenol (4M)

Figure 3.1 Structures, names and abbreviations (in brackets) of the six phenolics used.

3.2 Results and Discussion

3.2.1 Effect of phenolic concentration on adsorption capacity

The effect of initial phenolic concentration on adsorption was investigated at a concentration range from 25 to 200 mg L^{-1} at 298 K (Figure 3.2). Overall, for all adsorbents and phenols the adsorption capacity increased with increase in phenolic concentration due to improved interaction between the phenolic and Starbon® at higher concentrations.

For most of the phenolics saturation of the adsorbent can be observed above 150 mg L^{-1} indicating there are a finite number of adsorption sites available on the adsorbent.

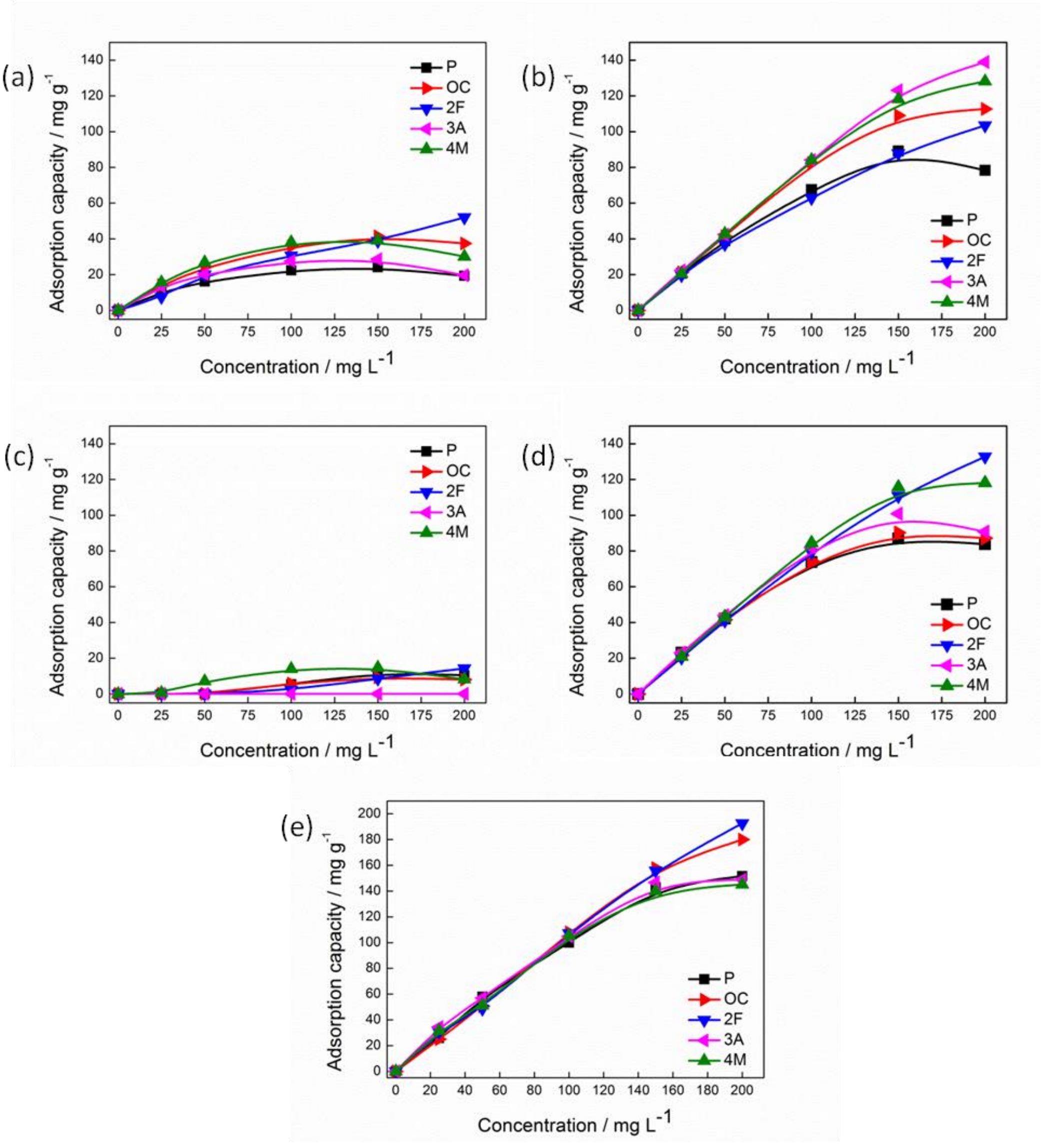

Figure 3.2 Effect of initial phenolic concentration on adsorption capacity of (a) S300, (b) S800, (c) A300, (d) A800 and (e) Norit.

The high temperature materials (S800 and A800) are the superior adsorbers for all of the different phenols, what these results demonstrate is that one of the limiting factors for adsorption is the surface properties of the adsorption material. Moreno-Castillia observed that surface chemistry of the adsorbent has a great influence on adsorbent-adsorbate interactions and he considered it the main factor in the adsorption mechanism from aqueous solutions.(*128*) In the case of aromatic compounds adsorption is generally understood to be achieved by interaction between the π-electrons of the aromatic ring and the surface of the adsorbent.(*129*) This mechanism of adsorption would explain the poor adsorption by S300 and A300 due to the oxygen-rich, highly functionalised surface of the adsorbent that can give rise to H-bonds with water and can vastly reduce adsorption.(*147*)

Table 3.1 Adsorption capacities of Starbon® compared with other adsorbents from the literature.

Adsorbent	Surface area [m^2 g^{-1}]	Phenol	Temp. [K]	Adsorption capacity [mg g^{-1}]	Ref.
S800	535	Phenol	298	87	Current work
		o-Cresol		90	
		2-fluorophenol		133	
		3-aminophenol		101	
		4-methoxphenol		118	
A800	265	Phenol	298	89	Current work
		o-Cresol		113	
		2-fluorophenol		104	
		3-aminophenol		139	
		4-methoxphenol		128	
Norit	798	Phenol		152	Current work
		o-Cresol		180	
		2-fluorophenol		193	
		3-aminophenol		149	
		4-methoxphenol		145	
Coir pith carbon	167	2-chlorophenol	308	18	(*148*)
Apricot stone shell 50% H$_3$PO$_4$ 500^{o}C	1306	Phenol	N/D	120	(*149*)
		m-Cresol		101	
		p-Cresol		108	
		2-chlorophenol		120	
Coconut shell	1062	*p*-chlorophenol	297	334	(*150*)
Wood; Pica	1699			309	
Coal; SP	865			231	
Straw	322			129	
Tire	346			206	

As in previous work, Norit was used here as a basis for comparing the performance of Starbon® with a commercially available activated carbon. Norit was seen to exhibit higher adsorption capacities than Starbon®. The small sizes of the phenolic compounds (relative to dye molecules for instance) allow them to access even the smaller pores of the adsorbent and therefore the high mesoporosity and wide pore diameters of Starbon® is no longer such an advantage for adsorption. The materials with larger surface areas, such as Norit, can uptake more of the adsorbate.(*151*) Comparison of Starbon® adsorption capacities with literature data for a range of other adsorbents supports this observation as the materials with the larger surface areas present the best phenolic uptake (Table 3.1).

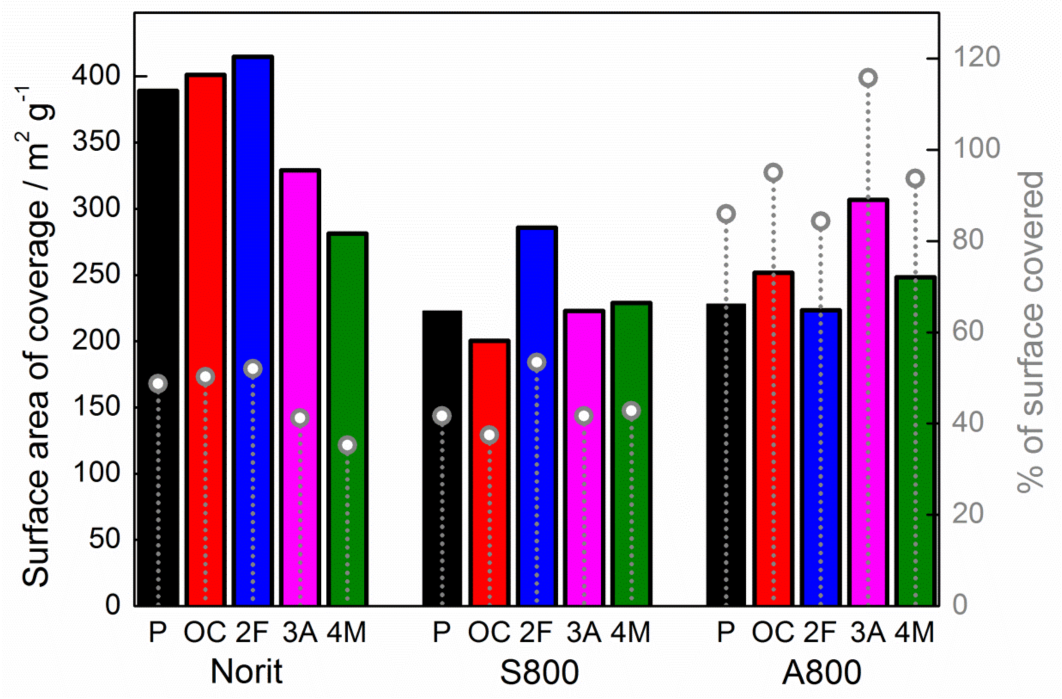

Figure 3.3 Surface area of phenolic coverage (bar) and % of adsorbent surface utilised during adsorption (line and dot) for Norit, S800 and A800.

A calculation of surface area of phenolic coverage and comparison of this with the surface area of the adsorbent used during adsorption (% surface coverage), Figure 3.3, gives more information about the affect adsorbent characteristics have on uptake.

Whilst Norit shows higher adsorbent capacity than both the Starbon® materials, analysis shows that approximately only 50% of the available surface area is being utilised. This is also true for S800, however for A800 percentage surface coverage is >85% with surface coverage of 3A being as high as 116% of the available surface.

Similar occurrences were previously observed for the adsorption of dyes (Chapter 2, Table 2.6) and demonstrate the importance of mesoporosity and large pore diameters of adsorbents to allow access to the entire interior pore structure of the material, thus enabling effective uptake. For example, if the surface area of A800 could be increased to that of Norit (while maintaining the same degree of mesoporosity) then an adsorption capacity of 416 mg g^{-1} for 3A could potentially be achieved.

3.2.2 Discussion about likely phenolic adsorption mechanisms

At this point, prior to more in depth analysis of the data it is important to discuss potential modes of adsorption that could be occurring for the uptake of phenolics to be referred to throughout the remainder of the chapter.

For this work a model of a π-system, proposed by Hunter and Sanders, where the aromatic ring is described as a positively charged σ-framework sandwiched in-between two negatively charged clouds of π-electron density will be used, illustrated in Figure 3.4 (a).(*152*)

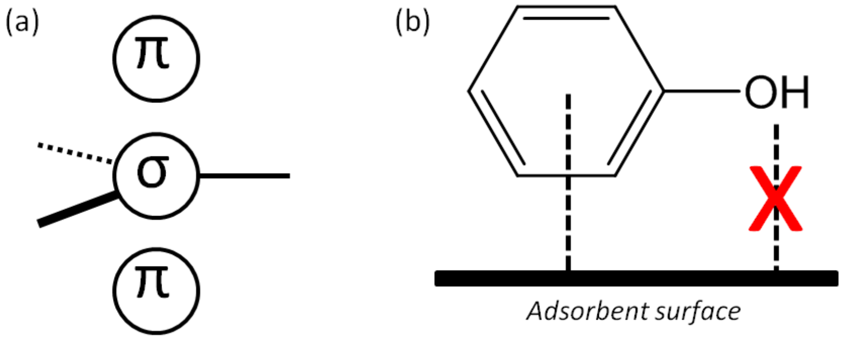

Figure 3.4 (a) An sp^2 hybridised atom in a π-system and (b) an illustration of how phenol interacts with adsorbent surface.(*152, 153*)

It is generally understood that small aromatic molecules interact with adsorbent surfaces through the π-electrons surrounding the aromatic ring rather than through the phenolic hydroxyl group or any other possible substituents present (Figure 3.4 (b)). Depending on the characteristics of the adsorbent surface a number of different interactions can occur, the major ones being:

3.2.2.1 H-π interactions

Hydrogen atoms present on the adsorbent surface can H-bond with the π-electrons of the aromatic ring. Bonding strength is comparable to that of benzene-water complexes, approximately 7.5 kJ mol^{-1}.(*154*) In aqueous systems, like the ones used in this chapter, competitive water adsorption could limit this type of interaction.(*155*)

3.2.2.2 n-π electron-donor acceptor interactions

These are electron-donor acceptor (EDA) interactions where *n* = non-bonding electrons at the adsorbent surface.(*155*) Such interactions have been shown to contribute significantly to retention of aromatic molecules onto adsorbent surfaces.(*156*)

3.2.2.3 π-π interactions

This type of interaction is favoured by strongly adsorbing aromatic π-systems such as the graphene sheets found on the surfaces of activated carbons.(*155, 157*) This type of interaction is strongly controlled by the electron-deficiency of the phenol ring and therefore is favoured in the presence of electron-withdrawing substituents.

The X-ray photoelectron spectroscopy (XPS) analysis of S800 and A800 (Chapter 2, Figure 2.8 and Table 2.5) shows that the surfaces of these two materials differ quite substantially; whilst 40% of S800 surface contains hydroxyl and carbonyl groups, only 18% of the A800 surface contains carbonyl functionality (with no hydroxyl groups being seen) with aromatic carbons making up the majority of the surface (45%). (Norit most closely resembles S800 in its surface characteristics.) From this it could be theorised that it is likely that for S800 adsorption is taking place predominantly through a combination of H-π and n-π interactions, whereas, the high aromatisation of the A800 surface would suggest that adsorption is most likely to happen via π-π interactions. The following isotherm and kinetic analysis of the adsorption data will serve to prove or disprove this hypothesis.

3.2.3 Adsorption isotherm analysis of phenolic adsorption

In order to investigate the mechanism of phenol (P), o-cresol (OC), 2-fluorophenol (2F), 3-aminophenol (3A) and 4-methoxyphenol (4M) adsorption on Starbon® and Norit the experimental data were applied to the Langmuir, Freundlich and Dubinin-Radushkevich (D-R) isotherm equations (Figure 3.5). The parameters of the isotherm equations for this adsorption process were calculated by regression using the linear form of the isotherm equations. The constant parameters and correlation coefficient (R^2) are summarized in Table 3.2 to Table 3.4.

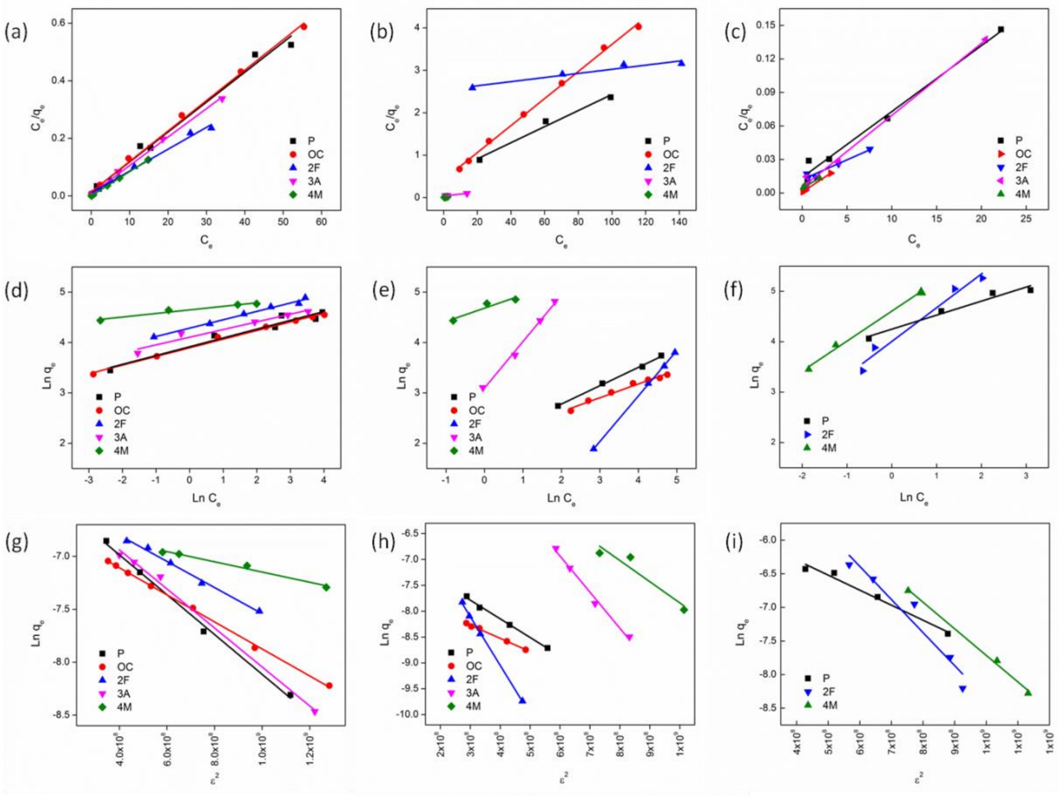

Figure 3.5 Langmuir adsorption isotherms for (a) S800, (b) A800, (c) Norit, Freundlich (d) S800, (e) A800, (f) Norit and D-R (g) S800, (h) A800, (i) Norit.

In most cases the data for Norit can be best modelled by the Langmuir equation with correlation coefficients between 0.9799 – 1.0000 this is in line with the previous results for dye adsorption and is a product of a relatively uniform adsorbent surface and a high degree of microporosity which prevents multilayer formation.

Table 3.2 Norit adsorption isotherm parameters.[a]

Isotherm parameters	P	OC	2F	3A	4M
Langmuir					
a_L [L mg^{-1}]	0.42 ± 0.12	7.4 ± 3.2	0.30 ± 0.01	1.3 ± 0.83	1.1 ± 3.9x10^{-4}
Q_0 [mg g^{-1}]	169.5 ± 12.2	188.0 ± 6.3	283.3 ± 36.7	155.0 ± 6.4	213.7 ± 0.31
R^2	0.9799	0.9966	0.9382	0.9933	1.0000
Freundlich					
Kf	70.0 ± 5.2	- - -	54.8 ± 5.4	- - -	100.1 ± 6.7
n	3.6 ± 0.49	- - -	1.5 ± 0.17	- - -	1.7 ± 0.14
R^2	0.9481	- - -	0.9618	- - -	0.9860
D-R					
q_m x10^{-4} [mol g^{-1}]	45.1 ± 6.6	- - -	321.4 ± 190.6	- - -	232.8 ± 58.8
K’ x10^{-9} [mol^2 J^{-2}]	2.2 ± 0.23	- - -	4.9 ± 0.73	- - -	4.0 ± 0.25
E [kJ mol^{-1}]	15.0 ± 0.77	- - -	10.1 ± 0.76	- - -	11.2 ± 0.36
R^2	0.9696	- - -	0.9173	- - -	0.9918

[a] Data with an R^2 less than 0.75 has not been included.

Table 3.3 S800 adsorption isotherm parameters.

Isotherm parameters	P	OC	2F	3A	4M
Langmuir					
a_L [L mg^{-1}]	1.4 ± 0.65	0.75 ± 0.47	0.72 ± 0.56	1.5 ± 1.3	15.5 ± 5.5
Q_0 [mg g^{-1}]	100.4 ± 1.2	94.6 ± 2.2	131.8 ± 5.9	101.2 ± 2.4	118.6 ± 0.32
R^2	0.9994	0.9966	0.9899	0.9972	1.0000
Freundlich					
Kf	50.2 ± 2.9	49.2 ± 0.84	72.6 ± 1.5	60.6 ± 2.7	104.2 ± 1.8
n	5.7 ± 0.66	5.8 ± 0.20	6.0 ± 0.32	6.6 ± 0.83	14.1 ± 1.8
R^2	0.9372	0.9924	0.9864	0.9401	0.9503
D-R					
q_m x10^{-4} [mol g^{-1}]	19.6 ± 1.2	13.6 ± 0.19	18.2 ± 0.73	20.3 ± 1.3	12.7 ± 0.52
K’ x10^{-9} [mol^2 J^{-2}]	1.9 ± 8.4 x10^{-2}	1.3 ± 1.9 x10^{-2}	1.2 ± 5.8 x10^{-2}	1.8 ± 8.7 x10^{-2}	0.48 ± 4.6x10^{-2}
E [kJ mol^{-1}]	16.3 ± 0.36	19.8 ± 0.15	20.1 ± 0.47	16.5 ± 0.39	32.2 ± 1.5
R^2	0.9940	0.9987	0.9952	0.9933	0.9733

Table 3.4 A800 adsorption isotherm parameters.

Isotherm parameters	P			OC			2F			3A			4M		
Langmuir															
a$_L$ [L mg^{-1}]	8.2 x10^{-2}	±	7.3 x10^{-3}	7.6x10^{-2}	±	6.2 x10^{-3}	1.9 x10^{-3}	±	2.8 x10^{-4}	0.1	±	1.4 x10^{-3}	3.4	±	0.60
Q$_0$ [mg g^{-1}]	40.3	±	7.1	31.4	±	0.64	206.2	±	37.7	241.6	±	15.2	146.0	±	6.3
R^2	0.9919			0.9975			0.9113			0.9919			0.9962		
Freundlich															
Kf	7.8	±	0.34	8.0	±	0.54	0.5	±	0.02	22.2	±	1.3	108.0	±	5.6
n	2.8	±	9.1 x10^{-2}	3.6	±	0.24	1.1	±	1.4 x10^{-2}	1.1	±	5.7 x10^{-2}	3.8	±	1.3
R^2	0.9966			0.9754			0.9996			0.9919			0.8339		
D-R															
q$_m$ x10^{-4} [mol g^{-1}]	12.3	±	0.81	5.5	±	0.18	51.1	±	3.4	642.5	±	215.9	235.6	±	318.6
K’ x10^{-9} [mol^2 J^{-2}]	3.6	±	0.16	2.6	±	8.5 x10^{-2}	9.4	±	0.19	7.0	±	0.48	4.1	±	1.3
E [kJ mol^{-1}]	11.8	±	0.26	14.0	±	0.23	7.3	±	7.3x10^{-2}	8.5	±	0.29	11.1	±	1.8
R^2	0.9942			0.9956			0.9988			0.9861			0.8345		

Similarly, S800 also correlates most favourably to the Langmuir model and as discussed in Section 3.2.1 as adsorption coverage is only ≈ 50% of the available surface area it is expected that adsorption will not go beyond the monolayer. In addition, since the surface of S800 is not entirely uniform, a result of residual oxygen functionality leading to heterogeneous energy across the surface, the Freundlich model also shows good fitting (R^2 0.9372 – 0.9924). The adsorption energies calculated from the D-R equation are slightly higher than those seen for dye adsorption, especially the energy for 4M uptake, 32 kJ mol^{-1}. For adsorption, the adsorption energy is the energy required to transfer 1 mol of adsorbate to the surface of the adsorbent and therefore high energy could be due to fewer possible groups available on the phenolic (compared to dyes) that can interact with the adsorbent surface (see Chapter 2, Figure 2.11) and thus it requires more energy to transfer the adsorbate from solution to the surface of the adsorbent.(*158, 159*)

The monolayer adsorption capacity for S800, Q_0, calculated from the Langmuir constants showed little change across the range of phenols. However, the values of Q_0 for A800 exhibit considerable variation, covering a range of 31.4 – 241.6 mg g^{-1} for the different phenolics. This result would suggest that adsorption by S800 is relatively unaffected by the nature of the phenolic molecule whereas it is influential for adsorption by A800. Large variation can be seen for A800 across all of the isotherm parameters (Table 3.4), whereas the S800 constants remain relatively similar regardless of the characteristics of the adsorbate molecule (Table 3.3). Figure 3.5 gives a clear visual representation of this observation. Interestingly, what this result could indicate is a difference in the modes of adsorption occurring for S800 and A800 which is likely to arise from the differences in the material characteristics, such as, the higher degree of surface aromatisation seen in A800 compared to S800 affecting the interaction with the adsorbate.

For A800 the calculated adsorption capacity increases in the order of: OC < P << 4M < 2F < 3A, it is interesting to observe that this data trend demonstrates a close correlation to the order of electron-density on the phenol ring which changes depending on the ring substituent: P > OC > 4M > 2F > 3A (Table

3.5). By the addition of electron withdrawing groups there is less electron density on the phenol ring which results in better uptake by A800, which may be indicative of adsorption through π-π interactions.(*129, 160*) From the surface area calculations for A800 (Figure 3.3) it is clear that multilayer adsorption, possibly through stacking of the phenolic molecules, is likely occurring for some of the adsorbates. The superior correlation of the A800 adsorption data with the Freundlich isotherm also serves to support this hypothesis.

Table 3.5 Charge distribution of phenolic compounds.

	Electron-density[a]	
	Aromatic ring	Phenol oxygen
Phenol	-0.51	-0.23
o-Cresol	-0.48	-0.23
2-Fluorophenol	-0.36	-0.22
3-Aminophenol	-0.09	-0.23
4-Methoxyphenol	-0.40	-0.23

[a] Calculated using HyperChem.

3.2.4 Stacking of phenolic molecules

When adsorption occurs via π-π interactions between the adsorbent surface and the phenol ring it is possible for further adsorption to take place beyond the surface of the adsorbent through self-stacking between aromatic structures to form adsorbate multilayers.(*155*) π-stacking of molecules is favourable as it maximises van der Waals interactions between the surfaces of the aromatic rings, however, this is not the overall force that controls stacking associations.(*153*) Two factors are responsible for driving or limiting π-stacking, both acting by affecting the electrostatic interactions of the molecules:(*147, 152, 153*)

1. Orientation of adsorbate molecules
2. The functional groups present on the aromatic ring.

Hunter and Sanders carried out experimental and computational work examining the stacking geometry of molecules containing π–systems.(*152*) From the computational calculations they proposed three likely orientations of the aromatic species (Figure 3.6). Experimental investigations showed that

(b) face-to-face stacking of molecules was unlikely to occur due to repulsion of the negatively charged π-electron clouds. To summarise the work they prepared a set of rules to explain how interactions of nonpolarised π-systems are governed:

Rule 1: π-σ attraction dominates in edge-to-face geometry (Figure 3.6 (a))

Rule 2: π-π repulsion dominates in face-to-face stacked geometry (Figure 3.6 (b)).

Rule 3: π-σ attraction dominates in an offset π-stacked geometry (Figure 3.6 (c)).

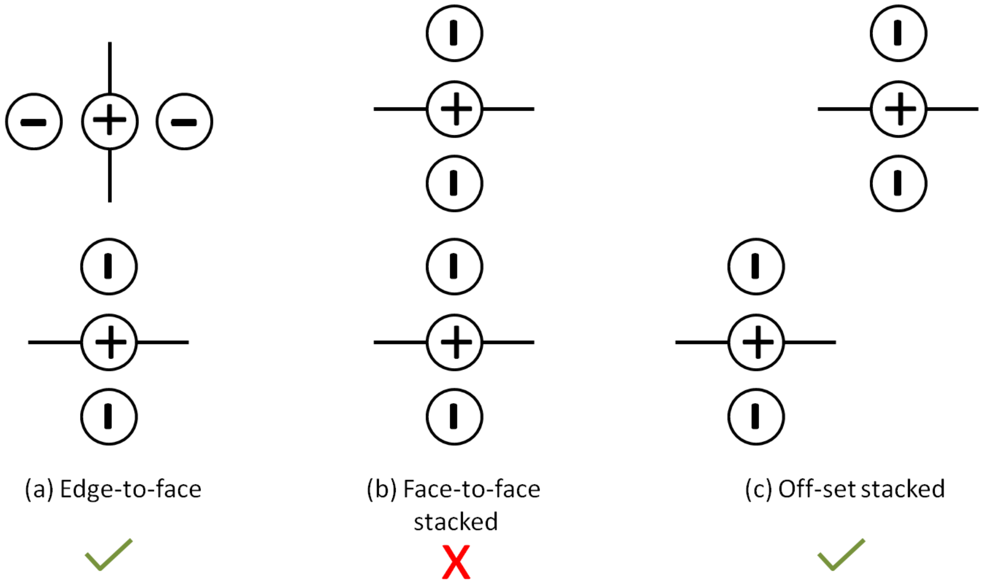

Figure 3.6 Possible arrangements of phenolics (a) edge-to-face, (b) stacked and (c) off-set stacked, with ticks denoting favourable attraction and crosses for repulsion of the molecules.

The addition of polarising substituent groups onto the aromatic π-systems has a major influence on the electrostatic interactions of the molecules and therefore affects the π-stacking geometries formed. An electron donating group (EDG) will increase the electron density in the π-system increasing electron repulsion which dominates any stacking geometry, inversely the presence of an electron withdrawing group (EWG) will remove electron density from the aromatic ring stabilising π-π interactions taking place between molecules, this effect is represented in Figure 3.7.(*153, 161*) For the adsorption of phenols by A800 it seems probable that stacking is arising via the off-set stacking geometry, with the degree of offset decreasing and the favourability of stacking increasing with the addition of stronger EWG's onto the ring, reflected by the trend in adsorption capacity.(*152*)

It is useful to note that the ability for π-π interaction is impeded by the presence of any additional, non-aromatic functional groups present on the adsorbent surface.(*147*) Therefore the increased hydroxyl and carbonyl surface functional groups present on S800 (Chapter 2, Table 2.5) will prevent this from occurring offering further explanation for the lower adsorption capacities of phenolics with strongly EWG's.

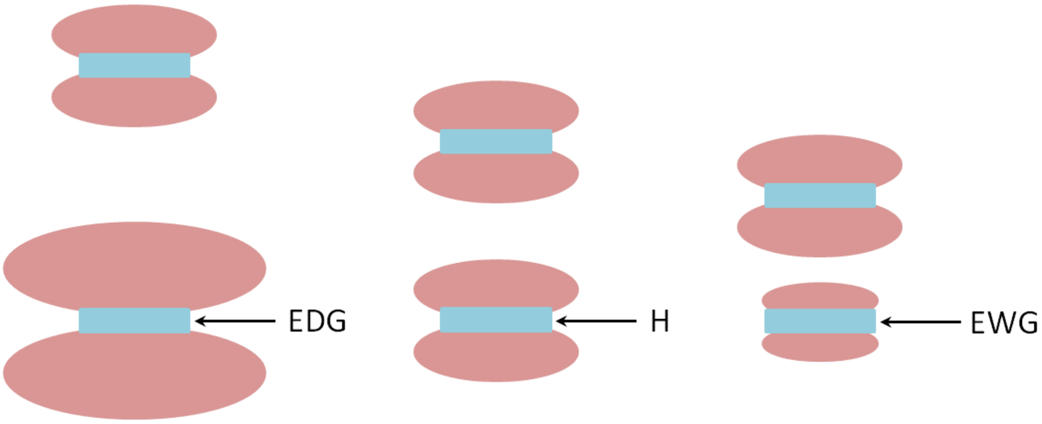

Figure 3.7 Schematic representation of the effect the substituent has on the attraction or repulsion of molecules in stacking, blue areas indicates the σ-framework, red areas are the π-electron clouds, EDG = electron donating group and EWG = electron withdrawing group.(*153*)

3.2.5 Effect of time on phenolic adsorption

Adsorption of phenolics over time was also investigated to determine how each of the different materials behaved (Figure 3.8). An initial phenolic concentration of 100 mg L^{-1} was used and samples were taken at regular time intervals for analysis of uptake.

What was clear from the results is that generally adsorption is taking place in two stages; initially fast adsorption takes place where the bulk of the phenolic is adsorbed, this is then followed by continued slow adsorption until equilibrium is reached (this occurs within 24 hours).(*143*) From closer examination of the data it would appear that S800 reaches equilibrium faster than the other two materials and in some cases, such as adsorption of (d) 3A and (e) 4M, only a one step adsorption process is occurring with no further uptake after the rapid, initial uptake.

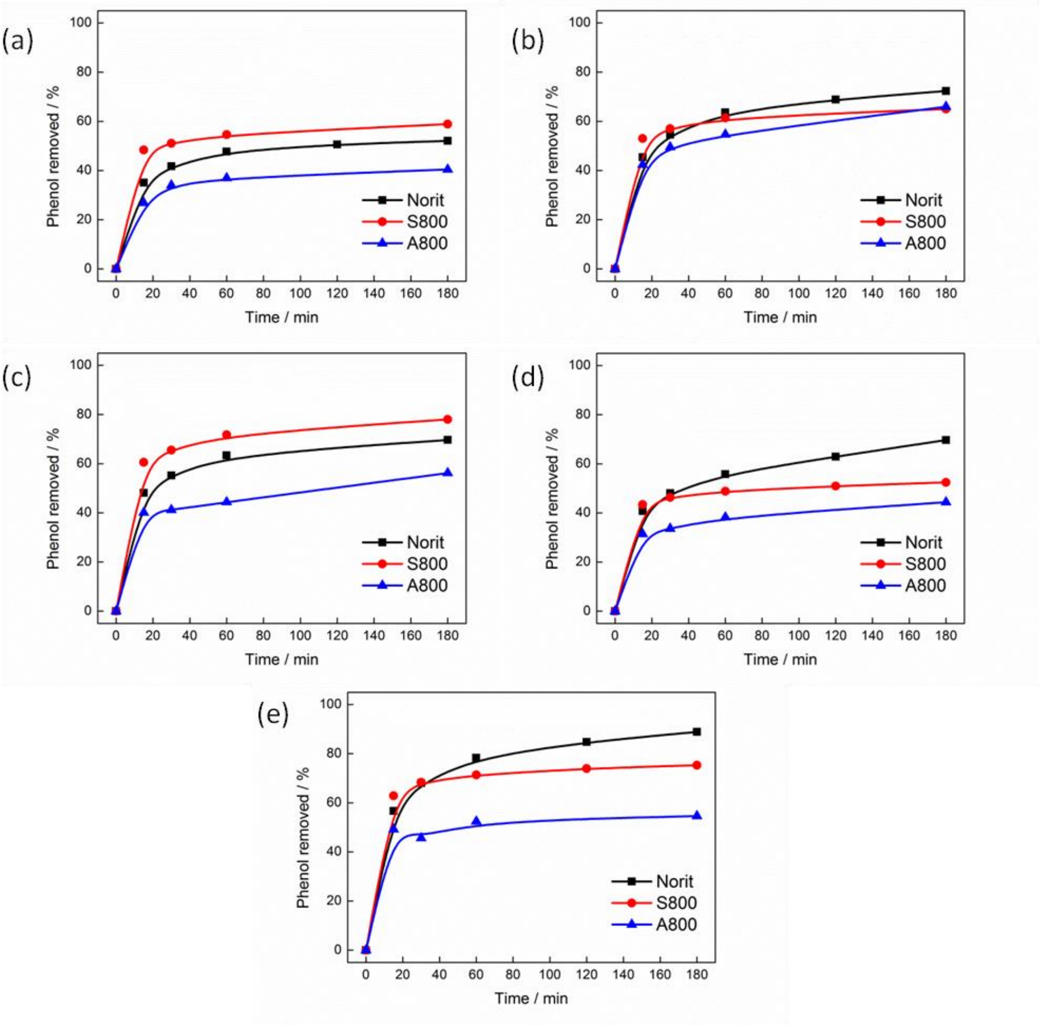

Figure 3.8 Rate of uptake of (a) phenol, (b) o-cresol, (c) 2-fluorophenol, (d) 3-aminophenol and (e) 4-methoxyphenol on Norit (black), S800 (red) and A800 (blue).

Norit and A800 however take considerably more time to reach equilibrium, in some cases hours longer, e.g. Figure 3.8 (b) and (d). For Norit this long second adsorption step is a likely result of the narrow pore diameters which limits adsorbate diffusion into the pore network.(*117, 146*) Conversely, for A800 it is the large pore diameters that affect the rate of adsorption and in this case the resulting ability of multilayer stacking to take place slows the process of reaching equilibrium.

3.2.6 Kinetic modelling of rate of phenolic adsorption

To further understand the rate of phenol adsorption a suitable kinetic model is required to examine the data and attempt to determine the contribution of different mechanisms towards adsorption and also potential rate controlling steps, i.e. mass transfer or chemical reactions.

There are a wide variety of models available that have been applied to describe adsorption in a batch process however the majority are impractical due to their mathematical complexity.(*162*) The most frequently applied kinetic models for adsorption from the liquid phase are the pseudo-first and second-order equations and commonly for these models adsorption process validity is based on R^2 values and q_e values.(*163*) Plots of all of the data can be found in Appendix 2.

3.2.6.1 Pseudo-first-order model

For this model the linearised form of the Lagergren pseudo-first-order equation is used:

$$\mathbf{\log(q_e - q_t) = -\frac{k_1}{2.303}t + \log(q_e)}$$

Where q_e is the amount of phenol adsorbed (mg g^{-1}) at equilibrium, q_t is the amount of phenol adsorbed at time t (min), k_1 (min^{-1}) is the pseudo-first-order rate constant of adsorption. A straight line of $\log(q_e-q_t)$ vs. t suggests the applicability of this kinetic model.(*164*)

3.2.6.2 Pseudo-second-order model

The following equation was used to determine the appropriateness of the pseudo-second-order model for the adsorption process:

$$\frac{t}{q_t} = \frac{1}{k_2 q_e^2} + \frac{1}{q_e} t$$

Where k_2 (g mg^{-1} min^{-1}) represents the pseudo-second-order rate constant.(*165*)

3.2.6.3 Bangham's equation

Using Bangham's equation the kinetic data can also be further used to determine whether pore-diffusion is the only rate controlling step in the adsorption process:

$$loglog\left(\frac{C_0}{C_0 - q_t m}\right) = log\left(\frac{k_B m}{2.303V}\right) + \alpha \log(t)$$

If the data fits the model it indicates that adsorption is solely limited by pore diffusion.(*143*) Where α (<1) and k_B are constants, v is the volume of solution (l) and m is the mass of adsorbate (g/l).

Comparison of the R^2 values for the pseudo-first-order and pseudo-second-order equations shows that the pseudo-first-order model is not as good a fit for the data as the pseudo-second-order model (Table 3.6). Also the values of q_e in the pseudo-first-order are much lower that the experimental values. The pseudo-second-order model exhibits excellent R^2 coefficients, between 0.9972 and 1.0000 for all of the adsorbents. The qe values calculated are closer to those seen in the experimental data although they are still slightly lower indicating that the adsorption process occurring is more complicated that this model suggests. The k_2 kinetic constants achieved for this data have been found to be comparable to those found in the literature for similar systems.(*143, 164*)

Bangham's equation shows reasonable fitting to the data although it is not adequate to suggest that pore-diffusion is the only rate limiting step in the adsorption process (Table 3.7). This result corresponds to the idea discussed in Chapter 2 that adsorption is a multistep process involving not just adsorption of the required adsorbent but also desorption of solvent molecules (water) adsorbed onto the adsorbent surface and is therefore dependent on a range of aspects. However, the good fitting does suggest that pore diffusion is an important factor in the uptake of phenol by Starbon® and also the trends seen in the rate constants (k_B) match the experimental trends seen for S800 and A800 which adds more validity to the data.(*161*)

For the pseudo-second-order model S800 exhibits the largest rate constants (k_2) indicating that this is the fastest adsorber of the three tested. Rate constants for Norit and A800 are lower, thus adsorption is slower which correlates well with the observed experimental data (Figure 3.8). Norit and S800 exhibit similar trends in the order at which the phenolics are adsorbed; P has the highest rate, followed by 2F, OC and 4M and finally 3A has the lowest rate constant.

In previous, separate studies carried out by Zogorski *et al*. and Liu *et al*. both have observed that steric effects of the phenolic are an important limiting factor in uptake especially in microporous adsorbents, such as Norit, as the molecules have difficulty in moving within small pores.(*161, 166*) This compares well to the data presented here as the compounds with bulkier substituent groups, i.e. 4M and 3A, are the slowest adsorbed.

The rate constants for A800 do not match this trend, with the rate constants decreasing in the order of: P>3A>4M>OC>2F. It is unclear what is causing this to occur and requires added investigation. However, it is interesting to note that the constants and trends obtained for S800 and A800 are again – as seen with the adsorption isotherms – almost completely opposing. Therefore, this further emphasises the difference in the mode of adsorption taking place for each adsorbent.

Table 3.6 Pseudo-first and second-order kinetic parameters for the removal of phenolics by different adsorbents.

Pseudo-1st-order

		q_e [mg g^{-1}]	k_1 x10^{-3} [min^{-1}]	R^2
Norit	P	16.0 ± 1.2	7.6 ± 1.5	0.8934
	OC	38.7 ± 1.1	7.2 ± 0.87	0.9575
	2F	28.0 ± 1.2	7.5 ± 1.4	0.8748
	3A	61.0 ± 1.0	3.7 ± 0.37	0.9607
	4M	38.4 ± 1.1	5.6 ± 0.85	0.9350
S800	P	13.5 ± 1.1	1.0 ± 0.87	0.9793
	OC	15.8 ± 1.1	9.7 ± 0.93	0.9818
	2F	18.5 ± 1.1	9.7 ± 1.0	0.9775
	3A	15.2 ± 1.0	3.6 ± 0.41	0.9615
	4M	13.8 ± 1.1	5.2 ± 0.66	0.9529
A800	P	19.8 ± 1.1	2.5 ± 0.58	0.9008
	OC	40.9 ± 1.1	4.8 ± 0.59	0.9558
	2F	38.0 ± 1.0	3.8 ± 0.17	0.9940
	3A	29.3 ± 1.0	3.5 ± 0.46	0.9482
	4M	19.8 ± 1.1	1.8 ± 0.57	0.8096

Pseudo-2nd-order

		q_e [mg g^{-1}]	k_2 x10^{-4} [g mg^{-1} min^{-1}]	R^2
Norit	P	57.0 ± 0.14	13.8 ± 1.5	1.0000
	OC	84.8 ± 0.51	5.5 ± 0.80	0.9998
	2F	78.7 ± 0.34	8.1 ± 1.2	0.9999
	3A	105.6 ± 2.4	1.7 ± 0.34	0.9972
	4M	104.9 ± 0.69	4.4 ± 0.68	0.9998
S800	P	61.3 ± 0.07	29.5 ± 3.4	1.0000
	OC	68.1 ± 0.10	23.7 ± 3.1	1.0000
	2F	80.6 ± 0.81	19.7 ± 2.6	0.9997
	3A	61.3 ± 0.49	9.8 ± 2.2	0.9997
	4M	81.4 ± 0.28	13.8 ± 2.6	0.9999
A800	P	55.8 ± 0.35	11.1 ± 2.2	0.9998
	OC	85.5 ± 1.1	3.3 ± 0.71	0.9995
	2F	77.2 ± 1.8	3.2 ± 1.0	0.9983
	3A	61.4 ± 1.7	5.6 ± 2.3	0.9976
	4M	70.8 ± 0.93	4.1 ± 0.90	0.9995

Table 3.7 Bangham's kinetic constants for the removal of phenolics by different adsorbents.

		α	k_B	R^2
Norit	P	0.21 ± 0.027	0.018 ± $8.9x10^{-4}$	0.9366
	OC	0.30 ± 0.023	0.018 ± $7.7\ x10^{-4}$	0.9773
	2F	0.25 ± 0.022	0.020 ± $8.2\ x10^{-4}$	0.9683
	3A	0.32 ± 0.011	0.017 ± $3.3\ x10^{-4}$	0.9955
	4M	0.38 ± 0.016	0.019 ± $5.7\ x10^{-4}$	0.9928
S800	P	0.12 ± 0.005	0.023 ± $2.1\ x10^{-4}$	0.9945
	OC	0.13 ± 0.015	0.024 ± $6.3\ x10^{-4}$	0.9635
	2F	0.20 ± 0.012	0.025 ± $5.0\ x10^{-4}$	0.9897
	3A	0.11 ± 0.004	0.022 ± $1.8\ x10^{-4}$	0.9930
	4M	0.13 ± 0.014	0.028 ± $6.9\ x10^{-4}$	0.9598
A800	P	0.12 ± 0.012	0.018 ± $4.0\ x10^{-4}$	0.9819
	OC	0.27 ± 0.011	0.018 ± $3.5\ x10^{-4}$	0.9948
	2F	0.26 ± 0.014	0.016 ± $5.3\ x10^{-4}$	0.9910
	3A	0.20 ± 0.008	0.016 ± $2.7\ x10^{-4}$	0.9928
	4M	0.17 ± 0.021	0.021 ± $9.8\ x10^{-4}$	0.9526

3.2.7 Effect of temperature of the adsorption of phenol

The effect of temperature and initial phenol concentration on adsorption capacity was also investigated at concentrations ranging from 25 to 200 mg L^{-1} and temperatures of 298 to 318 K (Figure 3.9). For A800 there was a clear correlation between an increase in adsorption capacity and increase in temperature, indicating that the process in endothermic.(*167*)

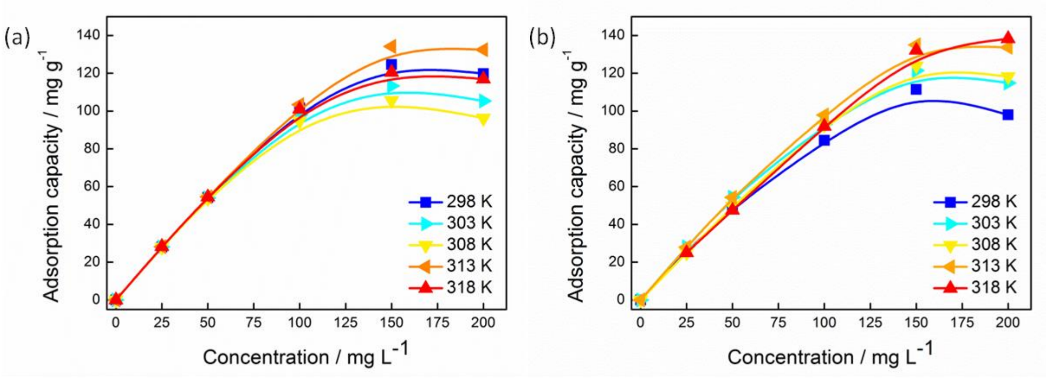

Figure 3.9 Effect of temperature on adsorption capacity of (a) S800 and (b) A800.

No such trend exists for S800, the adsorption capacity appears to decrease initially between the temperatures of 298 – 308 K followed by a marked increase at 313 K. Finally at 318 K the adsorption capacity decreases again below that at 298 K. Overall this could be considered a decrease in adsorption capacity with increase in temperature that would suggest that the process is exothermic.

There are a number of factors affecting adsorption at elevated temperatures that can affect both the adsorbate and adsorbent. These can include:

- Changes in the hydration spheres of adsorbate.(*168*)
- Possible increase in water adsorption with temperature.(*168*)
- Weakening of H-bonding (intra and intermolecular) of the adsorbate at higher temperatures making it more available for adsorption.(*167*)
- Distortion of adsorption sites on adsorbent and alterations to the chemistry of the adsorbent surface.(*168-170*)
- Potential for target molecules to escape the adsorbent surface at high temperatures.(*171*)

As these tests were carried out under the same conditions for both materials it seems fair to assume that the differing behaviour of the two materials is not due to any variation in the behaviour of the adsorbate. The controlling variable is most likely to be the differing surfaces of S800 and A800. The high hydroxyl content of the surface of S800 would be liable to accept water more readily at higher temperatures, thus disrupting H-π interactions with phenol.(*170*) The carbonyl groups that are most active in n-π interactions will also decrease in efficiency at higher temperatures thus leading to an overall decrease in capacity.(*168*) It is not clear why there is a sudden increase in adsorption capacity at 313 K. Such a sharp change in behaviour could suggest that an energy barrier has been overcome at this point and that the adsorption of phenol has become favourable over the adsorption of water, however further investigation would be needed to confirm this. What is more simple to explain is the decrease in capacity at 318 K which can be accounted for by the escape of phenol from the surface of the adsorbent due to H-π and n-π interactions not being sufficiently strong enough to trap the phenol.(*171, 172*)

For A800 water adsorption will also be increasing at higher temperatures as there is still some oxygen functionality present on the surface, however this appears not to inhibit adsorption – as there is an increase in uptake – demonstrating the H-π and n-π interactions are not the predominant adsorption mechanism occurring, but instead π-π interactions dominate. The increase in temperature results in a rise in the energy of the system facilitating adsorbent-adsorbate interactions and also the adsorbate-adsorbate π-stacking interactions leading to high adsorption capacities. The energy involved in these interactions is sufficiently great that within this temperature range phenol cannot escape from the surface.

3.2.8 Thermodynamic study of adsorption of phenolics

Thermodynamic parameters were also determined for the materials (Table 3.8, Table 3.9 and Table 3.10). For Norit and both Starbon® materials the ΔG values for all of the molecules studied were negative inferring that the adsorption is favourable and spontaneous in nature. ΔH and ΔS were calculated from the slope and intercept of the van't Hoff plots (graphs can be found in Appendix 2). The calculated values of ΔH are all below 40 kJ mol^{-1} indicative of physical adsorption which is in agreement with the values calculated from the D-R isotherm.

For S800 adsorption of OC and A800 adsorption of P, 3A, 4M, the values of enthalpy are positive indicating endothermic adsorption, thus uptake is increasing with increasing temperature. As discussed in Chapter 2 adsorption in a solid/liquid system such as the one presented here takes place in two steps:

1. desorption of the molecules of solvent (water) previously adsorbed by the adsorbent
2. adsorption of the adsorbate

Table 3.8 Thermodynamic parameters of phenolic adsorption by Norit.

Adsorbate	Temp. [K]	Ln K	ΔG [kJ mol^{-1}]	ΔH [kJ mol^{-1}]	ΔS [J mol^{-1} K^{-1}]	R^2
P	298	0.11	-0.27	4.3 ± 2.2	13.9 ± 7.1	0.5874
	303	-0.03	0.08			
	308	-0.04	0.11			
	313	0.08	-0.22			
	318	0.04	-0.11			
OC	298	1.2	-3.0	26.6 ± 3.8	97.2 ± 12.1	0.9608
	303	1.2	-2.9			
	308	1.3	-3.3			
	313	1.7	-4.3			
	318	1.7	-4.4			
2F	298	0.97	-2.4	17.3 ± 4.5	64.1 ± 14.6	0.8718
	303	0.87	-2.2			
	308	0.90	-2.3			
	313	1.2	-3.1			
	318	1.2	-3.1			
3A	298	1.6	-4.0	37.2 ± 0.2	138.2 ± 0.6	1.0000
	303	1.9	-4.7			
	308	1.7	-4.4			
	313	2.3	-6.1			
	318	3.1	-8.1			
4M	298	2.5	-6.2	35.4 ± 3.6	139.2 ± 11.9	0.9790
	303	2.7	-6.7			
	308	2.6	-6.6			
	313	3.5	-9.1			
	318	3.4	-8.9			

Endothermic adsorption suggests that the adsorbate and adsorbent are not strongly interacting on the surface and that the energy required to first displace the water molecules already adsorbed on the adsorbent is larger than the energy being produced by adsorbent/adsorbate interaction within this temperature range.(*143*) The value of entropy is also positive in these cases due to increased randomness at the solid/solution interface upon uptake of the phenolics. Due to disruption of the hydration layers around adsorbent and adsorbate leading to an increase in the degrees of freedom of water.(*173, 174*)

Table 3.9 Thermodynamic parameters of phenolic adsorption by S800.

Adsorbate	Temp. [K]	Ln K	ΔG [kJ mol^{-1}]	ΔH [kJ mol $^{-1}$]	ΔS [J mol^{-1} K^{-1}]	R^2
P	298	0.30	-0.74	-4.3 ± 0.70	-11.1 ± 2.2	0.9470
	303	0.35	-0.89			
	308	0.29	-0.75			
	313	0.27	-0.71			
	318	0.17	-0.46			
OC	298	0.65	-1.6	4.2 ± 0.31	19.5 ± 1.0	0.9838
	303	0.66	-1.7			
	308	0.56	-1.4			
	313	0.54	-1.4			
	318	0.74	-2.0			
2F	298	0.77	-1.9	-5.6 ± 1.4	-10.2 ± 4.3	0.8893
	303	0.94	-2.4			
	308	0.96	-2.4			
	313	0.92	-2.4			
	318	0.93	-2.5			
3A	298	0.22	-0.55	-10.4 ± 2.6	-24.4 ± 8.2	0.8855
	303	0.25	-0.63			
	308	0.17	-0.43			
	313	0.10	-0.26			
	318	0.19	-0.51			
4M	298	1.1	-2.7	-11.6 ± 0.64	-36.3 ± 2.1	0.9940
	303	1.2	-3.0			
	308	0.92	-2.4			
	313	1.1	-2.8			
	318	0.97	-2.6			

The adsorption of P, 2F, 3A and 4M onto S800 and OC and 2F onto A800 all exhibit negative enthalpy which corresponds to exothermic adsorption where uptake will decrease with increasing temperature.(*175*) The values of entropy are negative which shows a decrease in the degrees of freedom of the adsorbed species.(*176, 177*) The values of ΔH and ΔS indicate that adsorption could be reversible.(*177*)

Table 3.10 Thermodynamic parameters of phenolic adsorption by A800.

Adsorbate	Temp. [K]	Ln K	ΔG [kJ mol^{-1}]	ΔH [kJ mol $^{-1}$]	ΔS [J mol^{-1} K^{-1}]	R^2
P	298	0.06	-0.15	3.4 ± 0.36	11.2 ± 1.1	0.9782
	303	0.11	-0.29			
	308	0.03	-0.07			
	313	0.07	-0.18			
	318	0.06	-0.15			
OC	298	1.5	-3.6	-19.0 ± 3.2	-51.8 ± 9.9	0.9458
	303	0.17	-0.44			
	308	0.72	-1.9			
	313	0.64	-1.7			
	318	0.45	-1.2			
2F	298	0.88	-2.2	-12.5 ± 0.01	-34.7 ± 0.01	1.0000
	303	0.58	-1.5			
	308	0.85	-2.2			
	313	0.46	-1.2			
	318	0.47	-1.2			
3A	298	0.21	-0.52	34.0 ± 0.14	118.9 ± 0.45	0.9996
	303	0.11	-0.28			
	308	0.29	-0.76			
	313	0.48	-1.3			
	318	0.30	-0.82			
4M	298	0.57	-1.4	29.1 ± 0.40	97.0 ± 1.3	0.9999
	303	0.61	-1.5			
	308	1.0	-2.3			
	313	1.2	-3.2			
	318	0.94	-2.5			

A comparison of this data to that obtained for dye adsorption (Chapter 2, Table 2.14 and Table 2.15) shows that all of the parameters for phenolic adsorption are much smaller, this is not surprising as the decrease in size of the phenolic molecules compared with MB and AB it is expected that less water will be released from the adsorbent surface and less disruption of hydration spheres, thus resulting in lower ΔS. Also the occurrence of some exothermic ΔH values for phenolic adsorption could suggest that adsorption is more favourable than for larger organic molecules.

Finally, it is interesting to note that the values of ΔH and ΔS are almost entirely opposite when comparing S800 and A800 (whilst the values of ΔG are almost the same), as with the isotherm parameters these differences show that although adsorption capacity for the two materials is similar (and spontaneous) the mode of adsorption occurring is different.

3.3 Conclusion

The materials S800 and A800 have been shown to be suitable adsorbents for the removal of a range of phenolic compounds from aqueous waste. Adsorption capacity ranged from 87 – 139 mg L^{-1}, which was favourably comparable to other biobased adsorbents. The high mesoporosity and large pore diameter of A800 allowed for highly efficient uptake with >85% surface area coverage. If the surface area of A800 could be increased to that of Norit whilst maintaining the current mesoporosity this material would prove a highly efficient adsorbent. The adsorption data was successfully modelled using the Langmuir, Freundlich and D-R isotherms. The Langmuir model gave the best fitting for S800 whereas the Freundlich isotherm better described the A800 data. This indicated that multilayer adsorption was occurring for A800, most likely through π-π stacking of the adsorbate molecules.

S800 exhibited the fastest rate of uptake compared to A800 and Norit which were considerably slower to reach equilibrium adsorption capacity. The best kinetic model to represent adsorption by these materials was the pseudo-second-order based on the best R^2 and q_e values. Thermodynamic analysis of the adsorption data for S800 and A800 at different temperatures resulted in negative ΔG for all of the adsorbents indicating spontaneous, favourable adsorption. The values of ΔH and ΔS are lower for the adsorption of phenolics than those calculated for dye adsorption (Chapter 2) due to the effect of less water released from the adsorbent surface during phenol uptake.

Throughout analysis of all of the data for S800 and A800 it appears consistently opposite. This is most obvious in the case of the thermodynamic parameters where when S800 exhibits endothermic adsorption A800 is exothermic and vice versa. The major conclusion that can be drawn from this is that two different modes of adsorption are taking place for the two materials. Phenolic adsorption by S800 is most likely via H-π and n-π interactions between adsorbent and adsorbate, whilst for A800 π-π interactions dominate. Therefore the materials respond differently to variables such as temperature and phenolic character.

The key information gained about Starbon® from this chapter is that the different characteristics of the two materials strongly influences the way they adsorb. It could be concluded that for water treatment applications that S800 is the superior material for a number of reasons; firstly adsorption capacity is relatively unaffected by the characteristics of the phenolic and secondly the adsorption rate is faster than A800.

Chapter 4

Elemental sustainability and prospects for elemental recovery

Aspects of the work presented in this chapter have appeared in:

J. R. Dodson, A. J. Hunt, H. L. Parker, Y. Yang & J. H. Clark, Elemental sustainability: towards the total recovery of scarce metals, *Chemical Engineering and Processing: Process Intensification*, 2012, 51, 69-78

Interview for New Scientist "Urban mining – extracting metals from urban environments", November 2012

Book chapter titled "Mining municipal waste: prospective for elemental recovery" authored by J. Dodson and H. L. Parker for book called "Elemental Recovery and Sustainability", edited by A. J. Hunt, RSC Publishing, London, 2013

Some of the work included in this chapter was carried out in collaboration with Dr. J Dodson, Institute of Chemistry, Federal University of Rio de Janeiro, Cidade Universitaria, Rio de Janeire, 21941-909, Brasil.

Chapter 4.

Elemental sustainability and prospects for elemental recovery

4.1 The issue of elemental sustainability

Climate change and peak oil crises have been making headlines with increasing intensity over the past decade and consequently solutions are being sought to lessen our dependence on oil. With new legislation and key buzz phrases like “low carbon technology” and “a low carbon future” driving technological change, can we be assured that everyone in the world will be able to enjoy a sustainable, high standard of living in the future?

Unfortunately, there is a serious problem. As new technologies are developed to tackle one challenge we are creating another through resource deficit. Many of the new low carbon technologies that are being touted as our saviours; wind turbines, electric cars, energy saving light bulbs, fuel cells and catalytic converters, require rare and precious metals for their production.(*178*) But traditional supplies of these elements are running out. Reserves of indium for example, vital for LCD screens, solar cells and semiconductors, may be used up in 13 years.(*179*)

Unlike oil there are no bio-derived alternatives for palladium or platinum. These are unique and finite elements and we are quickly dispersing them throughout our environment, making their recovery costly and difficult. Additionally, it is not just the elements we consider exotic that are getting more difficult to access, many more elements that play a crucial role in our lives including phosphorous, aluminium and copper, are being depleted at a remarkable rate (Figure 4.1).

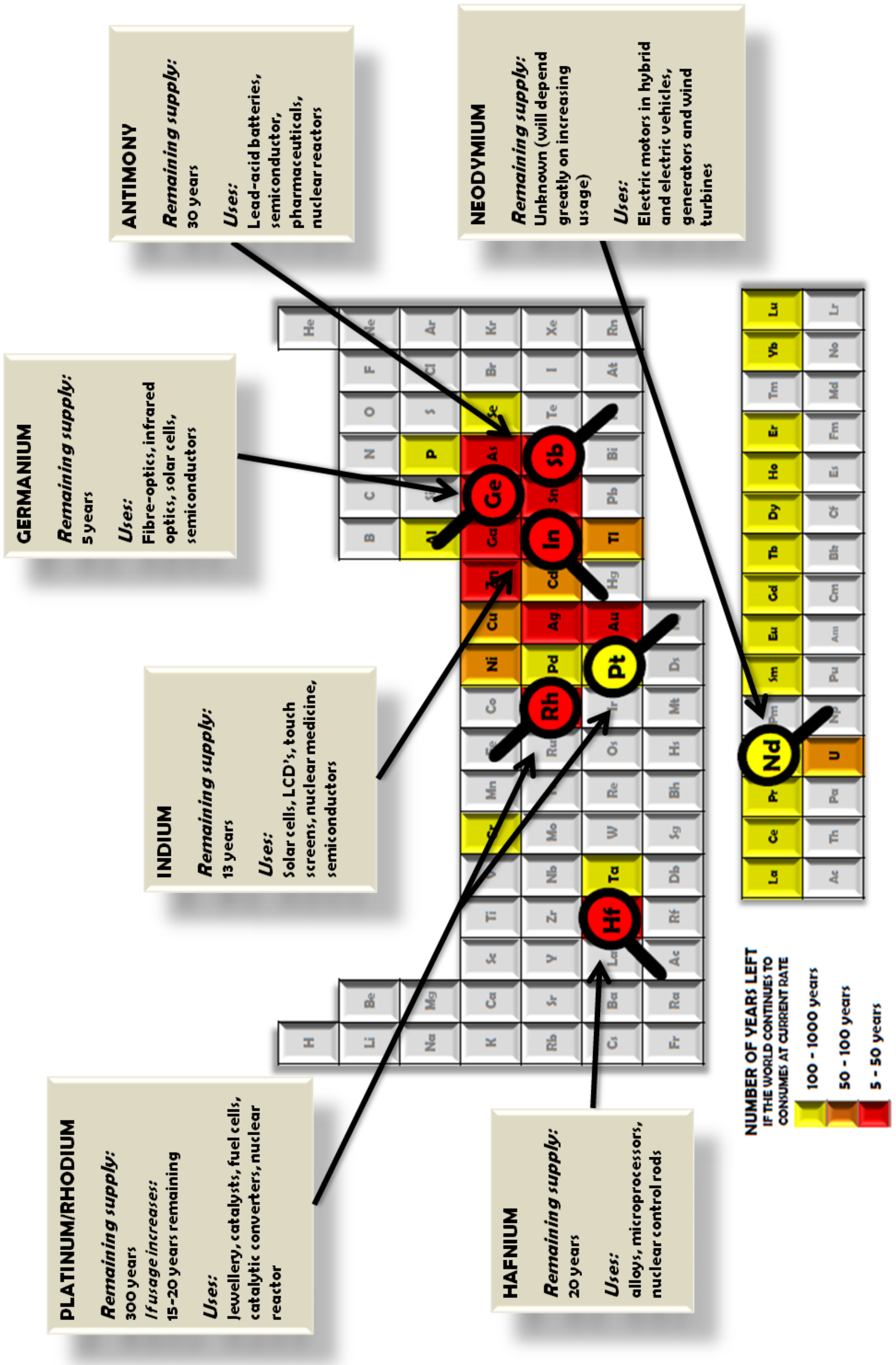

GERMANIUM
Remaining supply:
5 years
Uses:
Fibre-optics, infrared optics, solar cells, semiconductors

ANTIMONY
Remaining supply:
30 years
Uses:
Lead-acid batteries, semiconductor, pharmaceuticals, nuclear reactors

INDIUM
Remaining supply:
13 years
Uses:
Solar cells, LCD's, touch screens, nuclear medicine, semiconductors

NEODYMIUM
Remaining supply:
Unknown (will depend greatly on increasing usage)
Uses:
Electric motors in hybrid and electric vehicles, generators and wind turbines

PLATINUM/RHODIUM
Remaining supply:
300 years
If usage increases:
15-20 years remaining
Uses:
Jewellery, catalysts, fuel cells, catalytic converters, nuclear reactor

HAFNIUM
Remaining supply:
20 years
Uses:
alloys, microprocessors, nuclear control rods

NUMBER OF YEARS LEFT
IF THE WORLD CONTINUES TO CONSUMES AT CURRENT RATE
🟨 100 - 1000 years
🟧 50 - 100 years
🟥 5 - 50 years

Figure 4.1 Number of years remaining of rare and precious metal reserves if consumption and disposal continues at present rate.(*179*)

A key concern regarding the availability of these elements into the future is their abundance and ease of accessibility. Currently, the majority are mined and extracted from primary ore in highly energy intensive processes. Figure 4.2 shows the distribution of these elements across the globe. What is evident is that concentrations of these elements are localised in limited areas, for example, South Africa possesses 89% of the worlds platinum group metals (PGMs) reserve. As oil is to the Middle East so elements will become to their locations as demand continues to increase. China has already realised this potential and now has control of more than 95% of the world's supply of rare earth metals.(*180*) This raises issues about security of supply. Countries whose manufacturing or technology base depends on imported metals are beginning to look for alternative sources, whilst other countries and companies, including Toyota, dependent on rare earths are racing to secure control of mines in Australia, South Africa and Greenland.(*180*)

Current methods of mining also have a considerable impact on both the environment and our health. The discharge and dispersion of mining waste has led to elevated levels of metals in surrounding soil and water courses, resulting in destruction of vegetation and crops. This contamination can also enter the food chain due to initial uptake by edible plants.(*181*)

We have only to study the recent trends in the price of many metals to realise that demand is catching up with the supply. The price of indium rose a staggering 800% in 6 years from approximately $85/kg in 2002 to $685/kg in early 2008.(*182, 183*) As the recent economic crisis hit, manufacturing halted causing world commodity prices to plummet, indium alone dropped to $300/kg in 2009. However, this didn't remain for long. Indium is back up to $650/kg (2010) as consumer demand has once again risen with several governments introducing incentives for electronic goods or cars to kick-start their economies. This has resulted in predictions that the demand for some elements will soon outstrip supply.(*179*) The key question is what will happen to the prices next and how will demand for these metals that underpin our technologically advanced lifestyles be met sustainably in the future.

Location and proportion of world reserves by element[a,b]:

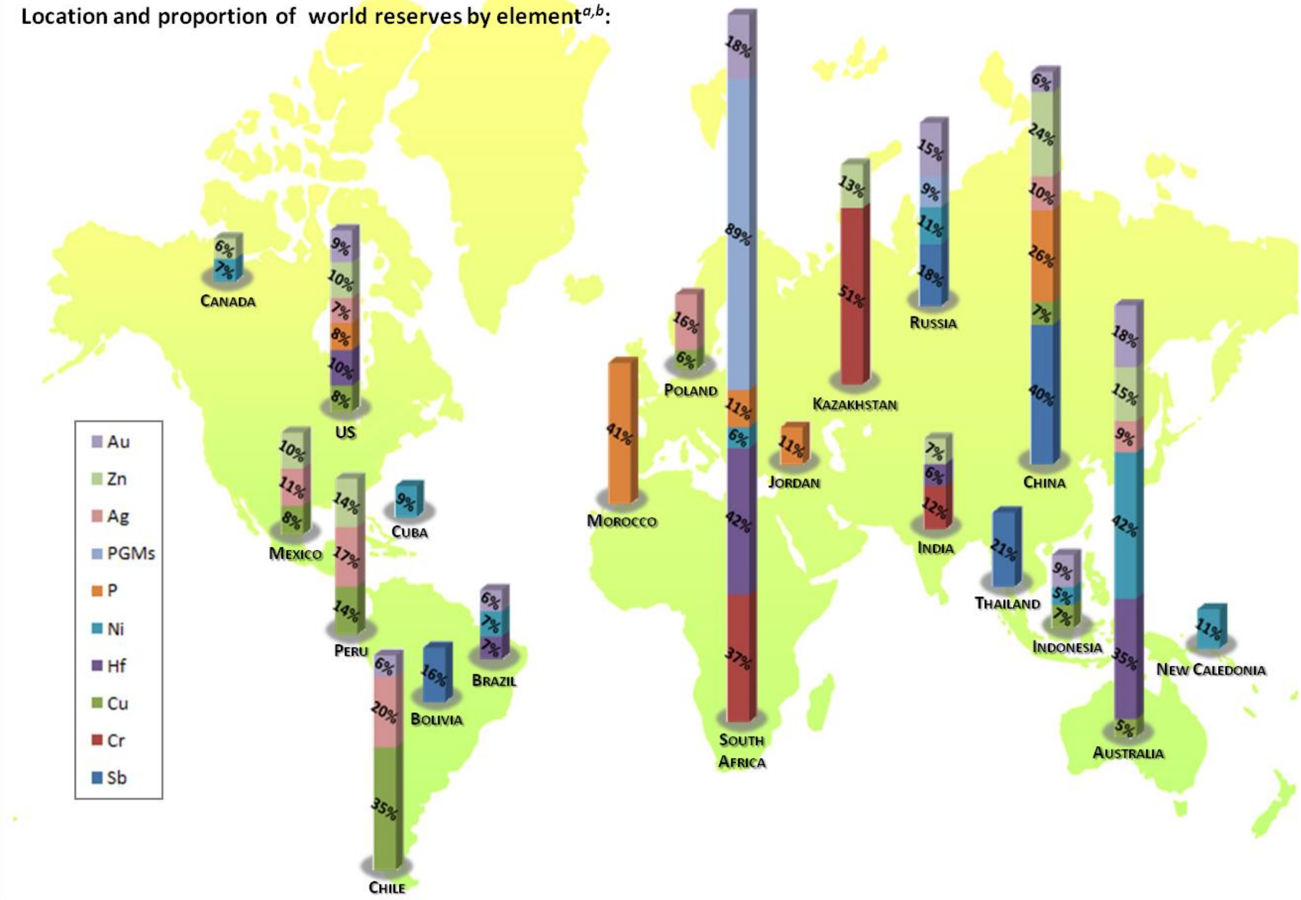

World total reserves by mass[a]:

Sb	2.1 (million tonnes)	Cr	350 (million tonnes)	Cu	540 (million tonnes)	Ni	71 (million tonnes)	P	16 (billion tonnes)
PGMs	71 (million kg)	Ag	400 (thousand tonnes)	Au	47 (thousand tonnes)	Hf	660 (thousand tonnes)	Zn	200 (million tonnes)

[a] Reserves: defined as known economically recoverable amount at time of survey, 2010. [b] Reserves below 5% not shown.

Figure 4.2 Distribution of rare and precious metal reserves around the world.(*184*)

Reuse, recover, recycle must be the answer. The recovery and recycling of metals from waste streams is a cost effective and environmentally beneficial route to valuable materials. Research has indicated that significant energy saving can be made through recycling of metals.(*185, 186*) Current aluminium recycling supports 49% of aluminium consumption in the US.(*187*) It saves 95% of the energy and generates only 5% of the CO_2 compared to the mining and electrolysis of alumina from bauxite ore.(*185*) Also, steel recycling saves 74% of the energy, 90% of virgin materials, reduces 86% of air pollution, 40% of water use, 76% of water pollution, 97% of mining waste and a considerable amount of consumer wastes generated, when compared with production from virgin materials.(*185*)

Table 4.1 Elements with the lowest remaining reserves, their main uses and their percentage supply supported by recycling.(*187*)

Element	Uses & Reliant Technologies	% consumption met by recycling
Hafnium	Alloying agent, nuclear control rods, computer chips	0%
Rhodium/ PGMs	Alloying agent, industrial catalyst, catalytic converters, fuel cells	0%
Silver	Catalyst, electronics, high-capacity batteries, antimicrobial in medicine	16%
Gold	Catalysts, electronics, coating space satellites, dental and medical implants, nanotechnology	43%
Gallium	Semiconductors, solar cells, MRI contrast agents	0%
Germanium	Semiconductors, solar cells, catalyst, optical equipment	35%
Indium	Alloys, photocells, LCD and touch screens	0%
Antimony	Semiconductors, alloys, batteries, pharmaceuticals, catalyst, flame retardants	0%

On the other hand, there is little or no recycling of elements that are important for current and emerging uses, e.g. platinum, indium, gallium and hafnium, Table 4.1. At the end of their life the products containing these elements; mobile phones, televisions and computers, are ending up in landfills or being incinerated and the elements are being lost. Japan has calculated that it has accumulated three times more gold, silver and indium in its waste, due to its high turnover of electronic goods, than the world uses in a year.(*188*) This emphasises the potential and necessity for a new approach to our waste. We must attempt to recover all elements and reuse them in close-looped systems either by recovering them through "urban mining" from landfill sites, incineration ashes or waste waters, or designing the direct recycling of elements through intelligently designed disassembly of materials at their end of life. These measures should limit the demand for new supplies of elements, increasing the lifetime of our reserves infinitely.

This chapter will go on to discuss methods for achieving elemental sustainability, discussing municipal solid waste as a viable source of metals, introducing current and developing techniques that could be used for their recovery and emphasising gaps in our knowledge. The main focus here will be on rare and precious metals.

4.2 Municipal solid waste

In comparison to the dispersed emissions of CO_2 from the combustion of fossil fuels, elements in solid waste have for many years, particularly in industrialised nations, been collected, separated and concentrated, making municipal solid waste (MSW) a prime target for the recovery and recycling of elements.

MSW is the waste that is collected from municipalities including households, small businesses and local governments and includes paper, plastic, organic waste, glass, textile and metals. Exact figures of the amount of MSW produced globally are difficult to obtain due to the use of different metrics and a lack of data collection in many countries or the presence of informal waste collection and recycling.(*189*) Data from the United Nations Environment Programme (UNEP) estimated 338 million tonnes of MSW were produced annually in 2001,(*189*) whilst 540 million tonnes were estimated by the Organisation of Economically Developed Countries (OECD).(*190*) Nevertheless although some areas of the world have reduced the levels produced, data indicates that globally MSW levels are on the rise as income levels increase.(*190*)

In the recent past, the majority of MSW generated in industrialised nations has ended in landfills as contained and controlled management systems. However, as a result of environmental concerns related to greenhouse gas emissions and leaching of toxic compounds, land use pressures and the economic costs of waste disposal, alternative waste disposal methods are being adopted. Levels of recycling and composting are on the rise, however, incineration or waste combustion has expanded quickly in many countries that can afford the infrastructure costs. This has occurred both for reasons of waste reduction and energy recovery, despite concerns about emissions (Figure 4.3).

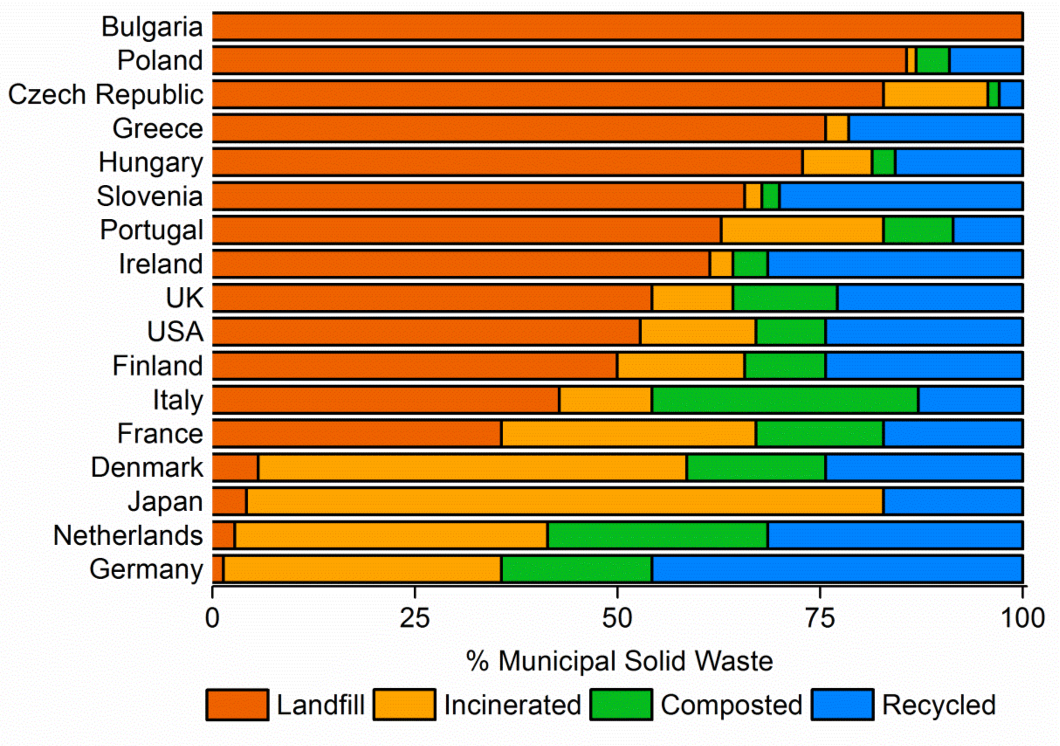

Figure 4.3 Contribution of different treatment methods to municipal solid waste disposal in different countries around the world.(*191, 192*)

Metals are a minor contribution in terms of the individual household MSW composition, with a typical Swiss rubbish bag containing 2.6 kg non-ferrous metal, 3.3 kg of iron and 1.2 kg of electronic and electrical waste a year, or 3.5% of the total waste.(*189*)

In terms of elemental sustainability, MSW is therefore a vital source for the capture of non-carbon elements. Current research areas include:

1. The source-separation and capture of elements through recycling programmes, “urban mining”.
2. The excavation of existing landfill sites, “landfill mining”.
3. Use of ashes from incineration plants.

4.3 Source-separation and recycling of metals from post-consumer waste

Developing closed-loop lifecycles via the source-separation and recycling of waste is vital for ensuring elemental sustainability. Frequently, when demand and costs increase for a particular element, alternative elements with similar properties can be used, however, this is not a solution to the challenge of elemental sustainability.

The recovery and recycling of metals from wastes is not new, however, many challenges remain to extend recycling systems to more elements and to improve current recycling rates. Particularly important is improving ‘functional recycling’ rates, such that the functionality of each metal remains, rather than it being incorporated into a larger bulk material as an impurity.(*193*)

4.3.1 Current recycling rates

Surprisingly, considering the importance of metals for technological advancements relatively little information is available on how efficiently non-renewable resources are recycled and how they flow from extraction to use to disposal. Recently the Global Metals Flows Group of UNEP’s International Resource Panel evaluated the global recycling rate information for sixty-nine metals, mainly based on order of magnitude expert assessments.(*193*)

For most ferrous metals the End of Life Recycling Rate (EOL-RR) was estimated to be over 50%, for non-ferrous metals the levels were mainly between 30 – 60%, for precious metals between 40 – 70% and for speciality metals the majority of recycling rates were below 1% (Table 4.2).(*193*) The influence that these levels of recycling have on the recycled content of new products mainly depends on the demand for the element in question. The lifetime of the product that the element is incorporated into can also restrict recycling as this causes a delay in the availability of elements from a product for recycling and reuse.

Table 4.2 Recycling rate of elements and recycled content of new products.(*193*)

Metal	Recycled Content of new products [%]	EOL-RR [%]
Ferrous elements		
Chromium	18-20	85-95
Manganese	37	53
Iron	30-50	70-90
Nickel	30-40	55-65
Niobium	22	50-55
Molybdenum	33	30
Vanadium	-	<1
Non-ferrous		
Magnesium	33	39
Aluminium	30-35	40-70
Titanium	52	91
Cobalt	32	68
Copper	20-37	42-53
Zinc	18-27	20-60
Tin	22	75
Lead	40-60	40-95
Precious metals		
Gold	30	15-96
Iridium	15-20	20-30
Palladium	50	60-70
Platinum	16-50	60-70
Rhodium	40	50-60
Ruthenium	50-60	5-15
Silver	20-30	30-95
Osmium	<1	<1
Speciality elements		
Antimony	<10-25	<5-85
Arsenic	<1	<1
Barium	-	-

Bismuth	-	<1
Boron	-	<1
Beryllium	10-25	<1-7
Cadmium	25-75	15
Gallium	25-50	<1
Germanium	35-50	<1-76
Indium	25-50	<1
Lithium	<1	<1
Mercury	25-50	1-60
Rhenium	10-25	>50
Scandium	-	<1
Selenium	1-10	<5
Strontium	-	<1
Tantalum	10-25	<1-35
Tellurium	-	<1
Thallium	0	0
Tungsten	46	10-65
Yttrium	0	0
Zirconium	1-10	<1
Rare-earth elements		
Lanthanum	1-10	<1
Cerium	1-10	<1
Praseodymium	1-10	<1
Neodymium	1-10	<1
Samarium	<1	<1
Europium	<1	<1
Gadolinium	1-10	<1
Terbium	<1	<1
Dysprosium	1-10	<1
Holmium	<1	<1
Erbium	<1	<1
Thulium	<1	<1
Ytterbium	<1	<1
Lutetium	<1	<1
Hafnium	-	<1

4.3.2 Technology

Metallurgical processes have been developed for the extraction and separation of ores which have particular elemental combinations that are found naturally in the earth's crust.(*194*) However, these combinations are different to those that are found in consumer products. The growing number of element combinations and the miniaturisation of electronic components make the recycling of products increasingly complex. Particularly when precious elements are diffused throughout a product at extremely low concentrations, or when both valuable and hazardous substances are interconnected.(*195*) Vehicles are a good example for demonstrating the complexity and challenges involved in creating closed-loop recycling systems (Figure 4.4).

4.3.3 Contamination

When products are sent for recycling they are usually only partially dismantled to separate valuable distinct fractions of recyclables before shredding to break the materials down and liberate the different elements. These processes, as well as the initial alloys used, can result in contamination of the recyclates.

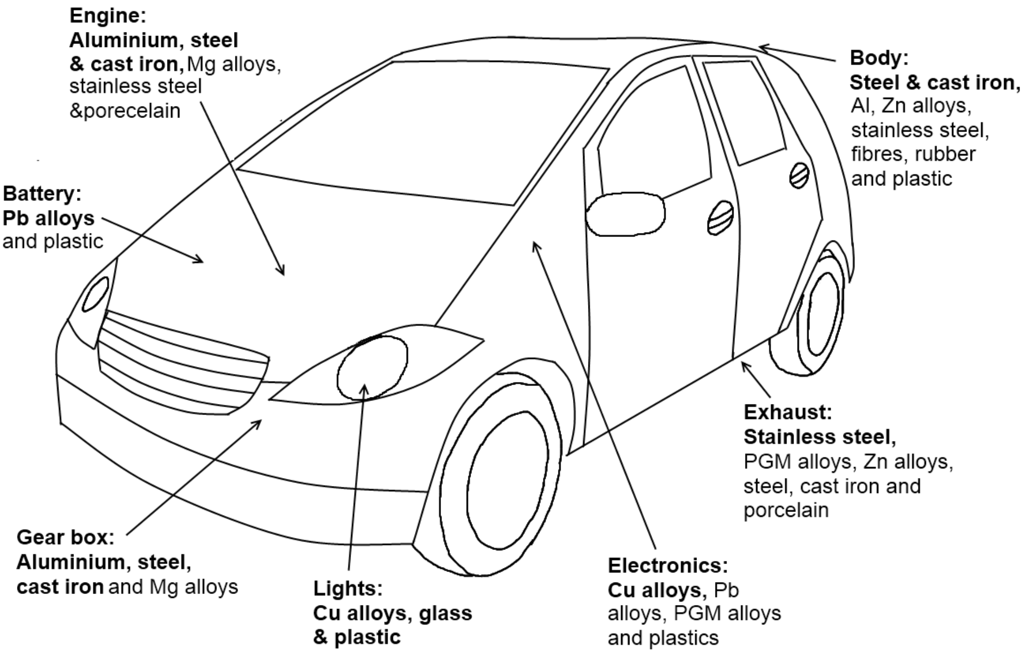

Figure 4.4 Location and combination of different elements in a typical passenger vehicle. (*194*)

This is particularly the case for EOL vehicles where shredded particles are physically separated into ferrous materials, aluminium, copper, zinc, stainless steel and Automotive Shredder Residue (ASR) mainly composed of non-metallic materials.(*196*) These separate streams will then enter metallurgical recycling processes, however, they will all be contaminated to some extent due to imperfect separation processes and shredding, particularly at joints connecting different materials.(*197*) The ultimate result of contamination is that contaminating elements will be lost from the functional elemental lifecycle, and that the quality of the contaminated elements will reduce after each lifecycle, downgrading its potential applications unless it is diluted with higher purity primary products (Figure 4.5).

In order to overcome this, new systems and methods are needed based on knowledge of the elements in products so that full disassembly of items occurs initially, when separation of the elements will not be possible during metallurgical processing.

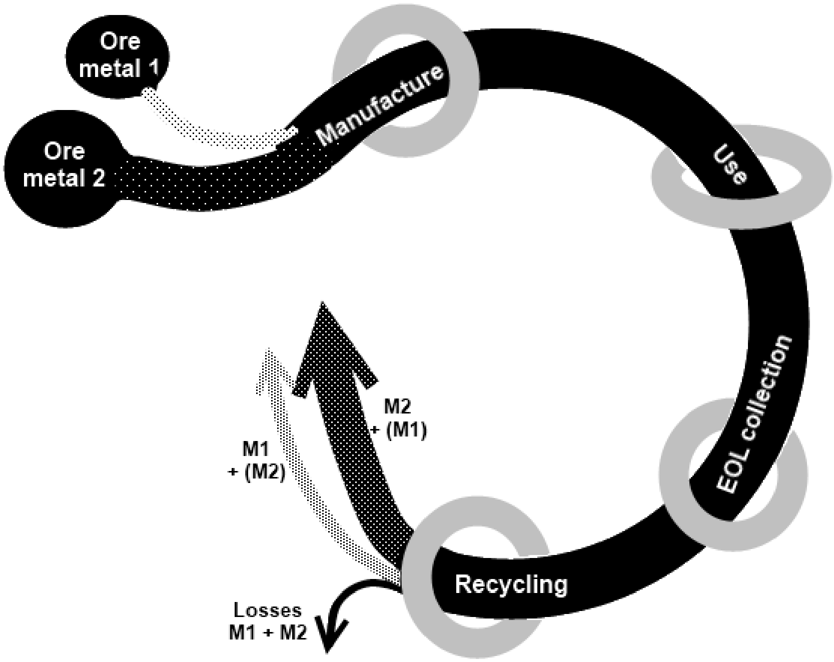

Figure 4.5 Contamination of metals by other elements during lifecycle.

For instance in a car with an engine made mainly of aluminium (Figure 4.4), every effort should be made to separate any iron such as bolts which will be difficult to remove from the molten metal. Meanwhile, Platinum Group Metals (PGMs) may be combined with copper scrap, in which they will dissolve easily and can be recovered by electrolytic refining.(*194*)

4.3.4 Precious and special metals

As hinted above particular challenges exist for the recycling and recovery of precious and special metals from post-consumer products. Although levels of recycling from many industrial applications, such as spent catalysts, can be greater than 90% levels, recovery from consumer products such as cars and electronics only reaches around 40 – 70% and down to less than 1% for some important elements such as indium used in LCD screens.(*193*)

The recovery of some of these elements are problematic due to their concentrations at ppm levels, such as PGMs in circuit boards or indium in LCD screens or distribution throughout an entire product, such as car electronics which are usually lost during shredding.(*195*) In contrast autocatalysts can be cut from the exhaust and fed directly into the appropriate recycling stream, although even with this easily separable component only about 50% of the PGMs contained within them are recovered.(*198*)

To overcome some of the challenges of low concentration distributive elements alternative approaches need to be taken such as designing products for disassembly. Changing consumer and industry attitudes towards products, for instance by leasing items so that they can be returned to the manufacturer at their end of life, could also help.

4.3.5 Design for disassembly

Design for disassembly is an approach that aims to design materials at their inception so that different parts of the product that cannot be easily recycled or reused together can be easily separated to aid the development of a closed-loop materials system. As discussed above particular problems are present when two materials that need to be recycled in different ways are bonded together or are difficult to separate, such as different types of plastics in a single toy or mixed cotton and synthetic polymer clothing.

An example of design for disassembly is the suggested redesign of the location of the wire harness in cars, the collection of wires that link the electronic devices and are rich in copper. Currently these are considered too labour intensive to remove and generally end up in the automotive shredder waste, however, some research has suggested that a different routing could make it accessible for extraction throughout the vehicle, whilst connecting it to the body of the car would make it easier to detach. This could enable a greater proportion of the copper from this component, around 10 kg per car, to be recovered.(*199*)

4.4 The excavation of existing landfill sites "landfill mining"

Considering the vast spectrum of MSW disposed of in municipal landfills it is clear that they could offer a potential source of a range of elements and as such the concept of landfill mining – excavating waste from landfills and subsequent extraction of resources – has been suggested as a means to exploit this supply.

The concept of landfill mining can be traced back as far as 1953 where it was used as a way to obtain fertilizers for orchards.(*200*) Since then interest has been sporadic reflected by the fluctuation in number of publications in the area over the last couple of decades (Figure 4.6), interest appears to peak in the mid-nineties but has since dropped off to only 1-2 studies per year.

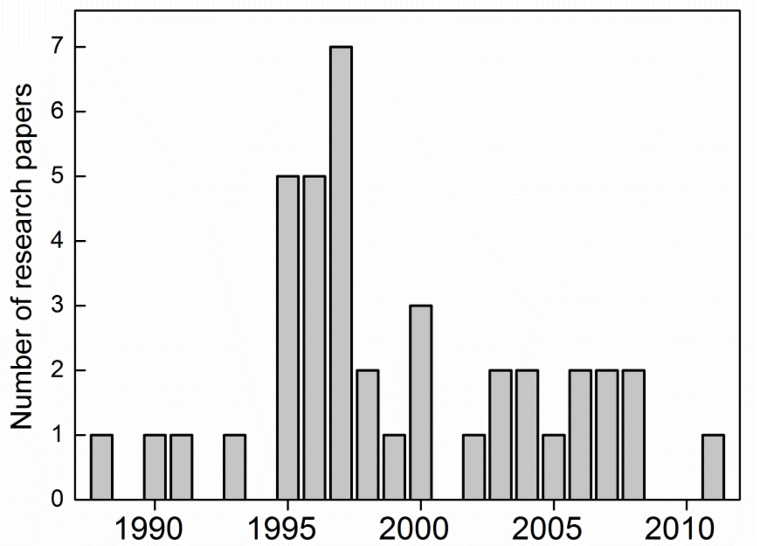

Figure 4.6 Number of research papers focusing on landfill mining from 1988 – 2011.(*201*)

There are a number of potential reasons for this lack of interest, such as, economic instability or less demand for landfill space due to alternative waste management technology being used. However, from studying the literature the most likely cause is a lack of feasibility of obtaining useable, recyclable products from landfill sites determined by past research.(*201*)

Theoretically, the recovery of resources by landfill mining would fit well in to a speculative idea of creating a circular economy. Unfortunately, in practice there is a significant lack of certainty to the whole area. One problem is that the specific contents of individual landfill sites are hard to ascertain, especially for those that have been used for a long period or were closed up some time ago. There is also insufficient information of what types of environmental or atmospheric pollution may be caused by opening up and disturbing sites. Finally, the development of suitable technologies to enable landfill mining and separation, recovery and reuse of the excavated contents is still very much in the early stages. Much more work is required to prove efficiency, capacity and suitability of different technologies for use in reality.(*201*)

Despite these difficulties with implementing landfill mining there is still a possible way to recover metals that does not require the necessity for excavation. A range of emissions are given off by current and sealed landfill sites, the most significant being a liquid leachate which contains a wide range of compounds including metals which could potentially be recovered.

4.4.1 Potential of metal recovery from landfill leachate

Landfill leachate is defined as the aqueous effluent generated as a consequence of rainwater percolation through wastes.(*202*) Leachate production increases for landfills that are open and those with less compacted waste as water can penetrate more easily. Landfill leachates contain a large number of compounds as a result of the biological and chemical breakdown of the refuse in the landfill.(*203*) The composition is greatly dependent on the type of waste, the location and the age of the landfill. Figure 4.7 illustrates the structure of a standard sanitary landfill, with leachate being collected at the bottom of the landfill using a collection system it then flows into the sump where it can be piped to the surface.

At present the research into the characterisation of landfill leachate is being carried out with a view to preventing environmental contamination by removal of harmful or toxic substances that it contains. However, the data collected by this work can be used to give an impression of the potential metal content of the leachate with a view to recovery in the future. Oman *et al.* has carried out a very thorough characterisation of landfill leachate samples from 12 Swedish landfill sites and have successfully identified 400 compounds, including 40 metals, in a range of concentrations contained within it (Table 4.3).

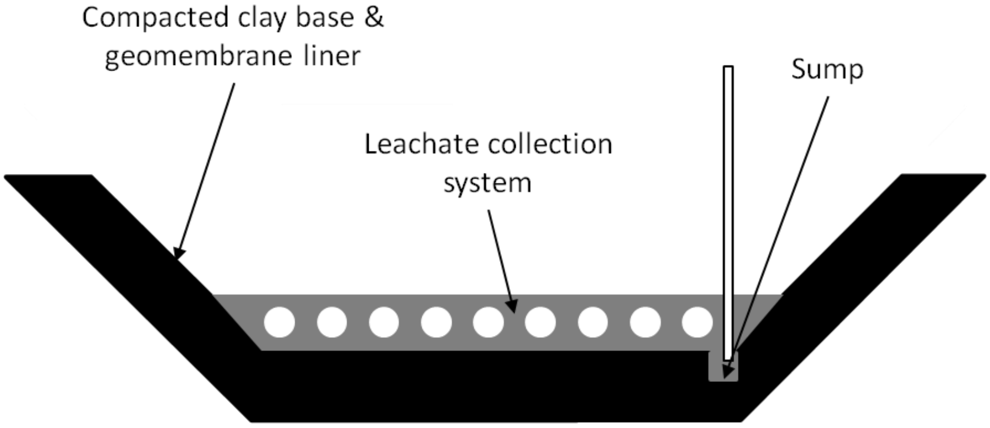

Figure 4.7 Structure of the base of a sanitary landfill showing leachate collection system.(*204*)

As this data demonstrates the concentrations of metals in leachate are not trivial, with significant concentrations across all classes of metals. Currently, research into leachate is focused on developing technologies that will treat leachate in order to lower toxicity through removal of a range of organic, inorganic and biological substances rather than to remove and concentrate the metals, considerable work is still required into developing suitable techniques and technologies for recovery of metals from this highly hazardous source. The wide range of metals present in the leachate does offer promise that in the future it could provide more economical and easier access to resources contained within landfills.

4.5 Use of ashes from incineration plants

The definition of incineration is the controlled burning of solid, liquid or gaseous waste. Due to the increases in MSW being produced incineration is becoming a large and integral part of modern municipal waste management, especially in countries with limited landfill space available.(*204*) The primary purpose and advantage of municipal solid waste incineration (MSWI) is the resulting reduction in the volume (up to 90%) and mass (up to 70%) of the waste.(*205, 206*) The recovery of heat energy produced by incineration to generate electricity offers a secondary advantage of this process.(*204, 205*)

Table 4.3 Metals found in landfill leachate and sediment samples.(*207*)

	Leachate [μg/l]			Leachate sediment [mg/kg]		
	Min		Max	Min		Max
Ferrous elements						
Chromium	1.4	-	1500	4.0	-	124
Manganese	30	-	1400000	954	-	3000
Iron	160	-	5500000	13500	-	285000
Nickel	10	-	13000	2.9	-	68
Niobium	0.04	-	0.9	14	-	0
Molybdenum	0.04	-	223	83	-	37
Vanadium	2.0	-	23	102	-	69
Non-ferrous						
Magnesium	13800	-	15000000	1680	-	6900
Aluminium	24	-	579	27400	-	7430
Cobalt	1.7	-	1500	0	-	26
Copper	5.0	-	10000	1.9	-	1890
Zinc	13	-	1000000	59	-	1890
Tin	0	-	3.5	95	-	32
Lead	1.0	-	5000	8.7	-	500
Precious metals						
Palladium	0.04	-	0.2	1.3	-	0.3
Platinum	0.04	-	0.02	0.05	-	0.002
Silver	0.04	-	0.3	1.6	-	0.7
Speciality elements						
Antimony	0.04	-	6.0	15	-	0
Arsenic	10	-	1000	0.9	-	258
Barium	2.0	-	1370	676	-	2950
Bismuth	0.02	-	0.1	0.7	-	0.2
Cadmium	0	-	400	0.1	-	11

Germanium	0.04 - 0.3	8.2 - 0.1
Indium	0.04 - 0.06	0.18 - 0.06
Lithium	0.4 - 622	111 - 11
Mercury	0.05 - 160	0 - 2.5
Scandium	0.3 - 1.0	24 - 14
Selenium	0.02 - 113	7.6 - 0.6
Strontium	0.2 - 1430	523 - 356
Tantalum	0.01 - 0.01	0.40 - 0.22
Tellurium	0.04 - 0.05	0.06 - 0.04
Thallium	0 - 0.28	0 - 0
Tungsten	0 - 2.9	0 - 0
Yttrium	1.0 - 6.6	146 - 50
Zirconium	1.0 - 10	291 - 160
Rare-earth elements		
Lanthanum	0.04 - 8.3	134 - 14
Cerium	1.4 - 1500	4.0 - 124
Neodymium	0.04 - 0.9	0 - 14
Samarium	0.2 - 1430	523 - 356
Terbium	0.04 - 0.05	0.06 - 0.04

Various incinerator designs are used however most are based on the mass-burn incinerator, as this is the most straightforward incineration technology available. This technology requires very little processing of the MSW received, generally only the removal of large bulky items (e.g. white goods), bulky combustible items (e.g. mattresses) and hazardous waste. The process consists of three main parts: incineration, energy recovery and air pollution control, a schematic diagram of a typical mass-burn incinerator is shown in Figure 4.8.

During MSWI a number of residues (or secondary wastes) are produced that can be categorised as:

- Flue gases (e.g. SO_2, NO_x, HCl, H_2O)
- Particulate matter carried by the gas stream, termed “fly ash”
- Incineration residue or “bottom ash”

Studies of waste input and subsequent output into these residues as a result of incineration show that any inorganic, metal-containing waste fed into the incinerator is contained within the bottom and fly ash fractions post incineration.(*208*) These residual ashes can be generated on large scales, for example, each year in Sweden waste incinerators produce about 700,000 tonnes of bottom ash and 200,000 tonnes of fly ash.(*209*) These ash fractions can contain a vast and varying mixture of potentially hazardous substances making their disposal complex as they present a threat if accidentally released into the environment. The most common method of disposal is landfilling with or without further treatment depending on the different requirements of the country where they are produced, although this is not an ideal solution. Importantly, apart from containing hazardous substances MSWI ashes can also contain significant amounts of valuable metals, such as: Cu, Zn, Ag and Au leading to interest in its prospective for exploitation and use as an "artificial ore".(*209, 210*)

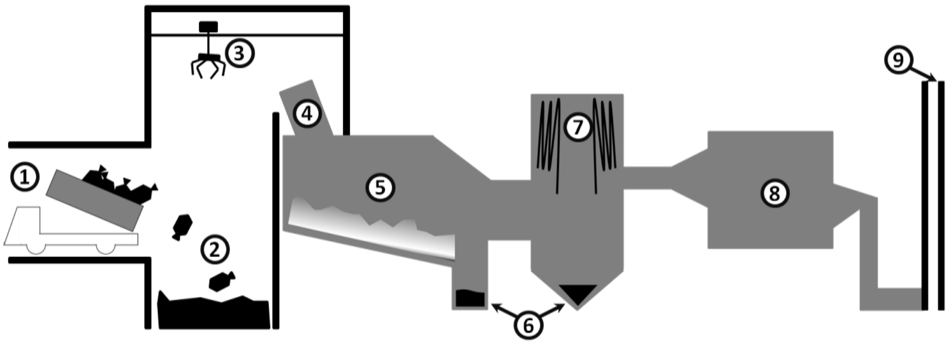

Figure 4.8 Schematic diagram of a typical mass-burn incinerator: (1) Tipping area (2) Storage area (3) Crane (4) Feeding chute (5) Combustion chamber (6) Bottom ash recovery (7) Boiler (8) Air pollution control (9) Flue (stack).(*208*)

4.5.1 Characterisation of and metal concentrations in MSWI ashes

Results from various studies into the metal content of bottom and fly ash produced from MSWI show the presence of a wide range of ferrous, non-ferrous, precious, speciality and rare earth metals within it (Table 4.4). What is apparent is that the concentrations of different metals can fluctuate extensively depending on the source of the ash which would suggest that metal content of ash is strongly influenced by the MSW feedstock being incinerated which in turn is largely influenced by locality and municipality of the incineration site.(*211*)

Table 4.4 Concentrations of elements identified in MSWI bottom and fly ash.

Metal	Concentration range [mg/kg] Bottom ash			Ref.	Concentration range [mg/kg] Fly ash			Ref.
Ferrous elements								
Chromium	13	-	1400	(*205, 212-214*)	13	-	1900	(*205, 212, 214*)
Manganese	0.8	-	8500	(*205, 212, 213*)	<0.7	-	3100	(*205, 212*)
Iron	32000	-	84000	(*212-214*)	420	-	10000	(*212, 214*)
Nickel	9.0	-	510	(*205, 212, 214*)	6.5	-	2000	(*205, 212, 214*)
Niobium	2.3	-	N/D	(*214*)	0.2	-	N/D	(*214*)
Molybdenum	7.9	-	33	(*212, 214*)	0.7	-	47	(*212, 214*)
Vanadium	10	-	90	(*205, 212-214*)	0.7	-	150	(*205, 212, 214*)
Non-ferrous								
Magnesium	9700	-	12000	(*212, 213*)	8200	-	14000	(*212*)
Aluminium	16000	-	85000	(*212-214*)	663	-	47000	(*213, 214*)
Cobalt	9.9	-	700	(*205, 212-214*)	1.1	-	1700	(*205, 212, 214*)
Copper	80	-	25000	(*205, 212-214*)	45	-	4000	(*205, 211, 212, 214*)
Zinc	200	-	20000	(*205, 212-214*)	605	-	150000	(*205, 211, 212, 214*)
Tin	31	-	1300	(*205, 212, 214*)	30	-	8200	(*205, 211, 212, 214*)
Lead	98	-	6500	(*205, 212, 214*)	200	-	19000	(*205, 211, 212, 214*)
Precious metals								
Gold	0.2	-	19	(*213-*	N/D	-	N/D	-

				215)				
Palladium	0.03	-	N/D	(*212*)	3.6	-	18	(*211, 212*)
Platinum	0.1	-	N/D	(*212, 214*)	<1	-	N/D	(*212*)
Silver	2	-	62	(*205, 212-215*)	1.2	-	700	(*205, 211, 212, 214*)
Speciality elements								
Antimony	7.6	-	120	(*212, 213*)	170	-	2600	(*211, 212*)
Arsenic	1.3	-	230	(*205, 213*)	15	-	751	(*205*)
Barium	47	-	2700	(*205, 213, 214*)	37	-	9000	(*205, 214*)
Bismuth	1.2	-	57	(*212, 214*)	1.6	-	142	(*211, 212, 214*)
Cadmium	0.3	-	61	(*205, 212, 214*)	5	-	2200	(*205, 212, 214*)
Gallium	1.9	-	24	(*212, 214*)	0.3	-	164	(*211, 212, 214*)
Germanium	0.2	-	1.5	(*212, 214*)	<1	-	27	(*211, 212, 214*)
Hafnium	1.8	-	2.7	(*213, 214*)	N/D	-	N/D	-
Indium	0.2	-	2	(*212, 214*)	0.1	-	23	(*211, 212, 214*)
Lithium	8.1	-	N/D	(*214*)	0.9	-	N/D	(*214*)
Mercury	<0.01	-	3	(*205*)	0.8	-	73	(*205*)
Scandium	0.9	-	2.1	(*213, 214*)	0.1	-	N/D	(*214*)
Selenium	0.2	-	N/D	(*214*)	0.2	-	N/D	(*214*)
Strontium	122	-	N/D	(*214*)	7.8	-	N/D	(*214*)
Tantalum	1.1	-	5.3	(*212-214*)	0.1	-	43	(*213, 214*)
Tellurium	<1	-	1.2	(*212*)	1.8	-	12	(*211, 212*)
Thallium	<1	-	N/D	(*212*)	<1	-	2.0	(*212*)
Tungsten	11	-	22	(*212, 213*)	6.0	-	9.0	(*212*)
Yttrium	4.8	-	N/D	(*214*)	3.0	-	N/D	(*214*)

Zirconium	65	-	81	(*212*, *214*)	27	-	57	(*212*, *214*)
Rare-earth elements								
Lanthanum	24	-	N/D	(*213*)	N/D	-	N/D	-
Cerium	35	-	N/D	(*213*)	N/D	-	N/D	-
Praseodymium	1.9	-	N/D	(*214*)	N/D	-	N/D	-
Neodymium	7.1	-	N/D	(*214*)	0.2	-	N/D	(*214*)
Samarium	1.7	-	N/D	(*213*)	N/D	-	N/D	-
Terbium	0.64	-	N/D	(*213*)	N/D	-	N/D	-

Waste containing large amounts of electrical goods for example would have much higher concentrations of the elements indium, antimony and gold compared with construction waste that is likely to contain higher concentrations of iron. Wastes containing large amounts of plastics have also been seen to have above average amounts of antimony which may be a result of antimony trioxide (Sb_2O_3) commonly used as a flame retardant in plastic products.(*216*) The presence of metals in bottom ash compared to fly ash is also seen to differ for separate incinerator plants and this is due to different incineration parameters which influence partitioning of metals into each ash.(*208*) What this data shows is that the metal content of ashes cannot be generalised, rather it must be determined on a case-by-case basis. This is problematic as MSWI residues cannot be relied upon therefore as a constant, continuous feedstock of metals.

4.5.2 Precious and special metals

The concentrations of precious and special metals in MSWI ash appears to be very small and potentially insignificant (palladium levels only 0.03 mg/kg) however a comparison of these measured concentrations in bottom and fly ash compared with concentrations for metals in the continental crust shows encouraging results: palladium present in fly ash is approximately 20,000 times higher than crust concentration (Figure 4.9 and Figure 4.10).

This is due to the MSWI concentrating these metals that are present only in small amounts in consumer products.(*211*) Yet, as seen with recycling of metals, due to the extremely heterogeneous nature of MSWI wastes the separation, recovery and reuse of these elements can be problematic and varying speciation and contamination is highly likely due to the presence of so many other elements.

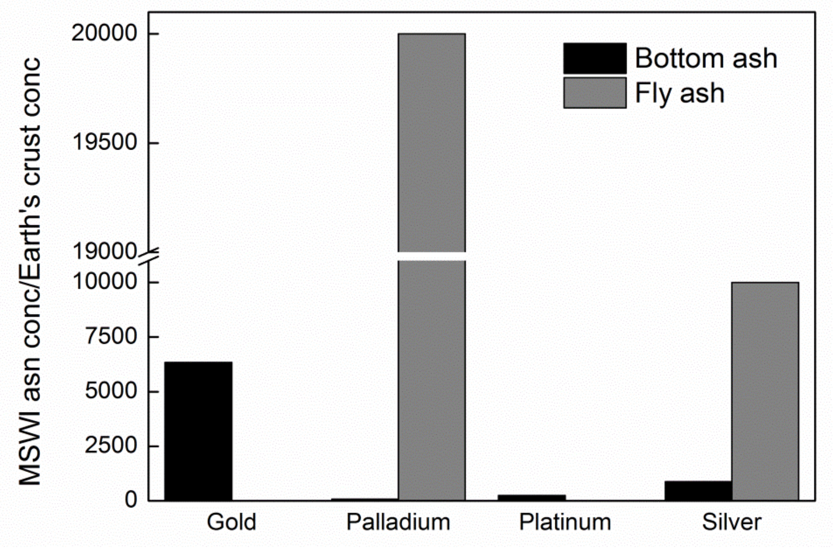

Figure 4.9 Ratio of the precious metal concentration measured in MSW and Taylor's concentration values in bottom and fly ash. (Ratio based on maximum concentration values achieved for each metal.)(*217*)

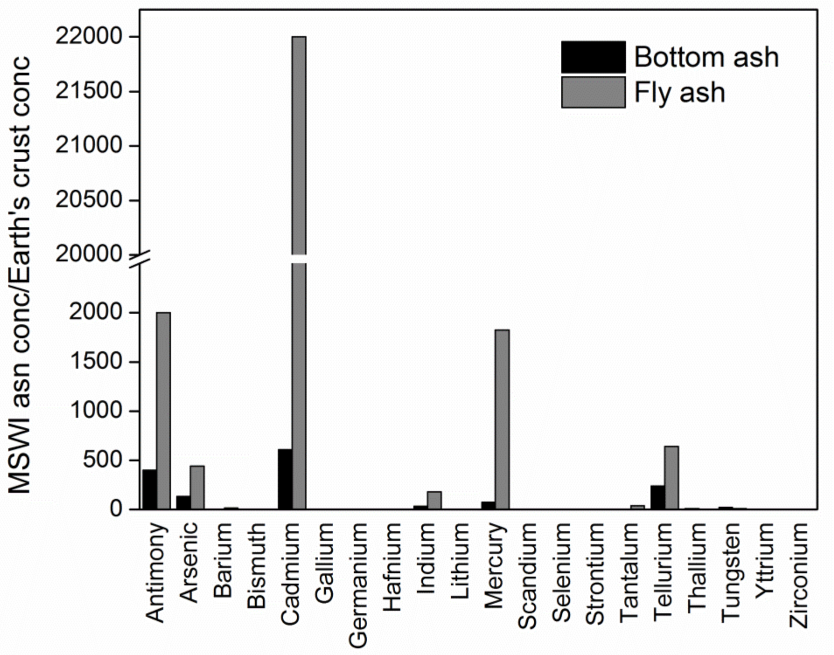

Figure 4.10 Ratio of the speciality element concentration measured in MSW and Taylor's concentration values in bottom and fly ash. (Ratio based on maximum concentration values achieved for each metal.)(*217*)

4.6 Techniques for metal recovery from MSW

There are several technologies that are currently available and many more that are being developed to attempt to make metal retrieval from liquid and solid MSW possible both scientifically and financially. The technique chosen for the recovery of metals depends on the characteristics of the residue and what follows is a description of different possible separation techniques.

4.6.1 Mechanical separation technique

4.6.1.1 Melting of solid residues

This is not a technique widely used in Europe however in 2009 approximately 10% of MSWI ash produced in Japan was treated using melting.(*216*) Electric, burner and blast melting type systems are available for solid residue melting, for metal recovery the electric melting system is the most appropriate due to the highest capacity, lowest energy requirements and lowest operating costs compared with the other techniques.(*218*)

The three most common types of furnaces used for electric melting are illustrated in Figure 4.11 and described as follows:

(a) Electric arc furnace: this furnace transfers electrical energy to heat in the form of an electric arc to melt the slag (ash) fed into the furnace.(*219*)
(b) Plasma arc furnace: in this case copper alloy rear electrodes are used to generate a plasma to heat the slag (ash).(*218*)
(c) Electric resistance furnace: here graphite electrodes are inserted directly into the melting bath to conduct current and melt the metals.(*218*)

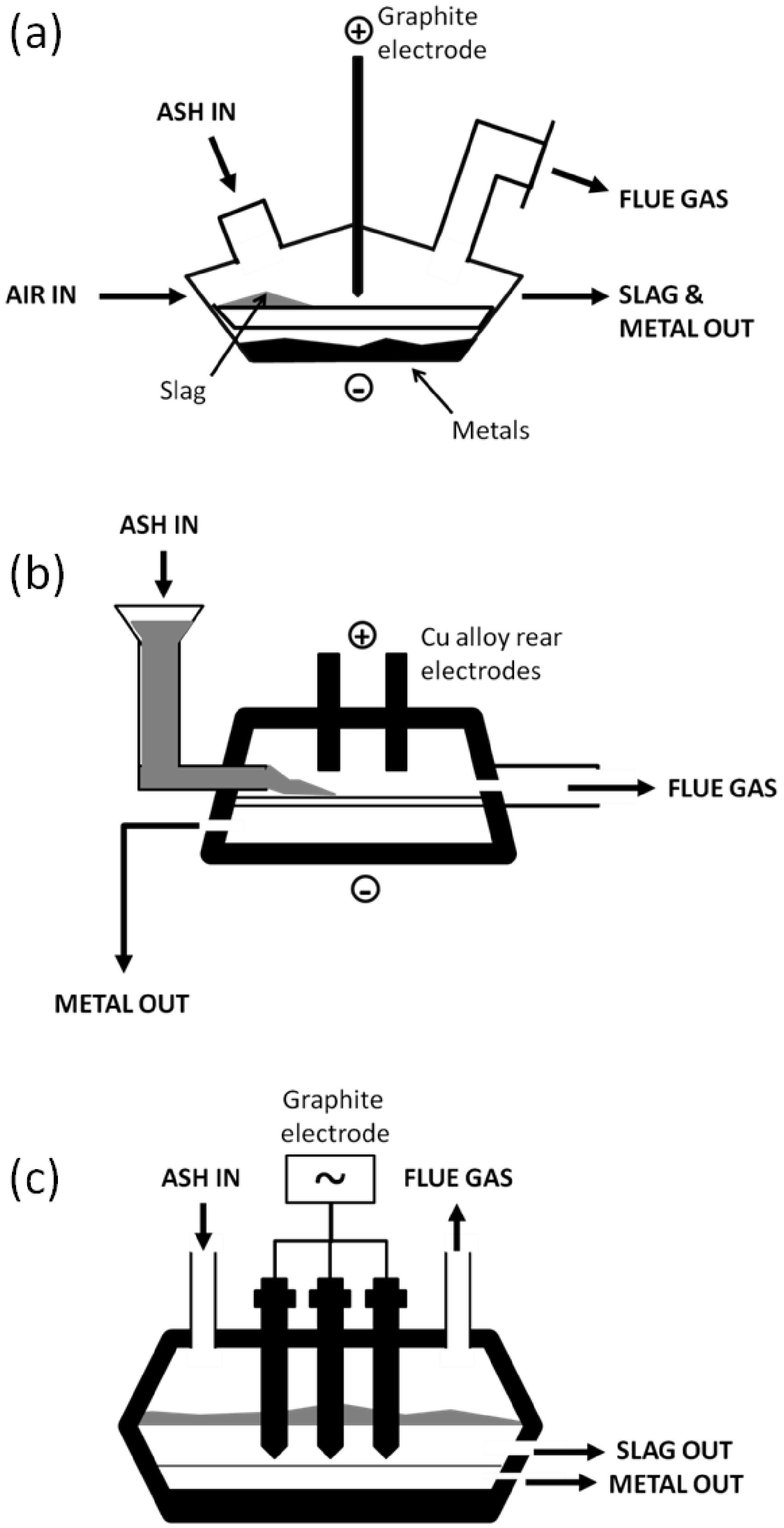

Figure 4.11 Furnace types for electric melting systems (a) electric arc furnace, (b) plasma arc furnace, (c) electric resistance furnace.(*218*)

4.6.2 Chemical separation technique

4.6.2.1 Acid leaching

This is the most wide spread method of metal removal/recovery from MSW residues.(*220*) Acid extraction leaches metals using an appropriate acid followed by recovery of the leached metal usually in the form of precipitates. This is an alternative technique to melting and offers a number of advantages over melting treatments. Firstly, if concentration of chlorine in the waste residue is too high then melting cannot be carried out, secondly, melting is more energy intensive and expensive than leaching and emits considerable amounts of CO_2 into the atmosphere. Finally, leaching is a relatively fast way of extracting metals allowing quicker processing of ash.(*221, 222*) In general, acid leaching is more successful than alkali, although alkali leaching can be used to selectively remove lead and zinc from ash leaving other metals behind which may be useful in certain situations.

Table 4.5 Leaching of metals from MSWI ash using a range of acids.

Metal	Acid used for metal extraction			
	H_2SO_4 *(221, 223)*	HCl *(221, 223)*	Acetic acid *(221, 223)*	Citric acid *(222)*
	Leaching (%)			
Ferrous elements				
Chromium	25	20	18	-
Iron	57	36	23	67
Non-ferrous				
Magnesium	65	53	47	-
Aluminium	73	43	88	100
Copper	50	50	100	100
Zinc	68	68	100	100
Lead	15	51	93	97
Speciality elements				
Cadmium	71	72	73	-

Table 4.5 shows the leaching of some heavy metals achieved by a range of inorganic acids (sulphuric, hydrochloric and acetic acid) and one organic acid (citric acid). The ability of different acids to solubilise metals in varying

amounts makes separation of metals possible. This process is simple and can be economically carried out on a large scale although it does result in considerable amounts of hazardous, acidic waste being produced.

In the last decade interest in bio-derived chemicals has increased, in the case of MSW leaching this has led to attention being given to the use of organic acids such as citric acid which can be easily extracted from many biomass sources, e.g. citrus fruits. Citric acid has been shown to be a successful metal leaching agent compared to other acids (Table 4.5), which has been attributed to its ability to chelate metals due to the presence of three carboxyl groups and one hydroxyl group in its structure. Unlike alternative synthetic chelating agents like EDTA, citric acid is biodegradable and environmentally benign.(*222*) In the future we may see a rise in chemicals such as this being employed more and more in waste treatment to increase the sustainability and decrease the environmental impact of processes.

4.6.2.2 Precious and special metal leaching

Information and data relating to the recovery of precious and special metals from MSW is difficult to find. Jung *et al.* have carried out a study looking at the affect of pH on the leaching of Ag, Bi, Ga, Ge, In, Pd, Sb, Sn, Te and Tl from incineration ash at a pH range of 2 - 13. In this study Ag, Ge and Sb showed maximum leaching at acidic pH with only minimal removal at neutral and alkali pH. In and Te leaching was only achieved at pH < 6. Bi, Sn and Ga were leachable at the extremes of strong acid or strong alkali but not at pHs between these. Pd and Tl were relatively unaffected by pH with leaching occurring across the whole range studied. Tl was easily leached and a large proportion of the amount inputted was removed, however, Pd leaching was very low compared with the feedstock concentration.(*216*) Whilst this work shows some success it is still in the developmental stages and further work is necessary before it can be decided if leaching is a feasible method for precious metal recovery.

4.6.3 Biological separation techniques:

4.6.3.1 Bioleaching

Over the last four decades many researchers have been investigating biotechnology as an alternative method for resource recovery.(*220*) Bioleaching of metals is the most widely employed of the different techniques available. The concept of bioleaching is based on the interaction between metal and microorganisms. This method allows metal recycling by similar processes to those used in natural biogeochemical cycles and it is therefore environmentally friendly.(*220*)

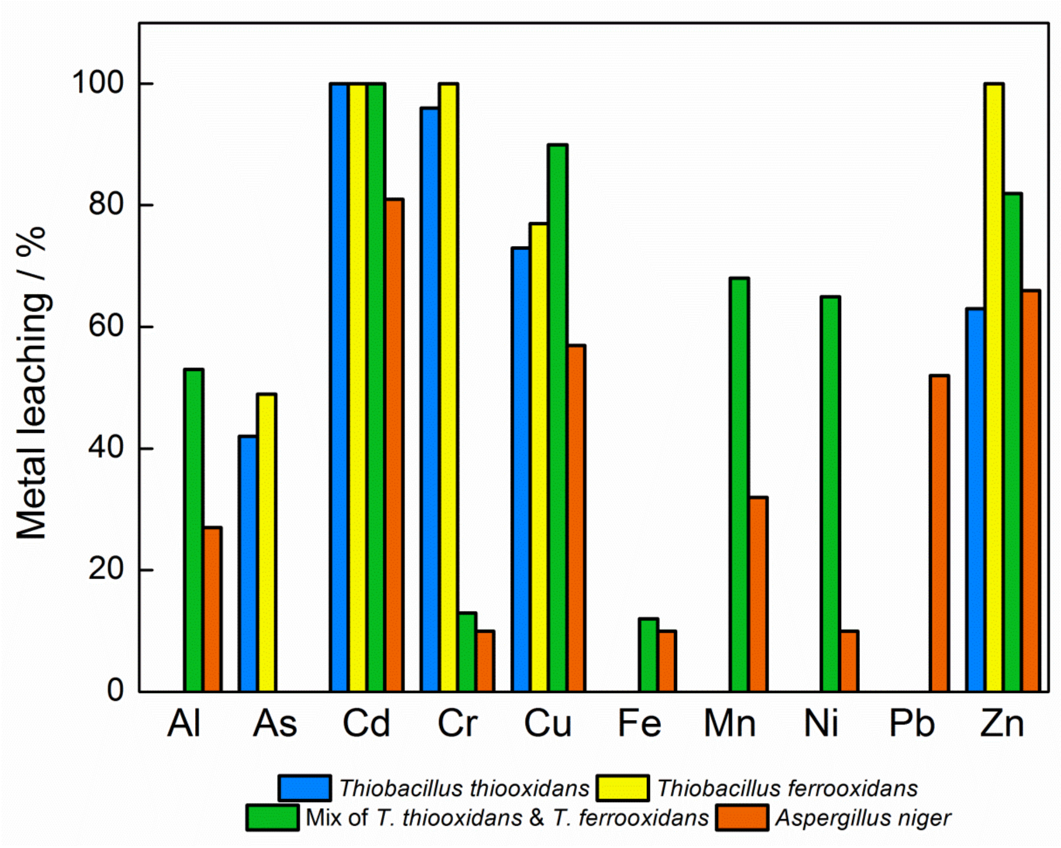

Figure 4.12 Metal bio-leaching from MSWI ash using *Thiobacillus thiooxidans* (black),(*210*) *Thiobacillus ferrooxidans* (dark grey),(*210*) Mix of *T. Thiooxidans* & *T. Ferrooxidans* (light grey)(*224*) and *Aspergillus niger* (white).(*225*)

Sulphur-oxidising and iron-oxidising bacteria are utilised in bioleaching with most experiments performed with different strains of *Thiobacilli* commonly, *T. thiooxidans* and *T. ferrooxidans*. The advantage of using these bacteria is that they produce a very acidic solution (approx pH 1) which dissolves the majority of metals, also the bacteria are tolerant of high concentrations of toxic and heavy metals.(*226*) A range of metals including Al, Cd, Cu and Zn have been successfully recovered using bioleaching with a range of microorganisms (Figure 4.12). Unfortunately no studies of the recovery of precious and special metals using bioleaching could be found.

The first efforts to develop bioleaching processes were more than 30 years ago, however, despite this the technique has not been widely utilised on a commercial scale. The key limiting factor for this is that the majority of research in this area has only been carried out on a lab scale and thus its feasibility and cost on a large scale has not been shown. Also this is a relatively slow technique, taking up to 50 days to achieve useful levels of metal leaching from ash which increases costs and thus lowers the economic practicality of this process.(*224*)

4.6.3.2 Phytoremediation

Phytoremediation defines the use of plants for environmental clean-up. The plants can be compared to solar driven pumps that have the ability to extract elements from different environments.(*227*) The advantages of phytoremediation are that it can effectively be used to decontaminate and capture elements from environmental media, such as soil and watercourses, without any need for excavation or processing. Also phytoremediation can be relatively cheap and less energy intensive than many other metal recovery techniques.(*228*)

Studies into the use of phytoremediation have predominantly focused on the recovery of toxic elements from contaminated soil, e.g. lead, but some work has investigated the potential for the recovery of precious metals due to their high economic value (Table 4.6). Anderson *et al.* published the first paper showing significant gold phytoremediation by *Brassica juncea* and calculated that a concentration of 17 $\mu g\ g^{-1}$ in the plants was sufficient to make a profit using phytoremediation for gold recovery.(*229*)

Table 4.6 Accumulation of metals by various plant species.(*230*)

Metal	Species	Mean metal concentration [mg kg^{-1}]^a	Biomass [t Ha^{-1}]
Ferrous elements			
Nickel	*Alyssum bertolonii*	13400	9
	Berkheya coddii	17000	22
Manganese	*Macadamia neurophylla*	55000	30
Non-ferrous			
Cobalt	*Haumaniastrum robertii*	10200	4
Copper	*Maumaniastrum katangense*	8356	5
Lead	*Thlaspi rotundifolium*	8200	4
Zinc	*Thalspi calaminare*	10000	4
Precious metals			
Gold	*Brassica juncea*	10	20
Speciality elements			
Cadmium	*Thalspi caerulescens*	3000	4
Selenium	*Astragalus pattersoni*	6000	5
Thallium	*Biscutella laevigata*	13768	4
	Iberis intermedia	4055	10

[a] Relative to plant dried weight.

Little is understood about the exact mechanisms of plant uptake and transport of metals within plant, what is known is that a large proportion of metal in soil is present adsorbed to soil constituents. In order for plants to be able to uptake these metals plants first have to mobilise them into the aqueous phase present in the soil.(*231*) There are a number of ideas of how plants mobilise metals:

1. Ribosomes present on plant roots excrete metal-chelating agents to solubilise and chelate the metals.
2. Plant roots release protons acidifying the soil around them in order to solubilise the metals.
3. Roots can reduce metal ions attached to soil using enzymes present in the plasma membrane.

Plants may use one or more of these mechanisms for mobilisation. Once the metal is mobilised it is taken into the plant and transported to the shoots, the plants can then be harvested and processed to recover the metal.(*231*)

4.6.4 Physical separation technique

4.6.4.1 Biosorption

Biosorption is another potential method for the recovery of metals from liquid waste. In the majority of processes the use of inactive or non-growing biomass was preferred for the treatment of liquid waste.(*232*) Biosorption of various metals including; Ag, Cr, Pb, Cu, Zn, Cd, Co and Ni from waste has been successfully achieved along with the removal of radio nucleotides e.g. uranium. Fungi, yeasts, algae and chitosan are some of the most commonly used biosorbents. Chitosan has achieved a lot of popularity due to the ease of which it can be modified thus enabling the tailoring of chitosan properties to favour the uptake of specific metal ions.(*233*) Macro algae also have excellent metal adsorbing properties. The rigid macrostructure of seaweeds enable them to withstand a variety of adsorption conditions that may be encountered when recovering metals from MSW.(*234*)

Table 4.7 Biosorption capacity of low cost adsorbents for precious metals.(*235*)

Metal	Biosorbents	Max uptake [mmol g^{-1}]
Gold	Chemically modified chitosan	3.4
	Tannin gel	40.0
	Dealginated seaweed waste	0.40
	Eggshell membrane	0.67
	Rice husk carbon	0.76
	Alfalfa	0.18
Platinum	Chitosan derivatives	3.2
	Cross-linked chitosan	1.6
	Immobilized tannin	0.23
Palladium	Aquatic moss	37.2 mg g^{-1}
	Chitosan derivatives	3.2
	Cross-linked chitosan	2.4
	Immobilized tannin	0.32

4.6.4.2 Precious metal biosorption

The biosorption of precious metals has also been effectively achieved, Table 4.7 gives examples of adsorption of precious metals using a range of different adsorbents from the literature. Chitosan has shown particularly good affinity for Au, Pt and Pd compared to other adsorbents.(*235*) Subsequent to biosorption of metals from waste desorption is commonly carried out. This has the advantage of recovering the metal in a more concentrated and potentially purer form and regenerating the adsorbent for subsequent use. Work by Ichikawa *et al.* has shown that >90% of gold adsorbed on to eggshell membrane can be desorbed using NaOH or NaCN treatment.(*236*) These results indicate the potential for development of an adsorption-desorption system for the recovery of metals from MSW in the future.

4.7 "Urban mining" in practice: platinum and palladium recovery from roadside dust

Automobile catalysts or catalytic converters are the largest annual users of platinum and palladium. Catalytic converters were first introduced around 1975 and are used to reduce harmful emissions of gases such as unburnt hydrocarbons (HC), NO_x and CO from exhaust fumes.(*237*) Figure 4.13 shows a simple diagram of a catalytic converter. Inside the converter the precious metals Pt, Pd and Rh are supported on a ceramic honeycomb and as the name suggests catalyse the degradation of the fumes. Ever since their introduction there have been concerns related to the magnitude and relevance of possible metal emissions from the converters due to mechanical and thermal impact on the active layer during use.(*238*)

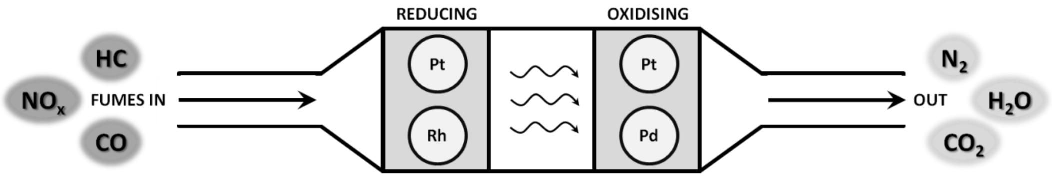

Figure 4.13 Diagram of a catalytic converter.

Catalytic converters contain approximately 0.08% platinum, 0.04% palladium and 0.007% rhodium – although presently the metal composition is changing, due to the increases in price of platinum it is being replaced by the cheaper metal palladium.(*239, 240*) Studies have shown that up to 80% of these PGMs are released from the catalytic converters during their lifetime (which with modern converters is usually the lifetime of a car), the majority of the metal is emitted in metallic form and is primarily deposited in the dust and soil along the roadside.(*241*) From here the metals can be further dispersed into the wider environment, for example, rain can wash the metals into drains which eventually lead out to the sea. It is not well known what impact the presence of these metals will have on the environment, wildlife or even humans, however what is clear is that these incredibly valuable and useful metals are being so heavily diluted and dispersed into the environment they are becoming irretrievable.

4.7.1 Levels of Pt and Pd in environmental matrices

All over the world road sweeping is carried out by local government or private companies to collect rubbish and debris from roadsides and prevent blockages of street drains. Another more minor result of this practice is that small particulate matter such as dust is also collected during sweeping. Characterisation of this dust has shown concentrations of PGMs can be as much as 1 ppm.(*242*)

A wider study by Helmers *et al.* has investigated the Pt and Pd concentrations of various environmental matrices surrounding roads and combined this with literature data to give a representative idea of contamination levels (Table 4.8).(*238*) The results show that Pt and Pd is indeed distributed into the surrounding environment and is accumulating to levels much higher than would naturally occur, however what is promising from their study, is that the highest concentrations of the metals are in the dust and has the potential to be recovered.

Table 4.8 Concentration ranges of Pt and Pt in various polluted matrices surrounding roads.(*238, 241*)

Matrix	Pt	Pd	Unit
Grass	3.4 - 7.7	<0.5 - 0.6	µg/kg
Rain	<5 - N/D	<5 - N/D	ng/l
Soil	10 - 253	2 - 77	µg/kg
Dust	51 - 360	5 - 2465	µg/kg
Sludge	<2 - 220	<1 - 260	µg/kg
Car Exhaust	120 - 700	0.3 - 480	ng/m^3
Background (Continental Crust)	0.4	0.4	µg/kg

4.7.2 Novel processing techniques for the recovery of Pt and Pd

At present once roadside dust is collected it is disposed of in landfill, no attempts are made to retrieve the PGMs due to current technology making it uneconomical to recover such low concentrations. Yet, within the last year a patent for the design of a new, economical, mechanical processing method has been filled for the separation of road side dust.(*242*) Also the world leading company in environmental services, Veolia, have also released plans for a treatment facility dedicated to roadside dust and the retrieval of palladium, aimed to be open in 2013.(*243*)

A schematic representation of their planned process is shown in Figure 4.14, it involves a variety of steps to not only separate the palladium but also other valuable and recyclable materials from the waste. Veolia is hoping to retrieve around £80,000 worth of palladium per year from their treatment plant plus other profitable materials such as steel, iron and aluminium.(*244*)

This is a fantastic example of how a potentially toxic waste that would cost money to be disposed of in landfill can be effectively "urban mined" to recover valuable resources for profit. Hopefully, other developments like this will occur in the near future.

4.8 Conclusions

Waste is a highly important resource and by exploiting the wealth of elements available from it society will be able to move closer to "closing the loop". In order to achieve this, the most important thing that needs to change is our attitude towards waste. We can no longer treat it as we have done in the past by treating it as one indistinct mass to be disposed of indiscriminately but rather as a combination of separate parts that can be divided up and treated individually to extract the most value. By segregating materials prior to disposal whether at the household level through individual bins for glass, paper, plastic and metals or at a production and manufacturing level by designing products to be easily disassembled at the end of their life, the process of recovering resources can be made significantly simpler.

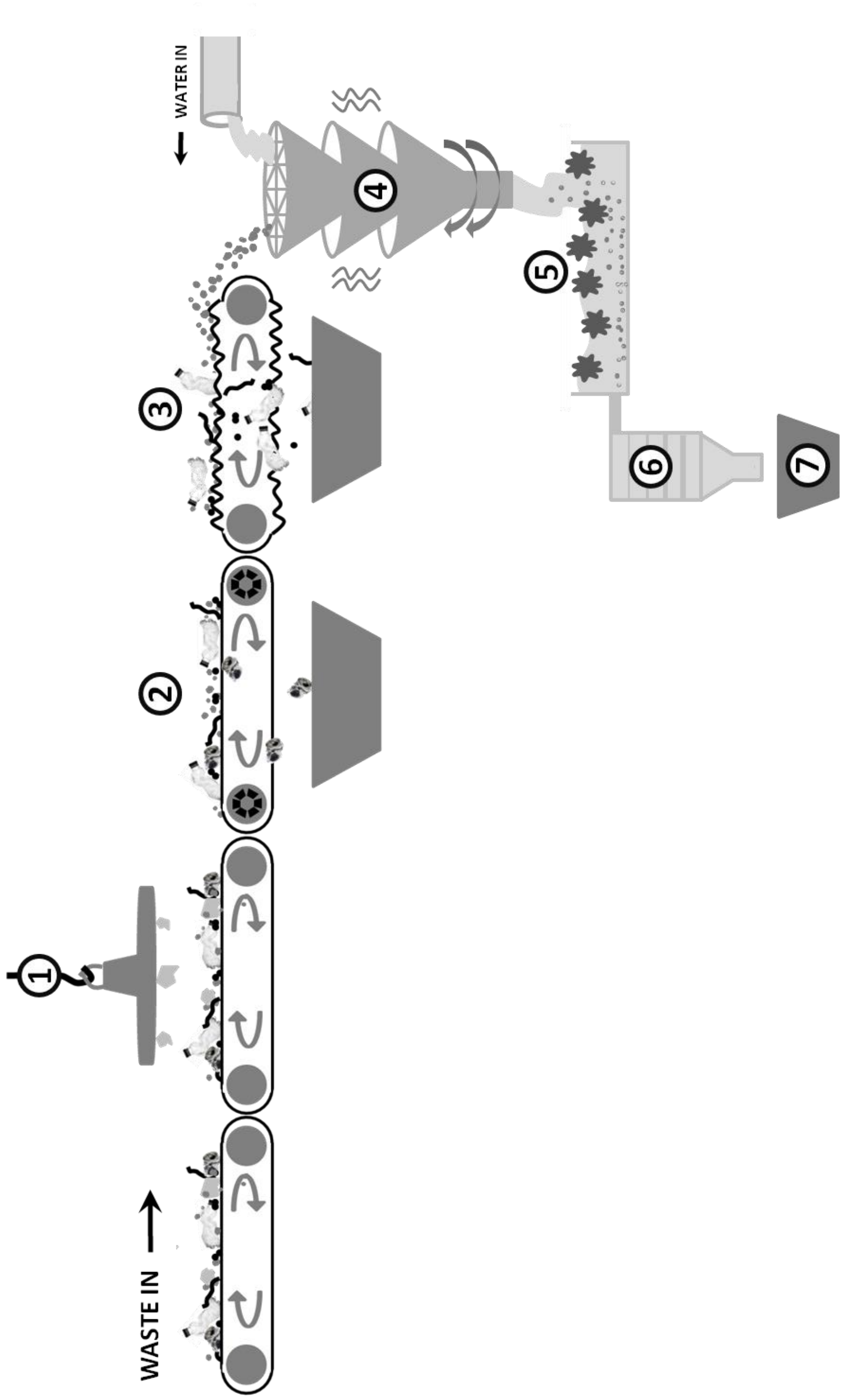

Figure 4.14 Representation of the palladium recovery process being developed by Veolia (1) Magnets to remove steel and iron (2) eddy current separator to remove aluminium cans, (3) vibration conveyor belts to remove plastics, twigs and grit (4) water added followed by filter, shake spin and sieve to remove grit and dust (5) "smart sponges" used to adsorb oil (6) membrane separation to catch dust particles (7) palladium collection.(*242, 244*)

As this chapter shows there are processes being used and researched to try and make the use of past and present waste possible but what is clear from literature is that these are not yet adequate solutions for the future. Technology, especially for the recovery of precious, speciality and rare metals, is not developed enough to make retrieval feasible on a large enough scale and fast enough turnover to be economical.

The world is still in the early stages of waking up to the problems that are going to arise from the lack of elemental sustainability but hopefully as prices rise and metal reserves become more difficult to mine we will see an increase in time, money and expertise being devoted to the area of “urban mining”.

Chapter 5

Direct synthesis of palladium nanoparticles on alginic acid and seaweed supports

Aspects of the work presented in this chapter have appeared in:

J. R. Dodson, A. J. Hunt, H. L. Parker, Y. Yang & J. H. Clark, Elemental sustainability: towards the total recovery of scarce metals, *Chemical Engineering and Processing: Process Intensification*, 2012, 51, 69-78

Oral presentation given at Alg'n'Chem: Algae, new resources for industry? Montpellier, France, November 2011

Palladium impregnation, drying and grinding of the seaweed material used in this chapter was carried out by Dr. J Dodson, Institute of Chemistry, Federal University of Rio de Janeiro, Cidade Universitaria, Rio de Janeire, 21941-909, Brasil.

Chapter 5.

Direct synthesis of palladium nanoparticles on alginic acid and seaweed supports

5.1 Introduction

Biosorption is a popular alternative to existing methods of metal recovery, for example, hydrometallurgical and chemical routes.(*245*) Compared to these methods biosorption offers many advantages including: high efficiency, low operating costs and minimal waste.(*246*) The mechanisms of biosorption are generally based on physico-chemical interactions between the adsorbate metal ions and functional groups of the biomass adsorbent. Functionalities commonly implicated in such interactions are carboxylate, hydroxyl and amine groups.(*247*) Alginic acid contains both carbonyl and hydroxyl groups which are excellent for the anchoring of metals.(*248-250*) It is also a highly abundant biomaterial with up to 39,000 tons extracted annually worldwide.(*251*) However, this naturally occurring polymer has so far captured very little attention for precious metal biosorption despite presenting these attractive properties.

Alginic acid-derived materials have already been presented in this thesis as efficient adsorbers of organic molecules and here they are further investigated for the adsorption of palladium. This chapter reports the synthesis of an alginic acid supported palladium nanoparticle catalyst. Catalytic activity of the catalysts has been determined via Heck and Suzuki C-C coupling reactions. By varying the heating rate during catalyst preparation materials with a range of different surface areas and porosities have been produced in order to determine the effect this has on catalytic activity and rate of reaction.

In the interest of green chemistry and with the aim of reducing the number of chemical steps required for the production of supported catalyst, results are also presented in this chapter from work investigating the direct impregnation of seaweed with palladium. Seaweed consists of approximately 25% alginic acid and therefore if it could be used as a successful catalyst it would eliminate the many steps necessary to extract alginic acid.(*252*)

Throughout this work palladium on carbon 1%, a commercially available supported palladium catalyst, was used as a basis for comparison with the novel alginic acid and seaweed catalysts.

5.1.1 Aims

The aims of the work presented herein:

- To demonstrate the affinity of expanded alginic acid for adsorption of palladium from solution and subsequent nanoparticle formation.
- To effectively process the alginic acid + palladium material in order to prepare stable, catalytically active materials.
- To determine the influence heating rate has on the catalyst properties and the resulting effect on catalytic performance.
- To investigate the potential of using seaweed directly for the preparation of palladium supported catalytic materials.

5.2 Results and Discussion

5.2.1 Formation & characterisation of alginic acid + palladium material

The first step in the preparation of the catalyst was to expand native alginic acid, using the same method as for Starbon® preparation, up to the solvent exchange step.(*117*) This expansion was carried out in order to open up the pore structure of the material to facilitate better uptake of the metal ions.

The resulting expanded alginic acid (AA) in ethanol was impregnated with palladium via adsorption of the metal species. To do this a portion of palladium acetate dissolved in a small amount of ethanol (concentration was approximately 1% palladium based on amount of expanded alginic acid used) was added to the expanded alginic acid ethanol suspension. The solution was stirred until all of the palladium had been adsorbed. During this process the solution turned from pale orange/yellow in colour to colourless with only the expanded alginic acid particles visible, indicating all of the palladium was removed. The impregnated material (AA+Pd) was dried using supercritical CO_2, using the same method as for Starbon®, in order to maintain the porosity of the material. A schematic representation of the procedure is shown in Figure 5.1.

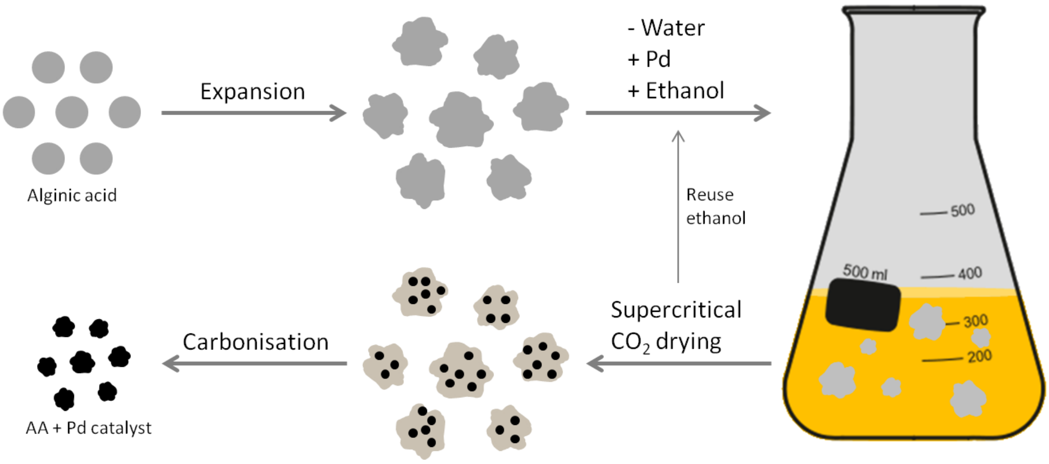

Figure 5.1 Schematic showing the formation of alginic acid supported palladium nanoparticles.

Infrared spectra (IR) of the resulting dried expanded alginic acid with and without palladium are shown in Figure 5.2. A high degree of similarity is observable between the two spectra, with key absorbance bands visible at 1722, 1250 and 1032 cm^{-1} which are characteristic of alginic acid.(*253*) These bands indicate the carbon-oxygen stretches of carboxylate groups and the carbon-oxygen (hydroxyl) stretches of the acid groups present in the alginic acid structure.(*254*)

There is an observed increase in the intensity of these peaks after the adsorption of palladium (AA+Pd line) however there are no clearly observable shifts in any of these absorbance bands. There is a minor peak shift (and reduction) that is visible of the carbon-carbon stretching band for the carbons in the polysaccharide ring from 1620 to 1639 cm^{-1}, outlined in blue in Figure 5.2. This may be an indication of the involvement of the polysaccharide ring in interacting with the adsorbed palladium species however this change is only very slight. The lack of any truly significant differences in the two spectra may indicate that there is little or no chemical bonding occurring between palladium and the alginic acid surface. Thus uptake of palladium did not significantly alter the original structure of the alginic acid.(*255*)

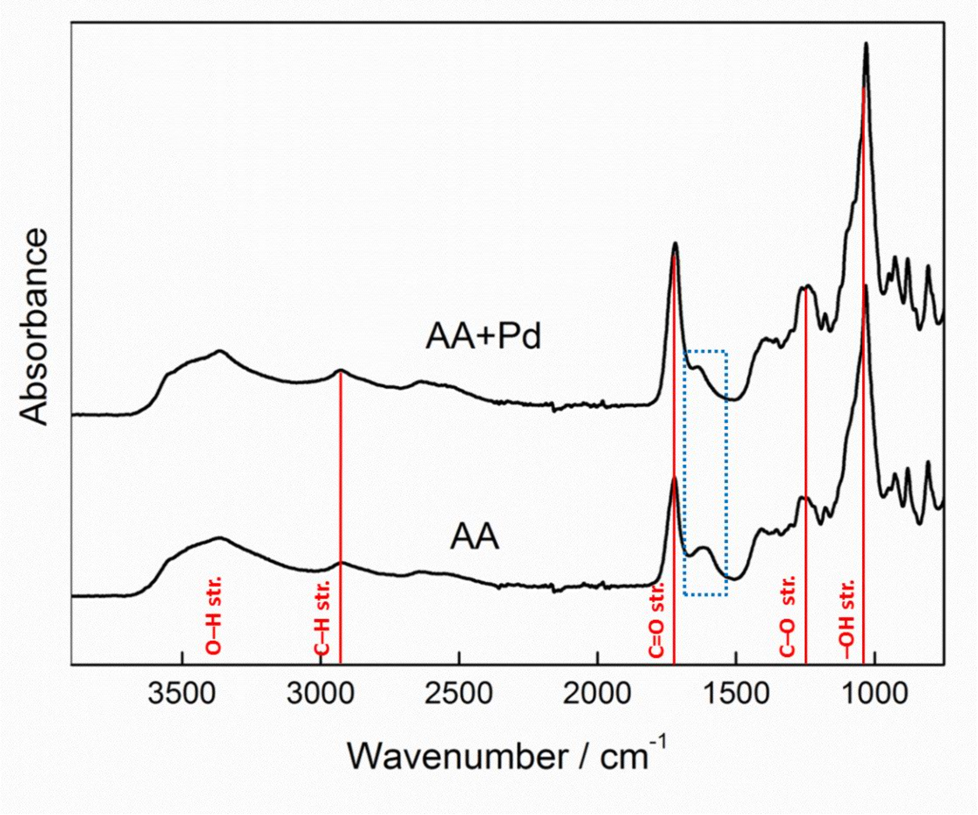

Figure 5.2 IR spectra of expanded alginic acid (AA) and expanded alginic acid + palladium (AA+Pd).

X-ray photoelectron spectroscopy (XPS) analysis was carried out in addition to IR analysis in order to elucidate more information about the surface of alginic acid upon adsorption of palladium. Table 5.1 shows the atomic concentrations of carbon, oxygen, sodium and palladium in the two samples, according to XPS spectra analysis. Interestingly, the apparent concentration of palladium is low, only 0.30%. Inductively coupled plasma (ICP) analysis of the AA+Pd material showed that the actual concentration of palladium on the alginic acid support was 0.86%.

Table 5.1 Content of elements in alginic acid materials with and without palladium from XPS analysis.

	Atomic %			
	C	O	Na	Pd
AA	60.7	38.8	0.49	0
AA+Pd	64.6	35.0	0.12	0.30

The XPS results suggest there is likely to only be a small amount of adsorbed palladium actually present on the alginic acid surface, the majority being contained within the interior pore structure of the material.

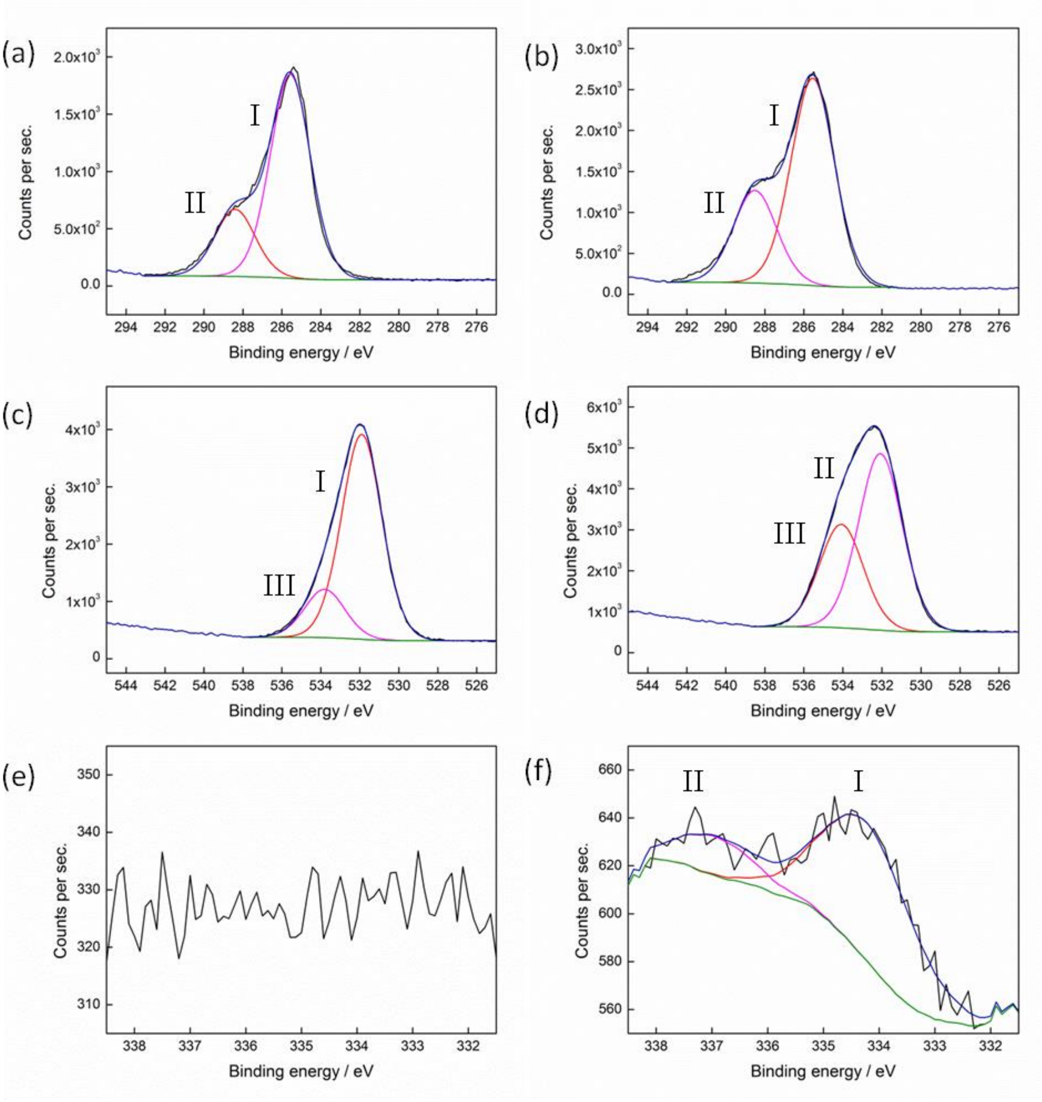

Figure 5.3 XPS spectra showing: carbon spectra (a) expanded alginic acid and (b) alginic acid + palladium, oxygen spectra (c) expanded alginic acid and (d) alginic acid + palladium and palladium spectra (e) expanded alginic acid and (f) alginic acid + palladium.

High resolution spectra for carbon, oxygen and palladium for AA and AA+Pd can be seen in Figure 5.3. There are distinguishable changes occurring in the surface morphology of the materials after uptake of palladium that were not visible in the IR spectra, detailed in Table 5.2. Murphy *et al*. has postulated that when seaweeds are exposed to metal containing solutions, metal cations may replace some of the alkali and alkali earth metals (e.g. K, Na, Mg) present in their cellular structure.(*256*) This change in metal can result in variations to the surface structure that is readily apparent using XPS analysis.

Table 5.2 Composition of expanded alginic acid (AA) and alginic acid + palladium (AA+Pd) components from XPS spectra.

	Peak	BE [eV]	Chemical State	%	
				AA	AA+Pd
Carbon	I	285.5 ± 0.2	C-C (ring)	75	69
	II	287.3 ± 0.2	C-O	-	-
	III	288.4 ± 0.2	C=O, O-C-O	25	31
	IV	289.5 ± 0.2	COO	-	-
Oxygen	I	531.2 ± 0.6	CO	81	-
	II	532.5 ± 0.2	C=O	-	63
	III	533.0 ± 0.2	C-O	-	-
	IV	534.0 ± 0.5	C-O (in COO)	19	37
Palladium	I	334.3 ± 0.2	$Pd^{(0)}$	-	74
	II	336.8 ± 0.2	PdO	-	26
	III	341.8 ± 0.2	$Pd^{(II)}$	-	-

Raize *et al*. indicated the cause of these changes is the difference in the electrostatic and coordinative bonding behaviour of different metals which alters the cross-linking between the metal and the cell wall polymers.(*254, 256*) XPS data shows the presence of sodium in alginic acid (Table 5.1) and a reduction is sodium concentration between AA and AA+Pd samples is observed. It could be hypothesized that the sodium present in alginic acid is being exchanged for palladium ions during adsorption, thus, leading to the discussed changes in the material surface.

The XPS palladium signal is weak for AA+Pd likely due to low surface concentration. It was possible to fit two peaks with binding energies of 334.3 and 336.9 eV which represent $Pd^{(0)}$ and palladium oxide, respectively. The presence of $Pd^{(0)}$ may indicate that the formation of palladium nanoparticles (PdNPs) has occurred on the alginic acid support.

5.2.2 Carbonisation of alginic acid + palladium material

To ensure catalyst stability during reactions, the AA+Pd was carbonised to 573 K in a nitrogen atmosphere, using the same method as used for Starbon® preparation. Heating the material in this way resulted in the removal of volatile species from the alginic acid so that it would be stable under a range of different reaction temperatures.

Table 5.3 Content of elements in alginic acid materials with and without palladium from XPS analysis.

	Atomic %			
	C	O	Na	Pd
AA-Carbonised	77.6	21.3	0.22	0.76
Pd/C	90.8	7.9	0.25	1.1

The loss of oxygen after carbonisation is clear from the XPS analysis of the carbonised alginic acid + palladium material (AA-Carbonised), Table 5.3 shows a 14% decrease in oxygen content compared to AA+Pd. As expected deconvolution of the carbon and oxygen spectra of the carbonised material show changes in the chemical species present, shown in Figure 5.4 and Table 5.4.

Most notable is the appearance of aliphatic carbons indicative of loss of the polysaccharide (ring) character of the alginic acid upon heating (Figure 5.4 (a)). There is also a shift in the palladium species present with a loss of reduced $Pd^{(0)}$ and an increase in the oxidised species PdO and $Pd^{(II)}$ (Figure 5.4 (e)). This may be caused by the oxygen being release from the alginic acid surface during heating and subsequently reacting with the palladium on the support.

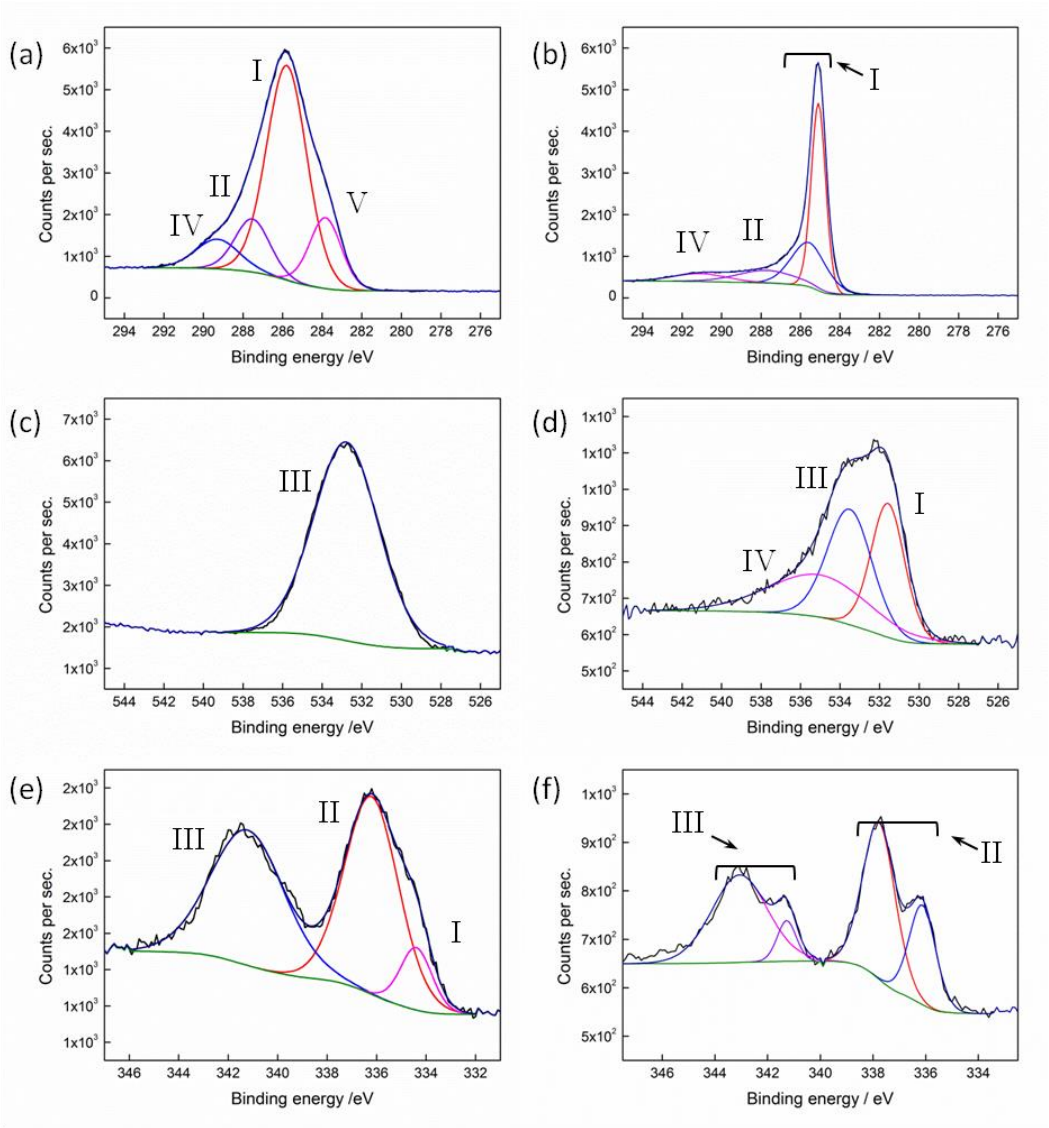

Figure 5.4 XPS spectra showing: carbon spectra (a) AA-Carbonised and (b) Pd/C, oxygen spectra (c) AA- Carbonised and (d) Pd/C and palladium spectra (e) AA- Carbonised and (f) Pd/C.

The results of XPS analysis of Pd/C are also included in Table 5.4 and displayed in Figure 5.4 for comparison with the alginic acid materials. Unlike AA-Carbonised the palladium peaks for Pd/C are stronger and more easily analysed, likely due to a larger percentage of palladium being located on the surface of the material as indicated by an atomic concentration of palladium of 1.1% shown by XPS (Table 5.3). The species of palladium present on Pd/C are seen to be PdO and $Pd^{(II)}$ with no peak for $Pd^{(0)}$ being determined.

Table 5.4 Composition of carbonised alginic acid + palladium (AA-Carbonised) and commercial material palladium on carbon 1% (Pd/C) components from XPS spectra.

	Peak	BE [eV]	Chemical State	% AA-Carbonised	Pd/C
Carbon	I	285.5 ± 0.2	C-C (ring)	62	78
	II	287.3 ± 0.2	C-O	13	14
	III	288.4 ± 0.2	C=O, O-C-O	-	-
	IV	289.5 ± 0.2	COO	9	8
	V	283.8 ± 0.2	C-C	16	-
Oxygen	I	531.2 ± 0.6	CO	-	32
	II	532.5 ± 0.2	C=O	-	-
	III	533.0 ± 0.2	C-O	100	37
	IV	534.0 ± 0.5	C-O (in COO)	-	31
Palladium	I	334.3 ± 0.2	$Pd^{(0)}$	9	-
	II	336.8 ± 0.2	PdO	47	58
	III	341.8 ± 0.2	$Pd^{(II)}$	43	42

To determine the effect heating rate would have on the material properties and their catalytic activity three catalysts were prepared at different rates – 1, 5 and 20 K min^{-1} – referred to as AA-SLOW, AA-MEDIUM and AA-FAST respectively. Nitrogen adsorption porosimetry was used to determine the surface area and pore volume of the materials (Table 5.5). Results showed that the BET surface area and pore volumes of the palladium impregnated materials were significantly lower than A300. This is likely due to palladium depositions within the pores and/or at pore entrances that effectively block the pores resulting in lower apparent porosities and surface area.(*82*)

Table 5.5 Porosimetry characteristics of alginic acid catalysts.

	AA-SLOW	AA-MEDIUM	AA-FAST	A300	Pd/C 1%
BET Surface Area [m^2g^{-1}]	131	2.90	0.15	280	965
Pore Volume [cm^3g^{-1}]	0.31	0.0031	0.001	1.41	0.58
% Micropores	25%	37%	-	8%	88%

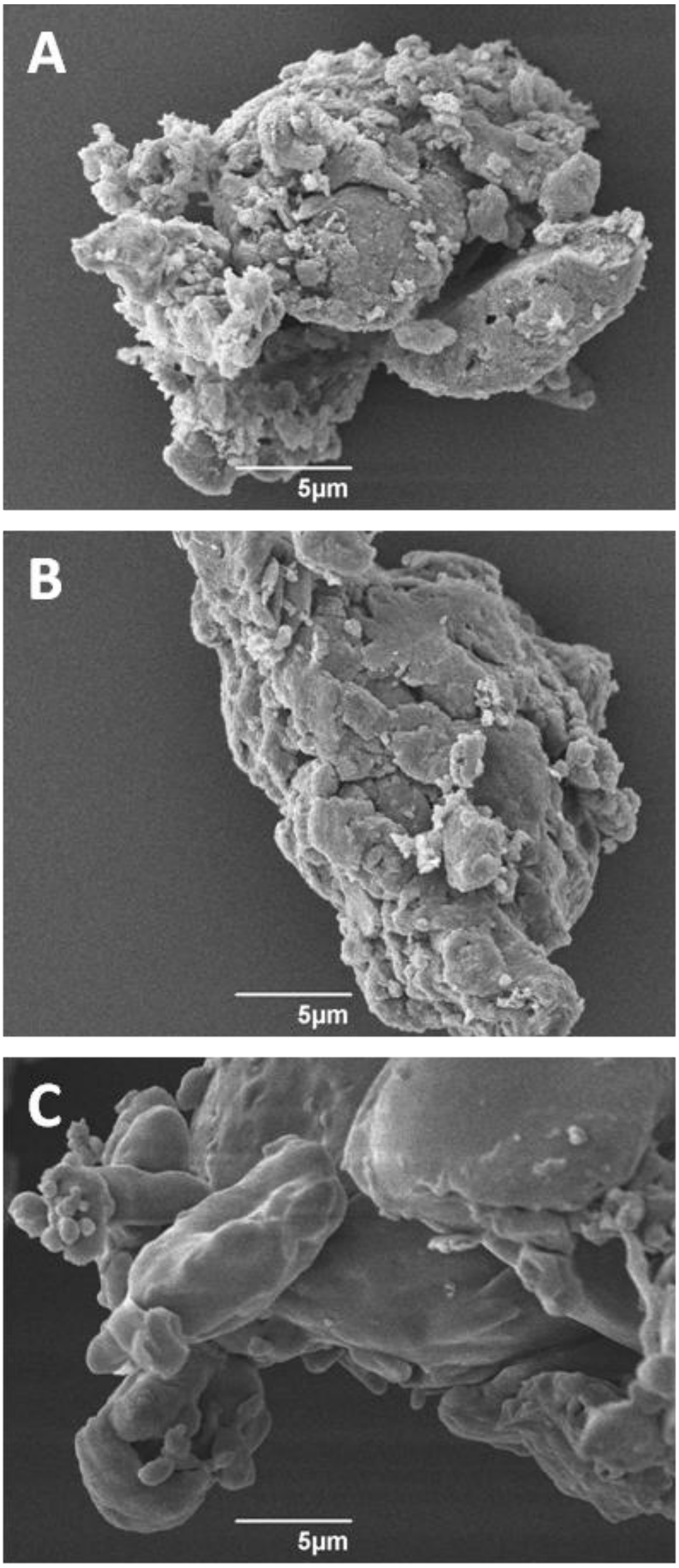

Figure 5.5 SEM images of (A) AA-SLOW, (B) AA-MEDIUM and (C) AA-FAST.

The surface area of Pd/C is much higher than the alginic acid derived materials due to the high degree of microporosity of this material. What the porosimetry results show is that as heating rate of the catalysts increased the pore volumes and surface areas all decreased, reaching almost zero for AA-FAST. The percentage of microporosity also appears to increase with heating rate, although microporosity could not be determined for AA-FAST.

Further characterisation of the alginic acid materials by scanning electron microscopy (SEM) gave a visual representation of the dramatic effect heating rate had on the textural properties of the materials (Figure 5.5). A noticeable smoothing of the surface of the materials can be seen to occur as the heating rate increased and the pore structure is lost. It has been shown previously that when heated alginic acid undergoes a decomposition at 523 K during which surface and bulk –OH groups are lost.(*65*) The loss of porosity seen when the catalysts are fast heated (i.e. 20 K min^{-1}) is a likely result of decomposition occurring very rapidly and causing the pore structure to collapse. (SEM images of Pd/C can be seen in Appendix 3.)

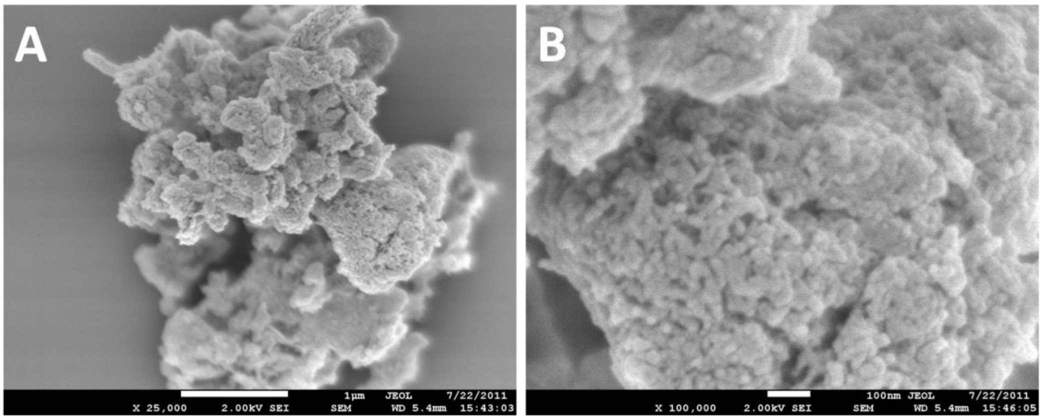

Figure 5.6 High resolution SEM images of AA-SLOW at (A) x25000 and (B) x100000 magnification.

High-resolution SEM images obtained of AA-SLOW shown in Figure 5.6, effectively displays the “fluffy” nature of the expanded material and the surface porosity is clearly visible. The high porosity of AA-SLOW compared to AA-MEDIUM and AA-FAST is likely an advantage for catalysis as it can facilitate diffusion of reagents to the active catalytic sites.

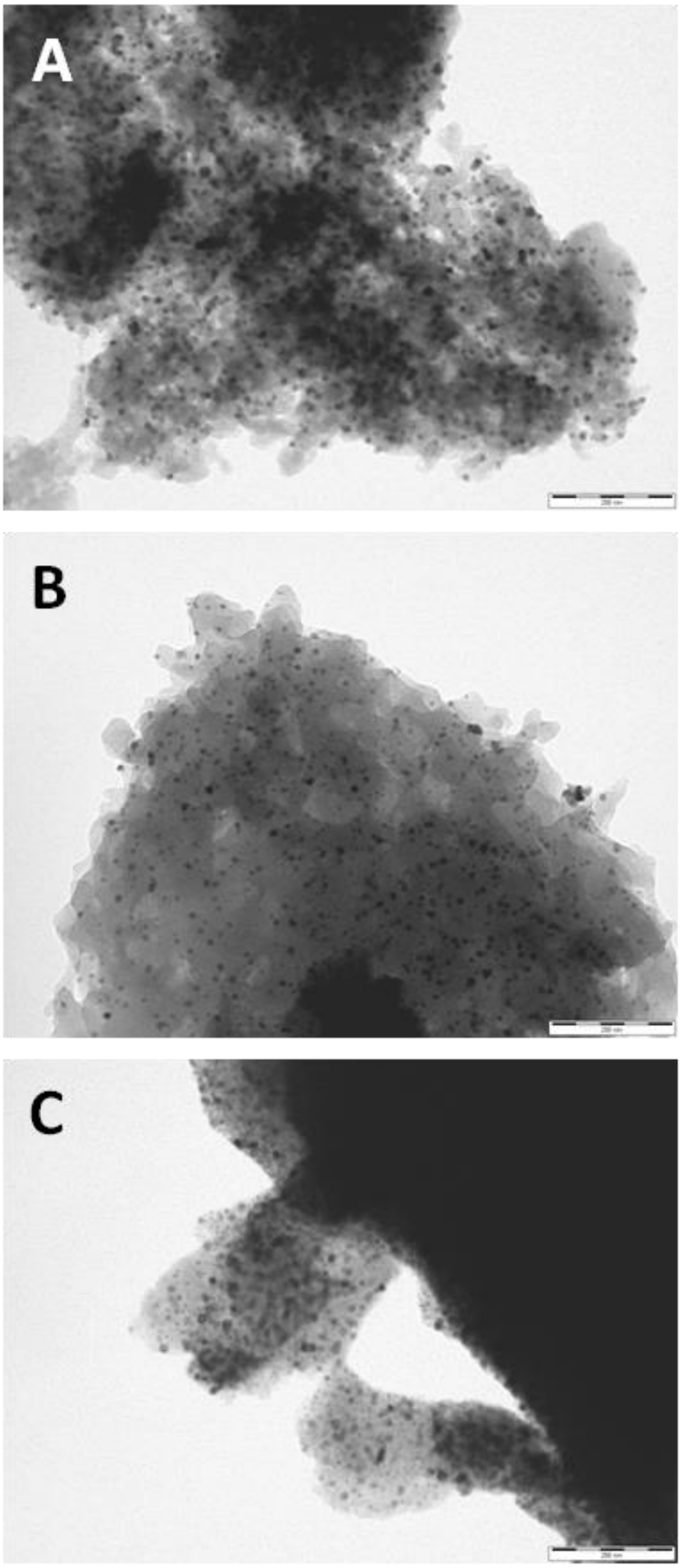

Figure 5.7 TEM images of (A) AA-SLOW, (B) AA-MEDIUM and (C) AA-FAST.

Transmission electron microscopy (TEM) images were used to determine whether the formation of PdNPs had occurred within the alginic acid supports (Figure 5.7). (TEM images of Pd/C can be seen in Appendix 3.) Images showed there was an even distribution of particles within the support after carbonisation irrespective of heating rate. The observed diameters (measured from the TEM images) were between 2 – 20 nm which is comfortably within the nano size range confirming these particles are indeed PdNPs. Whilst particles measuring < 2nm in diameter may be present within the materials it was not possible to visualise them using a standard TEM instrument.

The absence of large NPs within the alginic acid supports is an advantage and indicates that the PdNPs are stable within the support and significant NP agglomeration is being inhibited.

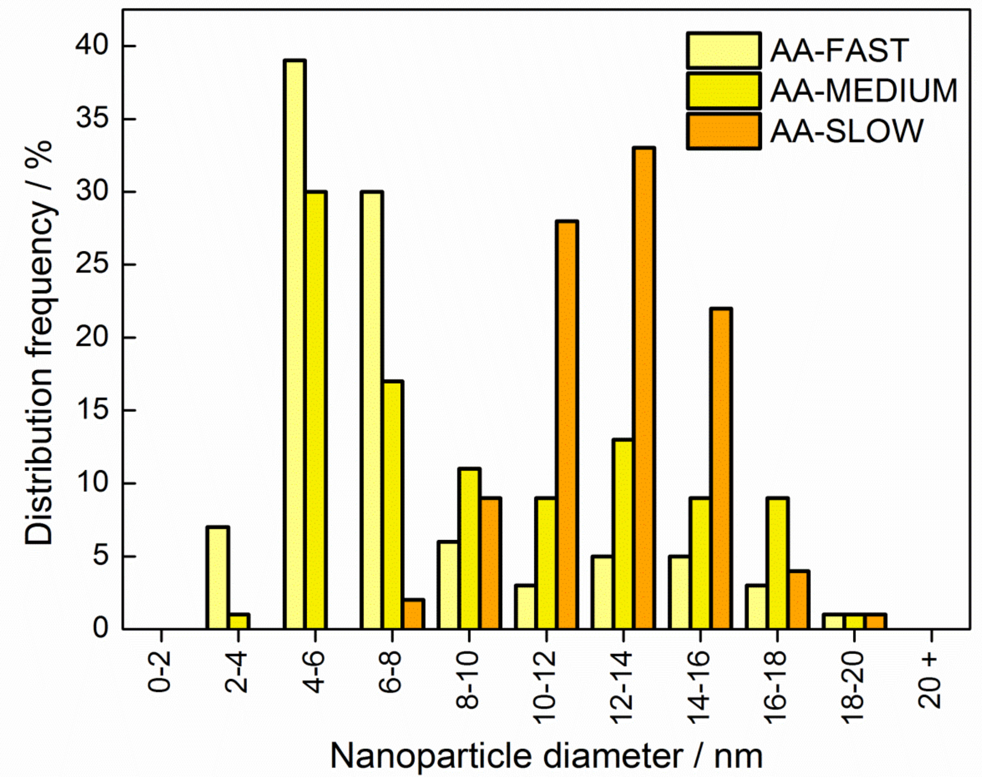

Figure 5.8 Nanoparticle size distributions for AA-SLOW catalyst.

Figure 5.8 shows the distribution of NP size within the different alginic acid supports. It appears that faster heating rates result in an increased distribution of NP size. For AA-FAST and AA-MEDIUM NP diameters are distributed across the whole size range observed. The distribution is also skewed towards smaller NPs with the average NP diameter of AA-FAST and AA-MEDIUM calculated as 7 and 9 nm, respectively. AA-SLOW has a more limited range of NP sizes (6 – 20 nm) with a more Gaussian distribution and an average particle diameter of 13 nm.

The higher proportion of larger NPs within AA-SLOW could be a result of a good pore network being maintained during heating of the AA+Pd allowing for NPs to shuttle around the alginic acid support when heated. The collapse of the pore structure in AA-FAST and AA-MEDIUM could likely trap particles and keep them separated within the support resulting in a higher number of small particles. If this has occurred it is expected that catalytic activity of these materials will be restricted as the NPs are not easily accessible during reactions.

5.2.3 Catalytic activity of alginic acid + palladium catalysts & comparison with commercial catalyst

To compare the different catalysts effectiveness their activity in the Heck reaction of iodobenzene with methyl acrylate was examined (Figure 5.9).

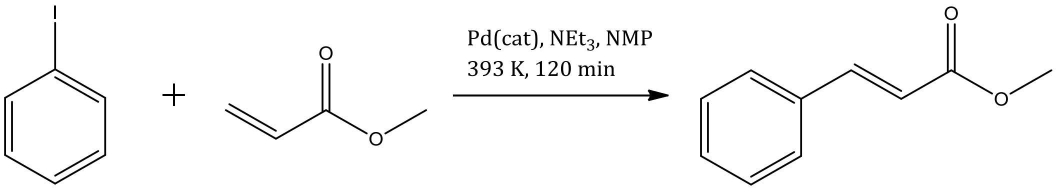

Figure 5.9 Reaction scheme for Heck reaction used to test catalyst activity.

To ensure that the results from the reactions were directly comparable, the amount of palladium was kept constant for each material throughout the work. The reactions containing each catalyst were allowed to react for 120 minutes and during this time samples were taken at specific time intervals in order to monitor the rate at which the reaction was proceeding. The results of this analysis are shown in Figure 5.10 (a). The results showed that AA-SLOW was the most active catalyst achieving a yield of 86%, AA-MEDIUM only reached a 28% yield whilst AA-FAST failed to react at all within the time the reaction was monitored. A blank reaction using expanded alginic acid was also carried out (results not shown) which also failed to react.

During the reaction, the palladium concentration in solution was also monitored in order to determine if palladium leaching from the catalytic support was taking place, this data is shown in Figure 5.10 (b). The results showed that as the reaction proceeded increasing amounts of palladium was being leached into the system. It is interesting to see that for AA-FAST where no reaction took place no palladium leaching occurred.

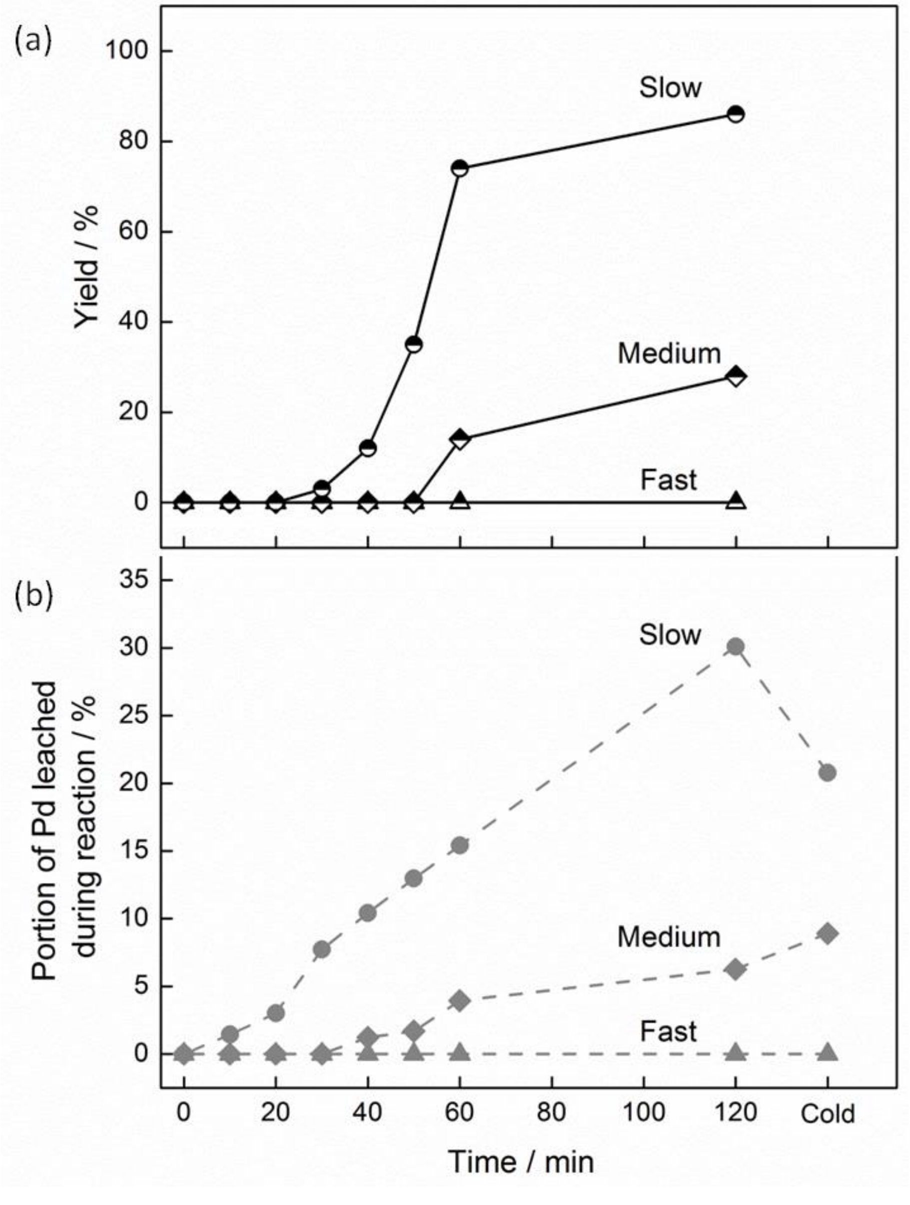

Figure 5.10 Comparison of (a) rate of reaction and (b) palladium leaching for alginic acid catalysts prepared at slow, medium and fast heating rates.

Figure 5.11 shows the data achieved for Pd/C in the same reaction. This catalyst reacted notably faster than the AA catalysts, reaching 71% yield in 20 minutes. Although the overall yield for Pd/C was lower than AA-SLOW, the best of the AA catalysts, achieving only 75% conversion within 120 minutes. Analysis of the palladium leaching from the support, also shown in Figure 5.11, was drastically higher than the AA catalysts, reaching a maximum leaching of 67% compared to 30% for AA-SLOW, this leaching also began earlier in the reaction and took place faster.

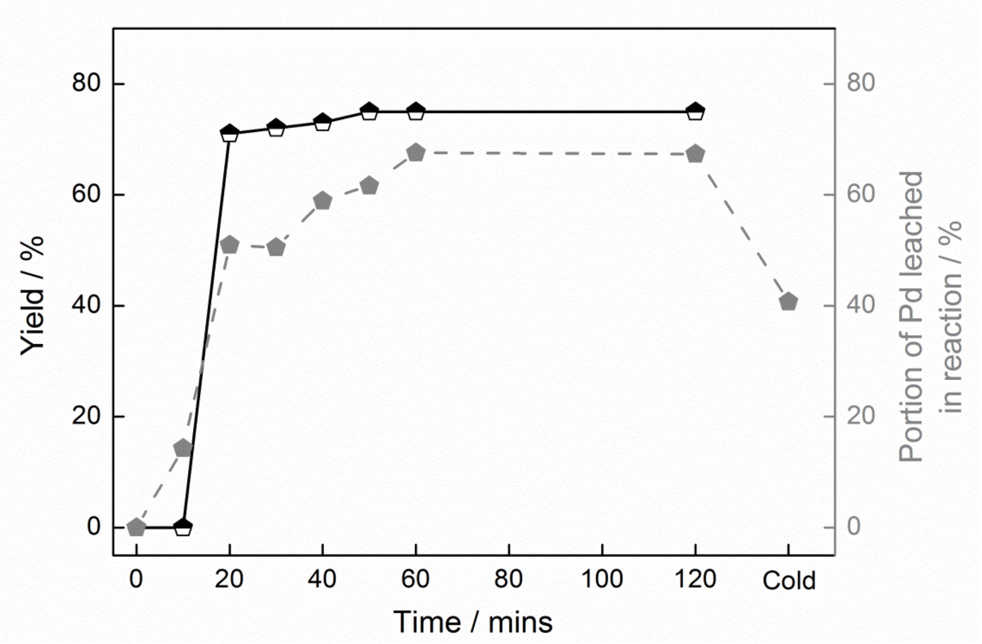

Figure 5.11 Rate of reaction and palladium leaching for Pd/C.

What these results indicate is a potential correlation between the extent of palladium leaching and the rate at which the Heck reaction is occurring. This result is not unusual and many previously published studies using PdNPs have also demonstrated this relationship.(*257-260*)

Currently, it is the widely acknowledged theory that PdNPs behave as a form of reservoir of palladium and during a reaction molecular palladium complexes are released into the reaction medium. It is these leached species that participate in the reaction rather than the NPs themselves.(*260*) The accepted mechanism involves three steps, illustrated in Figure 5.12 and described as follows:(*261*)

1. Oxidative addition of the aryl halide substrate to the surface of the PdNP.
2. Leaching of Pd$^{(II)}$ molecular species from the NPs that enter the catalytic cycle. (A diagram of the catalytic cycle for the Heck reaction can be found in Appendix 3.)
3. Reforming of nanoparticles at the end of the reaction.

Examination of the results for AA catalysts and Pd/C show that the reactions are starting after an induction period. Reetz *et al.* has suggested that this induction period is in agreement with step 1 in the above mechanism taking place, as this is the time taken for the formation of metallic colloids within the reaction medium.(*259*)

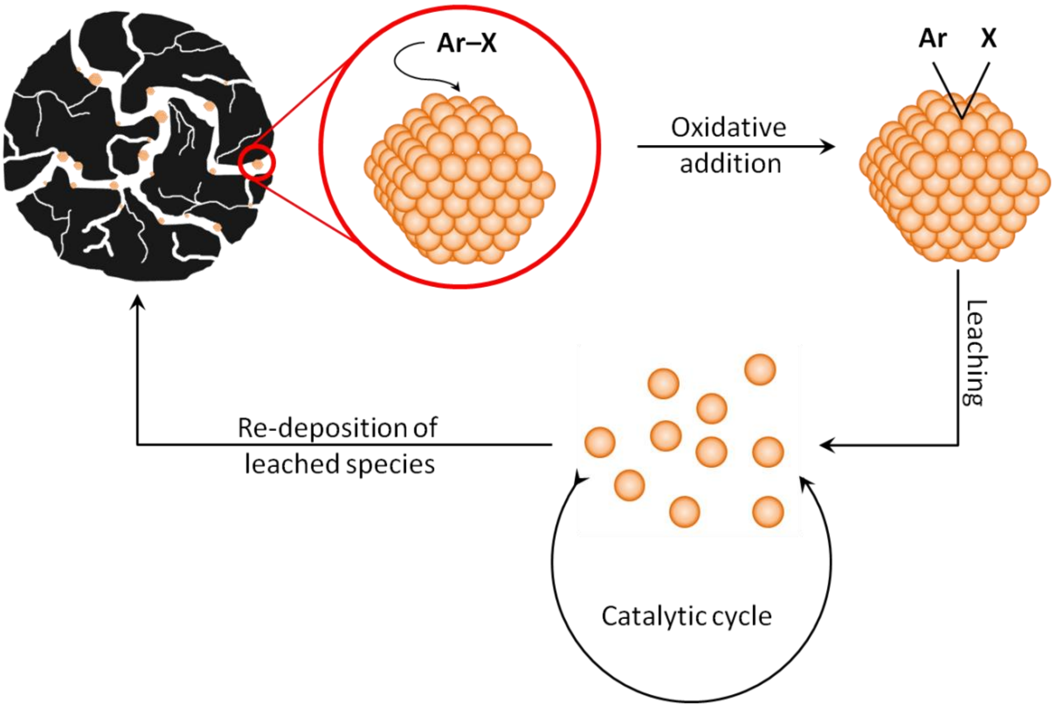

Figure 5.12 Schematic representation of accepted mechanism for Pd NP behaviour in Heck reactions.

The shorter induction period shown by Pd/C compared with the AA catalysts could potentially be explained by the fact that Pd/C has the largest surface area and pore volume of all of the catalysts tested. This will enable the faster leaching of active palladium species allowing the reaction to start earlier.

This also agrees with the results seen for the three AA catalysts where the material with the largest surface area and pore volume, AA-SLOW, gives the highest levels of palladium leaching. Whereas, with AA-FAST (that has minimal porosity and surface area) no palladium leaching is observed, resulting in no reaction taking place. Therefore, when designing supports for PdNPs significant porosity may be beneficial for facilitating the first step in the mechanism (Figure 5.12) and could lead to a high overall catalytic activity of the material.

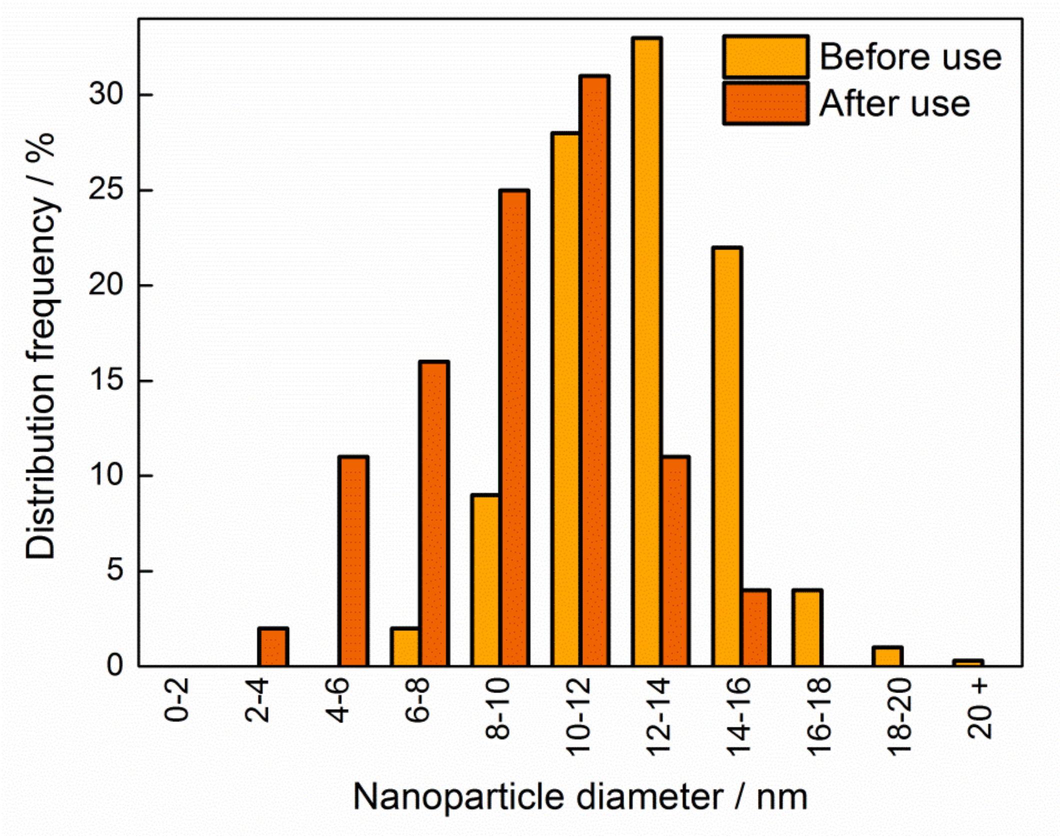

Figure 5.13 Nanoparticle size distributions of AA-SLOW before and after use.

A detailed investigation of the NP size distribution of AA-SLOW after use (Figure 5.13) demonstrates a shift in size towards smaller NPs with the average size decreasing from 13 nm before use to 9 nm after use. This change could be linked to the leaching of palladium species from the support during the reaction as described in step 2 of the mechanism for PdNP behaviour.

Analysis of the leached palladium concentration in solution after the reaction mixtures had cooled to room temperature was carried out for all of the catalysts. For AA-SLOW and Pd/C the palladium concentration was seen to decrease to 21% and 41%, respectively. This drop in concentration could be due to step 3 of the mechanism occurring and the palladium species being re-deposited or re-adsorbed back on to the supports once the reaction was over. Another cause of this NP shrinkage (Figure 5.13) could be due to the re-deposition of palladium back onto the support where it forms new NPs rather than rejoining already formed NPs present on the support which is likely to cause an increase in NP size.

Table 5.6 Comparison of yields for AA-SLOW and Pd/C across a range of C-C bond forming reactions.

Reaction	Reagents	Yield [%]	
		AA-SLOW	Pd/C
Heck	Iodobenzene + Styrene	54	67
Suzuki	Iodobenzene + Phenylboronic acid	47	44

The activity of AA-SLOW, the best AA catalyst, was further compared with the activity of Pd/C for two other C-C coupling reactions: the Heck reaction of iodobenzene with styrene and the Suzuki reaction of iodobenzene with phenylboronic acid (Table 5.6). For the Suzuki reaction AA-SLOW showed better activity than Pd/C, successfully giving a higher yield. Unfortunately this was not the case for the second Heck reaction however this could be improved with further work.

Overall, AA-SLOW was shown to be an efficient catalyst for the three reactions tested. The most exciting result is the lower levels of leaching seen for AA-SLOW compared with Pd/C meaning that less palladium is being lost from the catalyst support during each reaction.

5.2.4 Formation & characterisation of seaweed + palladium catalyst

The species of seaweed used for this study was *Laminaria digitata* (a brown alga with the common name Oarweed). This species was chosen as it grows in the North Atlantic and is commonly found around the British coastline making it readily available for this work.(*262*)

Preparation of the catalyst was carried out using a similar method as used for the formation of the alginic acid catalysts. First the seaweed was dried and ground to form a fine, brownish powder. As with the alginic acid catalysts the impregnation of the seaweed was carried out via adsorption of the metal species. To a known quantity of seaweed ethanol was added to form a suspension. Palladium acetate was dissolved in a small portion of ethanol and added to the seaweed ethanol suspension (the concentration of palladium was approximately 1% based on the amount of seaweed used). The solution was stirred until all of the palladium had been adsorbed. The impregnated seaweed was then recovered via filtration and dried.

As is expected for a complex natural material such as seaweed the XPS analysis reveals a wide variety of species are present in seaweed, including (but not limited to): C, O, N, S, Na, Mg, Ca, K and Si. Deconvolution of the C 1s, O 1s and Pd 3d XPS spectra for the two materials are shown in Figure 5.14 and peak assignments are given in Table 5.7. Interestingly, upon addition of palladium to the seaweed there are dramatic changes visible to the chemical states of the organic species.

The most significant change is the shift in the oxygen species from a mixture of CO, C-O and COO in SW to only C=O being seen in SW+Pd. This appearance of carboxylate species after impregnation is also seen for AA+Pd although not to the same extent. One potential explanation for this difference between the alginic acid and seaweed materials is that palladium adsorption is occurring more to the surface of the seaweed rather than being diffused into the interior of the structure as is proposed for alginic acid. This leads to more significant changes to the surface of the support being observed.

This hypothesis is supported by agreement between the concentration of palladium seen using XPS analysis (1.4%) and the concentration determined by ICP analysis (1.4%). Whereas, for AA+Pd XPS analysis showed only 0.30% palladium compared to the actual concentration of 0.86% (ICP). Analysis of the Pd 3d spectra for SW+Pd shows a high proportion of PdO and Pd$^{(II)}$ being present with only a very small amount of Pd$^{(0)}$ (Figure 5.14 (f) and Table 5.7).

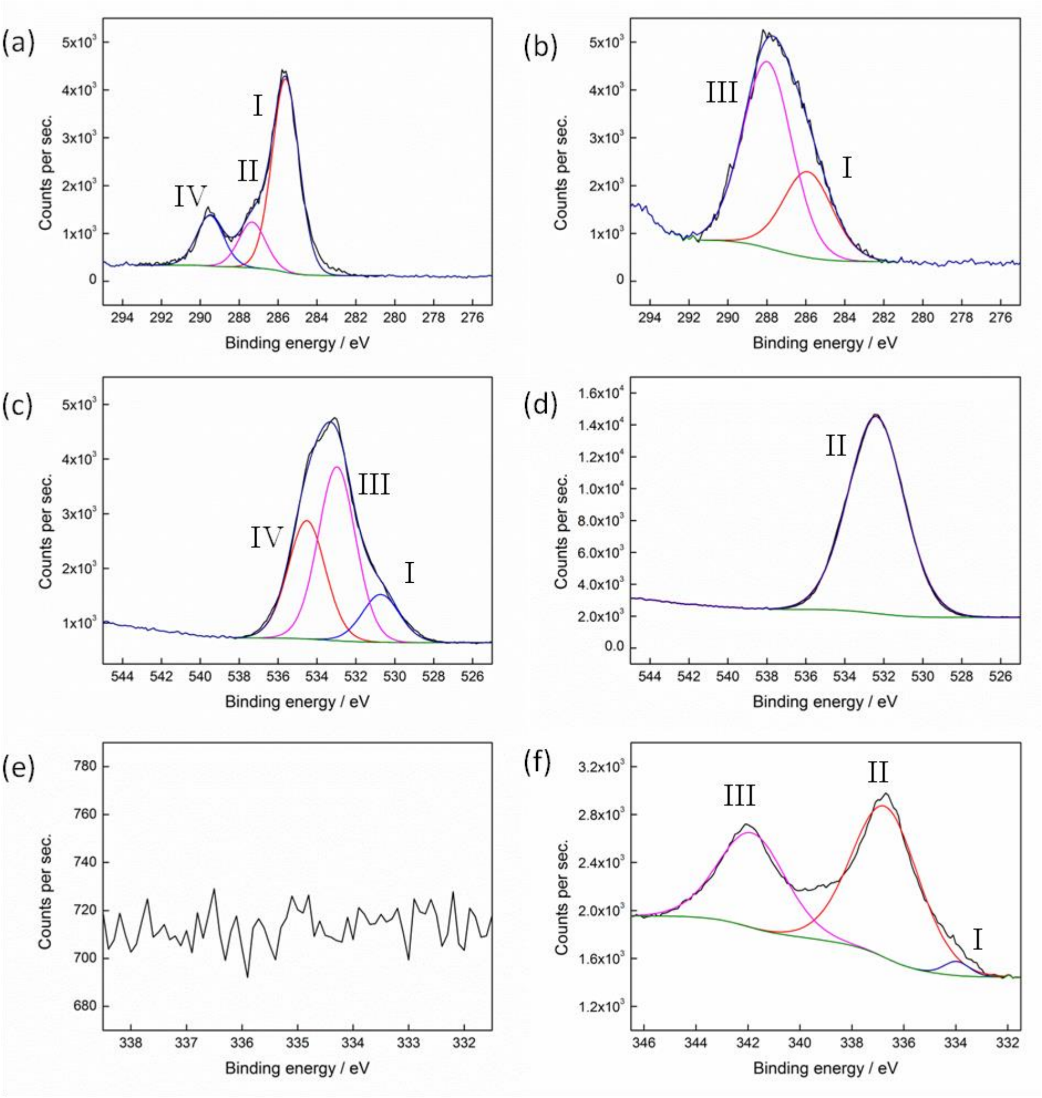

Figure 5.14 XPS spectra showing: carbon spectra (a) seaweed and (b) seaweed + palladium, oxygen spectra (c) seaweed and (d) seaweed + palladium and palladium spectra (e) seaweed and (f) seaweed + palladium.

Table 5.7 Composition of seaweed (SW) and seaweed + palladium (SW+Pd) components from XPS spectra.

	Peak	BE [eV]	Chemical State	%		
				SW	SW+Pd	SW-Carbonised
Carbon	I	285.5 ± 0.2	C-C (ring)	67	32	62
	II	287.3 ± 0.2	C-O	18	-	-
	III	288.4 ± 0.2	C=O, O-C-O	-	68	38
	IV	289.5 ± 0.2	COO	17	-	-
Oxygen	I	531.2 ± 0.6	CO	14	-	25
	II	532.5 ± 0.2	C=O	-	100	75
	III	533.0 ± 0.2	C-O	51	-	-
	IV	534.0 ± 0.5	C-O (in COO)	35	-	-
Palladium	I	334.3 ± 0.2	$Pd^{(0)}$	-	2	19
	II	336.7 ± 0.2	PdO	-	60	70
	III	341.8 ± 0.2	$Pd^{(II)}$	-	38	12

As with the alginic acid catalysts the SW+Pd was carbonised at 300 °C to stabilise the support for use under a range of reaction conditions. Microscopy analysis of the heated seaweed (SW-Carbonised) was carried out to give an idea of the textural properties of the resulting material. SEM images of SW-Carbonised at different magnifications are shown in Figure 5.15. The seaweed is visually very different to the alginic acid. Where the alginic acid appears quite compact and smooth the seaweed is much more interesting and intricate with a more open structure consisting of many folds and layers.

As for the alginic acid catalysts, XPS analysis of heated seaweed showed changes in the chemical states of species present (Figure 5.16). However, in contrast to AA-Carbonised the palladium XPS spectra of SW-Carbonised showed there was an increase in the reduced palladium species ($Pd^{(0)}$) and a loss of $Pd^{(II)}$ after heating (Figure 5.16 (c) and Table 5.7). It is unclear why this is occurring although it could be attributed to the different textural structure of the seaweed compared to alginic acid which allows the oxygen released during heating to escape the material more easily and therefore reducing the likelihood it will interact with the palladium particles.

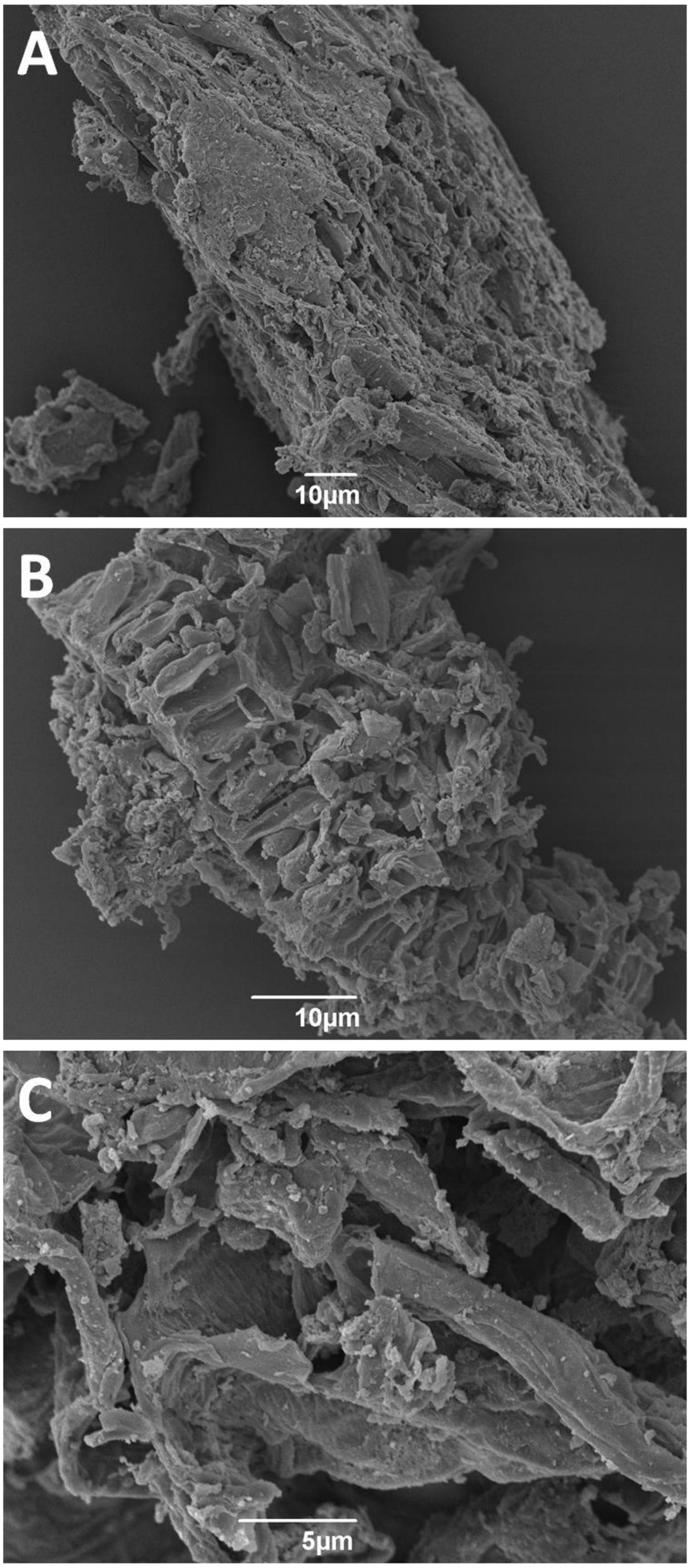

Figure 5.15 SEM micrographs SW-Carbonised at (A) x1000, (B) x2000 and (C) x4500 magnification.

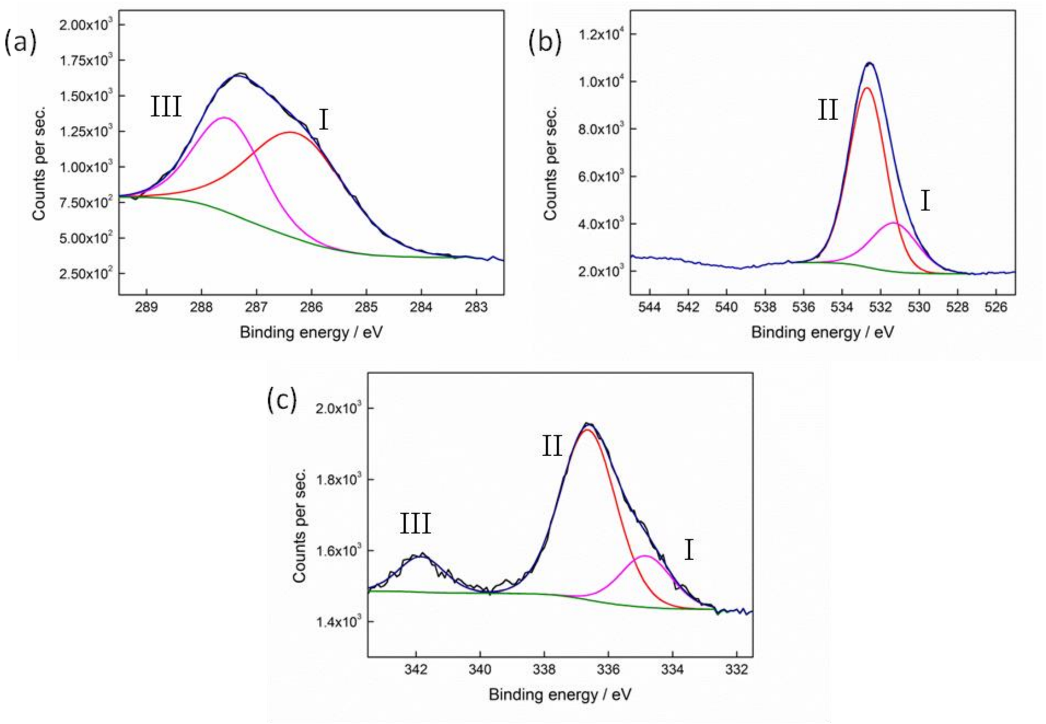

Figure 5.16 XPS spectra of carbonised seaweed + palladium (SW-Carbonised) showing (a) carbon, (b) oxygen and (c) palladium.

Clear TEM images of the seaweed were difficult to obtain due to its open, 3-dimensional structure however it was still possible to elucidate the presence of palladium particles within the SW-Carbonised (Figure 5.17 (a)). Measurement of the particles was carried out from the TEM images. A plot of the distribution of the particles present showed that they fell into two distinct size ranges; 2 – 12 nm and 14 – 20+ nm with the majority (42%) of the observed particles between 4 – 6 nm (Figure 5.17 (b)).

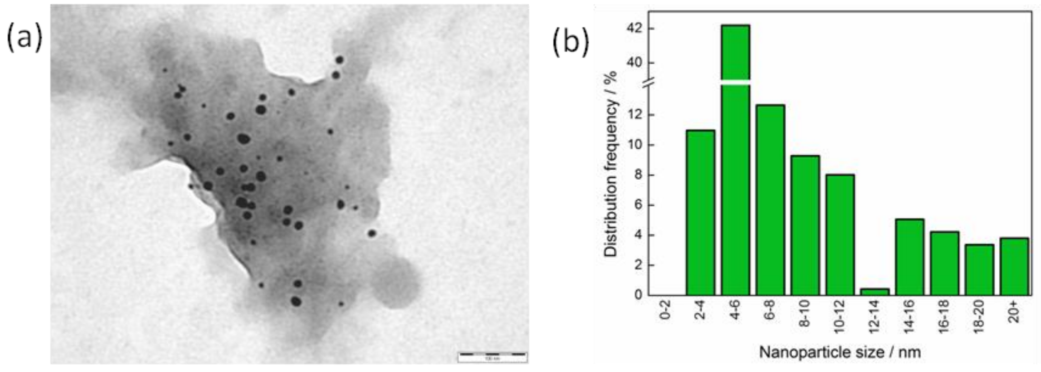

Figure 5.17 (a) TEM image of SW-Carbonised and (b) nanoparticle size distribution.

5.2.5 Catalytic activity of seaweed + palladium catalyst

The reaction of iodobenzene and methyl acrylate used in the alginic acid studies (Figure 5.9) was also used to determine the catalytic activity of SW-Carbonised material. The reaction was monitored over 120 minutes and results are shown in Figure 5.18.

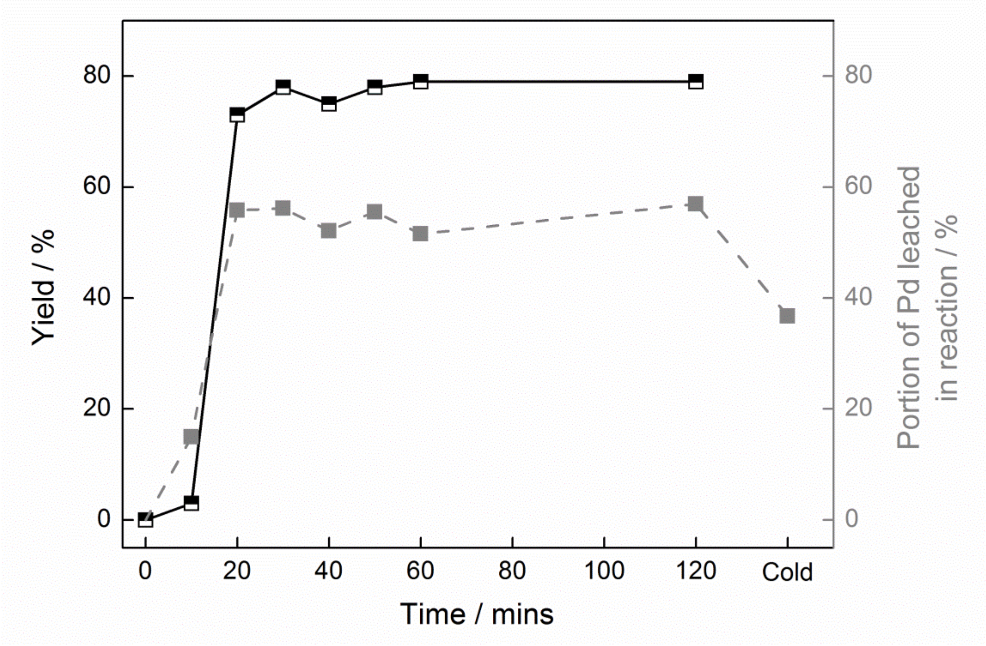

Figure 5.18 Rate of reaction and palladium leaching for SW-Carbonised catalyst.

The reaction trace of SW-Carbonised appears almost identical to that of Pd/C: As was seen for Pd/C the reaction of SW-Carbonised occurs very quickly, considerably faster than the alginic acid catalysts, with a 75% yield being achieved after 20 minutes. There is also considerable palladium leaching (up to 57%) taking place during the reaction. SW-Carbonised dose offer a slight improvement over Pd/C in the amount of palladium remaining in solution after the reaction has cooled is lower, 37% compared to 41% for Pd/C, although overall these catalysts are effectively directly comparable in their performance. A blank reaction using seaweed was also carried out (results not shown) which failed to react.

5.2.6 Reusability comparison of alginic acid, seaweed and commercial supported palladium catalyst

One of the main advantages of using heterogeneous or supported catalysts over homogeneous catalysts is the ease at which the materials can be recovered and reused in subsequent reactions.(*263*) Therefore, it was important to determine if it was possible to recycle the alginic acid and seaweed catalysts used in this chapter.

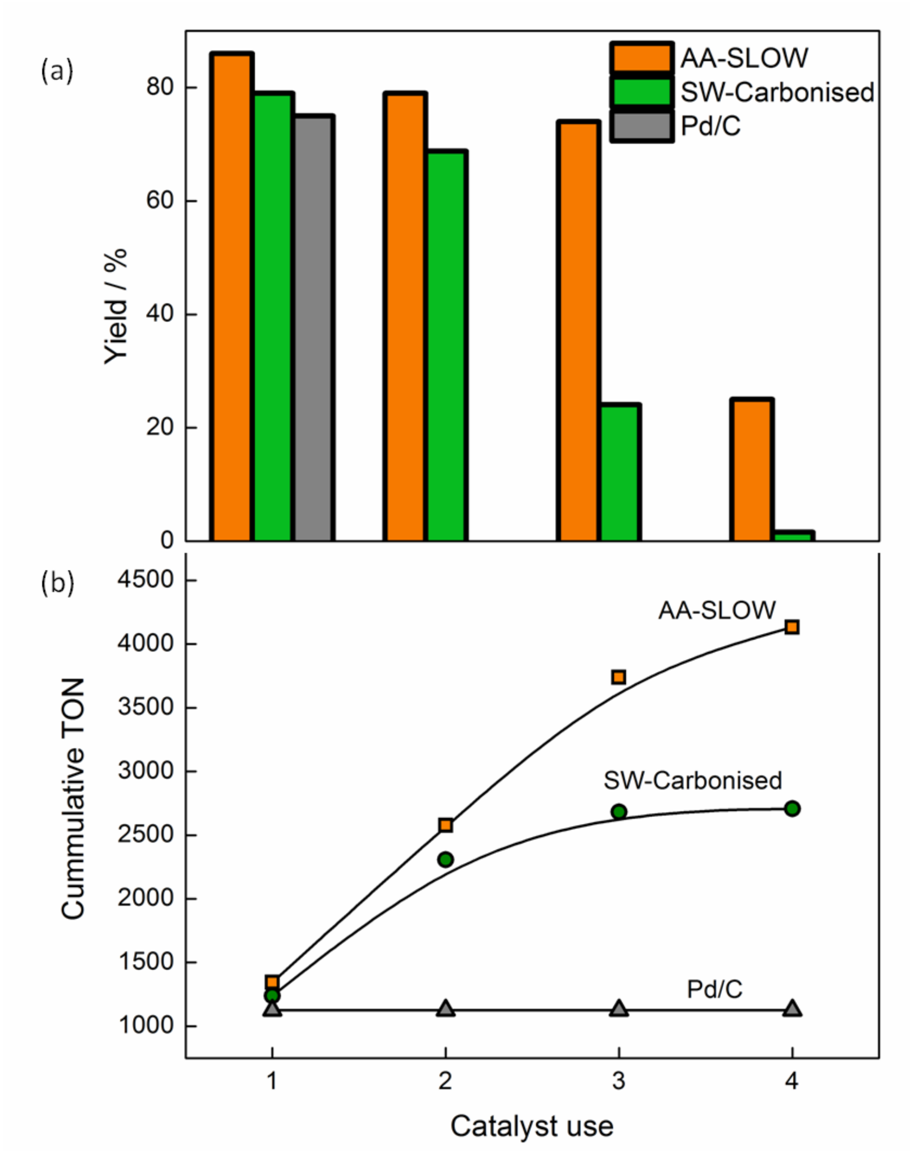

Figure 5.19 (a) Reuse of catalysts AA-SLOW, SW-Carbonised and Pd/C for the reaction of iodobenzene and methyl acrylate and (b) cumulative turnover number (TON) achieved.

In order to do this fresh catalyst was used for the Heck reaction of iodobenzene and methyl acrylate (Figure 5.9) the reaction was heated for 120 minutes before it was stopped and allowed to cool to room temperature. The reaction mixture was then centrifuged resulting in the solid catalyst collecting in the bottom of the centrifuge tube. It was then possible to decant off the reaction solution which could be analysed to determine the yield of the reaction. The catalyst was then washed out of the tube and into a fresh reaction vessel using NMP, fresh reagents were then added and a second reaction was allowed to proceed. This process was repeated up to four times for each catalyst and the results are displayed in Figure 5.19.

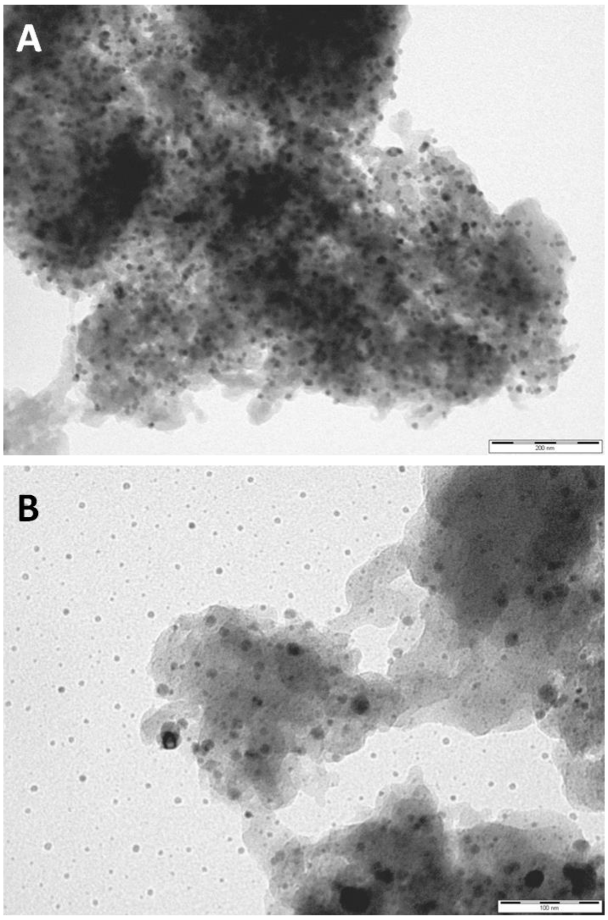

Figure 5.20 TEM images of AA-SLOW showing nanoparticles (A) before and (B) after use.

As the results show, AA-SLOW was successfully reused three times without any significant loss in yield, taking into account slight loss of catalyst on recovery. Unfortunately, when used a fourth time the yield drop significantly to only 25%. This performance compares well to previous work carried out by Budarin *et al* investigating PdNPs supported on starch.(*82*) The SW-Carbonised catalyst was not as successful only being used for two reactions before the yield dropped to 24%. However both materials performed considerably better than Pd/C which could only be used once and failed to react further which renders the use of a supported catalyst worthless.

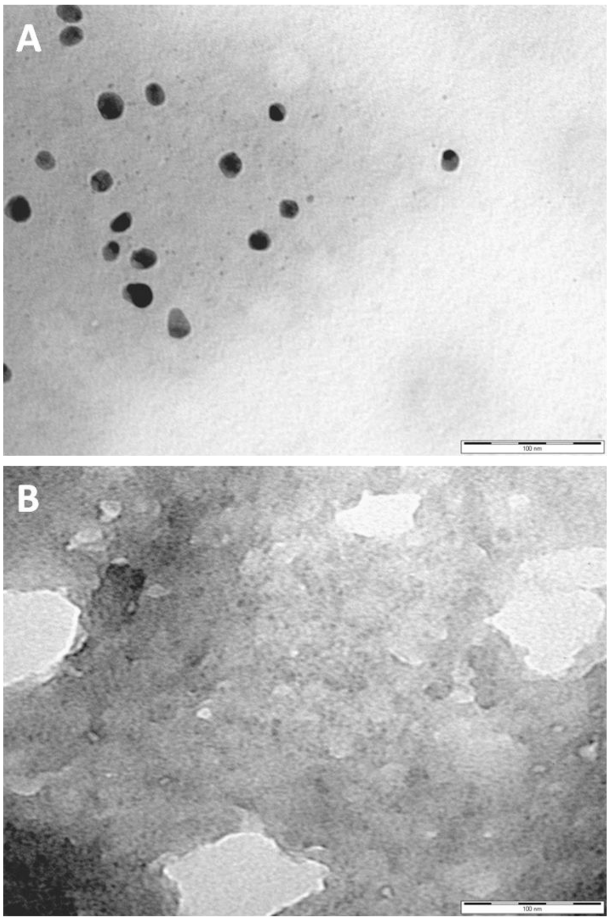

Figure 5.21 TEM images of SW-Carbonised showing nanoparticles (A) before and (B) after use.

Included in Figure 5.19 are the cumulative turnover numbers (TON) achieved for each of the materials. This enables a quantitative comparison of their performance over four reactions. The cumulative TON achieved for AA-SLOW, SW-Carbonised and Pd/C were ca. 4100, 2700 and 1100 respectively. These values clearly emphasise the impressive performance of AA-SLOW compared to the conventional material, Pd/C.

Continued leaching of the palladium from the catalysts is the most likely cause of the drop in activity with use. Even though some of the palladium is redeposited back onto the supports after the reaction cools there are still considerable losses made. TEM analysis of AA-SLOW clearly shows leached PdNPs present around the material after use, also the amount of NP visible in the solid material is considerably less than for the fresh catalyst (Figure 5.20). Images of SW-Carbonised show that there is no clearly visible palladium remaining in the seaweed after multiple uses (Figure 5.21).

5.3 Conclusion

In conclusion the direct synthesis of palladium catalysts using alginic acid and seaweed supports has been successfully achieved. For the alginic acid catalysts it was shown that the heating rate used during the stabilisation of the material had a direct effect on the activity of the catalyst. The materials prepared at faster heating rates, AA-MEDIUM and AA-FAST, were much slower to react than the material prepared at a slower heating rate, AA-SLOW. Over 120 minutes AA-SLOW achieve an 81% yield for the Heck reaction of iodobenzene with methyl acrylate.

The seaweed supported catalyst also showed excellent catalytic activity. It behaved in a similar manner to Pd/C, showing comparable rates of reaction, overall yield and palladium leaching. The seaweed and alginic acid catalysts were successfully reused 2 and 3 times respectively, which was an improvement over Pd/C which was not reusable. Overall, this work has shown that active nanoparticles of palladium could be produced using sustainable raw materials and green chemical processes. To the best of the authors knowledge this is the first time alginic acid and seaweed have been employed in this way.

Chapter 6

Nano-palladium catalysts directly from plants

Aspects of the work presented in this chapter have appeared in:

Interview for Chemistry and Industry “Precious plants”, February 2013

Oral presentation given at 4th International IUPAC Conference on Green Chemistry, Iguassu Falls, Brazil, August 2012

Oral presentation given at 4th NORthern Sustainable Chemistry meeting (NORSC), York, UK, October 2012

Growth of Arabidopsis and subsequent palladium impregnation, drying and grinding of the plants used in this chapter was carried out by Dr. L. Rylott, CNAP, Department of Biology, University of York, York, YO10 5DD.

Chapter 6.

Nano-palladium catalysts directly from plants

6.1 Introduction

The use of plants to capture specific elements, usually metals, from contaminated soils or aqueous waste has long been recognized as a potential method for environmental clean-up.(*227, 264*) The advantage of using this technique, known as phytoremediation, over adsorption is that metal can be recovered from solid media as well as liquid media. There has only been a limited number of studies into platinum group metals (PGMs) accumulation by plants, with most work focusing on the capture of other metals, such as, nickel, zinc and cadmium.(*265, 266*) Whilst efforts to use plants as a tool for remediation of contaminated areas has demonstrated some promise, to date, no research has fully realized the possible value that could be achieved from this process.

Manufacture of metallic nanoparticles (MNPs) by plants as a viable, and greener, alternative to current physical and chemical production procedures for MNPs is becoming a highly popular field.(*93*) Previous work in the use of plant extracts, algae and bacteria to form bio-Pd nanoparticles has shown some promise but, there are significant limitations due to complex and lengthy production methods.(*93, 267-271*) Other earlier work investigating greener MNP production methods has also commonly attempted extraction of MNPs from biomass using methods such as: freeze-thawing, burning of the plant, chemical leaching and osmotic shock. However, these activities are laborious, energy intensive and can destroy the NP structure thus interfering with the desired nano-material properties.(*93, 272*)

To overcome these problems, exploration of living plants to produce MNPs and directly use these as chemical catalysts without extraction is required. In this chapter, preliminary work investigating the efficient uptake of palladium ions by *Arabidopsis thaliana.* Subsequent plant mediated reduction from $Pd^{(II)}$ to $Pd^{(0)}$ and formation of nanoparticles inside the plant tissues is demonstrated. The in situ catalytic function of these palladium nanoparticles (PdNPs) is shown through their ability to catalyze a range of C-C coupling reactions. This is the first time that PdNPs have been synthesized and used in this way. It is important to mention that this work was predominantly carried out as a "proof-of-concept" study and therefore solutions of palladium synthesised in the laboratory were used rather than "real" waste samples. It is hoped however that this work will later lead on to the use of waste sources of palladium as detailed in Chapter 4.

6.1.1 Aims

The aims of the work presented herein:

- To investigate the potential of *Arabidopsis thaliana* to uptake palladium and form metallic nanoparticles when grown in a hydroponic system.
- To optimise the processing of the metal containing plant material for the formation of stable catalysts.
- To demonstrate the efficacy of the plant derived catalysts towards Heck and Suzuki reactions.

6.2 Results and Discussion

6.2.1 Growing the plant catalysts – Pd uptake and nanoparticle formation by *Arabidopsis thaliana* (L.)

The preparation of Pd plant materials utilized techniques and methodologies adapted from previously published work by Sharma *et al.* for the synthesis of gold nanoparticles.(*273, 274*) For the work presented here first three-week-old, liquid culture-grown *Arabidopsis thaliana* (L.) (Arabidopsis) ecotype Col0 were dosed with an aqueous solution of potassium tetrachloropalladate (II) over a period of 24 hours. A liquid culture was chosen over a soil-based system in order to easily control accurate dosing of metals (Figure 6.1). This method also allows the plant material to easily be washed clean from the growth substrate after dosing, thus reducing contamination with non-plant material. After 24 hours from the time of dosing with palladium the plants appeared brown and wilted (Figure 6.2), and were removed from the growth medium, washed, dried and ground to a powder.

Figure 6.1 Arabidopsis being grown hydroponically using a liquid culture.

Transmission electron micrograph (TEM) images of sections of the plant showed that within three hours of dosing, the plants had successfully formed well-dispersed, spherical NPs with a mean profile diameter of 3 nm (Figure 6.2 C and D). Increasing concentrations and diameters of NPs were observed over time, with larger particles up to 32 nm formed by the end of the incubation (Figure 6.2 C). NPs were distributed evenly adaxially to abaxially across the leaf (see Appendix 4, supplementary figure 4.1), predominantly concentrated in the wall and apoplast regions of cell junctions. Inductively coupled plasma (ICP) analysis of palladium concentration in the plants with time showed the plants reached maximum palladium concentration after 18 hours of exposure (Figure 6.2 D & Appendix 4, supplementary figure 4.2).

Analysis using X-ray Photoelectron Spectroscopy (XPS) on the dried Pd-plant material confirmed that the observed NPs were palladium deposits. The spectra showed two chemically distinct spin-orbit pairs in the Pd 3d levels, centred at 334.5 eV and 339.7 eV binding energies, these peaks were not present in the blank plant (Figure 6.3 (g) and (h) and Table 6.1). The lower binding energy corresponds to fully reduced Pd$^{(0)}$ nanoparticles, whilst the higher binding energy peak is due to unreduced Pd$^{(2+)}$ ions.(*275*)

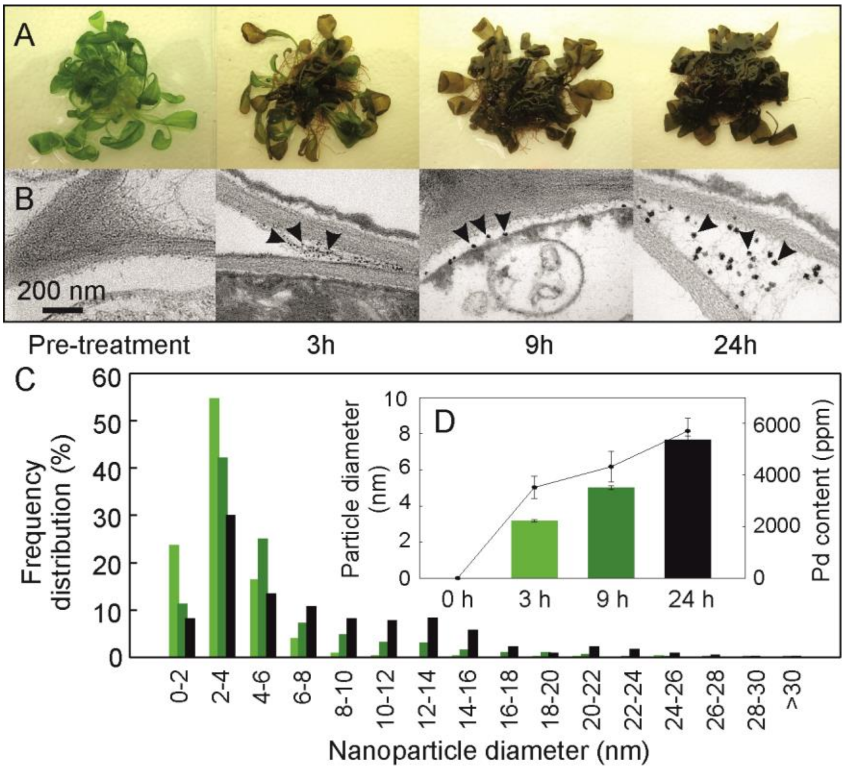

Figure 6.2 Pd uptake and PdNP formation in Arabidopsis (A) 3-week-old plants treated with potassium tetrachloropalladate (B) TEM showing accumulation over time of larger PdNPs in cell wall corners (C) Distribution of NP sizes in leaf tissues at 3, 9 and 24 hours (D) Mean PdNP diameter and palladium concentration with time.

A comparison of the blank and Pd plant XPS spectra for carbon, oxygen and nitrogen showed no discernible change in the carbon or oxygen spectra upon addition of palladium to the plant (Figure 6.3). This was also noted by Pethkar *et al.* for the adsorption of gold by the fungus *C. cladopsorioides,* who suggested that a result such as this could indicate that the palladium is not interacting with the carbon or oxygen structures within the plant during uptake and PdNP formation.(*276*)

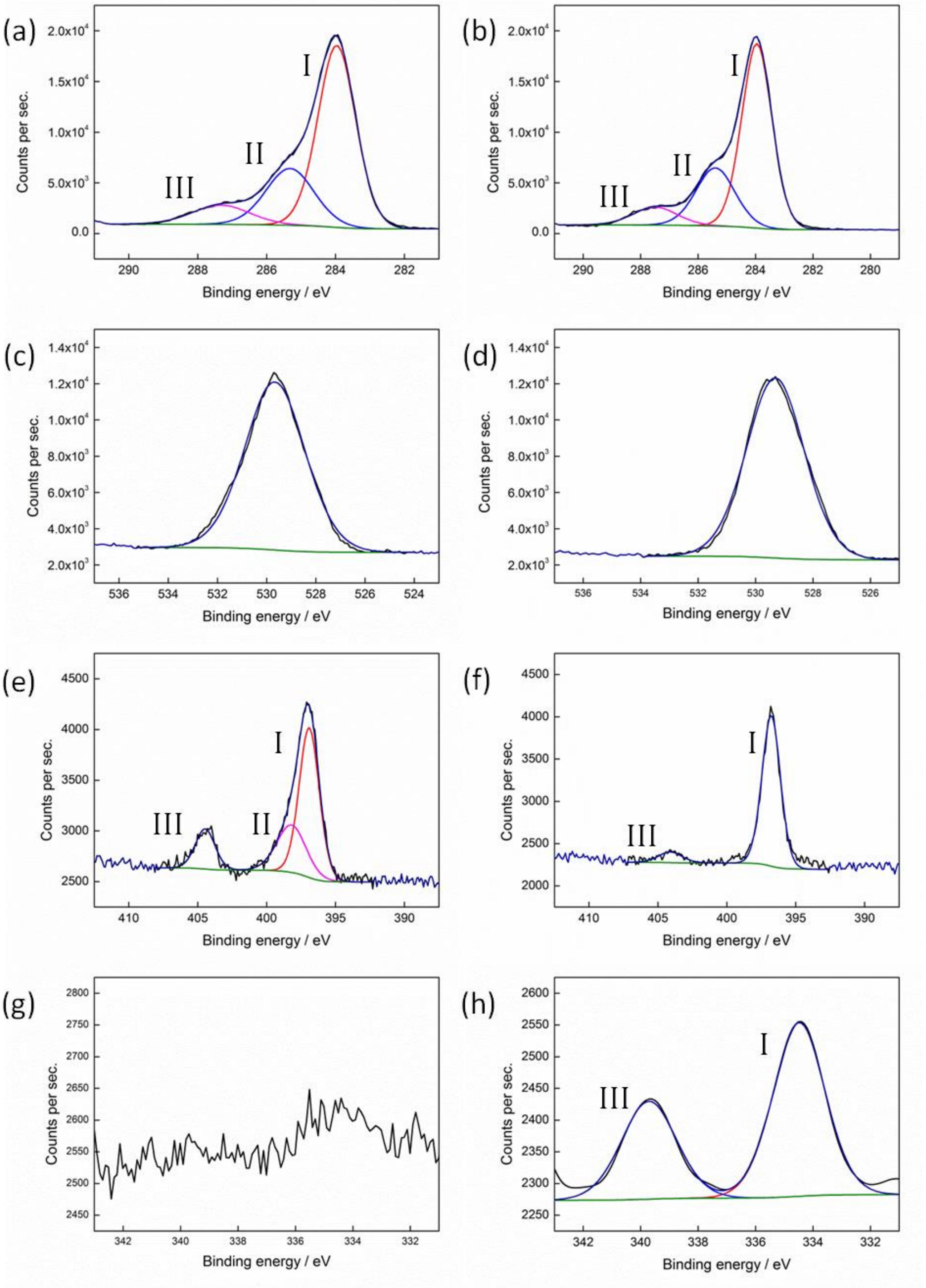

Figure 6.3 XPS spectra showing: C 1s (a) blank plant, (b) dried Pd plant, O 1s (c) blank plant, (d) dried Pd plant, N 1s (e) blank plant and (f) dried Pd plant and Pd 3d (g) blank plant and (h) dried Pd plant.

Table 6.1 Composition of chemical species present in blank plant and dried Pd plant from XPS spectra.

	Peak	BE [eV]	Chemical state	%	
				Blank plant	Dried Pd plant
Carbon	I	284.1 ± 0.2	C-C	64	64
	II	285.4 ± 0.2	C-C (Ar)[a]	26	26
	III	287.4 ± 0.2	C-O [a]	10	10
Oxygen		530.0 ± 0.5	CO	100	100
Nitrogen	I	396.8 ± 0.1	Cyano species	58	92
	II	398.2	Pyridine	15	-
	III	404.3 ± 0.2	N-oxide	27	8
Palladium	I	334.5	Pd$^{(0)}$	-	63
	II	336.8 ± 0.2	PdO	-	-
	III	340.0 ± 1.0	Pd$^{(2+)}$	-	37

[a] Could also possibly be attributed to some C-N.

Interestingly, a marked change in the nitrogen XPS spectra was observed between the two materials (Figure 6.3 (e) and (f)). For the blank plant three peaks with binding energies at approximately 396, 398 and 404 eV were seen. As detailed in Table 6.1 the peaks at 398 and 404 eV represent pyridine and N-oxide nitrogen type species, respectively, that are naturally present as part of complex structures within the plant, e.g. chlorophyll.(*277*) These peak are commonly seen when analyzing carbon rich, natural materials by XPS.(*278, 279*) The peak at 396 eV is less commonly seen and an examination of the literature has shown that it could be attributed to cyano nitrogen species.(*280*)

Further characterisation of the materials using infrared spectroscopy supports the observations made from the XPS spectra (Figure 6.4 and Table 6.2). The most obvious difference between the blank plant and the dried Pd plant is the loss of the sharp peak at 1381 cm^{-1} after dosing with palladium. This peak is attributable to C-N stretch within the material and its loss could be due to the loss of pyridine type nitrogen species seen in the XPS data.(*281*)

There are also slight changes in the N-H bend peak and the O-H and N-H "hump" in the infrared spectra which could also indicate further alterations occurring in the nitrogen species after palladium uptake.

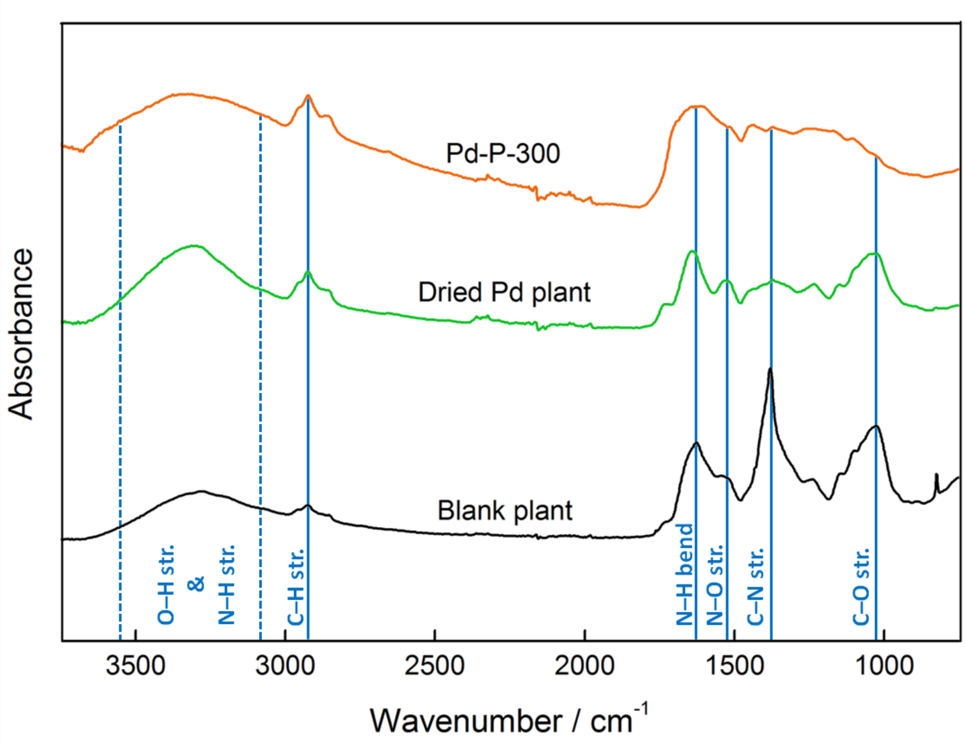

Figure 6.4 Infrared spectra for blank plant, dried Pd plant and carbonised plant (Pd-P-300).

Table 6.2 Major chemical constituents in the plant and their designated IR peaks.(*282*)

Wavenumber [cm^{-1}]	Designation	Major component of plant
≈ 1750	Ester	Cell wall pectin
≈ 1700 – 1600	Amide	Proteins
> 1500	Fingerprint	Carbohydrates

Plants such as Arabidopsis contain a large number of glucosinolates.(*283*) Glucosinolates are nitrogen and sulphur rich organic molecules bioderived by plants from glucose and amino acids.(*284*) The main role of these compounds within the plant is to act as a defence mechanism when the tissue of the plant is damaged or the plant is stressed. When this occurs the enzyme myrosinase is released by the plant, this enzyme hydrolyses the glucosinolate compounds to produce a range of potentially toxic cyanate and nitrile species (Supplementary Figure 4.3, Appendix 4).(*285, 286*)

The shift observed in the nitrogen species shown by the XPS analysis could potentially signify this defence mechanism occurring within the plant as the palladium is being adsorbed and transported through its structure. The loss of the pyridine and N-oxide peaks could be caused by the breakdown of glucosinolates leading to the increase in the cyano species peak as hydrolysis products are formed. This cannot be proved conclusively here; further analysis of the plant material using techniques such as ^{15}N solid state NMR could help to elucidate more evidence of whether this is taking place.

6.2.2 Carbonisation and further characterization of the plant catalysts

In order to provide an effective support for the PdNPs the dried Pd plant material was subjected to controlled carbonisation under nitrogen. This process resulted in the diminution of heteroatoms such as oxygen and hydrogen as volatile gaseous emissions. To determine the effect of carbonisation temperature on PdNP state and any potential effect this could have for catalytic activity, the dried Pd-plant material was carbonised to 573 K (300 ^{o}C) and 1073 K (800 ^{o}C) to produce materials named Pd-P-300 and Pd-P-800 respectively.

Thermal gravimetric-infrared (TGIR) analysis of the material during carbonisation demonstrated a 45% mass loss between 373 and 573 K, attributed to the loss of water and carbon dioxide (Figure 6.5). A mass decrease of only 0.1% occurred on heating to 1073 K showing excellent stability of the support at high temperatures. These catalytic materials contained a palladium concentration of 8.3%, determined by ICP, with the remainder of the material made up predominantly of carbon and oxygen (Appendix 4, supplementary table 4.1).

The loss of heteroatoms during carbonisation can also be seen in infrared analysis (Figure 6.4) and XPS analysis of Pd-P-300 (Figure 6.6 (b) and (c)). An increase in the presence of C-O and the appearance of PdO can also be observed on the carbon and palladium XPS spectra of Pd-P-300. The most likely explanation for this occurrence is that the material used for analysis was not fresh and during storage had adsorbed oxygen from the atmosphere. Although, further analysis of fresh material is required to fully determine this.

Analysis using TEM revealed highly dispersed, spherical PdNPs in both catalytic materials (Figure 6.7 A). Closer analysis of Pd-P-300 revealed the mean cross-sectional diameter and frequency distribution of PdNPs was broadly similar to the pre-carbonised samples (Figure 6.7 B). However, for Pd-P-800 a marked shift in PdNP size was observed, with a 400% increase in mean diameter and wider frequency distribution compared to the pre-carbonised plant. This indicates that serious aggregation (increase in the mean particle size) of the PdNPs was taking place between 573 and 1073 K, this is consistent with previous observations by others, including Joo et al. and Jiang et al.(*287, 288*)

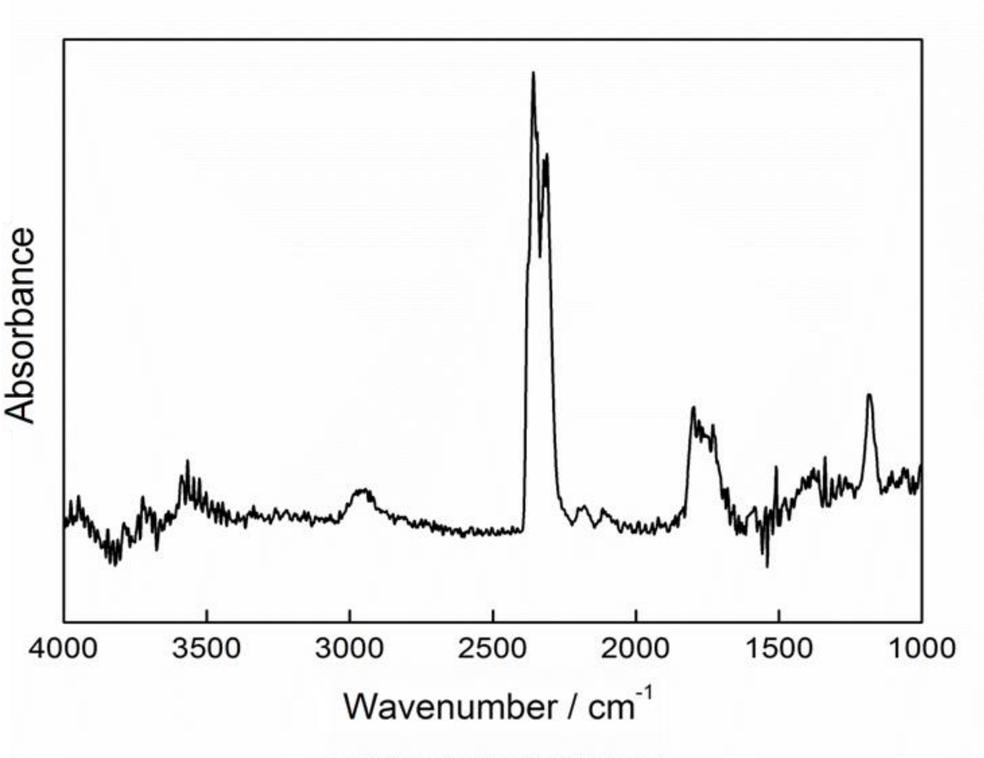

Figure 6.5 IR spectrum of emission during plant material carbonisation.

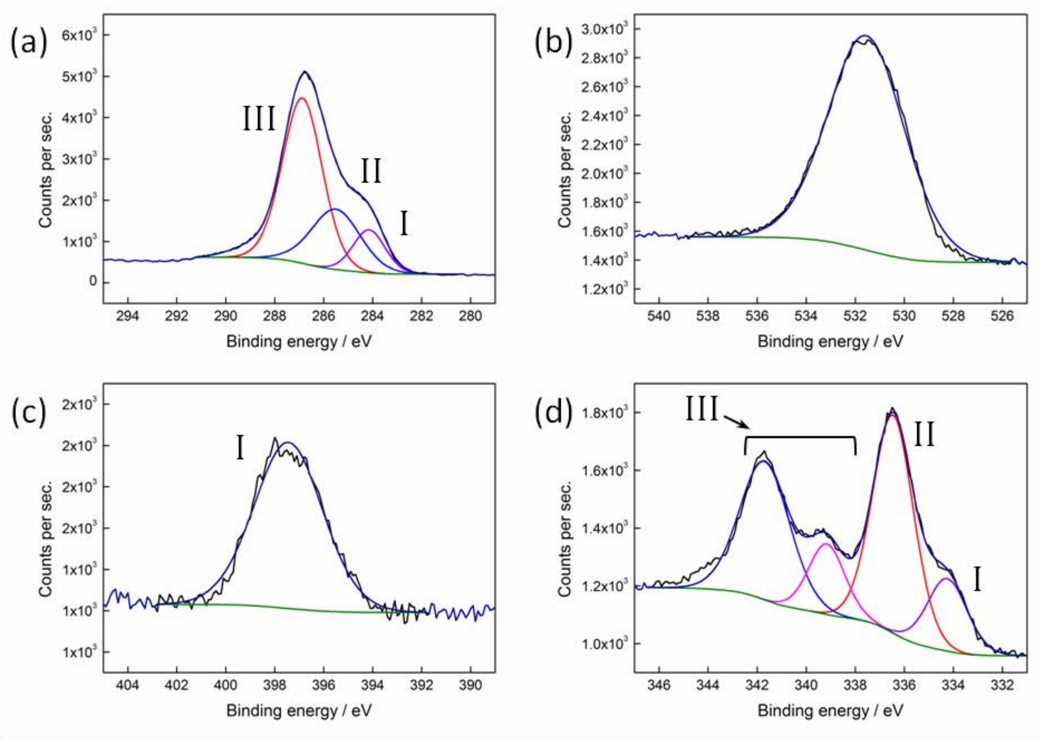

Figure 6.6 XPS spectra of Pd-P-300 (a) carbon. (b) oxygen, (c) nitrogen and (d) palladium.

Table 6.3 Composition of chemical species present in carbonised palladium plant (Pd-P-300) from XPS spectra.

	Peak	BE [eV]	Chemical state	% Pd-P-300
Carbon	I	284.1 ± 0.2	C-C	12
	II	285.4 ± 0.2	C-C (Ar)[a]	26
	III	287.4 ± 0.2	C-O [a]	62
Oxygen		530.0 ± 0.5	CO	100
Nitrogen	I	396.8 ± 0.1	Cyano species	100
	II	398.2	Pyridine	-
	III	404.3 ± 0.2	N-oxide	-
Palladium	I	334.5	Pd$^{(0)}$	14
	II	336.8 ± 0.2	PdO	42
	III	340.0 ± 1.0	Pd$^{(2+)}$	44

[a] Could also possibly be attributed to some C-N.

The driving force for NP aggregation comes from the higher chemical potential and increased surface free energy of metal atoms in small NPs in comparison with bulk metal surfaces and often leads to the deactivation of heterogeneous catalysts. This therefore may affect the catalytic activity of Pd-P-800.(*289, 290*)

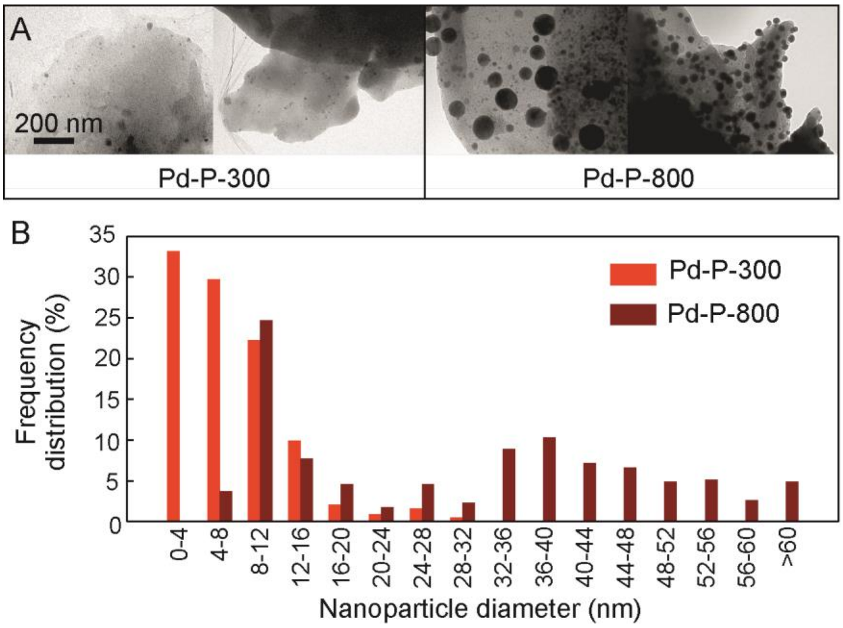

Figure 6.7 (A) TEM showing PdNPs in Pd-P-300 and Pd-P-800 (B) Distribution of PdNP sizes in the plant catalysts.

6.2.3 Determining catalytic activity and reusability of the plant catalysts in C-C bond forming reactions

Palladium catalyzed C-C bond forming reactions, such as Heck and Suzuki, are important methods for the synthesis of pharmaceutical intermediates and other high value molecules. A range of these reactions are commonly seen in the literature to test new catalytic materials, and these were chosen to test the activity of the plant catalysts.(*291-296*)

Initially, the activities of Pd-P-300 and Pd-P-800 were examined using a kinetic comparison of the Heck reaction of iodobenzene with methyl acrylate, to determine any effects caused by differing preparation temperatures (Figure 6.8 (a)). After an initial induction period of 5 minutes, Pd-P-300 showed high catalytic activity, reaching 81% yield after 55 minutes with a maximum turnover frequency of 1.8 s^{-1}. Pd-P-800 showed considerably lower activity, achieving a yield of only 11% over the same time period.

As previously suggested, this poor performance can be attributed to the large PdNPs formed by agglomeration in the high temperature materials. The presence of smaller PdNPs in Pd-P-300 vastly increases the amount of NP surface area available and therefore the number of reactive palladium sites that can participate in the reaction resulting in a dramatically faster rate of reaction.(*85*) Due to the results of this kinetic study Pd-P-300 was used for the remainder of the work.

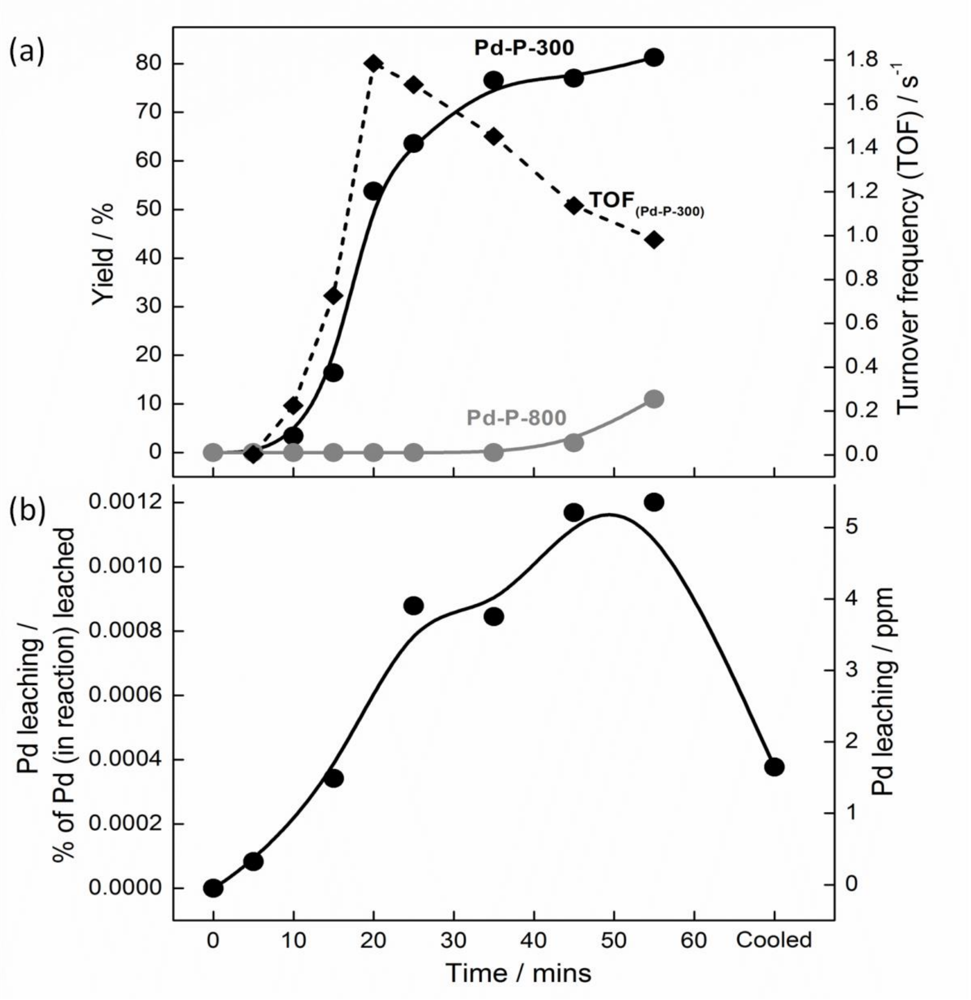

Figure 6.8 (A) Kinetic analysis of the activity of Pd-P-300 and Pd-P-800 for the Heck reaction of iodobenzene and methyl acrylate (solid lines) and turnover frequency (TOF) during Pd-P-300 reaction (dotted line) (B) Pd leaching during reaction of Pd-P-300.

To investigate the catalysis mechanism of Pd-P-300, the extent of palladium leaching during the reaction was determined using ICP analysis of the reaction liquor (Figure 6.8 (b)). Results showed palladium concentration in solution increased as the reaction proceeded, reaching the highest concentration after 55 minutes. After completion of the reaction, the mixture was allowed to cool, and the palladium concentration was observed to have decreased to 0.0012% of the initial Pd concentration in the reaction (1.7 ppm). These results indicate the catalyst proceeds, at least to some extent, via a similar mechanism to other carbon supported palladium catalysts, as described in the literature:

1. Palladium disassociation from the support, accounting for catalyst induction period.
2. The coupling reaction is carried out quasi-homogeneously with palladium in solution as the catalytically active species.
3. The palladium re-deposits on to the support at the end of the reaction resulting in recovery of the PdNPs.(*94*)

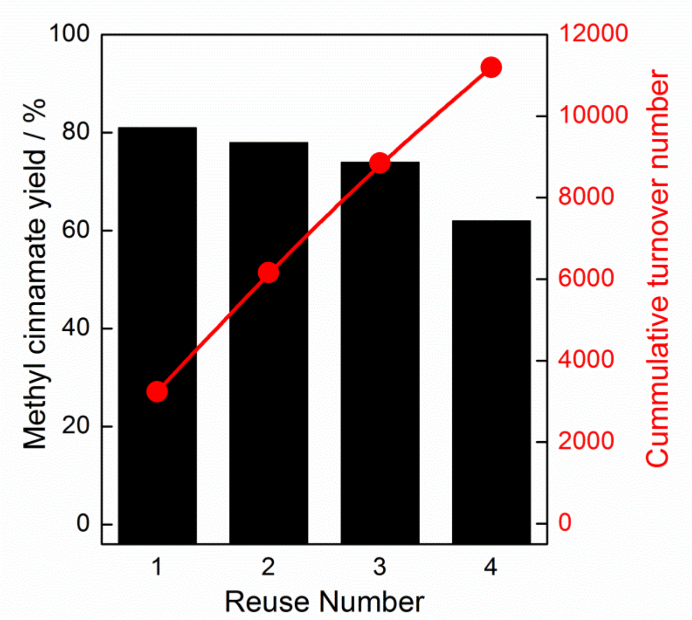

Figure 6.9 Reuse of Pd-P-300 and cumulative turnover number (mol of product/mol of Pd initially added to reaction).

Pd-P-300 was successfully reused four times for the same Heck reaction with only a marginal decrease in catalytic activity with repeated use (Figure 6.9), which is competitive to other studies using alternatively supported PdNPs.(*287, 291, 297*) TEM analysis of the catalyst after repeated use showed some reduced dispersion of the PdNPs and a shift towards larger PdNP, caused by the repeated exposure to high temperatures and the constant disassociation and re-deposition of palladium during the reactions (Figure 6.10).(*298*)

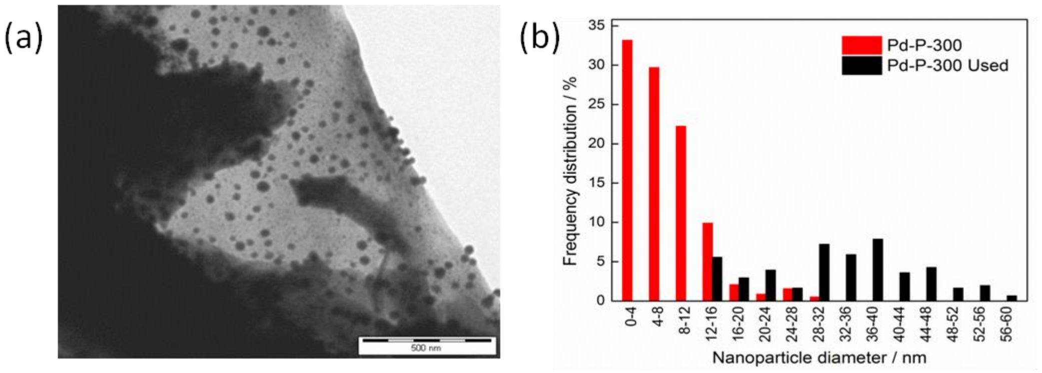

Figure 6.10 (a) TEM of Pd-P-300 after 4 uses (b) Nanoparticle size distribution.

Finally, the activity of Pd-P-300 was compared to commercial catalysts: palladium on carbon (Pd/C) and palladium acetate ($Pd(OAc)_2$). The results for the activity of the three catalysts across a range of Heck and Suzuki reactions are summarized in Figure 6.11. To enable a direct comparison of catalyst performance, a constant palladium concentration of 0.007 mmol Pd was used for all materials and reactions. Encouragingly, Pd-P-300 consistently demonstrated higher yields than Pd/C and gave comparable yields to the homogeneous catalyst $Pd(OAc)_2$ for all of the reactions.

Figure 6.12 shows a schematic representation of the process steps required to produce Pd/C compared to Pd-P-300. What is clearly highlighted in this image is the increased number of steps required for Pd/C production (ca. 9 steps for Pd/C compared to 4 steps for Pd-P-300). All of these extra steps require the addition of chemicals and energy and result in the production of significant amounts of potentially hazardous waste.

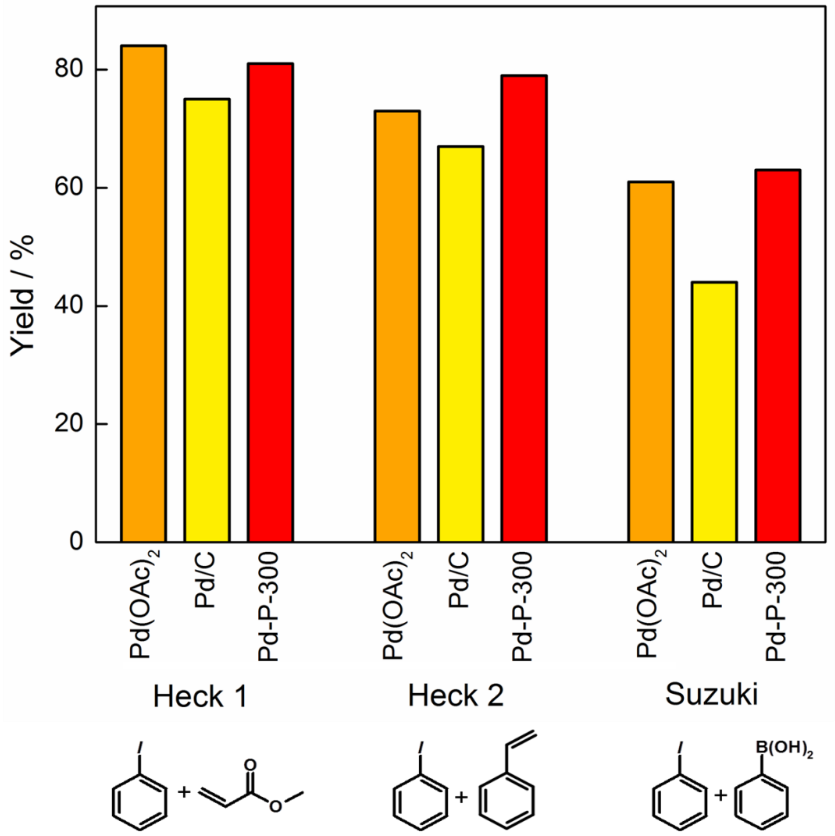

Figure 6.11 Comparison of catalytic activity of plant catalyst and currently used commercial catalysts for a range of reactions.

The use of living plants for the formation of Pd-P-300 eliminates the need for lots of chemical steps, which in turn eliminates a lot of the energy and resources previously required, as the plant is carrying out the synthesis itself. The promisingly high catalytic activity of Pd-P-300 coupled with the simplicity of its production process compared to Pd/C, shows that Pd-P-300 could offer a more economically and environmentally friendly alternative to traditional supported catalysts.

6.3 Conclusion

The successful formation of plant synthesized PdNPs has been achieved in this work. The results showed that the plant possesses the ability to reduce the $Pd^{(II)}$ to $Pd^{(0)}$ to form PdNP deposits around cells and in the junctions between cells.

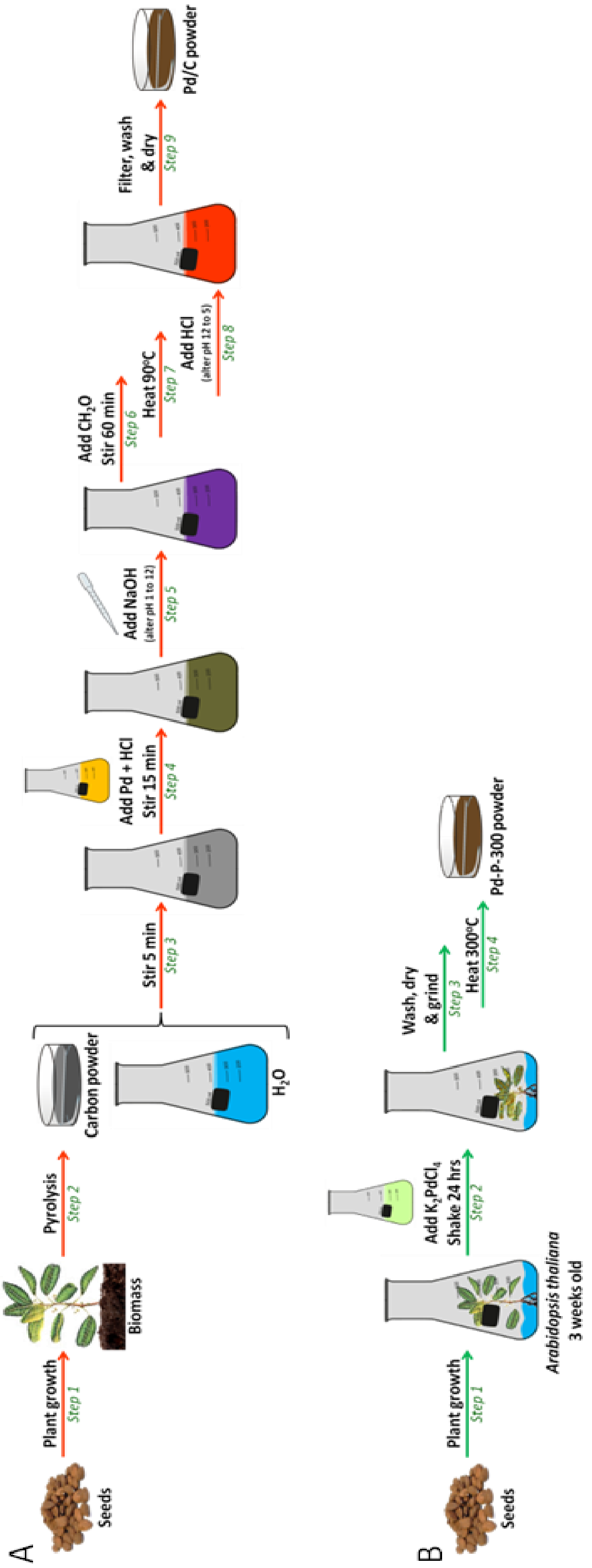

Figure 6.12 Schematics for (A) the preparation of commercially available palladium on carbon (Pd/C) and (B) the preparation of Pd-P-300.

The plant synthesised and supported PdNPs could be effectively utilized in situ for catalysis of a range of Heck and Suzuki reactions. It is particularly exciting that the plant derived PdNPs show comparable or higher activities in comparison with conventional catalysts.

In conclusion, this work offers an introduction to a novel technique for a benign and sustainable method for the production of PdNPs using living plants. The effective production of catalysts using plants to accumulate metals could open new doors in sustainable materials production and present solutions to the looming problem of critical element availability. Typical industrial waste streams are complex and represent a significant challenge for the recovery of rare metals. Future work will focus on meeting this challenge and ensuring the sustainability of the process from waste streams.

Chapter 7

Experimental

Chapter 7.

Experimental

7.1 Chemicals

Purified high amylose corn starch was purchased from National Starch Food Innovation Plc. (Manchester, UK) and used as received. Alginic acid (from brown algae; 61% mannuronic acid and 39% guluronic acid) was purchased from Sigma-Aldrich and was used as received.

Methylene blue (high purity, biological stain) was purchased from Alfa Aesar. Acid blue 92, Nile blue A, Mordant yellow 10, phenol, *o*-cresol, 2-fluorophenol, 3-aminophenol and 4-methoxyphenol were all purchased from Sigma-Aldrich. Palladium acetate, palladium on carbon 3% and 10% and potassium tetrachloropalladate(II) were also all purchased from Sigma-Aldrich. Activated charcoal (Norit) was purchased from Fluka and was washed with deionised water at 80 ^{o}C, filtered and dried in a vacuum oven before use.

7.2 General analytical and characterisation techniques

7.2.1 Electron microscopy

All electron microscopy images were acquired with the help of Ms Meg Stark at the Technology Facility in the Department of Biology, University of York, UK.

Scanning electron microscopy (SEM) micrographs were recorded using a JEOL JSM-6490LV. Samples were mounted on alumina plates and coated with a 7 nm layer of Au/Pd using a high resolution sputter SC-7640 coating device prior to analysis. Typical magnifications used were x1000, x2000 and x4500.

Tunnelling electron microscopy (TEM) micrograph images were recorded using a Tecnai 12 BioTwin at 120kV. Samples were suspended in ethanol and deposited on to carbon grids via solvent evaporation.

All TEM analysis was carried out with the assistance of Ms Meg Stark, Biosciences Technology Facility, Biology Department, University of York, York, YO10 5DD.

7.2.2 Infrared spectroscopy

Infrared analysis was performed using a Bruker Vertex 70 FT-IR fitted with a Specac Golden Gate ATR attachment with diamond top plate analysis window. This was controlled by Opus software. The spectrum was scanned from 4000 – 600 cm^{-1}. The number of background scans and sample scans were set at 32 and 16 respectively. The resolution was selected to be 4 cm^{-1}.

7.2.3 NMR spectroscopy

^{1}H NMR spectra were obtained using a JOEL JNM-ECS400 NMR operating at 400 MHz, 1024 scans were taken for each sample. Spectral referencing was with respect to tetramethylsilane.

Solid state ^{13}C-MAS NMR analysis was carried out by Dr David Apperley, EPSRC Solid State NMR service at the University of Durham, Department of Chemistry, Durham, DH1 3LE.

^{13}C-MAS NMR spectra were obtained using a Varian VNMRS spectrometer at 100.56 MHz for ^{13}C. The spin rate of the MAS was set to 12 kHz spinning, with a wide spectral width and a rotor-synchronised echo. Spectral referencing was with respect to tetramethylsilane.

7.2.4 UV-Vis analysis

UV-visible spectral analysis was recorded using a JASCO V550 UV-visible spectrophotometer between 200 and 900 nm against a water reference.

Calibrations were carried out for all dyes and phenolic compounds used in this thesis. Standard aqueous solutions of known concentrations were prepared and analysed. Distilled water was used as the background.

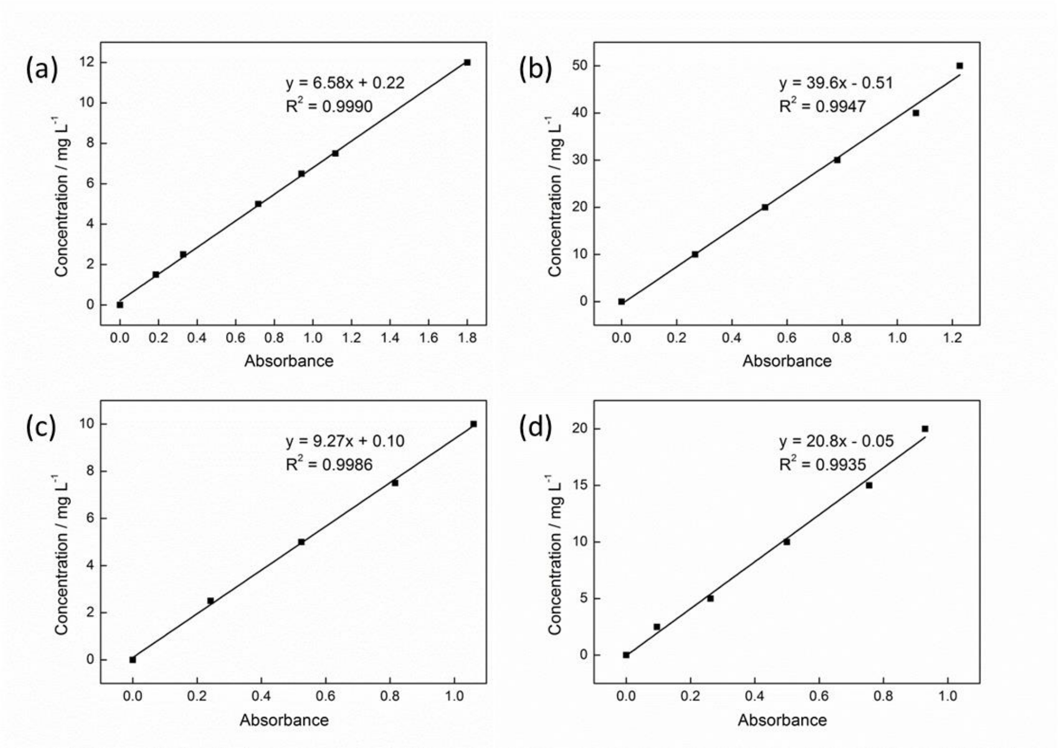

Figure 7.1 Calibration graphs for (a) methylene blue (b) acid blue 92 (c) Nile blue A and (d) mordant yellow 10.

Table 7.1 UV-vis wavelength of maximum absorption used for analysis of dye molecules.

Dye	λ_{max} [nm]
Methylene blue	664
Acid blue 92	570
Nile blue A	634
Mordant yellow 10	355

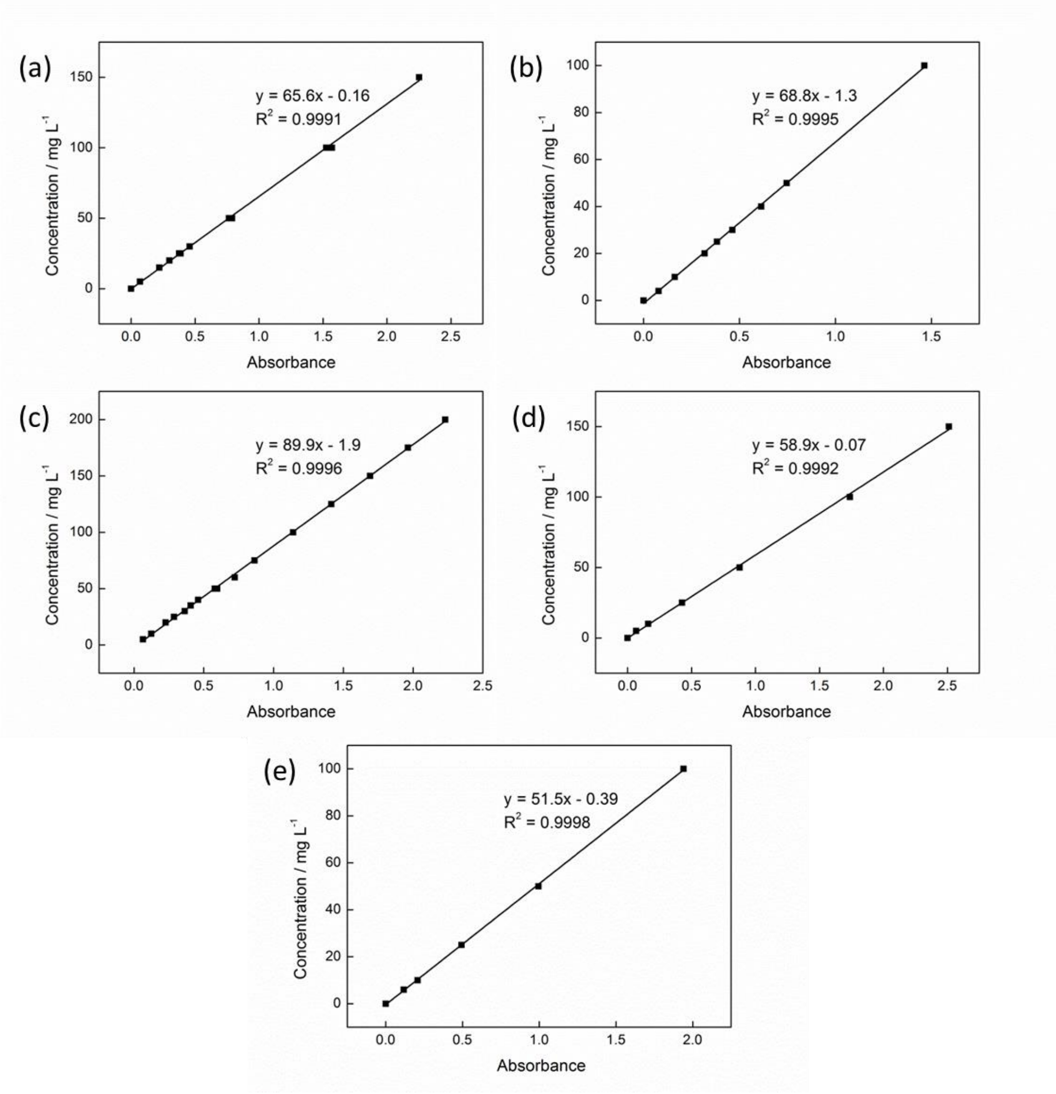

Figure 7.2 Calibration graphs for (a) phenol (b) o-cresol (c) 2-fluorophenol (d) 3-aminophenol and (e) 4-methoxyphenol.

Table 7.2 UV-vis wavelength of maximum absorption used for analysis of phenolics.

Phenolic	λ_{max} [nm]
Phenol	270
O-Cresol	270
2-Fluorophenol	267
3-Aminophenol	282
4-Methoxyphenol	288

7.2.5 Thermal gravimetric analysis

Thermal gravimetric (TG) analysis was carried out using a Netsch 409 STA thermal analyser. Samples were mounted in a 3.5 ml ceramic crucible and heated under a flow of nitrogen (50 ml min^{-1}), prior to analysis the oven chamber was evacuated and backfilled twice with nitrogen. Samples were heated at either 1, 5 or 20 K min^{-1} to either 578 or 1073 K. For the TGIR studies the TG was coupled to a Bruker Equinox 55 infrared spectrometer via a transfer line. The flow of nitrogen used was 100 ml min^{-1}.

7.2.6 Inductively coupled plasma spectroscopy

Inductively coupled plasma (ICP) analysis was carried out on a Varian ICP with axial OES. The samples were digested in reverse aqua-regia using a CEM mars Xpress microwave.

7.2.7 Porosimetry analysis

Nitrogen adsorption-desorption isotherms, surface area and porosimetry measurements (including pore volumes and porous distributions) were conducted using a Micrometrics ASAP 2010 volumetric adsorption analyser at -196 ^{o}C. Prior to analysis samples were out-gassed at 333 K under reduced pressure for 1 hour, followed by 393 K for a further 1 hour. Specific surface areas were determined using the Brunauer, Emmett and Teller (BET) isotherm shown below:(*299*)

$$\frac{\mathbf{1}}{\boldsymbol{v}[(\boldsymbol{P_o}/\boldsymbol{P})-\mathbf{1}]}=\frac{\boldsymbol{c}-\mathbf{1}}{\boldsymbol{v_m c}}\left(\frac{\boldsymbol{P}}{\boldsymbol{P_o}}\right)+\frac{\mathbf{1}}{\boldsymbol{v_m c}}$$

Where P is the equilibrium pressure and P_o the saturation pressure, v the adsorbed gas quantity, v_m monolayer adsorbed gas quantity and c the BET constant which is calculated using the equation:

$$\boldsymbol{c}=\boldsymbol{e}^{(\boldsymbol{E_1}-\boldsymbol{E_L}/\boldsymbol{RT})}$$

Where E_1 is the heat of adsorption for the first layer and E_L is that for further layers and is equal to the heat of liquefaction.

Pore size distributions and mesopores volumes were calculated using the Barrett, Joyner and Halenda (BJH) method and nitrogen desorption data.(*300*) Dubinin-Radushkevich (DR) isotherm was used to determine micropore volumes and surface energies:(*301*)

$$\boldsymbol{W = W_0 e^{[-A/(\beta E_o)^2]}}$$

Where W is the volume of gas adsorbed at the relative pressure P/P_o, W_0 the total volume of the micropores, A the adsorbent constant and β the adsorbate constant. E_o is the characteristic energy of the micropore structure of the adsorbent.

7.2.8 X-Ray photoelectron spectroscopy

X-ray photoelectron spectroscopy (XPS) was conducted by Dr David Morgan, EPSRC XPS service at the University of Cardiff, Cardiff Catalysis Institute, School of Chemistry, Cardiff, CF10 3AT or Dr Benjamin Johnson, EPSRC XPS service at the University of Leeds, School of Physics and Astronomy, Leeds, LS2 9JT.

XPS spectra were recorded on a Kratos Axis Ultra DLD photoelectron spectrometer using a hemispherical photoelectron analyser with a monochromatic AlKα X-ray source (75-150 W) and analyser pass energies of 160 eV (for survey scans) and 40 eV (for detailed scans). Samples were mounted using double-sided tape. Binding energies were referenced to the C 1s binding energy 285 eV. Prior to analysis samples were degassed overnight at ultrahigh vacuum ($<5\times10^{-10}$ Torr). CasaXPS software was used to carry out analysis of the spectra.

7.2.9 Gas chromatographs and Mass spectral analysis

Sample preparation was carried out with 0.5 ml of reaction mixture was diluted with 0.5 ml tetrahydrofuran (THF). A standard solution of diethyl succinate in THF was prepared at a concentration of 4 mg/500 ml and was used as the standard for all GC analysis throughout the project. To prepare the GC sample 0.2 ml of the diluted reaction mixture was added to 0.5 ml of standard and 3 ml of THF. This solution was filtered to remove any solid particles and analysed.

Quantitative analysis of products was conducted using an Agilent 6890 N gas chromatograph with a flame ionisation detector (GC-FID). This was fitted with a DB5HT capillary column (30m x 250 μm x 0.25 μm nominal) at constant pressure of 21.54 psi. The carrier gas used was helium and flow rate was set at 2.2 ml min^{-1} in constant flow mode. The split ratio used was 40:1. The initial oven temperature was maintained at 323 K for 4 minutes. The temperature was then ramped at a rate of 10 K min^{-1} to 573 K and held for 10 minutes. The injector was set at 563 K and the FID was maintained at 613 K.

Peaks were identified by comparison with standard compounds. Quantification of yield was determined using peak area comparison between product peak and diethyl succinate standard. Prior to analysis a calibration was carried out for each reaction. The mass ratios of known samples were plotted against area ratios. Response factor (Rf) values of the corresponding samples were then calculated using the equation given below:

$$Mass_{(product)} \big/ Mass_{(standard)} = R_f \ x \ Peak\ area_{(product)} \big/ Peak\ area_{(standard)}$$

The calibration graphs and equations used are shown in Figure 7.3.

High temperature gas chromatograph mass spectrometry (HT-GC-MS) was performed on a Perkin Elmer Clarus 500 GC coupled with a Clarus 560 S quadrapole mass spectrometer. This was fitted with a DB5HT capillary column (30m x 250 μm x 0.25 μm nominal) at constant pressure of 22.35 psi with a helium carrier gas. The temperature of the injector was maintained at 623 K and the flow rate was set to 1.00 ml min^{-1}. The split ratio used was 10:1. The temperature of the injector was maintained at 573 K and transfer line at 623 K. The initial oven temperature was maintained at 333 K for 1 minute. The temperature was then ramped at a rate of 281 K min^{-1} to 633 K and held for 10 minutes. The Clarus 500 quadrapole mass spectra was operated in the electron ionisation mode (EI) at 70 eV, a source temperature of 573 K, with the quadrapole at 573 K and a scanning mass range of 30 - 1200 amu. per second. The data was collected with the PerkinElmer enhanced TurboMass (Ver5.4.2) chemical software and compounds were identified by comparison of mass fragmentation patterns with spectra contained in the NIST library (v. 2.2) and by direct comparison with standard compounds.

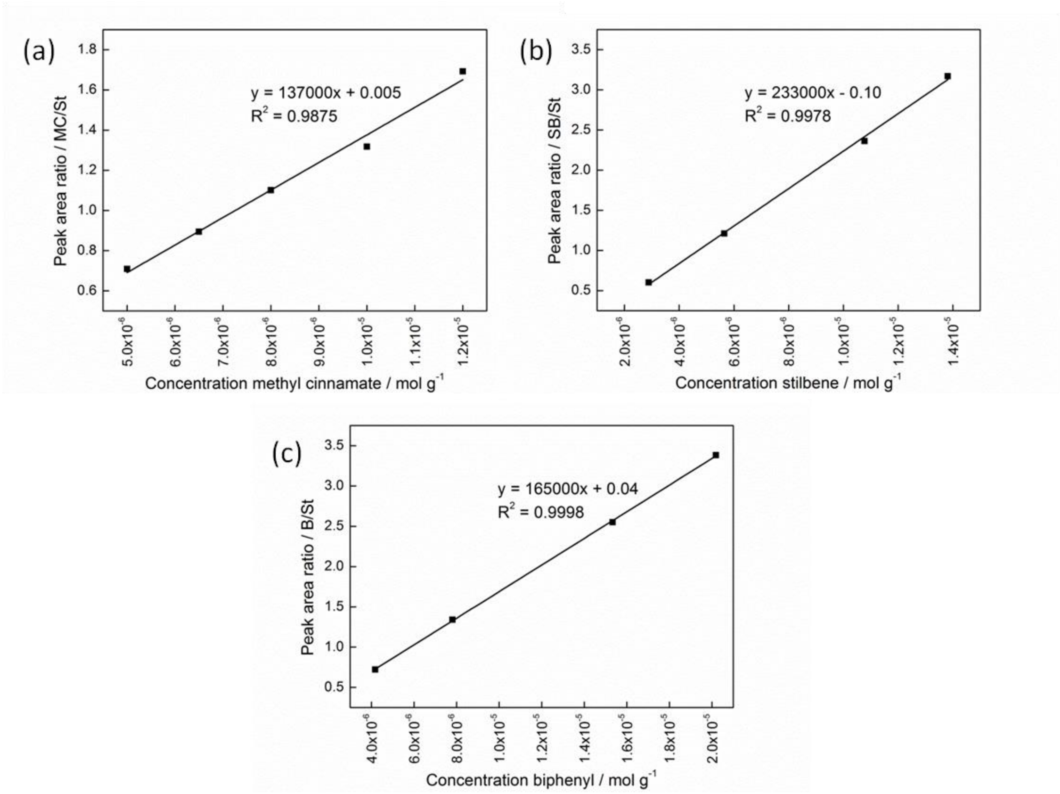

Figure 7.3 GC calibration graphs for (a) methyl cinnamate (b) stilbene and (c) biphenyl.

7.3 Chapter 2. Starbon® Characterisation and Application in Bulky Dye Adsorption

7.3.1 Starch derived Starbon® preparation

Corn starch (1.6 kg) was added to 10 L pressure cooker containing 8 L of deionised water. The resulting slurry was stirred and heated at 393 K/80 kPa for 45 minutes to form a gel. The gel was cooled to room temperature before being transferred to 2 L plastic jars and was stored at 278 K for 48 hours. The resulting mixture was filtered to remove excess water. The gel was subject to 5 solvent exchanges with ethanol: 1L of ethanol was added to each jar, the mixture was stirred for 2 hours, stirring was then stopped and the mixture was left to separate until a clear liquid and solid phase were visible. The ethanol was decanted off and the process repeated. For the last solvent exchange the mixture was not allowed to settle, instead after 2 hours stirring the mixture was vacuum filtered using a sintered funnel to remove as much ethanol as possible. The filtered material was then oven dried at 393 K for 10 hours to yield dried, expanded starch.

Dried expanded starch (300 g) was doped with *p*-toluenesulfonic acid (5% w/w) and added to a 2 L flask containing 1 L of toluene. The system was fitted with a condenser and heated under reflux for 6 hours. The resulting material was filtered and dried at 353 K under reduced pressure in a vacuum oven to yield a Starbon® precursor. This Starbon® precursor was heated at 1 K min^{-1} in an inert nitrogen atmosphere to the required temperature. Starbon® used in adsorption studies was prepared up to 573 K (S300), 723 K (S450) and 1073 K (S800).

7.3.2 Alginic acid derived Starbon® preparation

Alginic acid (40 g) was added to 2 L flask containing 800 ml of deionised water. The slurry was heated at 363 K for 2 hours and then allowed to cool to room temperature before being stored for 12 hours at 278 K. The resulting liquid was then filtered to remove excess water. The gel was subjected to 5 solvent exchanges with ethanol: 500 ml of ethanol was added to each jar, the mixture was stirred for 2 hours, stirring was then stopped and the mixture was left to separate until a clear liquid and solid phase was visible. The ethanol was decanted off and the process repeated. For the last solvent exchange the mixture was not allowed to settle, instead after 2 hours stirring the mixture was vacuum filtered using a sintered funnel to remove as much ethanol as possible. The expanded alginic acid was then dried using a Thar SFE500 supercritical CO_2 extractor operating at 313 K/100 bar/40 g min^{-1} for 3 hours. The resulting material was heated at 1 K min^{-1} in an inert nitrogen atmosphere to the required temperature. Starbon® used in adsorption studies was prepared up to 573 K (A300), 723 K (A450) and 1073 K (A800).

7.3.3 Dye adsorption experiments

Standard solutions of the four dyes used were prepared in volumetric flasks using deionised water at the following concentrations: methylene blue (MB) 10 mg/L, acid blue 92 (AB) 40 mg/L, Nile blue A (NB) 10 mg/L, mordant yellow 10 (MY) 15 mg/L. All dyes were fully dissolved with vigorous stirring and samples taken to be analysed for initial concentration before use in adsorption studies.

For the isothermic and kinetic absorption studies a flask was filled with dye solution volumes ranging from 30 ml to 2.5 L and stirred for 5 minutes prior to adding the adsorbent and sealing the vessel. Samples were taken for the adsorption studies and at 5, 15, 30, 60, 240 minutes and 24 hours. For the seven adsorbents used concentrations ranged from 3 mg/L to 300 mg/L.

The adsorption capacity of the materials (qe, mg g^{-1}) was determined by:

$$\boldsymbol{q_e = (C_o - C_e)\frac{v}{m}}$$

Where C_0 (mg L^{-1}) is the initial concentration of the solution, Ce (mg L^{-1}) the concentration of the sample solution, v the volume of solution used (L) and m the mass of adsorbent used (g).

Thermodynamic adsorption studies were performed using a standard solution of acid blue 92 (40 mg/L) and methylene blue (30 mg/L). The temperatures used for the study were 298, 303, 308, 313 and 318 K. The samples were placed in silicone oil baths and allowed to reach the required temperature before the adding adsorbent. These were then left to stir for 24 hours before samples were taken.

A Jasco V-550 UV-visible spectrophotometer was used to determine the extent of dye adsorption onto Starbon®, compounds were identified using max wavelengths; MB λ = 664 nm, AB λ = 570 nm, NB λ = 635 nm, MY λ =360 nm.

7.4 Chapter 3. Use of Starbon® for Adsorption of Phenols

7.4.1 Phenolic adsorption experiments

To determine the adsorption capacity of the materials, batch experiments were employed. Adsorption isotherms were recorded over a concentration range of 25 to 200 mg L^{-1} of phenolic solution at 298 K. For the experiments 20 ml of solution and 20 mg of adsorbent were stirred, samples were taken at 24 hours for the equilibrium studies and 15, 30, 60 and 120 minutes for the kinetic studies. The adsorption capacity of the materials (qe) was determined by:

$$\boldsymbol{q_e = (C_o - C_e)\frac{v}{m}}$$

Where C_0 is the initial concentration of the solution, Ce the concentration of the sample solution, V the volume of solution used (L) and m the mass of adsorbent used (g). A Jasco V-550 UV-visible spectrophotometer was used to determine the extent of phenolic adsorption onto Starbon®, compounds were identified using max wavelengths; P λ = 270 nm, OC λ = 270 nm, 2F λ = 267 nm, 3A λ = 282 nm, 4M λ = 288 nm.

Thermodynamic adsorption studies were performed using a 100 mg L^{-1} solution of the required phenolic. The temperatures used for the study were 298, 303, 308, 313 and 318 K. The samples were placed in silicone oil baths and allowed to reach the required temperature before adding the adsorbent. These were then left to stir for 24 hours before samples were taken.

7.5 Chapter 5. Direct synthesis of palladium nanoparticles on alginic acid and seaweed supports

7.5.1 Alginic acid catalyst preparation

To prepare the catalyst expanded alginic acid prepared using the method in Section 7.3.2 was used for the preparation of the catalyst. Expanded alginic acid (20 g) was added to ethanol (250 ml) in a round bottom flask and subjected to stirring. Once the mixture was well mixed (approximately 10 min) palladium acetate (1 w/w% of expanded alginic acid) was then added. The solution appeared pale orange/yellow due to the dissolved palladium acetate. The solution was stirred until this colour was no longer visible – indicating that all of the palladium had been adsorbed. The expanded alginic acid was dried using a Thar SFE500 supercritical CO_2 extractor operating at 313 K/100 bar/40 g min^{-1} for 3 hours, followed by carbonisation at 1 K min^{-1} under an inert atmosphere of nitrogen to 573 K

7.5.2 Seaweed catalyst preparation

The preparation of palladium impregnated seaweed was kindly carried out by Dr. J Dodson, Institute of Chemistry, Federal University of Rio de Janeiro, Cidade Universitaria, Rio de Janeire, 21941-909, Brasil.

To prepare the catalyst dried and ground seaweed (20 g) was added to ethanol (250 ml) in a round bottom flask and subjected to stirring. Once the mixture was well mixed (approximately 10 min) palladium acetate (1 w/w% of expanded alginic acid) was then added. The solution appeared pale orange/yellow due to the dissolved palladium acetate. The solution was stirred until this colour was no longer visible – indicating that all of the palladium had been adsorbed. The seaweed was dried using a Thar SFE500 supercritical CO_2 extractor operating at 313 K/100 bar/40 g min^{-1} for 3 hours, followed by carbonisation at 1 K min^{-1} under an inert atmosphere of nitrogen to 573 K.

7.5.3 Testing catalytic activity

7.5.3.1 Heck reaction 1 – formation of methyl cinnamate:

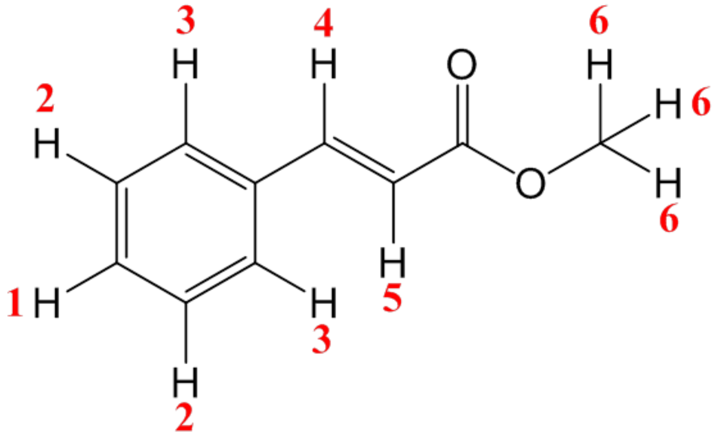

For the reaction of iodobenzene with methyl acrylate typical reaction conditions used were: Into a 25 ml round bottom flask the following reagents were measured; iodobenzene (20 mmol), methyl acrylate (25 mmol), triethylamine (25 mmol). *N*-methylpyrollidone (NMP) 7 ml was then added and the flask heated with stirring to 393 K. Once the flask had heated to the required temperature Pd catalyst was added, equivalent amount of catalyst was added to achieve a 0.3 mol% Pd concentration (based on iodobenzene concentration). For control experiments no catalyst was added. The reaction was allowed to proceed for 2 hours at 393 K. Reaction was monitored by GC-FID using diethyl succinate as a standard. Methyl cinnamate: ^{1}H NMR: (500 MHz, $CDCl_3$): δ [ppm] = 3.82 (s, 3H, 6), 6.47 (d,1H, J = 16 Hz, 4), 7.37-7.57 (m, 6H, 1-3), 7.72 (d, 1H, J = 16 Hz, 5). GCMS: (*m/z*) = 162, 131 (100), 103, 77, 51.

7.5.3.2 Heck reaction 2 – formation of stilbene:

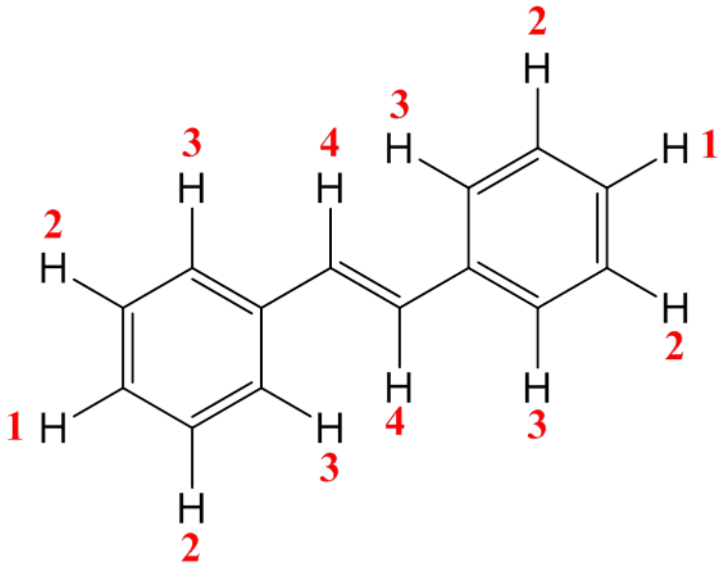

For the reaction of iodobenzene with styrene typical reaction conditions used were: Into a 25 ml round bottom flask the following reagents were weighed; iodobenzene (20 mmol), styrene (25 mmol), triethylamine (25 mmol), then NMP 7 ml was added. The flask was heated with stirring to 393 K. Once the flask had heated to the required temperature Pd catalyst was added, equivalent amount of catalyst was added to achieve a 0.3 mol% Pd concentration (based on iodobenzene concentration). For control reaction no catalyst was added. The reaction was allowed to proceed for 2 hours at 393 K. Reaction was monitored by GC-FID using diethyl succinate as a standard. Stilbene: ^{1}H NMR: (500 MHz, $CDCl_3$): δ [ppm] = 7.13 (s, 2H, 4), 7.26 (t, 2H, J = 7.8 Hz, 1), 7.36 (t, 4H, J = 7.8, 2), 7.53 (d, 4H, J = 7.2 Hz, 3). GCMS: (*m/z*) = 181, 180 (100), 179, 178, 165, 89, 76.

7.5.3.3 Suzuki reaction – formation of biphenyl:

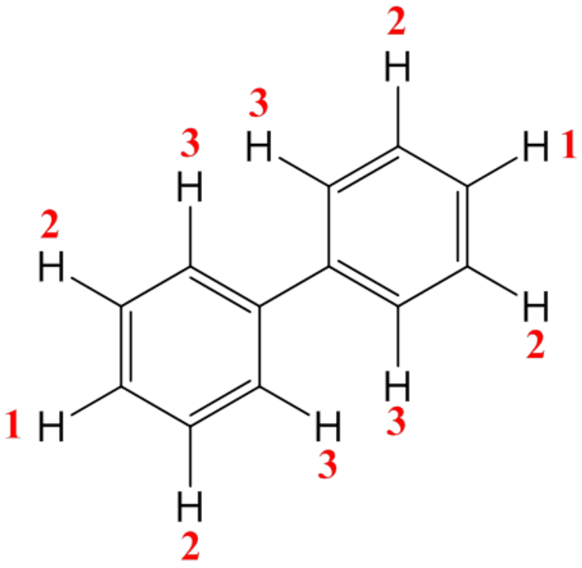

For the reaction of iodobenzene with benzeneboronic acid typical reaction conditions used were: Into a 25 ml round bottom flask the following reagents were weighed; iodobenzene (5 mmol), benzeneboronic acid (7.5 mmol), potassium carbonate (5.5 mmol), then NMP 10 ml and water 4 ml were added. The flask was heated with stirring to 393 K. Once the flask had heated to the required temperature Pd catalyst was added, equivalent amount of catalyst was added to achieve a 0.3 mol% Pd concentration (based on iodobenzene concentration). For control reaction no catalyst was added. The reaction was allowed to proceed for 24 hours at 393 K. Reaction was monitored by GC-FID using diethyl succinate as a standard. Biphenyl: ^{1}H NMR: (500 MHz, $CDCl_3$): δ [ppm] = 7.37 (t, 2H, J = 7.8 Hz, 1), 7.46 (t, 4H, J = 7.8 Hz, 2), 7.62 (dd, 4H, J = 7.8 Hz, 3). GCMS: (*m/z*) = 155, 154 (100), 153, 152, 76, 51.

7.5.4 Recycling of the catalysts

The reaction of iodobenzene with methyl acrylate was used to investigate recyclability of the catalyst. The conditions were the same as Section7.5.2. After 2 hours the mixture was cooled to room temperature and transferred to a centrifuge tube. The solid and liquid materials were separated by centrifugation at 3000 rpm for 10 minutes. The liquid was decanted and saved for analysis. The solid was washed with NMP. Solid and liquid were separated again and the liquid removed. The solid was then washed into a new 25 ml round bottom flask using NMP containing fresh reagents and the Heck reaction was carried out again, without adding any fresh catalyst. Up to 4 successive runs were performed without a substantial drop in yield being observed.

7.5.5 Determination of leaching of Pd during reaction

7.5.5.1 Inductively coupled plasma analysis

For a quantitative analysis of the extent of leaching palladium concentration was determined using inductively coupled plasma (ICP) analysis. Analysis conditions are described in Section 7.1.

7.6 Chapter 6. Nano-palladium catalysts directly from plants

7.6.1 Growth of *Arabidopsis* containing palladium

The Arabidopsis plants used in this work were kindly prepared by Dr Liz Rylott, CNAP, Department of Biology, University of York, York, YO10 5DD. The typical procedure used is described below:

Wild-type Arabidopsis ecotypes Col-0 were obtained from the Nottingham Arabidopsis Stock Centre at the University of Nottingham. Seeds were imbibed for 4 days at 277 K on agar plates containing 20 mM sucrose and half strength Murashige and Skoog salts (purchased from Sigma-Aldrich). Seedlings were grown in 16 h of light with 125 mmol m^{-2} s^{-1} white light. For liquid culture experiments, individual seedlings were transferred to 100-mL conical flasks containing 20 mL of half-strength Murashige and Skoog medium and 20 mM sucrose. Plants were grown under 20 mmol m^{-2} s^{-1} light on a rotary shaker at 130 rpm. The medium was then replaced with 10 mM potassium tetrachloropalladate(II). The plants remained in the palladium solution for 24 hours. Samples were taken for TEM periodically to 24 hours, then remaining tissue was washed, dried and ground to a powder.

7.6.2 Transmission electron microscopy

The preparation of the plant samples was kindly carried out by Ms Meg Stark at the Technology Facility, Department of Biology, University of York, York, YO10 5DD. The typical procedure used is shown below:

Plant leaf tissues were fixed in 2.5 % (v/v) glutaraldehyde, 4% formaldehyde (v/v) in 50 mM phosphate buffer for 3.5 hours a secondary fix of 1% osmium tetroxide. Samples were then dehydrated through a 25-100 % acetone series and infiltrated with Spurrs resin (Agar Scientific) (25, 50 and 75 %) with overnight polymerisation at 343 K. Sections were mounted on 400 mesh thin-bar Athene grids (Agar Scientific), stained with saturated uranyl acetate and Reynolds lead citrate and viewed using a Tecnai 12 Bio Twin TEM operating at 120 kV.

7.6.3 Formation of the catalyst

Two catalysts were prepared from the plant material. To produce the catalysts the dried plant powder was pyrolised using the Netzsch STA 409 under N_2 at 1 K min^{-1} to 573 K (300 ^{o}C) (Pd-P-300) and1073 K (800 ^{o}C) (Pd-P-800) respectively.

7.6.4 Testing catalytic activity

Heck and Suzuki reactions were carried out using the same method as described in Section 7.5.2.

7.6.5 Experiment to determine rate of reaction

The reaction of iodobenzene with methyl acrylate was used to investigate reaction kinetics. Reaction conditions used were: into a 25 ml round bottom flask the following reagents were measures; iodobenzene (20 mmol), methyl acrylate (25 mmol), triethylamine (25 mmol). *N*-methylpyrollidone (NMP) 7 ml was then added and the flask heated with stirring to 120 ^{o}C. Once the flask had heated to the required temperature Pd catalyst was added, equivalent amount of catalyst was added to achieve a 0.3 mol% Pd concentration (based on iodobenzene concentration). For control experiments no catalyst was added. Reaction was monitored by GC-FID using diethyl succinate as a standard. Samples (0.5 ml) of the reaction mixture were taken at 5 minute intervals for 2 hours.

7.6.6 Recycling of the catalysts

This was carried out as described in Section 7.5.3. Up to 4 successive runs were performed before a substantial drop in yield was observed.

7.6.7 Determination of leaching of Pd during reaction

This was carried out as described in Section 7.5.4.

Chapter 8

Thesis conclusions and future work

Chapter 8.

Thesis conclusions and future work

8.1 Concluding remarks

8.1.1 Investigation of Starbon® as adsorbents

The aim of chapters 2 and 3 was to determine whether Starbon® were effective materials for the capture of potentially harmful compounds from aqueous waste streams.

Highly efficient removal of a range of dyes and phenols has been achieved using Starbon® prepared from starch and alginic acid at a range of different preparation temperatures. For dye removal the work demonstrated that adsorbents with a high mesoporous character A300 and A800 were found to be particularly effective adsorbers. This mesoporosity facilitated fast, multilayer adsorption that was not possible for microporous materials such as Norit.

In the adsorption of phenols the Starbon® performed well although their mesoporosity was not such as advantage. Due to the small size of the phenolics adsorption was no longer limited by pore size. However, surface area coverage of adsorbate calculations revealed that Starbon® were more efficient compared to the traditional adsorbent tested.

What the work in these chapters highlighted most clearly was that the character of the polysaccharide starting materials greatly influenced the properties of the final Starbon®. This was the first time the alginic acid and starch derived materials had been directly compared for the same processes. It was clear from the work that the differences between the materials affected how they behaved as adsorbents. The starch derived Starbon® contained a higher concentration of surface hydroxyl and carbonyl groups and it was concluded that the main mode of adsorption was occurring via interaction between these groups and the adsorbate. Whereas, A800 showed a higher degree of surface aromatization and results suggested that adsorption took place through π-π interactions between the surface and the adsorbent.

Overall, the work with Starbon® was very successful. The dye adsorption work led to a full paper publication and a further publication focused on phenolic adsorption is currently in preparation. Much more is now understood about how these materials behave as adsorbents in aqueous media.

8.1.2 Elemental sustainability and prospects for 'urban mining'

The aim of chapter 4 was partly to highlight the growing problems associated with element supply, in particular for technologically important metals, such as the PGMs and indium. Also the potential for metal recovery from waste was discussed in depth to show the possibility of "urban mining" as an alternative to extraction of elements from virgin ores. The main conclusion that can be drawn from this chapter is that before the potential for extraction can be fully realised further work is required focusing on the development of extraction techniques. In particular, the scaling up of techniques is important as the majority have only presently been tested on a lab scale.

This chapter inspired the work in chapters 4 and 5, investigating green methods for the recovery of metals that has the potential to be applied to waste streams in the future.

8.1.3 Green synthesis of palladium nanoparticles

The aim of chapters 5 and 6 was the development of greener methods for the production of supported palladium nanoparticles. Two very different methods were employed to achieve this aim:

Firstly, in chapter 5 the more traditional approach using adsorption of the metal was carried out utilising novel, biobased supports. Alginic acid and seaweed were both successfully employed to adsorb palladium from an ethanol solution. Nanoparticle deposits were successfully formed on/in both of the bioderived supports.

In chapter 6 the more innovative approach was taken towards nanoparticle synthesis using phytoremediation by living plants. The results demonstrated that the plants had the ability to uptake palladium from an aqueous solution. Once inside the plant the palladium ions were reduced by the plant to form nanoparticle deposits.

All of the materials made in chapters 5 and 6 exhibited excellent catalytic activity across a range of C-C coupling reactions. The plant derived catalysts in particular performed impressively showing very low levels of palladium leaching and high reusability.

Overall, the work presented in these chapters is very promising and has the potential to change the way nanoparticles are synthesised in the future and develop novel methods for elemental recovery and reuse.

8.2 Further work

8.2.1 Adsorption from industrial aqueous waste

It was not possible during this work to obtain any “real” industrial waste samples to test the adsorption of Starbon®. It is important for future work to test the materials in these waste samples to ascertain their true efficiency and effectiveness.

At present the Starbon® have only been tested using model, single component solutions, however in reality it is safe to assume that more than one adsorbate will be present in waste samples. It is necessary to see how Starbon® performs, for example, whether the materials behave selectively and could therefore be used in order to separate multi-component waste streams. Or the materials may adsorb indiscriminately which would be highly effective for the purification of water.

8.2.2 Regeneration of Starbon® adsorbents

Development of a method for the regeneration of Starbon® adsorbents after use is required. This is necessary to reduce waste and increase the green credentials of the materials process. A method that not only regenerates the Starbon® but also recovers and enables collection of the adsorbate (i.e. the adsorbate is not destroyed) would be ideal. This way both the adsorbent and adsorbate could be reused. Suggested methods for non-destructive regeneration of Starbon® could be: desorption of adsorbate using solvent, temperature, pH changes or supercritical CO_2.

8.2.3 Improvement of seaweed support for catalysis

More work is needed to further improve the seaweed support. Whilst this material showed good activity initially this was lost quickly due to high leaching levels of palladium. The material could possibly be improved by expansion of the dried seaweed, in the same was as alginic acid, prior to impregnation to encourage diffusion of palladium into the support rather than attaching to the surface. Alternatively, live seaweed may prove effective at uptake of palladium rather than dried.

8.2.4 Investigation into other plant species for phytoremediation

The Arabidopsis plants used for the work in chapter 6 are predominantly used only in laboratory based experiments. For the future of this work it is important to investigate other types of plants that would be more appropriate for use in field trials. Ideally a plant that is fast growing would be best for this work as it would shorten the growing time required.

8.2.5 Use of "real" metal containing wastes for catalysis preparation

For all of the different catalysts prepared in this work model palladium containing solutions were used. However, to fully realize the potential of the process "real" waste streams, as described in chapter 4, are required as metal feedstocks. As shown in chapter 4 these wastes are highly complex containing many different metal elements and it will be interesting to investigate the influence this has on the resulting materials.

In general, moving forward with all of the work presented in this thesis it is important to start applying it beyond the laboratory. By employing “real” wastes and working on larger scales the real potential of this technology can begin to be realised.

Appendices

Appendix 1.

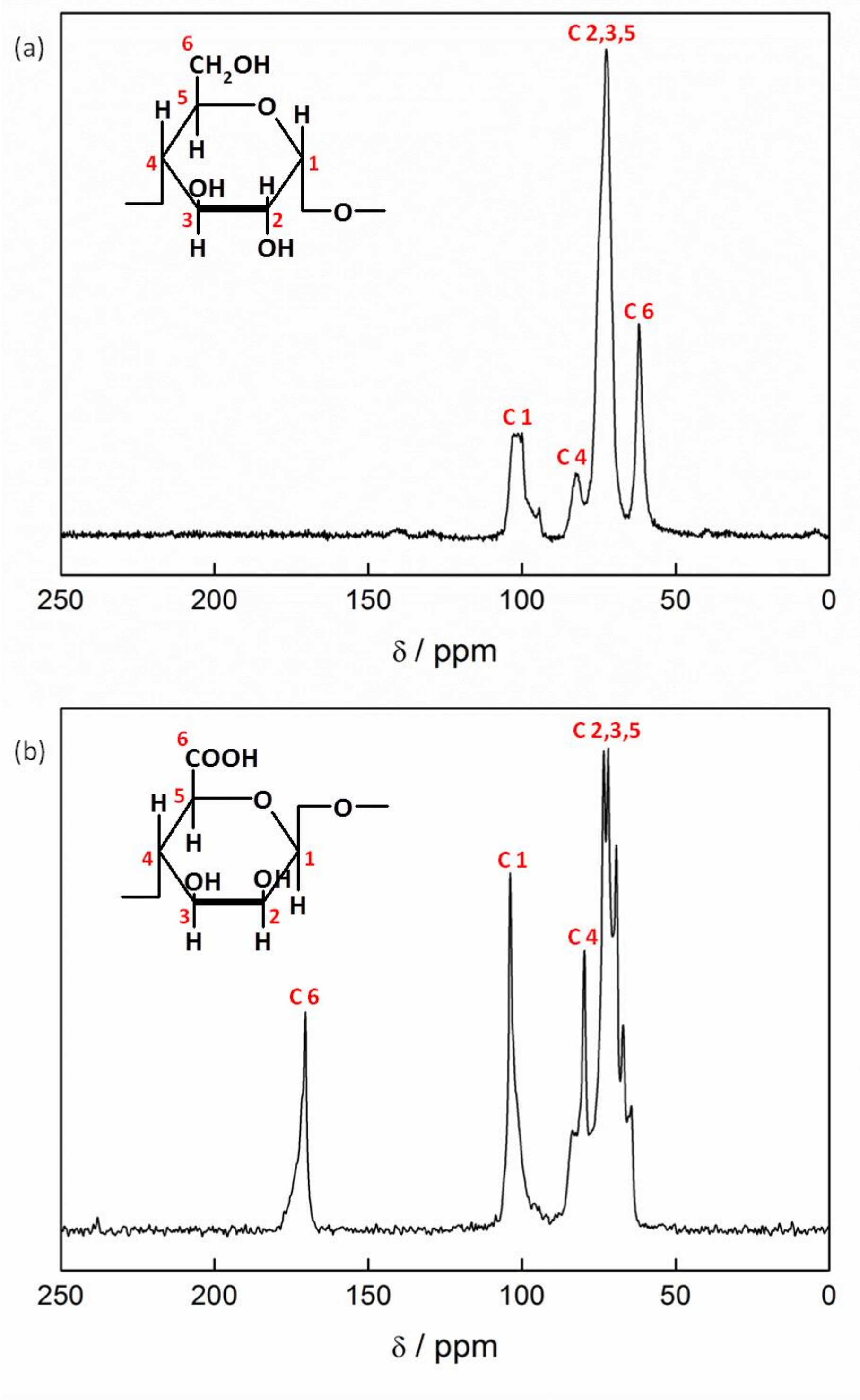

Supplementary Figure 1.1 ^{13}C MAS NMR spectra with labelling of peaks of (a) expanded starch and (b) expanded alginic acid.

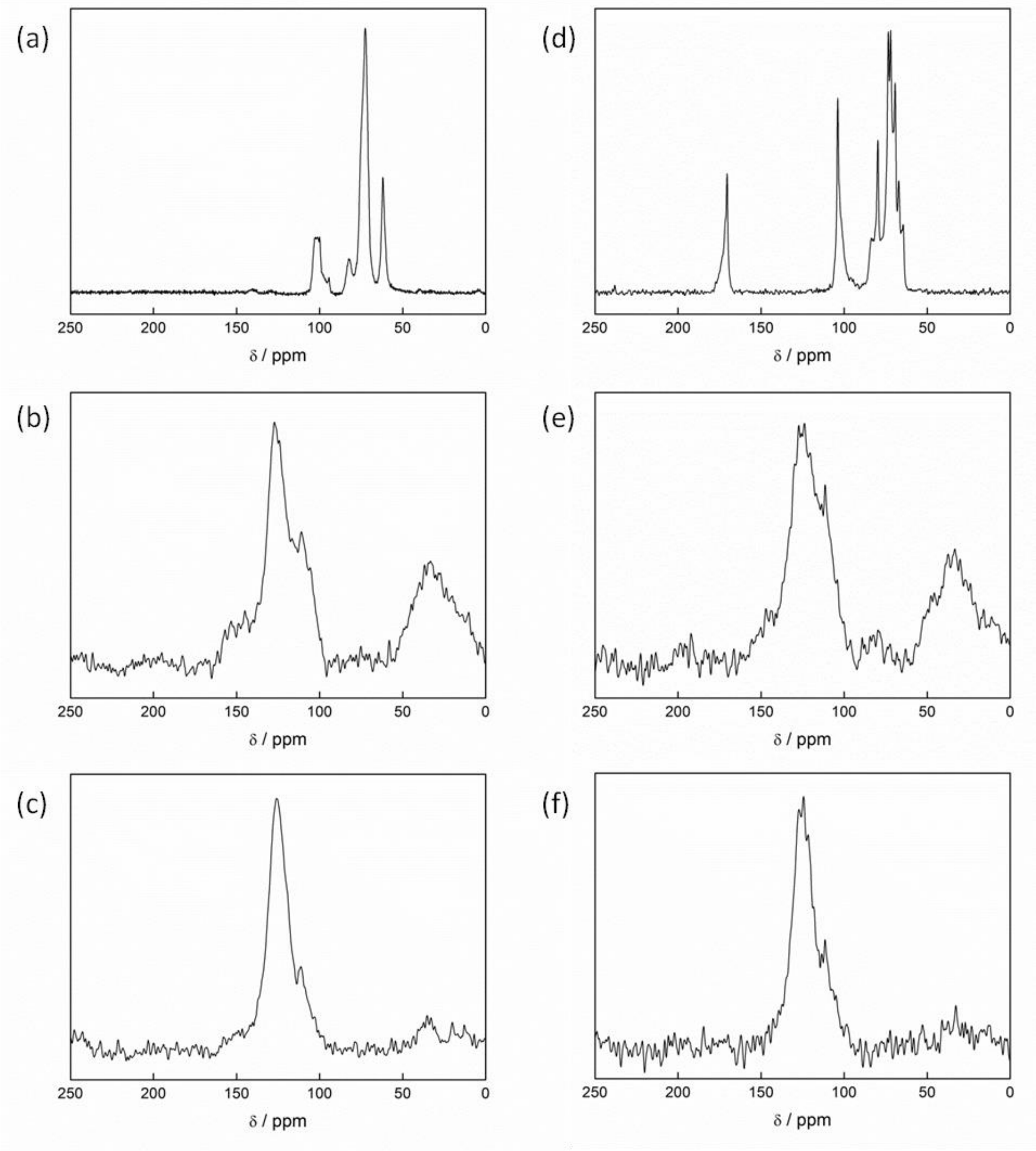

Supplementary Figure 1.2 ^{13}C MAS NMR spectra of (a) expanded starch, (b) S300, (c) S450, (d) expanded alginic acid, (e) A300 and (f) A450.

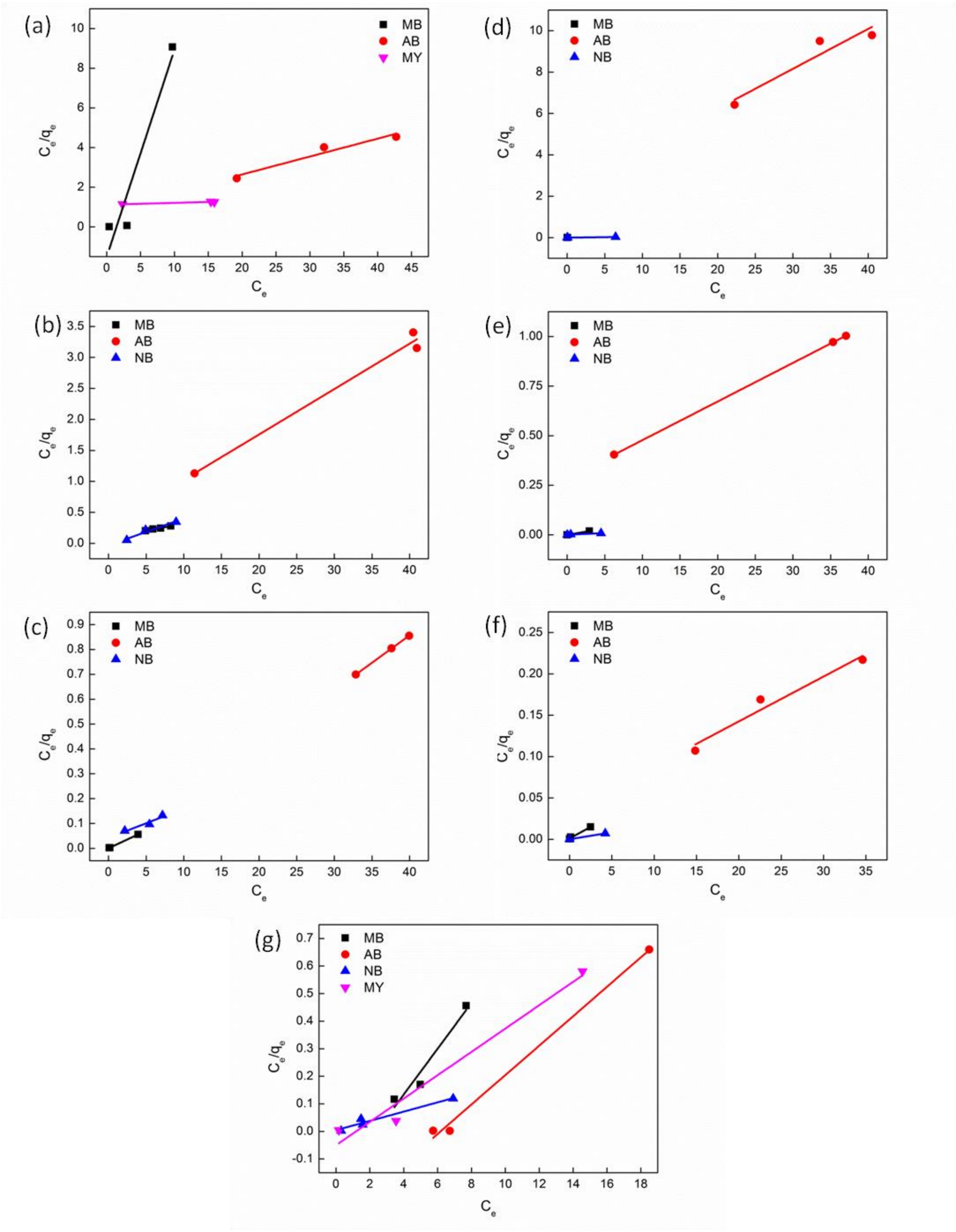

Supplementary Figure 1.3 Langmuir isotherm fitting graphs for (a) S300, (b) S450, (c) S800, (d) A300, (e) A450, (f) A800, (g) Norit.

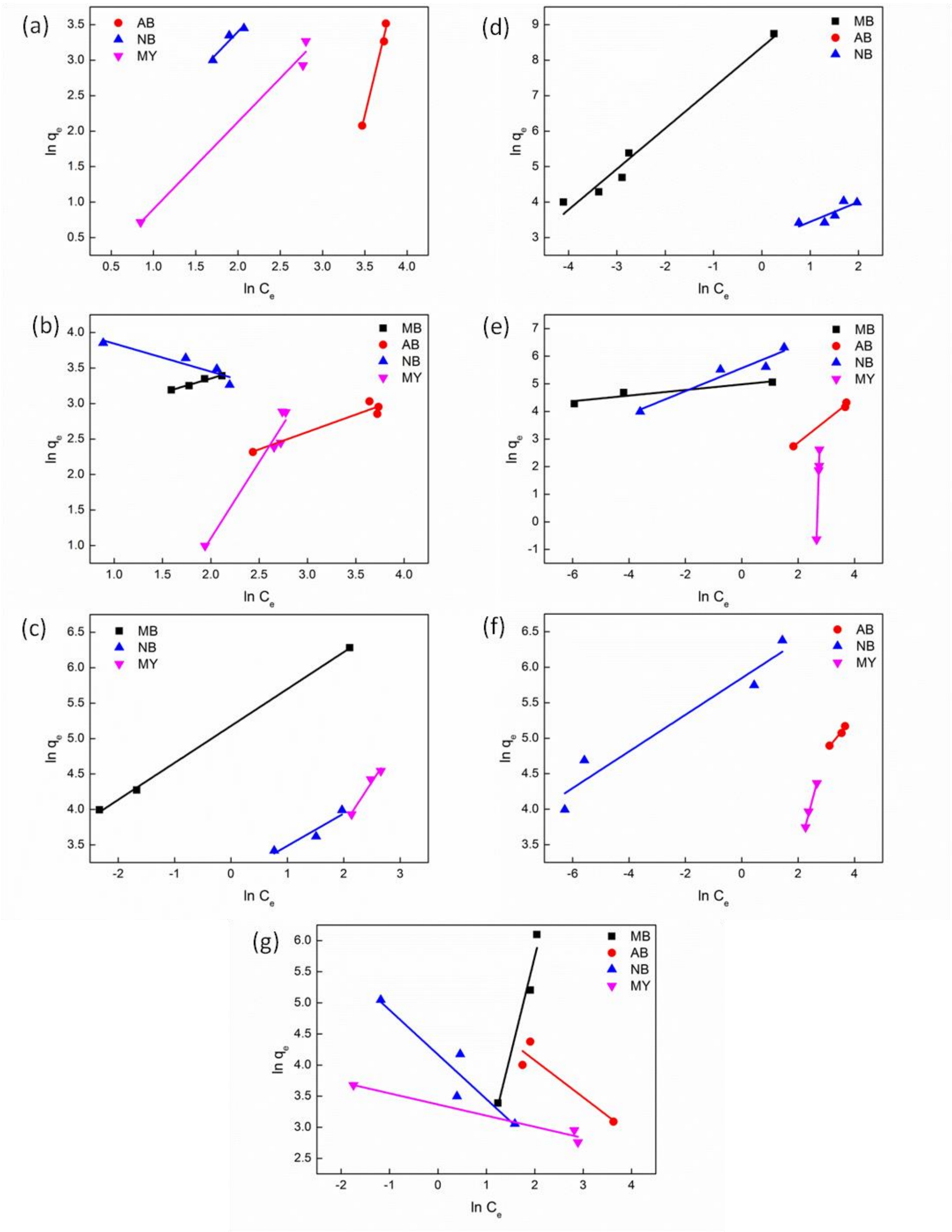

Supplementary Figure 1.4 Freundlich isotherm fitting graphs for (a) S300, (b) S450, (c) S800, (d) A300, (e) A450, (f) A800, (g) Norit.

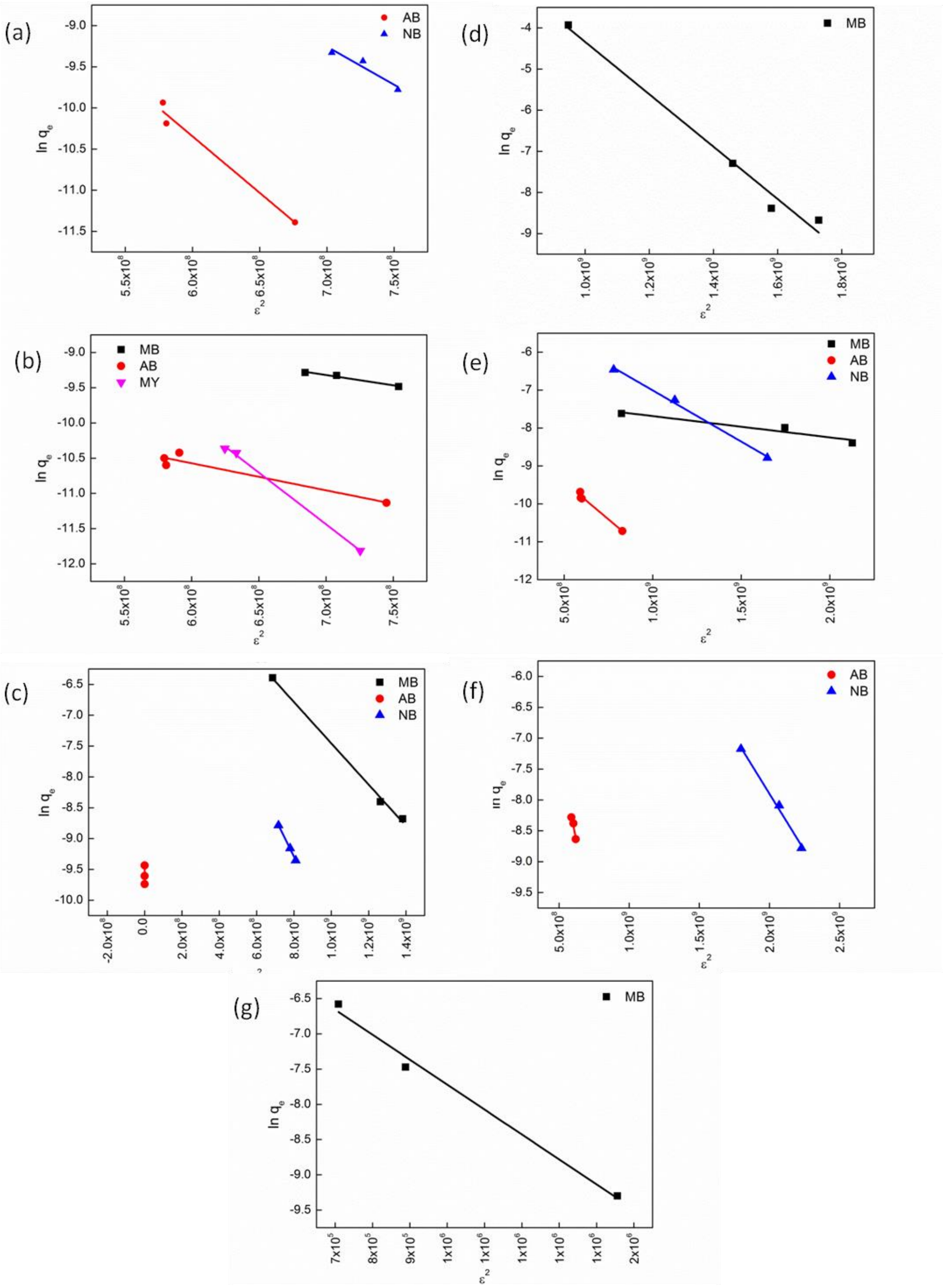

Supplementary Figure 1.5 D-R isotherm fitting graphs for (a) S300, (b) S450, (c) S800, (d) A300, (e) A450, (f) A800 and (g) Norit.

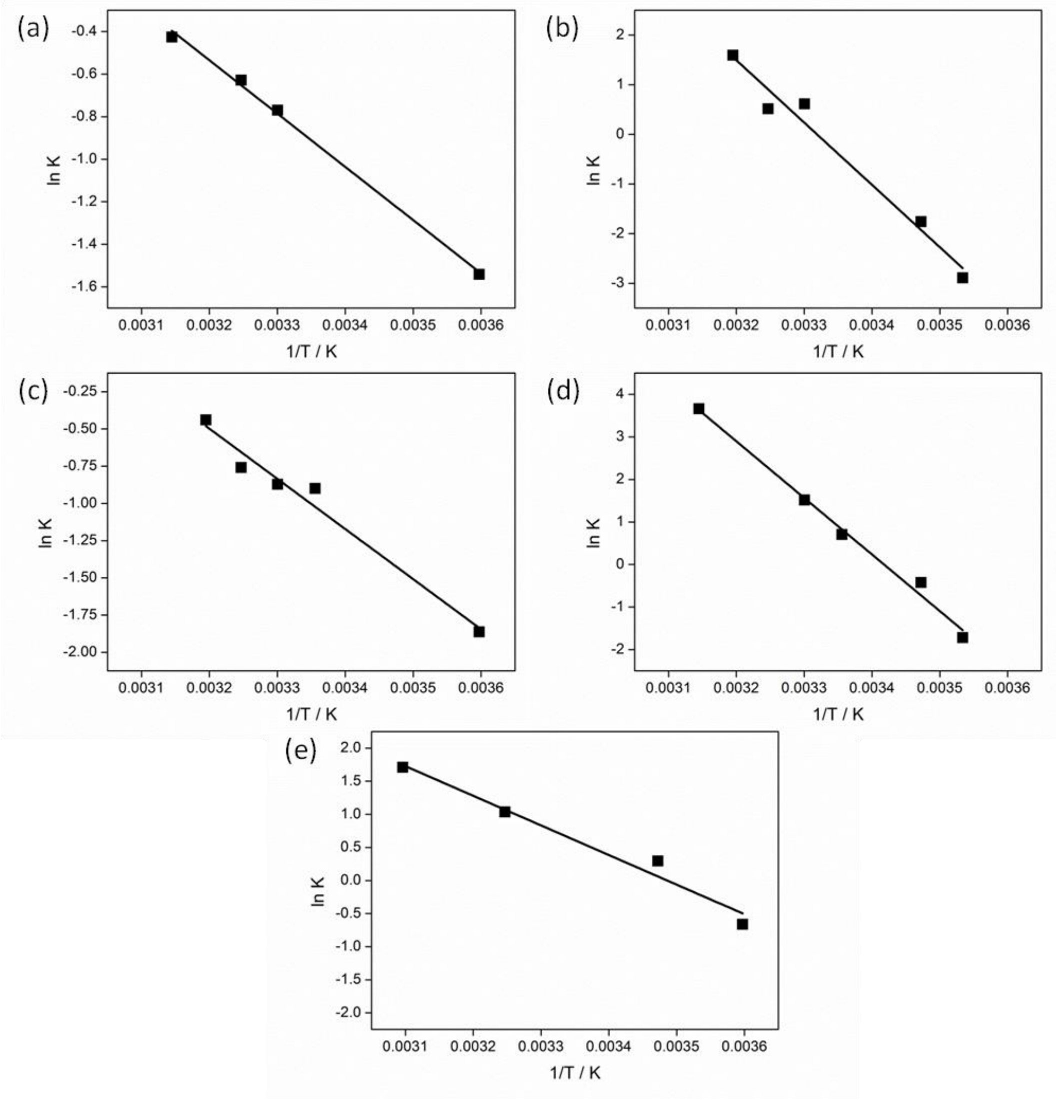

Supplementary Figure 1.6 Thermodynamic fitting graphs for methylene blue adsorption on to (a) S300, (b) A300, (c) S800, (d) A800, and (e) Norit.

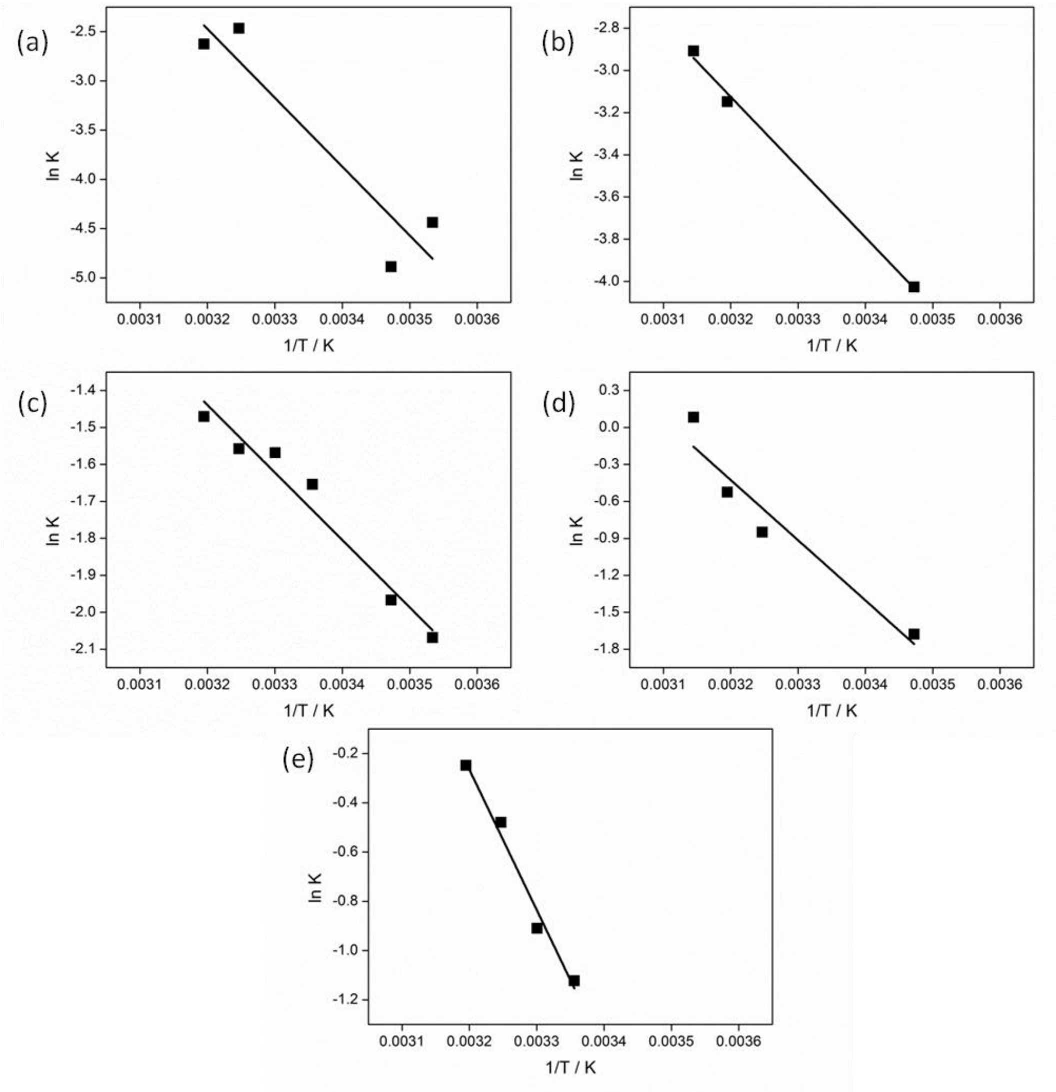

Supplementary Figure 1.7 Thermodynamic fitting graphs for acid blue 92 adsorption on to (a) S300, (b) A300, (c) S800, (d) A800, and (e) Norit.

Appendix 2.

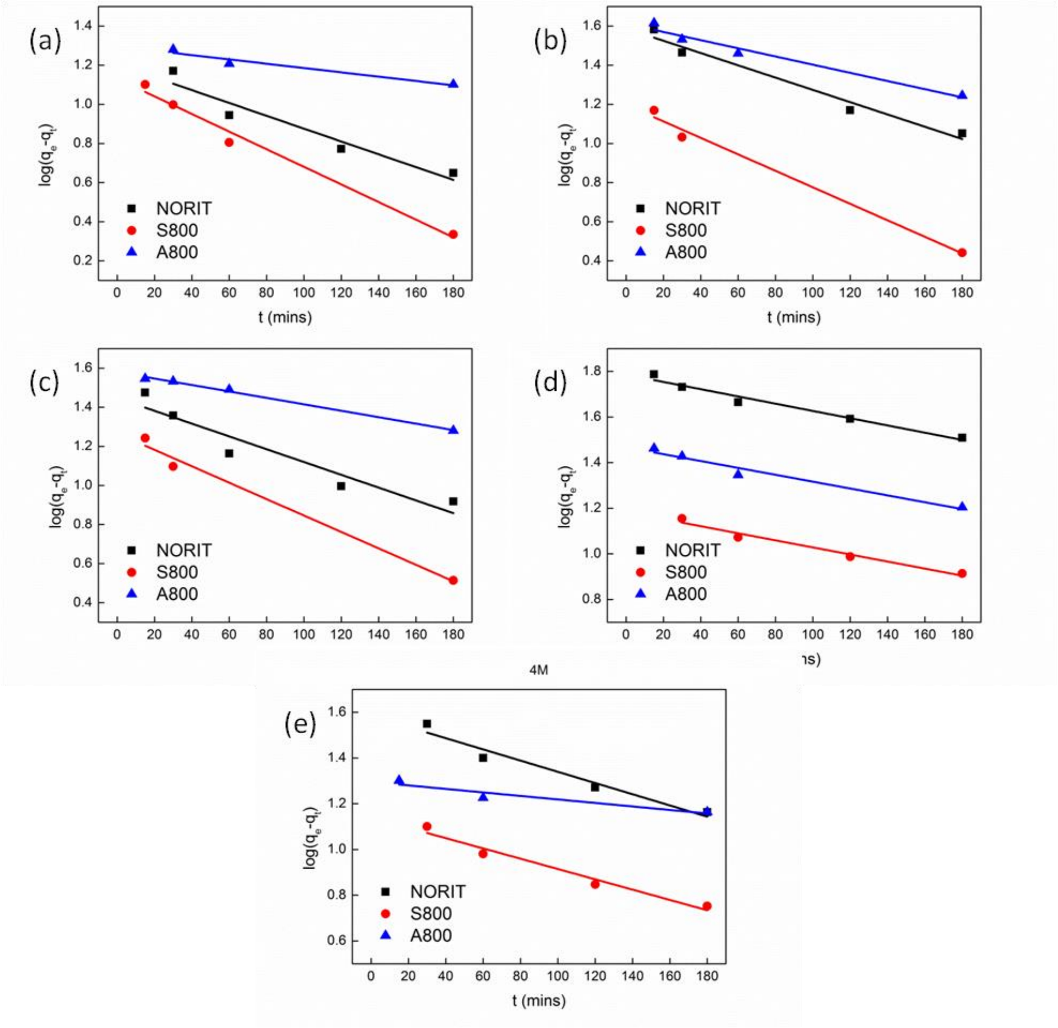

Supplementary Figure 2.1 First order kinetics (a) phenol, (b) o-cresol, (c) 2-fluorophenol, (d) 3-aminophenol and (e) 4-methoxphenol.

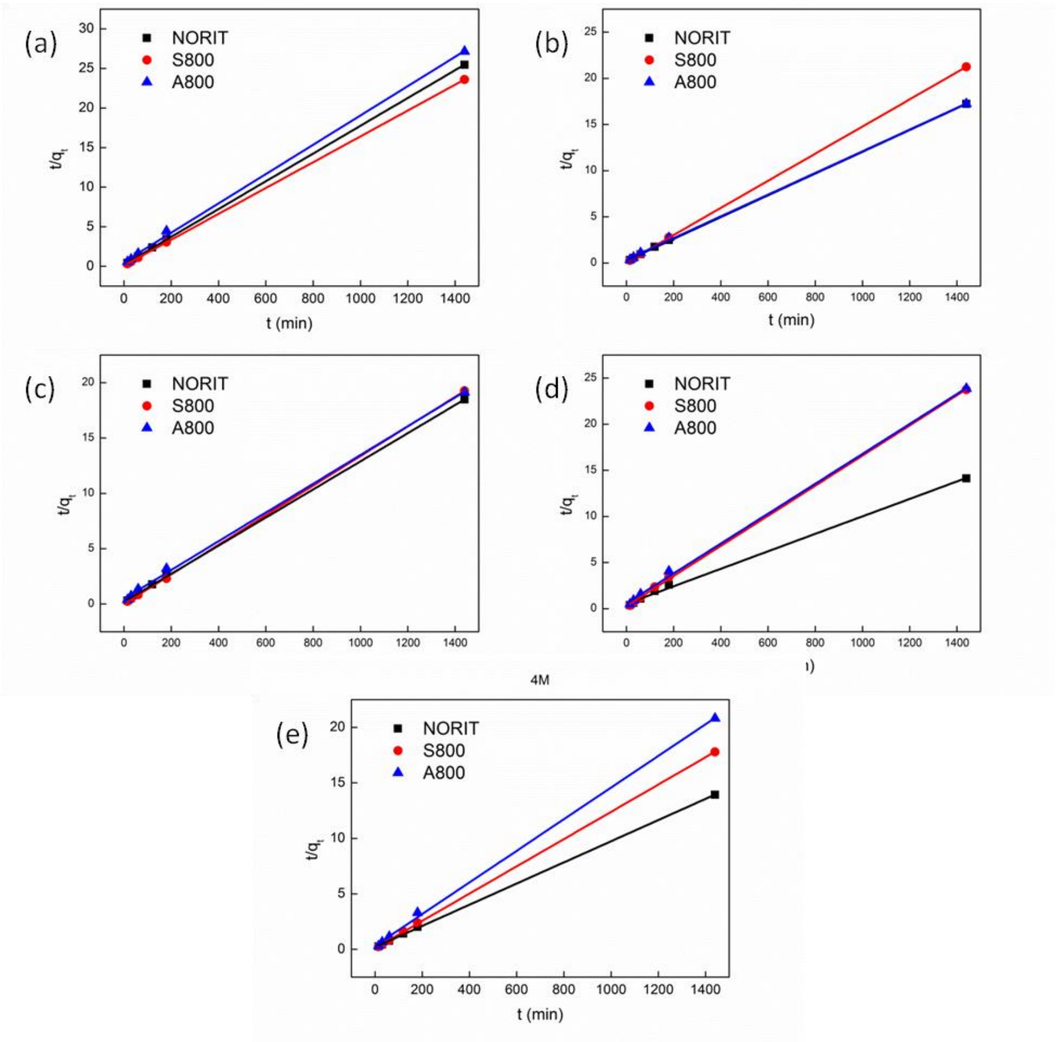

Supplementary Figure 2.2 Second order kinetics (a) phenol, (b) o-cresol, (c) 2-fluorophenol, (d) 3-aminophenol and (e) 4-methoxphenol.

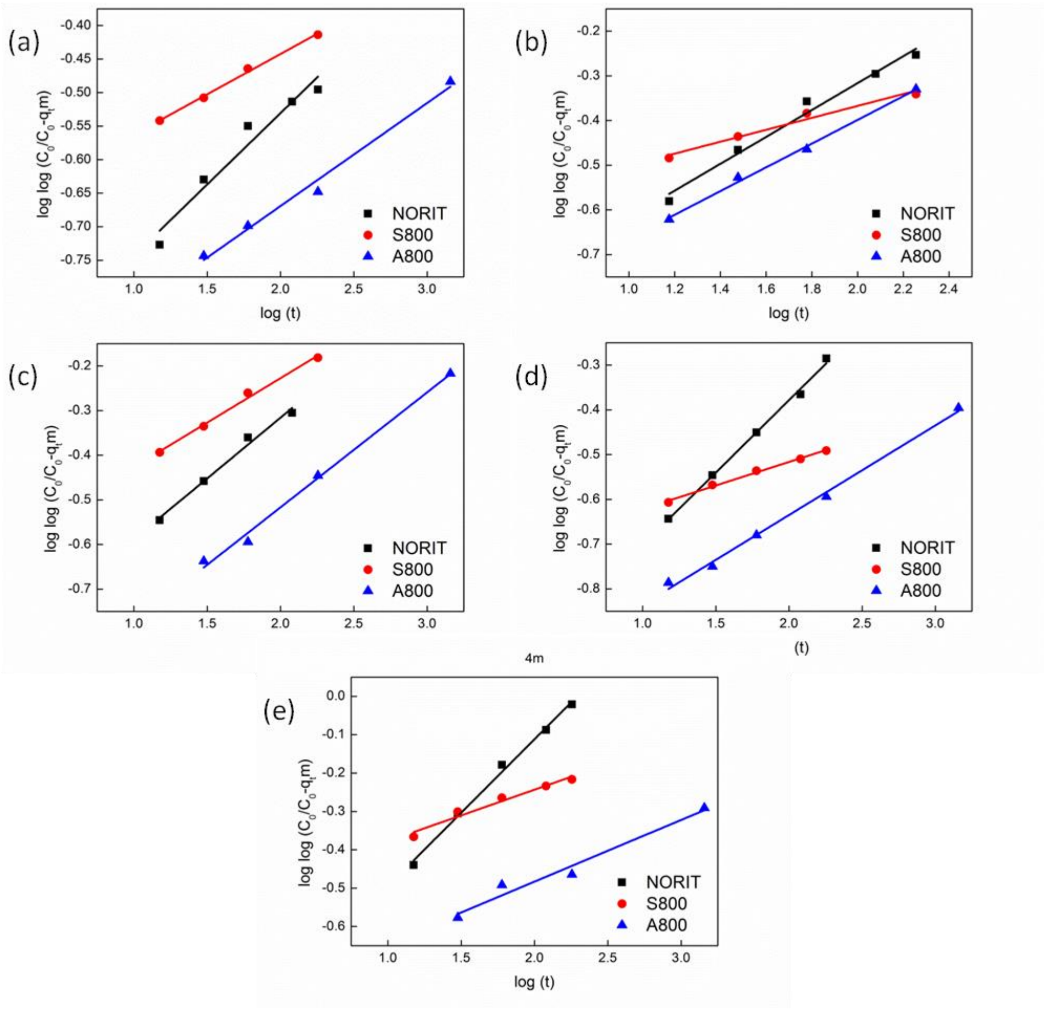

Supplementary Figure 2.3 Bangham's model kinetics (a) phenol, (b) o-cresol, (c) 2-fluorophenol, (d) 3-aminophenol and (e) 4-methoxphenol.

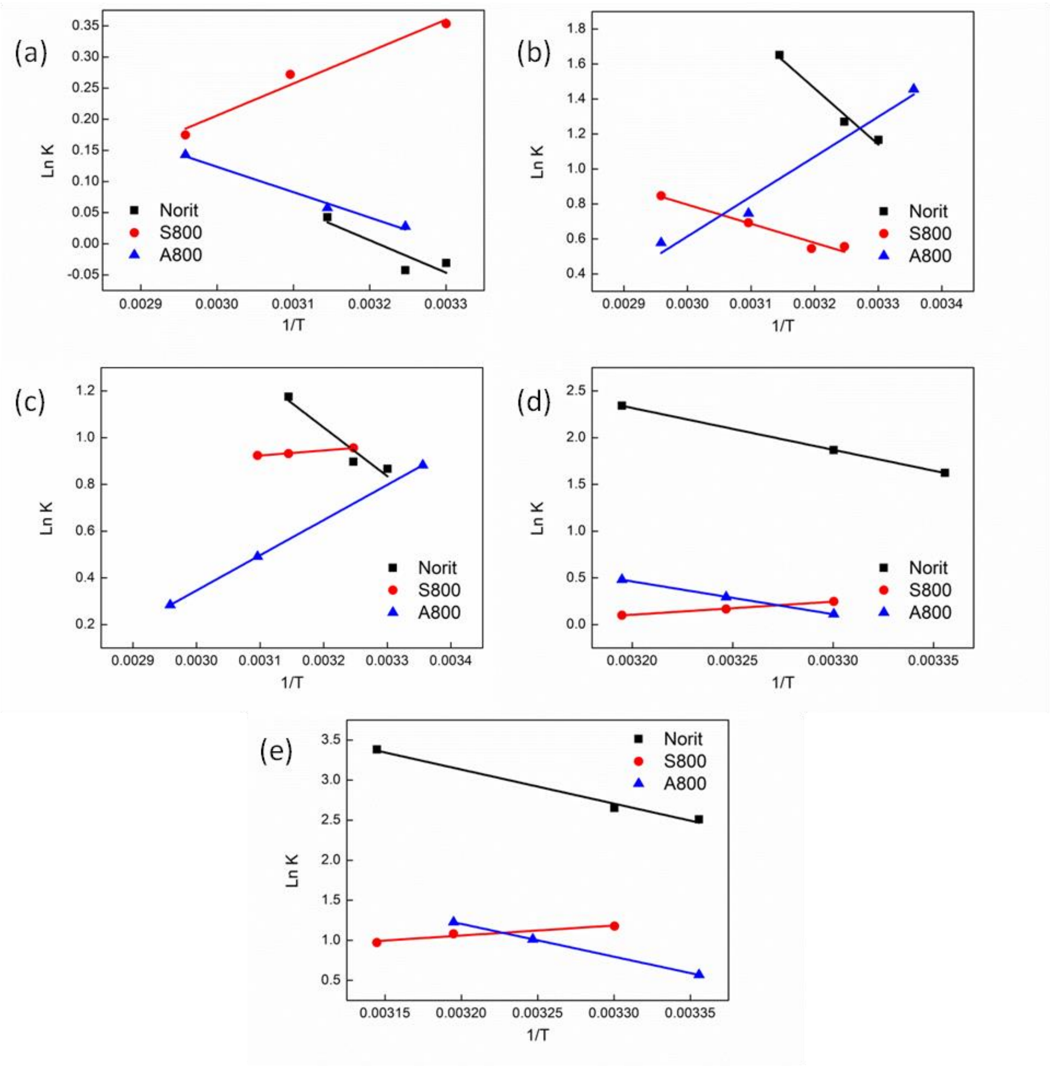

Supplementary Figure 2.4 Thermodynamic graphs (a) phenol, (b) o-cresol, (c) 2-fluorophenol, (d) 3-aminophenol and (e) 4-methoxphenol.

Appendix 3.

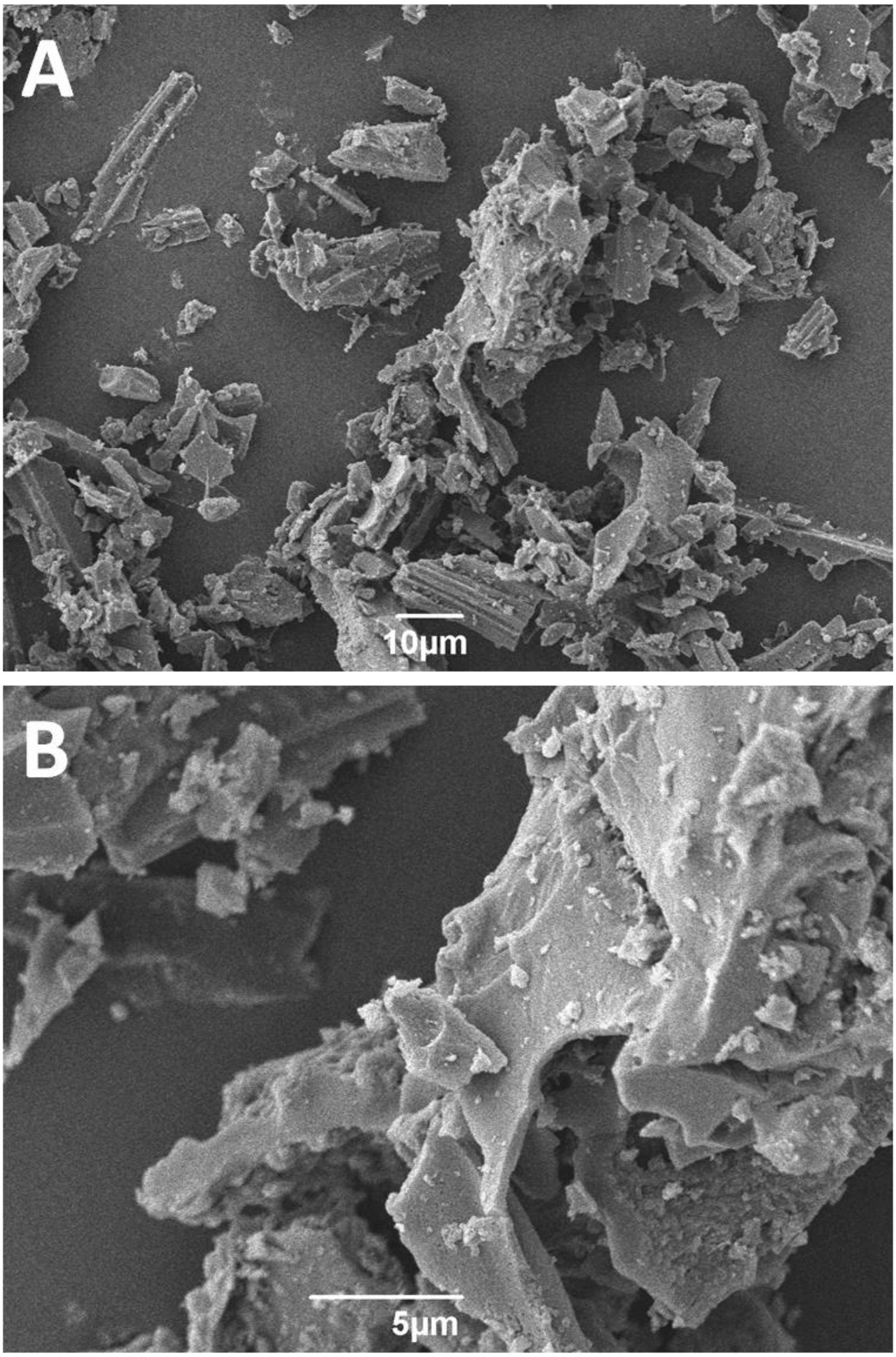

Supplementary Figure 3.1 Palladium on carbon 1% SEM images taken at (A) x1000 and (B) x4500 magnification.

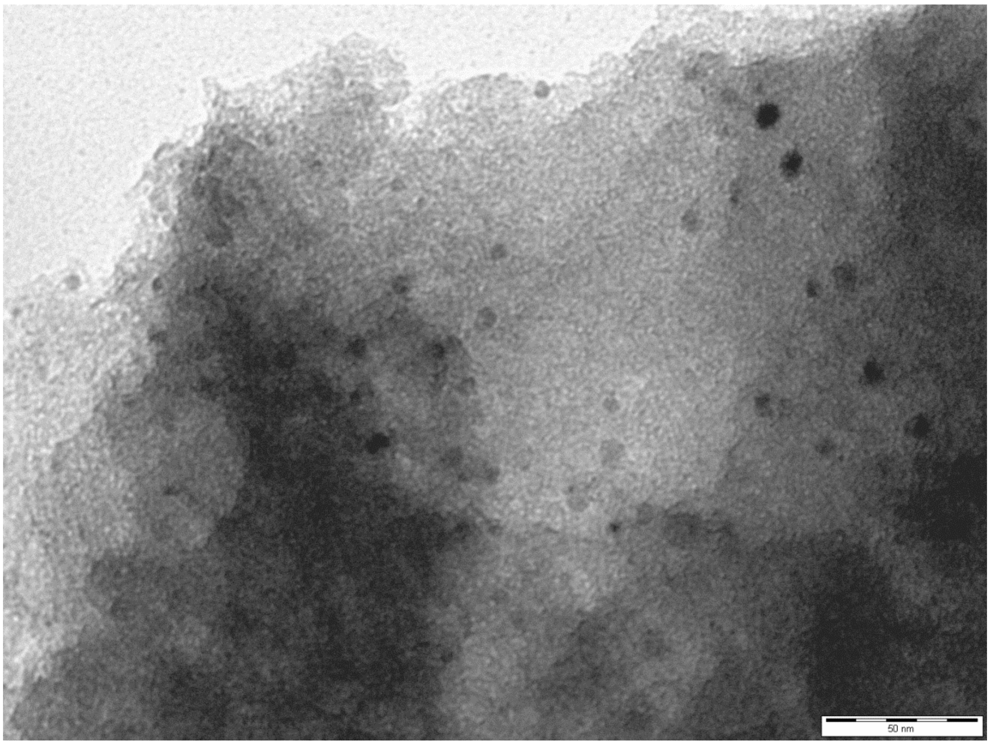

Supplementary Figure 3.2 Palladium on carbon 1% TEM image.

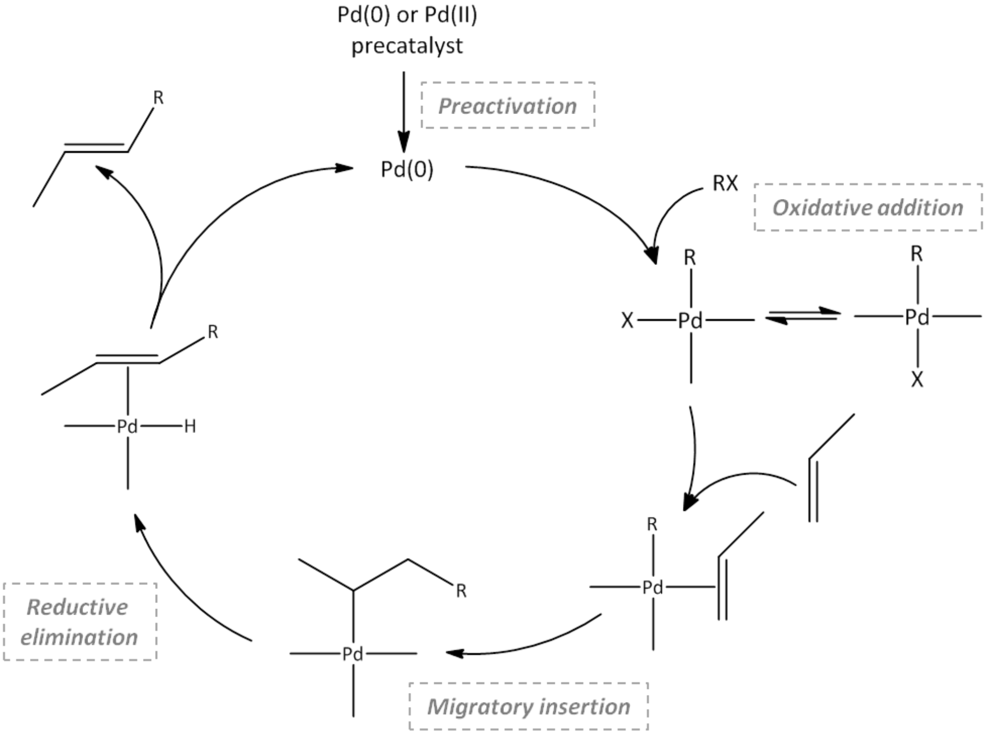

Supplementary Figure 3.3 A simplified representation of the catalytic cycle for the Heck reaction.(*302*)

Appendix 4.

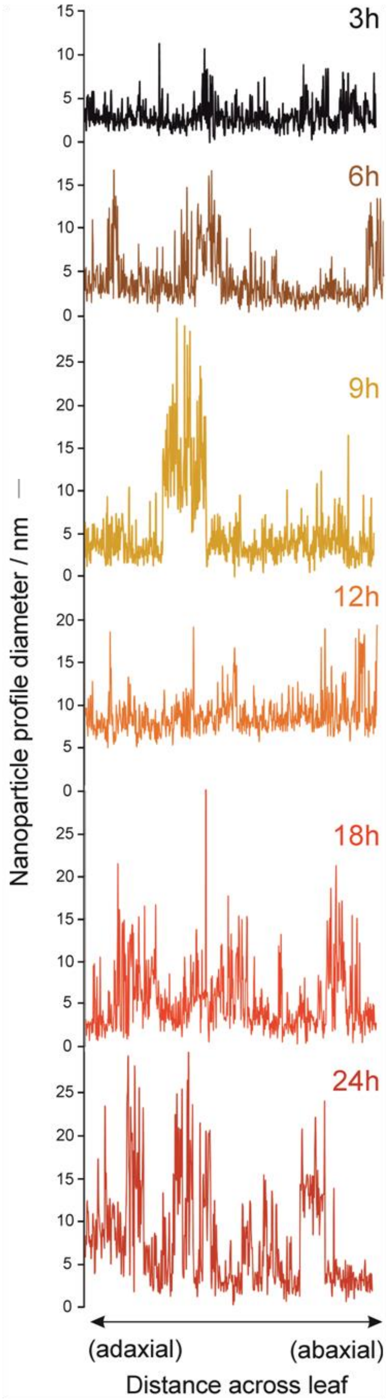

Supplementary Figure 4.1 Mean nanoparticle diameter in cells from adaxial to abaxial leaf surface. TEM sections from 3-week-old, liquid, culture grown Arabidopsis plants were treated with 10 mM potassium tetrachloropalladate and the mean palladium nanoparticle profile areas measures across the leaf over time.

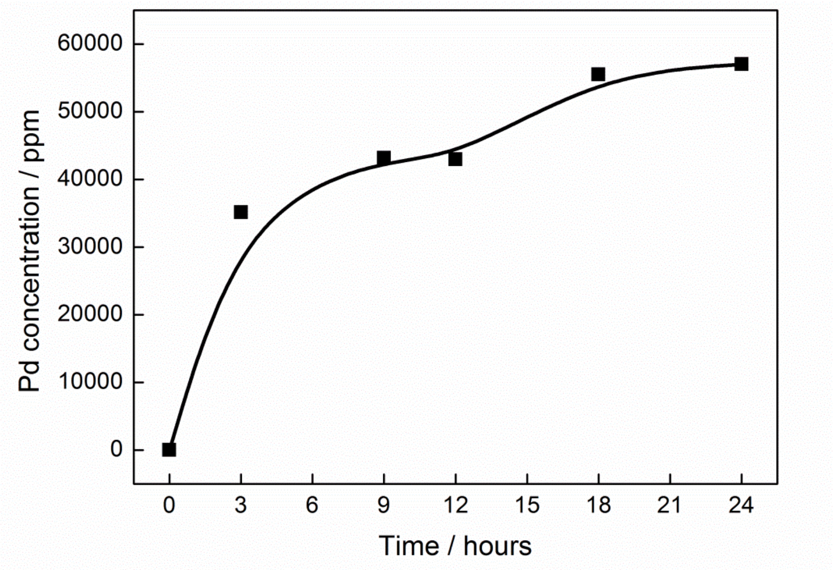

Supplementary Figure 4.2 Palladium concentration in plant vs time of exposure to palladium solution.

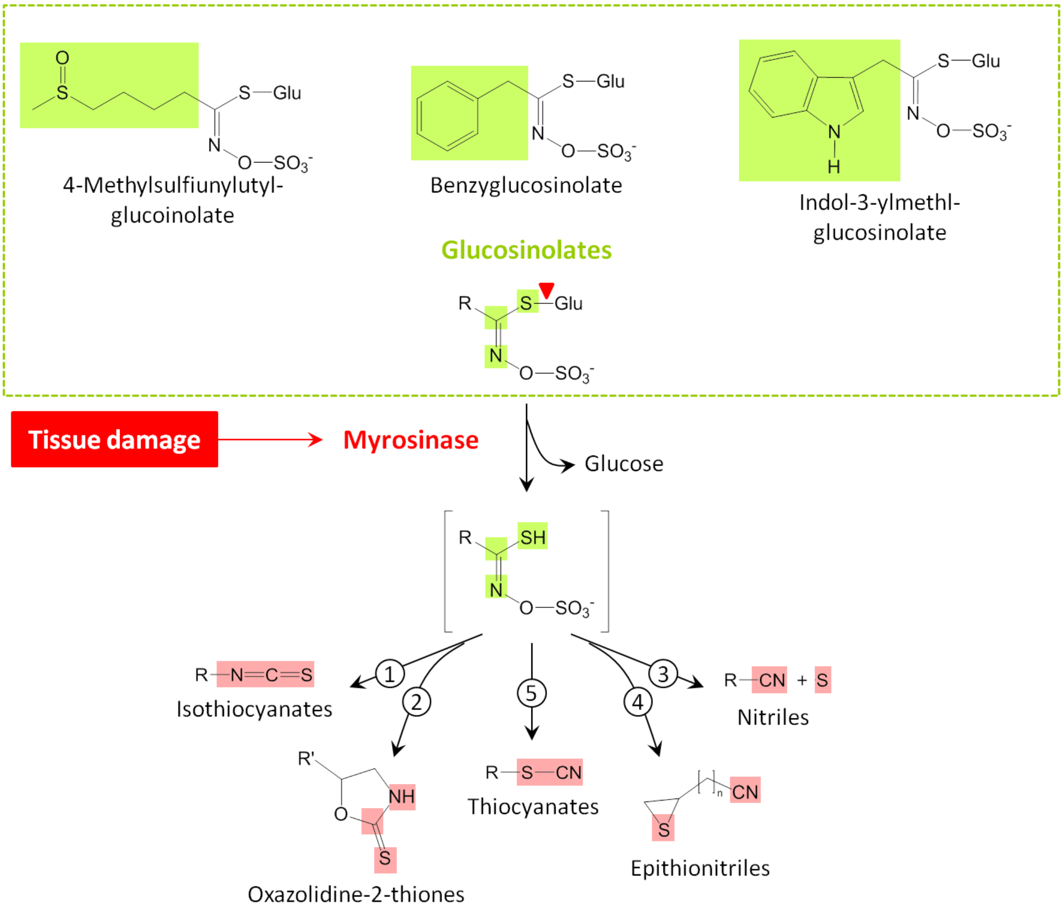

Supplementary Figure 4.3 Schematic showing the glucosinolate-myroinase system within plants: when tissue damage occurs the enzyme breaks down the glucosinolates to form cyano species that are potentially toxic.**(*286*)**

Supplementary Table 4.1 Atomic composition of dried Pd-plant determined by XPS analysis.

	Atomic %					
	C	O	N	Ca	Cl	Pd
Blank plant	77.4	18.6	3.8	0.2	0	0
Dried Pd plant	79.7	16.3	3.3	0	0.6	0.1

List of abbreviations

The following abbreviations are included in this thesis in addition to the Mendeleev periodic table symbols:

amu	Atomic mass unit
ASR	Automotive shredder residue
ATR	Attenuated total reflectance
BE	Binding energy
BET	Brunauer Emmett and Teller
BJH	Barrett Joyner and Halenda
CNAP	Centre for Novel Agricultural Products
CPS	Counts per second
DP	Degree of polymerisation
D-R	Dubinin-Radushkevich
DSC	Differential scanning calorimetry
EDA	Electron-donor acceptor
EDTA	Ethylenediaminetetraacetic acid
EDG	Electron donating group
EI	Electron ionisation
EOL	End of life
EOL-RR	End of life recycling rate
EPSRC	Engineering and Physical Sciences Research Council
EU	European Union
eV	Electron volts
EWG	Electron withdrawing group
FID	Flame ionisation detector
FT	Fourier transform
G	α-L-guluronic acid
GC	Gas chromatography
GCMS	Gas chromatography mass spectrometry
ICP	Inductively coupled plasma

IR	Infrared
IUPAC	International union of pure and applied chemistry
LCD	Liquid crystal display
M	β-D-mannuronic acid
MAS NMR	Magic angle spinning nuclear magnetic resonance
MCM	Mobil composition of matter
MSW	Municipal solid waste
MSWI	Municipal solid waste incineration
MNP	Metallic nanoparticle
NIST	National Institute of Standards and Technology
NMP	*N*-methylpyrollidone
NMR	Nuclear magnetic resonance
NP	Nanoparticle
OECD	Organisation of Economically Developed Countries
OES	Optical emission spectrometry
PdNP	Palladium nanoparticle
$Pd(OAc)_2$	Palladium acetate
PGM	Platinum group metals
ppm	Parts per million
R^2	Correlation coefficient
Rf	Response factor
rpm	Revolutions per minute
S	Surface area
S_{BET}	Surface area from BET isotherm
$scCO_2$	Supercritical carbon dioxide
SEM	Scanning electron microscopy
TEM	Transmission electron microscopy
TGA	Thermal gravimetric analysis
TGIR	Thermal gravimetric infrared analysis
THF	Tetrahydrofuran
TOF	Turnover frequency
TON	Turnover number
UK	United Kingdom

UNEP	United Nations Environmental Programme
US/USA	United States/United States of America
UV-Vis	Ultraviolet-visible
v/v	Volume/volume
w/w	Weight/weight
XPS	X-ray photoelectron spectroscopy

References

(*1*) M. Braungart and W. McDonough, *Cradle to cradle: Re-making the way we make things*, Jonathan Cape, London, 2008.

(*2*) P. T. Anastas and J. C. Warner, *Green Chemistry: Theory and Practice*, Oxford University Press, Oxford, 1998.

(*3*) M. Poliakoff, J. M. Fitzpatrick, T. R. Farren and P. T. Anastas, *Science*, 2002, **297**, 807-810.

(*4*) P. T. Anastas and R. L. Lankey, *Green Chem.*, 2000, **2**, 289-295.

(*5*) J. H. Clark, *Green Chem.*, February 1998, 1-8.

(*6*) T. Colburn, D. Dumanoski and J. Peterson Myers, *Our stolen future*, Dutton, New York, 1996.

(*7*) C. Hessel, C. Allegre, M. Maisseu, F. Charbit and P. Moulin, *J. Environ. Manage.*, 2007, **83**, 171-180.

(*8*) WHO, http://www.who.int/docstore/water_sanitation_health/vector/water_resources.htm, Accessed 25 January 2013.

(*9*) V. K. Gupta, I. Ali, T. A. Saleh, A. Nayak and S. Agarwal, *RSC Adv.*, 2012, **2**, 6380-6388.

(*10*) R. Connor, *Managing water under uncertainty and risk*, United Nations Educational, Scientific and Cultural Organization (UNESCO), 2012.

(*11*) R. Loos, B. M. Gawlik, G. Locoro, E. Rimaviciute, S. Contini and G. Bidoglio, *Environ. Pollut.*, 2009, **157**, 561-568.

(*12*) V. K. Gupta, P. J. M. Carrott, M. M. L. Ribeiro Carrott and Suhas, *Critical Reviews in Environmental Science & Technology*, 2009, **39**, 783-842.

(*13*) H. Genc, J. C. Tjell, D. McConchie and O. Schuiling, *J. Colloid Interface Sci.*, 2003, **264**, 327-334.

(*14*) USGS, *Bauxite and Alumina, USGS Mineral Commodity Summaries*, 1996.

(*15*) USGS, *Bauxite and Alumina, USGS Mineral Commodity Summaries*, 2012.

(*16*) M. Rafatullah, O. Sulaiman, R. Hashim and A. Ahmad, *J. Hazard. Mater.*, 2010, **177**, 70-80.

(*17*) G. Crini, *Bioresour. Technol.*, 2006, **97**, 1061-1085.

(*18*) F. Carrasco-Marin, M. A. Alvarez-Merino and C. Moreno-Castilla, *Fuel*, 1996, **75**, 966-970.

(*19*) S. Babel and T. A. Kurniawan, *J. Hazard. Mater.*, 2003, **B97**, 219-243.

(*20*) S. E. Bailey, T. J. Olin, R. M. Bricka and D. D. Adrian, *Water Res.*, 1999, **33**, 2469-2479.

(*21*) S. Kesraoui-Ouki, C. R. Cheeseman and R. Perry, *J. Chem. Technol. Biotechnol.*, 1994, **59**, 121-126.

(*22*) I. Bouzaida and M. B. Rammah, *Mater. Sci. Eng.*, 2002, **C21**, 151-155.

(*23*) G. Annadurai, L. Y. Ling and J.-F. Lee, *J. Hazard. Mater.*, 2008, **152**, 337-346.

(*24*) E. Demirbas, N. Dizge, M. T. Sulak and M. Kobya, *Chem. Eng. J.*, 2009, **148**, 480-487.

(*25*) F. Ferrero, *J. Hazard. Mater.*, 2007, **142**, 144-152.

(*26*) R.-S. Juang, P.-C. Wu and R.-L. Tseng, *Colloids Surf., A*, 2002, **201**, 191-199.

(*27*) M. Otero, F. Rozada, L. F. Calvo, A. I. Garcia and A. Moran, *Dyes and pigments*, 2003, **57**, 55-65.

(*28*) M. Arami, N. Y. Limaee, N. M. Mahmoodi and N. S. Tabrizi, *J. Hazard. Mater.*, 2006, **135**, 171-179.

(*29*) G. Annadurai, R.-S. Juang and D.-J. Lee, *J. Hazard. Mater.*, 2002, **92**, 263-274.

(*30*) P. Janos, H. Buchtova and M. Ryznarova, *Water Res.*, 2003, **37**, 4938-4944.

(*31*) V. K. Gupta, A. Mittal, L. Kurup and J. Mittal, *J. Colloid Interface Sci.*, 2006, **304**, 52-57.

(*32*) K. G. Bhattacharyya and S. S. Gupta, *Sep. Purif. Technol.*, 2006, **50**, 388-397.

(*33*) V. Sarin and K. K. Pant, *Bioresour. Technol.*, 2006, **97**, 15-20.

(*34*) G. McKay, J. F. Porter and G. R. Prasad, *Water, Air, Soil Pollut.*, 1999, **114**, 423-438.

(*35*) A. Aygun, S. Yenisoy-Karakas and I. Duman, *Microporous Mesoporous Mater.*, 2003, **66**, 189-195.

(*36*) Y. Z. Fu and T. Viraraghavan, *Water Qual. Res. J. Can.*, 2000, **35**, 95-111.

(*37*) F. A. Pavan, E. C. Lima, S. L. P. Dias and A. C. Mazzocato, *J. Hazard. Mater.*, 2008, **150**, 703-712.

(*38*) V. Ponnusami, S. Vikram and S. N. Srivastava, *J. Hazard. Mater.*, 2008, **152**, 276-286.

(*39*) W.-T. Tsai, H.-C. Hsu, T.-Y. Su, K.-Y. Lin and C.-M. Lin, *J. Hazard. Mater.*, 2008, **154**, 73-78.

(*40*) B. H. Hameed, *J. Hazard. Mater.*, 2009, **162**, 344-350.

(*41*) B. M. W. P. K. Amarasinghe and R. A. Williams, *Chem. Eng. J.*, 2007, **132**, 299-309.

(*42*) G. Sun and X. Xu, *Ind. Eng. Chem. Res.*, 1997, **36**, 808-812.

(*43*) Y. H. Magdy and A. A. M. Daifullah, *Waste Manage.*, 1998, **18**, 219-226.

(*44*) S. Wang and Z. H. Zhu, *J. Hazard. Mater.*, 2006, **136**, 946-952.

(*45*) C. Namasivayam and D. Arasi, *Chemosphere*, 1997, **34**, 401-417.

(*46*) B. H. Hameed and A. A. Ahmad, *J. Hazard. Mater.*, 2009, **164**, 870-875.

(*47*) R. S. Blackburn, *Environ. Sci. Technol.*, 2004, **38**, 4905-4909.

(*48*) V. Budarin, J. H. Clark, F. E. I. Deswarte, J. J. E. Hardy, A. J. Hunt and F. M. Kerton, *Chem. Commun.*, 2005, 2903-2905.

(*49*) J. O. B. Carioca, H. L. Arora, P. V. Pannir Selcam, F. C. A. Tavares, J. F. Kennedy and C. J. Knill, *Starch*, 1996, **9**, 322-326.

(*50*) http://www.starch.dk/isi/market/index.asp, Accessed 31/1/2013.

(*51*) A. Higson, *NNFCC Renewable Chemicals Factsheet: Starch*, NNFCC, 2011.

(*52*) R. Parker and S. G. Ring, *J. Cereal Sci.*, 2001, **24**, 1-17.

(*53*) R. J. White, *Porous polysaccharide-derived materials,* PhD Thesis, University of York, 2008.

(*54*) S. Hizukuri, *Carbohydr. Res.*, 1985, **141**, 295-306.

(*55*) K. Koizumi and M. Fukuda, *J. Chromatogr. A*, 1991, **585**, 233-238.

(*56*) N. J. Atkin, R. M. Abeysekera and A. W. Robards, *Carbohydr. Polym.*, 1998, **36**, 193-204.

(*57*) N. J. Atkin, R. M. Abeysekera, S. L. Cheng and A. W. Robards, *Carbohydr. Polym.*, 1998, **36**, 173-192.

(*58*) J.-Y. Li and A.-I. Yeh, *J. Food Eng.*, 2001, **50**, 141-148.

(*59*) V. Budarin, J. H. Clark, J. J. E. Hardy, R. Luque, K. Milkowski, S. J. Tavener and A. J. Wilson, *Angew. Chem.*, 2006, **118**, 3866-3870.

(*60*) M. Seguchi, *Cereal Chem.*, 1995, **72**, 602-608.

(*61*) M. Robitzer, F. Di Renzo and F. Quignard, *Microporous Mesoporous Mater.*, 2011, **140**, 9-16.

(*62*) F. Quignard, R. Valentin and F. Di Renzo, *New J. Chem.*, 2008, **32**, 1300-1310.

(*63*) D. F. Pindar and C. Bucke, *Biochem. J*, 1975, **152**, 617-622.

(*64*) J. E. Scott, *Biochim. Biophys. Acta*, 1968, **170**, 471-473.

(*65*) R. J. White, C. Antonio, V. Budarin, E. Bergstrom, J. Thomas-Oates and J. H. Clark, *Adv. Funct. Mater.*, 2010, **20**, 1834-1841.

(*66*) K. I. Draget, G. Skjak-Braek and O. Smidsrod, *Int. J. Biol. Macromol.*, 1997, **21**, 47-55.

(*67*) M. E. Davis, *Nature*, 2002, **417**, 813-821.

(*68*) U. Ciesla and F. Schuth, *Microporous Mesoporous Mater.*, 1999, **27**, 131-149.

(*69*) L. B. McCusker, F. Liebau and G. Engelhardt, *Microporous Mesoporous Mater.*, 2003, **58**, 3-13.

(*70*) C. Liang, Z. Li and S. Dai, *Angew. Chem. Int. Ed.*, 2008, **47**, 3696-3717.

(*71*) C. T. Kresge, M. E. Lenonowicz, W. J. Roth, J. C. Vartull and J. S. Beck, *Nature*, 1992, **359**, 710-712.

(*72*) R. Ryoo, S. Hoon Joo and S. Jun, *J. Phys. Chem. B*, 1999, **103**, 7743-7746.

(*73*) S. H. Joo, S. J. Ghoi, I. Oh, J. Kwak, Z. Liu, O. Terasaki and R. Ryoo, *Nature*, 2001, **412**, 169-172.

(*74*) M. Kruk, M. Jaroniec, T.-W. Kim and R. Ryoo, *Chem. Mater.*, 2003, **15**, 2815-2823.

(*75*) S. Jun, S. H. Joo, R. Ryoo, M. Kruk, M. Jaroniec, Z. Liu, T. Ohsuna and O. Terasaki, *J. Am. Chem. Soc.*, 2000, **122**, 10712-10713.

(*76*) R. Luque, D. J. Macquarrie, V. Budarin, J. H. Clark, K. Milkowski and R. J. White, **US 2009/0078913 A1**.

(*77*) V. Budarin, J. H. Clark, R. Luque and R. J. White, *Material Matters*, 2009, **4**, 19-25.

(*78*) V. Budarin, J. H. Clark, R. Luque and D. J. Macquarrie, *Chem. Commun.*, 2007, **6**, 634-636.

(*79*) R. Luque, V. Budarin, P. S. Shuttleworth and J. H. Clark, *Boletin del Grupo Espanol del Carbon*, 2012, **24**, 7-11.

(*80*) A.-H. Lu, W.-C. Li, W. Schmidt and F. Schuth, *Microporous Mesoporous Mater.*, 2005, **80**, 117-128.

(*81*) V. Budarin, J. H. Clark, R. Luque, D. J. Macquarrie, A. Koutinas and C. Webb, *Green Chem.*, 2007, **9**, 992-995.

(*82*) V. Budarin, J. H. Clark, R. Luque, D. J. Macquarrie and R. J. White, *Green Chem.*, 2008, **10**, 382-387.

(*83*) R. J. White, R. Luque, V. Budarin, J. H. Clark and D. J. Macquarrie, *Chem. Soc. Rev.*, 2009, **38**, 481-494.

(*84*) S. Eustis and M. A. El-Sayed, *Chem. Soc. Rev.*, 2005, **35**, 209-217.

(*85*) A. T. Bell, *Science*, 2003, **299**, 1688-1691.

(*86*) J. Virkutyte and R. S. Varma, *Chem.Sci.*, 2011, **2**, 837-846.

(*87*) G. Bystrzejewska-Piotrowska, J. Golimowski and P. L. Urban, *Waste Manage.*, 2009, **29**, 2587-2595.

(*88*) S. Sharifi, S. Behzadi, S. Laurent, M. Laird Forrest, P. Stroeve and M. Mahmoudi, *Chem. Soc. Rev.*, 2012, **41**, 2323-2343.

(*89*) D. D. Caspi, *The adaptive nature of palladium reactivity in synthesis*, PhD Thesis, California Institute of Technology, 2008.

(*90*) J. Tsuji, *Palladium Reagents and Catalysis: New Perspectives for the 21st Century*, John Wiley & Sons, Ltd, 2004.

(*91*) D. Astruc, *Inorg. Chem.*, 2007, **46**, 1884-1894.

(*92*) D. Astruc, *Nanoparticles and Catalysis*, Wiley-VCH Verlag GmbH & Co., 2008.

(*93*) S. Iravani, *Green Chem.*, 2011, **13**, 2638-2650.

(*94*) D. Astruc, F. Lu and J. R. Aranzaes, *Angew. Chem. Int. Ed.*, 2005, **44**, 7852-7872.

(*95*) D. I. Gittins and F. Caruso, *Angew. Chem. Int. Ed.*, 2001, **40**, 3001-3004.

(*96*) A. Bhatnagar and A. K. Jain, *J. Colloid Interface Sci.*, 2005, **281**, 49-55.

(*97*) J. W. Lee, S. P. Choi, R. Thiruvenkatachari, W. G. Shim and H. Moon, *Dyes and Pigments*, 2006, **69**, 196-203.

(*98*) I. A. W. Tan, B. H. Hameed and A. L. Ahmad, *Chem. Eng. J.*, 2007, **127**, 111-119.

(*99*) T. Robinson, G. McMullan, R. Marchant and P. Nigam, *Bioresour. Technol.*, 2001, **77**, 247-255.

(*100*) I. J. Muhammad and A. N. Muhammad, *J. Hazard. Mater.*, 2007, **139**, 57-66.

(*101*) I. M. Banat, P. Nigam, D. Singh and R. Marchant, *Bioresour. Technol.*, 1996, **58**, 217-227.

(*102*) Y. Al-Degs, M. A. M. Khraisheh, S. J. Allen and M. N. Ahmad, *Water Res.*, 2000, **34**, 927-935.

(*103*) M. Dogan, Y. Ozdemir and M. Alkan, *Dyes and Pigments*, 2007, **75**, 701-713.

(*104*) K. R. Ramakrishna and T. Viraraghavan, *Water Sci. Technol.*, 1997, **36**, 189-196.

(*105*) C. O'Neill, F. R. Hawkes, D. L. Hawkes, N. D. Lourenco, H. M. Pinheiro and W. Delere, *J. Chem. Technol. Biotechnol.*, 1999, **74**, 1009-1018.

(*106*) G. E. Walsh and L. H. Bahner, *Environ. Pollut.*, 1980, **21**, 169-179.

(*107*) K. G. Bhattacharyya and A. Sharma, *J. Environ, Manag.*, 2004, **71**, 217-229.

(*108*) V. Golob and A. Ojstrek, *Dyes and Pigments*, 2005, **64**, 57-61.

(*109*) Q. Sun and L. Yang, *Water Res.*, 2003, **37**, 1535-1544.

(*110*) K. K. H. Choy, G. McKay and J. F. Porter, *Resour. Conserv. Recy.*, 1999, **27**, 57-71.

(*111*) B. H. Hameed, A. L. Ahmad and K. N. A. Latiff, *Dyes and Pigments*, 2007, **75**, 143-149.

(*112*) J. Avom, K. J. Mbadcam, C. Noubactep and P. Germain, *Carbon*, 1997, **35**, 365-369.

(*113*) B. K. Singh and N. S. Rawat, *J. Chem. Technol. Biotechnol.*, 1994, **61**, 307-317.

(*114*) V. Budarin, J. H. Clark, F. E. I. Deswarte, J. J. E. Hardy, A. J. H. Hunt and F. M. Kerton, *Chem. Commun.*, 2005, 2903-2905.

(*115*) R. J. White, V. Budarin and J. H. Clark, *ChemSusChem*, 2008, **1**, 408-411.

(*116*) N. J. Atkin, R. M. Abeysekera and A. W. Robards, *Carbohydr. Polym.*, 1998, **36**, 193-204.

(*117*) H. L. Parker, A. J. Hunt, V. Budarin, P. S. Shuttleworth, K. L. Miller and J. H. Clark, *RSC Adv.*, 2012, **2**, 8992-8997.

(*118*) A. Haug, 1968, **US Patent 3,396,158**.

(*119*) M. Jung, K. Ahn, Y. Lee, K. Kim, J. Rhee, J. T. Park and K. Paeng, *Microchem. J.*, 2001, **70**, 123-131.

(*120*) M. Valix, W. Cheung and G. McKay, *Langmuir*, 2006, **22**, 4574-4582.

(*121*) K. S. W. Sing, D. H. Everett, R. A. W. Haul, L. Moscou and T. Siemieniewska, *Pure Appl. Chem.*, 1985, **57**, 603-619.

(*122*) F. Rouquerol, J. Rouquerol and K. S. W. Sing,*Adsorption by powders & porous solids: Principles, methodology & applications*, Academic Press, London, 1999, pp. 204-206.

(*123*) L. Tellez, J. Rubio and J. L. Oteo, *Mater. Charact.*, 2009, **60**, 506-512.

(*124*) X. Zhuang, Y. Wan, C. Feng, Y. Shen and D. Zhao, *Chem. Mater.*, 2009, **21**, 706-716.

(*125*) P. C. C. Faria, J. J. M. Orfao and M. F. R. Pereira, *Water Res.*, 2004, **38**, 2043-2052.

(*126*) Z. Yoshida, E. Osawa and R. Oda, *J. Phys. Chem. A*, 1964, **68**, 2895-2898.

(*127*) L. Abramian and H. El-Rassy, *Chem. Eng. J.*, 2009, **150**, 403-410.

(*128*) C. Moreno-Castilla, *Carbon*, 2004, **42**, 83-94.

(*129*) C. Moreno-Castilla, J. Rivera-Utrilla, M. V. Lopez-Ramon and F. Carrasco-Marin, *Carbon*, 1995, **33**, 845-851.

(*130*) I. Langmuir, *J. Am. Chem. Soc.*, 1918, **40**, 1361-1403.

(*131*) S. J. Allen, G. McKay and J. F. Porter, *J. Colloid Interface Sci.*, 2004, **280**, 322-333.

(*132*) C. A. Basar, *J. Hazard. Mater.*, 2006, **135**, 232-241.

(*133*) Y. Wong, Y. Szeto, W. Cheung and G. McKay, *Langmuir*, 2003, **19**, 7888-7894.

(*134*) Y. Wong, Y. Szeto, W. Cheung and G. McKay, *Process Biochem.*, 2004, **39**, 693-702.

(*135*) B. Acemioglu, *J. Colloid Interface Sci.*, 2004, **274**, 371-379.

(*136*) A. Kuleyin, *J. Hazard. Mater.*, 2007, **144**, 307-315.

(*137*) Y. Kim, C. Kim, I. Choi, S. Rengaraj and J. Yi, *Environ. Sci. Technol.*, 2004, **38**, 924-931.

(*138*) A. Benhammou, A. Yaacoubi, L. Nibou and B. Tanouti, *J. Colloid Interface Sci.*, 2005, **282**, 320-326.

(*139*) D. D. Do, *Adsorption analysis: Equilibria and kinetics*, Imperial College Press, 1998.

(*140*) M. Pu, Y.-H. Lui, L.-Y. Lui, X.-Z. Dong, J. He and D. G. Evans, *J. Phys. Chem. Solids*, 2008, **69**, 1084-1087.

(*141*) C. A. Basar, *J. Hazard. Mater.*, 2006, **B135**, 232-241.

(*142*) K. G. Bhattacharyya and A. Sharma, *Dyes and Pigments*, 2005, **65**, 51-59.

(*143*) V. C. Srivastava, M. M. Swamy, I. D. Mall, B. Prasad and I. M. Mishra, *Colloids Surf., A*, 2006, **272**, 89-104.

(*144*) H. Tang, W. Zhou and L. Zhang, *J. Hazard. Mater.*, 2012, **209-210**, 218-225.

(*145*) E. Guibal, P. McCarrick and J. M. Tobin, *Sep. Sci. Technol.*, 2003, **38**, 3049-3073.

(*146*) A. Kumar, S. Kumar, S. Kumar and D. V. Gupta, *J. Hazard. Mater.*, 2007, **147**, 155-166.

(*147*) P. S. Bauerlein, J. E. Mansell, T. L. ter Laak and P. de Voogt, *Environ. Sci. Technol.*, 2012, **46**, 954-961.

(*148*) C. Namasivayam and D. Kavitha, *J. Hazard. Mater.*, 2003, **98**, 257-274.

(*149*) A. A. M. Daifullah and B. S. Girgis, *Water Res.*, 1998, **32**, 1169-1177.

(*150*) M. Streat, J. W. Patrick and M. J. Camporro Perez, *Water Res.*, 1995, **29**, 467-472.

(*151*) C.-T. Hsieh and H. Teng, *Carbon*, 2000, **38**, 863-869.

(*152*) C. A. Hunter and J. K. M. Sanders, *J. Am. Chem. Soc.*, 1990, **112**, 5525-5534.

(*153*) C. A. Hunter, K. R. Lawson, J. Perkins and C. J. Urch, *J. Chem. Soc. Perkin Trans.*, 2001, **2**, 651-669.

(*154*) S. C. Ringwald and J. E. Pemberton, *Environ. Sci. Technol.*, 2000, **32**, 259-265.

(*155*) M. Keiluweit and M. Kleber, *Environ. Sci. Technol.*, 2009, **43**, 3421-3429.

(*156*) S. B. Haderlein and R. P. Schwarzenbach, *Environ. Sci. Technol.*, 1993, **27**, 316-326.

(*157*) D. Q. Zhu and J. J. Pignatello, *Environ. Sci. Technol.*, 2005, **35**, 2033-2041.

(*158*) A. Ozcan, E. Mine Oncu and A. Safa Ozcan, *Colloids Surf., A*, 2006, **277**, 90-97.

(*159*) I. A. W. Tan and B. H. Hameed, *Chem. Eng. J.*, 2007, **127**, 111-119.

(*160*) A. Dabrowski, P. Podkoscielny, Z. Hubicki and M. Barczak, *Chemosphere*, 2005, **58**, 1049-1070.

(*161*) Q.-S. Liu, T. Zheng, P. wang, J.-P. Jiang and N. Li, *Chem. Eng. J.*, 2010, **157**, 348-356.

(*162*) R.-L. Tseng, F.-C. Wu and R.-S. Juang, *Carbon*, 2003, **41**, 487-495.

(*163*) L. J. Kennedy, J. J. Vijaya, G. Sekaran and K. Kayalvizhi, *J. Hazard. Mater.*, 2007, **149**, 134-143.

(*164*) R. Aravindhan, J. R. Rao and B. U. Nair, *J. Hazard. Mater.*, 2009, **162**, 688-694.

(*165*) Y. S. Ho and G. McKay, *Process Biochem.*, 1999, **34**, 451-465.

(*166*) J. S. Zogorski, S. D. Faust and J. H. Hass, *J. Colloid Interface Sci.*, 1975, **55**, 329-341.

(*167*) M. N. Amin, A. I. Mustafa, M. I. Khalil, M. Rahman and I. Nahid, *Clean Techn. Environ. Policy*, 2012, **14**, 837-844.

(*168*) A. Gundogdu, C. Duran, H. B. Senturk, M. Soylak, D. Ozdes, H. Serencarn and M. Imamoglu, *J. Chem. Eng. Data*, 2012, **57**, 2733-2743.

(*169*) M. Kilic, E. Apaydin-Varol and A. E. Putun, *J. Hazard. Mater.*, 2011, **189**, 397-403.

(*170*) A. P. Terzyk, *J. Colloid Interface Sci.*, 2003, **268**, 301-329.

(*171*) K.-L. Chang, J.-F. Hsieh, B.-M. Ou, M.-H. Chang, W.-Y. Hseih, J.-H. Lin, P.-J. Huang, K.-F. Wong and S.-T. Chen, *Sep. Sci. Technol.*, 2012, **47**, 1514-1521.

(*172*) Y. S. Ho and C. C. Chiang, *Adsorption*, 2001, **7**, 139-147.

(*173*) H. Tang, W. Zhou and L. Zhang, *J. Hazard. Mater.*, 2012, **209-210**, 218-225.

(*174*) G. D. Sheng, D. D. Shao, X. M. ren, X. Q. Wang, J. X. Li, Y. X. Chen and X. K. Wang, *J. Hazard. Mater.*, 2010, **178**, 505-516.

(*175*) M. A. Salam and R. C. Burk, *Water, Air, Soil Pollut.*, 2010, **210**, 101-111.

(*176*) L. Khenniche and F. Benissad-Aissani, *J. Chem. Eng.*, 2010, **55**, 4677-4686.

(*177*) S. L. Gayatri and M. Ahmaruzzaman, *Assam Uni. J. Sci. Technol., Phys. Sci. Technol.*, 2010, **5**, 156-166.

(*178*) M. Z. Jacobson and M. A. Delucchi, in *Scientific American*, November 2009, pp. 58-95.

(*179*) C. Rhodes, *Chemistry & Industry*, 25th August 2008, **16**, 21-23.

(*180*) D. Kramer, *Physics Today*, 2010, **63**, 22-24.

(*181*) T. Dolenec, T. Serafimovski, G. Tasev, M. Dobnikar, M. Dolenec and N. Rogan, *Environ. Geochem. Health*, 2007, **29**, 21-32.

(*182*) J. D. Jorgenson, *Mineral Commodities Yearbook: Indium* 2002.

(*183*) A. C. Tolcin, *2002 Mineral Commodities Yearbook: Indium*, 2008.

(*184*) *USGS Minerals Commodity Summaries*, January 2010.

(*185*) J. Cui and E. Forssberg, *J. Hazard. Mater.*, 2003, **B99**, 243-263.

(*186*) J. Johnson, B. K. Reck, T. Wang and T. E. Graedel, *Energy Policy*, 2008, **36**, 181-192.

(*187*) D. Cohen, *New Scientist*, 2007, **2605**, 34-41.

(*188*) C. H. Jung and M. Osako, *Resour. Conserv. Recycl.*, 2009, **53**, 301-308.

(*189*) E. Baker, E. Bournay, A. Harayama and P. Rekacewicz, *Vital Waste Graphics*, UNEP, 2004.

(*190*) L. F. Mortensen and H. Mountford, *OECD Environmental Outlook*, OECD, Paris, 2001.

(*191*) K. Halada, UK-Japan Symposium on Green Manufacturing and Eco-Innovation, 2010, http://www.nims.go.jp/genso/lecture/0ej00700000030pw-att/0ej00700000034on.pdf, Accessed 23/05/13.

(*192*) K. Halada, K. Ijima, M. Shimada and N. Katagiri, *Journal of Japan Institute of Metals*, 2009, **73**, 151-160.

(*193*) T. E. Graedel, J. Allwood, J.-P. Birat, B. K. Reck, S. F. Sibley, G. Sonnemann, M. Buchert and C. Hagelucken, *Recycling Rates of Metals - A Status Report, A Report of the Working Group on the Global Metal Flows of the International Resource Panel*, UNEP 2011.

(*194*) M. B. G. Castro, J. A. M. Remmerswaal, M. A. Reuter and U. J. M. Boin, *Resour. Conserv. Recy.*, 2004, **43**, 1-19.

(*195*) C. Hageluken, *The Challenge of Open Cycles, R'07 8th World Congress, Davos, Switzerland,* 2007.

(*196*) M. B. Castro, J. A. M. Remmerswaal, J. C. Brezet, A. van Schaik and M. A. Reuter, *International Journal of Mineral Processing*, 2005, **75**, 255-281.

(*197*) M. B. G. Castro, J. A. M. Remmerswaal, J. C. Brezet and M. A. Reuter, *Resour. Conserv. Recy.*, 2007, **52**, 219-233.

(*198*) C. Hagelucken and C. Meskers, in *Strüngmann Forum Report: Linkages of Sustainability*, eds. T. E. Graedel and E. van der Voet, MIT Press, Cambridge, 2010, pp. 163-197.

(*199*) E. Brahmst, *Copper in End-of-Life Vehicle Recycling*, Centre for Automotive Research, 2006.

(*200*) G. M. Savage, C. G. Colueke and E. L. Von Stein, *Biocycle*, 1993, **34**, 58-61.

(*201*) J. Krook, N. Svensson and M. Eklund, *Waste Manage.*, 2012, **32**, 513-520.

(*202*) S. Renou, J. G. Givuadan, S. Poulain, F. Dirassouyan and P. Moulin, *J. Hazard. Mater.*, 2008, **150**, 468-493.

(*203*) P. Kjeldsen, M. A. Barlaz, A. P. Rooker, A. Baun, A. Ledin and T. H. Christensen, *Crit. Rev. Env. Sci. Technol.*, 2002, **32**, 297-336.

(*204*) J. Pichtel, *Waste management practices: municipal, hazardous and industrial*, Taylor & Francis Group, 2005.

(*205*) C. H. K. Lam, A. W. M. Ip, J. P. Barford and G. McKay, *Sustainability*, 2010, **2**, 1943-1968.

(*206*) G. Li and Y. Hu, *Mechanic Automation and Control Engineering (MACE), 2010 International Conference, IEEE, Wuhan, China, 2010*

(*207*) C. B. Oman and C. Junestedt, *Waste Manage.*, 2008, **28**, 1876-1891.

(*208*) P. H. Brunner and H. Monch, *Waste Manage. Res.*, 1986, **4**, 105-119.

(*209*) S. Karlsson, P. Carlsson, D. Aberg, K. K. Fedje, J. Krook and B.-M. Steenari, *Linnaeus ECO-TECH*, 2010, **10**, 22-24.

(*210*) T. Ishigaki, A. Nakanishi, M. Tateda, M. Ike and M. Fujita, *Chemosphere*, 2005, **60**, 1087-1094.

(*211*) C.-H. Jung and M. Osako, *Resour. Conserv. Recy.*, 2009, **53**, 301 - 308.

(*212*) C.-H. Jung and M. Osako, *Chemosphere*, 2007, **69**, 279-288.

(*213*) Y.-S. Chung, J.-H. Moon, S.-H. Kim, S.-H. Kang and Y.-J. Kim, *J. Radioanal. Nucl. Chem. Art.*, 2007, **271**, 339-344.

(*214*) L. S. Morf, R. Gloor, O. Hagg, M. Haupt, S. Skutan, F. D. Lorenzo and D. Boni, *Waste Manage.*, 2013, **3**, 634.

(*215*) Y. Hu, M. Bakker, G. Brem and G. Chen, *Waste Manage.*, 2011, **31**, 259-266.

(*216*) C.-H. Jung and M. Osako, *Waste Manage.*, 2009, **29**, 1532-1540.

(*217*) K. H. Wedepohl, *Geochim. Cosmochim. Acta*, 1995, **59**, 1217-1232.

(*218*) H. Ecke, H. Sakanakura, T. Matsuta, N. Tanaka and A. Lagerkvist, *Waste Manage. Res.*, 2000, **18**, 41-51.

(*219*) I. Vervenne, *3rd IEEE Benelux Young Researchers Symposium in Electrical Power Engineering*, Ghent, Belgium, 2006.

(*220*) U. U. Jadhav and H. Hocheng, *Journal of Achievements in Materials and Manufacturing Engineering*, 2012, **54**, 159-167.

(*221*) S. Nagib and K. Inoue, *Hydrometallurgy*, 2000, **56**, 269-292.

(*222*) K. Huang, K. Inoue, H. Harada, H. Kawakita and K. Ohto, *J. Mater. Cycles Waste Manage.*, 2011, **13**, 118-126.

(*223*) J. Xue, W. Wang, Q. Wang, S. Lui, J. Yang and T. Wui, *J. Chem. Technol. Biotechnol.*, 2010, **85**, 1268-1277.

(*224*) C. Brombacher, R. Bachofen and H. Brandl, *Applied and Environmental Microbiology*, 1998, 1237-1241.

(*225*) P. P. Bosshard, R. Bachofen and H. Brandl, *Environ. Sci. Technol.*, 1996, **30**, 3066-3070.

(*226*) W. Krebs, R. Bachofen and H. Brandl, *Hydrometallurgy*, 2001, **59**, 283-290.

(*227*) D. E. Salt, M. Blaylcock, N. P. B. A. Kumer, V. Dushenkov, B. D. Ensley, I. Chet and I. Raskin, *Nat. Biotechnol.*, 1995, **13**, 468-474

(*228*) I. D. Pulford and C. Watson, *Environmental International*, 2003, **29**, 529-540.

(*229*) C. W. N. Anderson, R. R. Brooks and R. B. Stewart, *Nature* 1998, **395**, 553-554.

(*230*) C. W. N. Anderson, R. R. Brooks, A. Chiarucci, C. J. LaCoste, M. Leblanc, B. H. Robinon, R. Simcock and R. B. Stewart, *Journal of Geochemical Exploration*, 1999, **67**, 407-415.

(*231*) I. Raskin, R. D. Smith and D. E. Salt, *Curr. Opin. Biotechnol.*, 1997, **8.2**, 221-226.

(*232*) B. Mattuschka and G. Straube, *J. Chem. Technol. Biotechnol.*, 1993, **58**, 57-63.

(*233*) J. R. Dodson, A. J. Hunt, H. L. Parker, Y. Yang and J. H. Clark, *Chem. Eng. Process.*, 2012, **51**, 69-78.

(*234*) B. Volseky and Z. R. Holan, *Biotechnol. Progr.*, 1995, **11**, 235-250.

(*235*) N. Das, *Hydrometallurgy*, 2010, **103**, 180-189.

(*236*) S. I. Ichikawa, K. Suyama, K. Arihara and M. Itoh, *Bioresour. Technol.*, 2002, **81**, 201-206.

(*237*) V. F. Hodge and M. O. Stallard, *Environ. Sci. Technol.*, 1986, **20**, 1058-1060.

(*238*) E. Helmers, M. Schwarzer and M. Schuster, *Environ. Sci. & Pollut. Res.*, 1998, **5**, 44-50.

(*239*) F. Zereini and F. Alt, eds., *Palladium Emissions in the Environment: Analytical Methods, Environmental Assessment and Health Effects*, Springer, Verlag Berlin Heidelberg, 2006.

(*240*) M. E. Farago, P. Kavanagh, R. Blanks, J. Kelly, G. Kazantzis, I. Thornton, P. R. Simpson, J. M. Cook, S. Parry and G. M. Hall, 1996, **354**, 660-663.

(*241*) J. D. Whiteley and F. Murray, *Sci. Total Environ.*, 2003, **317**, 121-135.

(*242*) *A. Murray Pat.*, US 2012/0000832 A1, 2012.

(*243*) Veolia, http://www.veolia.com/en/, Accessed 19/11/12.

(*244*) D. Derbyshire, http://www.davidderbyshire.co.uk-/stories240911.html, Accessed 19/11/12.

(*245*) K. Deplanche and L. E. Macaskie, *Biotechnol. Bioeng.*, 2008, **99**, 1055-1064.

(*246*) B. Pangeni, H. Paudyal, M. Abe, K. Inoue, H. Kawakita, K. Ohto, B. B. Adhikari and S. Alam, *Green Chem.*, 2012, **14**, 1917.

(*247*) C. Mack, B. Wilelmi, J. R. Duncan and J. E. Burgess, *Biotechnol. Adv.*, 2007, **25**, 264-271.

(*248*) C. Jeon, J. Y. Park and Y. J. Yoo, *Water Res.*, 2002, **36**, 1814-1824.

(*249*) H. Mimura, H. Ohta, K. Akiba and Y. Onodera, *J. Radioanal. Nucl. Chem. Art.*, 2001, **247**, 33-38.

(*250*) Y. Konishi, S. Asai, Y. Midoh and M. Oku, *Sep. Sci. Technol.*, 2006, **28**, 1691-1702.

(*251*) S. P. J. N. Senanayake, N. Ahmed and J. Fichtali, *Nutraceuticals and bioactives from Marine Algae, in handboon of seafood quality, safety and health applications*, Wiley-Blackwell, Oxford, UK, 2010.

(*252*) Solimabi and S. W. A. Naqvi, *National Instisute of Oceanography, Dona Paula - Goa*, 1975, **8**, 97-99.

(*253*) E. Fourest and B. Volesky, *Environ. Sci. Technol.*, 1996, **30**, 277-282.

(*254*) O. Raize, Y. Argaman and S. Yannai, *Biotechnol. Bioeng.*, 2004, **87**, 451-458.

(*255*) P. Zhou, H. Wang, J. Yang, J. Tang, D. Sun and W. Tang, *RSC Adv.*, 2012, **2**, 1759-1761.

(*256*) V. Murphy, S. A. M. Tofail, H. Huges and P. McLoughlin, *Chem. Eng. J.*, 2009, **148**, 425-433.

(*257*) Y. Ji, S. Jain and R. J. Davis, *J. Phys. Chem. B*, 2005, **109**, 17232-17238.

(*258*) J. D. Webb, S. MacQuarrie, K. McEleney and C. M. Crudden, *J. Catal.*, 2007, **252**, 97-109.

(*259*) M. T. Reetz and E. Westermann, *Angew. Chem. Int. Ed.*, 2000, **39**, 165-168.

(*260*) A. V. Gaikwad, A. Holuigue, M. B. Thathagar, J. E. ten Elshof and G. Rothenberg, *Chem. Eur. J.*, 2007, **13**, 6908-6913.

(*261*) J. Durand, E. Teuma and M. Gomez, *Eur. J. Inorg. Chem.*, 2008.

(*262*) https://seaweedindustry.com/seaweed/type/laminaria-digitata, Accessed 25/3/2013.

(*263*) D. J. Cole-Hamilton, *Science*, 2003, **299**, 1702-1706.

(*264*) R. R. Brooks, *Plants that Hyperaccumulate Heavy Metals*, International, New York, NY, 1998a.

(*265*) B. Sures, S. Zimmermann, J. Messerscmidt and A. von Bohlen, *Ecotoxicol. Environ. Saf.*, 2002, **11**, 385-392.

(*266*) X. E. Yang, X. X. Long, H. B. Ye, Z. L. He, D. V. Calvert and P. J. Stoffella, *Plant Soil*, 2004, **259**, 181-189.

(*267*) J. A. Bennett, N. J. Creamer, K. Deplanche, L. E. Macaskie, I. J. Shannon and J. Wood, *Chem. Eng. Sci.*, 2010, **65**, 282-290.

(*268*) L. S. Sobjerg, A. T. Lindhardt, T. Skrydstrup, K. Finster and R. L. Meyer, *Colloids and Surfaces B: Biointerfaces*, 2011, **85**, 373-378.

(*269*) T. Hennebel, S. van Nevel, S. Verschuere, S. De Corte, B. De Gusseme, C. Cuvelier, J. P. Fitts, D. van der Lelie, N. Boon and W. Verstraete, *Appl. Microbiol. Biotechnol.*, 2011, **91**, 1435-1445.

(*270*) G. Singaravelu, J. S. Arockiamary, V. Ganesh Kumar and K. Govindaraju, *Colloids and Surfaces B: Biointerfaces*, 2007, **57**, 97-101.

(*271*) S. De Corte, T. Hennebel, B. De Gusseme, S. Verschuere and N. Boon, *Microbial Biotechnology*, 2012, **5**, 5-17.

(*272*) G. Losfeld, V. Escande, P. V. La Blache, L. L'Huillier and C. Grison, *Catal. Today*, 2012, **189**, 111-116.

(*273*) N. C. Sharma, S. V. Sahi, S. Nath, J. G. Parsons, J. L. Gardea-Torresdey and P. T., *Environ. Sci. Technol.*, 2007, **41**, 5137-5142.

(*274*) J. L. Gardea-Torresdey, J. G. Parsons, E. Gomez, J. Peralta-Videa, H. E. Troiani, P. Santiago and M. Jose Yacaman, *Nano Lett.*, 2002, **2**, 397-401.

(*275*) S. Mandal, D. Roy, R. V. Chaudhari and M. Sastry, *Chem. Mater.*, 2004, **16**, 3714-3724.

(*276*) A. V. Pethkar, S. K. Kulkarni and K. M. Paknikar, *Bioresour. Technol.*, 2001, **80**, 211-215.

(*277*) I. Fleming, *Nature*, 1967, 151-152.

(*278*) S. R. Kelemen, M. Afeworki, M. L. Gorbaty and P. J. Kwiatek, *Energy Fuels*, 2002, **16**, 1507-1515.

(*279*) R. J. J. Jansen and H. van Bekkum, *Carbon*, 1995, **33**, 1021-1027.

(*280*) J. M. Lindquist, J. P. Ziegler and J. C. Hemminger, *Surf. Sci.*, 1989, **210**, 27-45.

(*281*) T. Maiyalagan and B. Viswanathan, *Mater. Chem. Phys.*, 2005, **93**, 291-295.

(*282*) J. Yang and H. Yen, *Plant Physiol. Biochem.*, 2002, **130**, 1032-1042.

(*283*) L. R. Hogge, D. W. Reed and E. W. Underhill, *J. Chromatogr. Sci.*, 1988, **26**, 551-556.

(*284*) B. A. Halkier and J. Gershenzon, *Annu. Rev. Plant Biol.*, 2006, **57**, 303-333.

(*285*) V. Lambrix, M. Reichelt, T. Mitchell-Olds, D. J. Kliebenstein and J. Gershenzon, *The Plant Cell*, 2001, **13**, 2793-2807.

(*286*) U. Wittstock and B. A. Halkier, *TRENDS in Plant Science*, 2002, **7**, 263-270.

(*287*) S. H. Joo, J. Y. Park, C.-K. Tsung, Y. Yamada, P. Yang and G. A. Somorjai, *Nature Materials*, 2009, **8**, 126-131.

(*288*) L. Jiang, A. Hsu, D. Chu and R. Chen, *J. Electrochem. Soc.*, 2009, **156**, B643-B649.

(*289*) S. R. Challa, A. T. Delariva, T. W. Hansen, S. Helveg, J. Sehested, P. L. Hansen, F. Garzon and A. K. Datye, *J. Am. Chem. Soc.*, 2011, **133**, 20672-20675.

(*290*) A. K. Datye, Q. Xu, K. C. Kharas and J. M. McCarty, *Catal. Today*, 2006, **111**, 59-67.

(*291*) J. H. Clark, D. J. Macquarrie and E. B. Mubofu, *Green Chemistry*, 2000, **2**, 53-56.

(*292*) I. P. Beletskaya and A. V. Cheprakov, *Chem. Rev.*, 2000, **100**, 3009-3066.

(*293*) F. Zhao, M. Shirai, Y. Ikushima and M. Arai, *J. Mol. Catal. A: Chem.*, 2002, **180**, 211-219.

(*294*) F. Zhao, B. M. Bhanage, M. Shirai and M. Arai, *Chem. Eur. J.*, 2000, **6**, 843-848.

(*295*) L. S. Sobjerg, D. Gauthier, A. T. Lindhardt, M. Bunge, K. Finster, R. L. Meyer and T. Skrydstrup, *Green Chem.*, 2009, **11**, 2041-2046.

(*296*) C. Torborg and M. Beller, *Adv. Synth. Catal.*, 2009, **351**, 3027-3043.

(*297*) A. Molnár, *Chem. Rev.*, 2011, **111**, 2251-2320.

(*298*) Z. Wang, P. Xiao, B. Shen and N. He, *Colloids and Surfaces A: Physicochemical and Engineering Aspects*, 2006, **276**, 116-121.

(*299*) S. Bruanauer, P. H. Emmett and E. Teller, *J. Am. Chem. Soc.*, 1938, **60**, 309-319.

(*300*) E. P. Barrett, L. G. Joyner and P. P. Halenda, *J. Am. Chem. Soc.*, 1951, **73**, 373-380.

(*301*) B. McEnaney, *Carbon*, 1967, **25**, 69-75.